University of Alberta

Three-dimensional Numerical Models of Drilling Induced Core Fractures

by

Lei Zhang

A thesis submitted to the Faculty of Graduate Studies and Research
in partial fulfillment of the requirements for the degree of

Master of Science

in

Geophysics

Department of Physics

©Lei Zhang
Fall 2011
Edmonton, Alberta

Examining Committee

Dr. Claire Currie, Department of Physics

Dr. Douglas R. Schmitt, Department of Physics

Dr. Walied Moussa, Department of Mechanical Engineering

Dr. Mathieu Dumberry, Department of Physics

Abstract

Drilling-induced fractures in borehole cores have distinct morphologies (e.g., petal, petal-centreline, saddle, and disk) and are produced under pure tensional stress, although most in-situ stresses are compressive. 3D numerical models show that tensile stress concentrations occur near the bottom of a vertical borehole. A new algorithm is developed to trace 3D tensile fractures for a range of crustal stress conditions. In a normal fault regime, fractures change from petal/petal-centreline to saddle to disk with increasing minimum horizontal stress (Sh). In a strike-slip regime, saddle fractures occur, except where Sh is much less than the vertical stress and petal centre-line fractures are found. In a thrust fault regime, saddle and disk fractures occur at low and high Sh, respectively. The results demonstrate that in-situ stress is the dominant control on fracture morphology; variations in Poisson's ratio and core stub length primarily affect the magnitude of tensile stress.

Table of Contents

List of Tables

List of Figures

Chapter 1
Introduction

1.1 Motivation

The stress regime in the crust controls crustal deformation, the initiation of earthquakes and micro seismicity, landslides, wellbore stability, natural fracture permeability, and hydraulic fracture initiation and propagation. However, it is difficult to make direct measurements of in situ crustal stress. Common techniques for assessing crustal stress include the study of borehole breakouts and controlled hydraulic fracturing ('mini-fracs'). Another indicator that is less well known, but not completely unrecognized, is the drilling induced core fractures [*Li and Schmitt*, 1998]. These fractures, or zones of damage, within the core stub are observed to have distinct morphologies, referred to as petal, petal-centreline, saddle, cup, and core-edge. Example photographs of the range of drilling induced fractures are shown in Figure 1.1 that highlight both the different types of shapes and the uniform spacing seen. Disc fractures appear as a circular line on the edge of the core with a flat fracture surface, uniformly spaced in core, as shown in Figure 1.1(a). Saddle fractures appear as a waved line on the edge of the core with a non-flat fracture surface, also uniformly spaced in core, as shown in Figure1.1(b). Petal fractures appear as a rapidly downward propagating fracture, 1.1(b). Petal fractures appear as a rapidly downward propagating fracture, 1.1(b). Petal fractures appear as a rapidly downward propagating fracture, Petal fractures
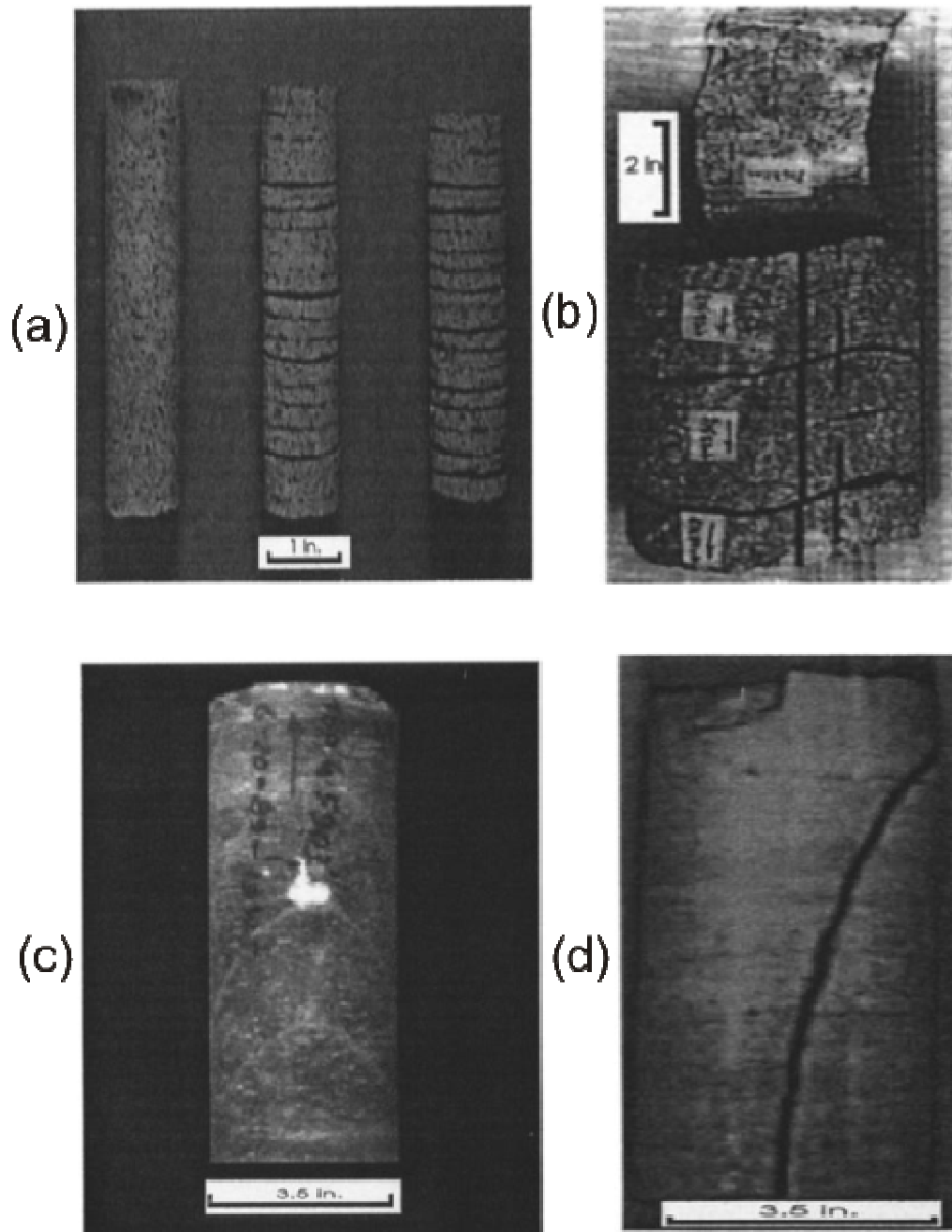
Figure 1.1: Fracture Morphology: (a) disc; (b) saddle; (c) petal; (d) petal centre line. Figure used courtesy of American Geophysical Union according to their reasonable use policy.

appear as a rapidly downward propagating fracture, uniformly spaced in core, as shown in Figure 1.1(c). A petal centreline fracture (Figure 1.1(d)) is similar to the petal fracture in shape, but it is tangential to the centre of the core stub.

All these observations can be classified into various categories as shown in Figure 1.2.
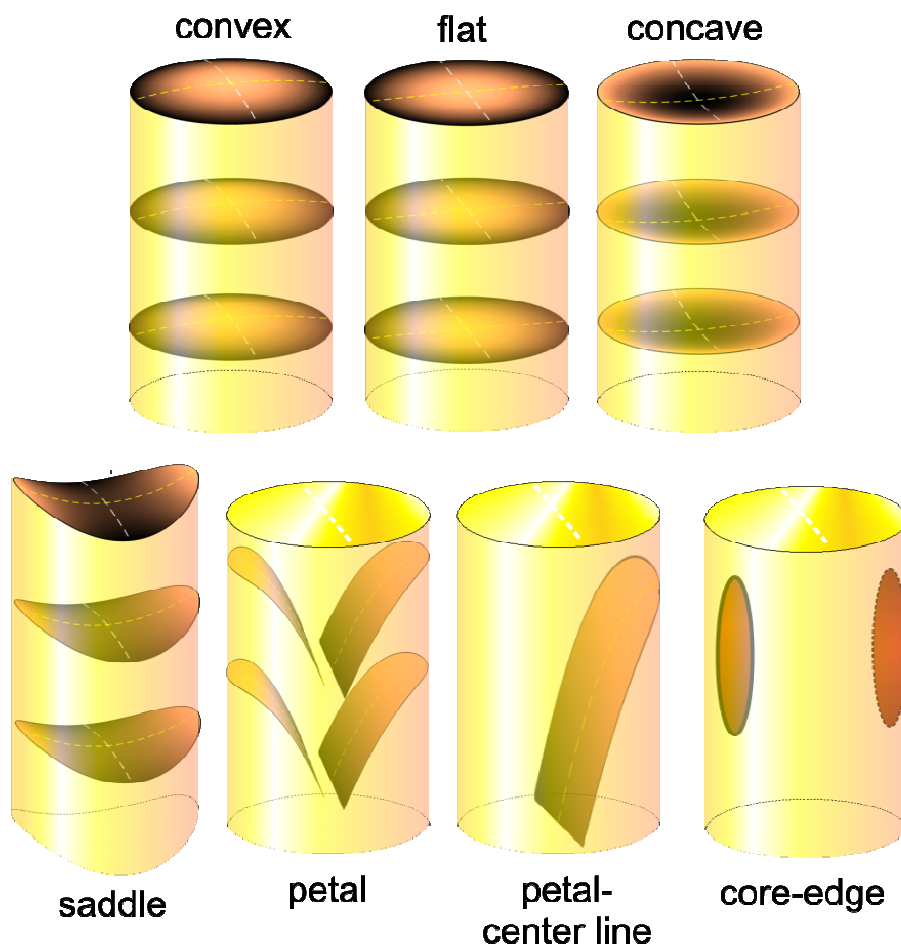
Figure 1.2: Classification of the types of drilling induced core fractures. Figure used courtesy of D.R. Schmitt.

Surprisingly, the morphology of the fractures suggests they are produced under a pure tensional stress, despite the fact that in almost all in situ conditions the state of stress within the crust is entirely compressive. Earlier numerical modeling [*Li and Schmitt*, 1997, 1998] has demonstrated that such pure tensions result from complex stress concentrations around the cylindrical geometry of a core stub before it is broken from the rock mass during borehole drilling. It is inferred that the morphology of the fractures and the point at which they initiate contain substantial information on the in situ stress state within the crust. Therefore, these fractures can provide an additional, independent constraint on principal stress directions and the relative magnitudes of the three principal stresses within the crust. The motivation of this thesis research is to determine the relationship between drilling-induced core fractures and crustal stress state.

1.2 Methodology

It is proposed that the distribution and morphology of borehole core fractures are related to the in-situ crustal stress. Consequently, a better understanding of these fractures requires detailed quantitative knowledge of the distribution of stresses within the rock at the bottom of the borehole during coring. However, the 3D bottom-hole geometry, particularly if a still attached core stub remains, is a formidable challenge to an analytic solution and a numerical one must be employed. In this study, 3D finite element models are used to investigate the origin of drilling-induced fractures and the stress conditions under which they form.

As a borehole is drilled into the crust, the pre-existing in-situ stress field will be modified in the vicinity of the borehole, resulting in stress concentrations which may lead to fracturing. First, the stress distribution near the bottom of a vertical borehole is calculated for different in situ stress conditions. The numerical solution for the stress distribution is obtained through a finite element package (the ANSYS™ program).

The calculated stress distribution is then used to evaluate the development of fractures within the core sample. The location of the maximum tensile stress is assumed to be the initiating point of the fracture. The location of this point varies depending on the in situ stress conditions, but usually it is located on the inner boundary of the drilling bit or the central line of the core. Fractures are then modeled as tensile failure and their trajectory is determined by the stress distribution within the core. This work builds on earlier studies [e.g., *Li and Schmitt*, 1997], which modeled fracture development in 2D, and this work extends this method to three dimensions.

1.3 Objectives

There are four main objectives for this thesis:

(1) Development of an accurate model of 3D stresses in the vicinity of a borehole. This model is generated with finite element package ANSYS™, and three different methods are applied to test the solution. This is a most important step as it determines the outcome of subsequent work.

(2) Creation of a database of 'base' stress solutions for different core stub lengths and Poisson's ratio. This database can be used to rapidly generate any in situ crustal stress condition using superposition.

(3) Development of an algorithm to calculate 3D fracture trajectories in the core, based on the stress distribution in the core and under the assumption of tensile failure of the core material.

(4) Investigation of the effect of in situ stress, core stub length and Poisson's ratio on the development of drilling-induced core fractures.

1.4 Outline of Thesis

This thesis consists of 5 chapters and 3 appendices. This first chapter, introduces the motivation for investigating the drilling induced core fracture, the significance of the in situ stress in producing such fractures, the methodology, and the objectives of the research.

Chapter 2 focuses on background information, including analysis of the concept of stress, the definitions used in the study, the illustration of the concepts of stress concentrations near cavities in a continuum, and rock failure criteria. These are all the tools necessary to understand the latter chapters. Further, an extensive review of qualitative and quantitative crustal stress measurement techniques is presented with particular focus on stress determination using, borehole geophysics, hydraulic fracturing, borehole breakout, and drilling induced tensile fractures. This chapter concludes with a review of the drilling induced core fracture

literature especially over the last ten years. Note that this chapter is currently in preparation for submission to the journal Tectonophysics.

Chapter 3 describes the numerical modelling approach used in this study. First, the geometry of the numerical model is given. Then the details of the ANSYS^{TM} stress calculations are provided, including the construction of the finite element mesh, the material parameters and the boundary conditions. Further, some care is taken to demonstrate the accuracy of the numerically calculated stress field. This is followed by a description of the 'base' solutions that form a database to be used to rapidly calculate any in situ stress field. Finally, the algorithm that was developed for tracing 3D tensile fractures through a core stub is given.

Chapter 4 applies the stress database and fracture modelling algorithm to the problem of drilling-induced core fractures. 3D stress models and fracture models are generated for a range of in situ crustal stresses, Poisson's ratios and core stub lengths in order to understand how these parameters influence the development of fractures. In particular, the fracture morphology, the point of fracture initiation and the likelihood of fracturing (given by the magnitude of tensile stress) are assessed.

Chapter 5 provides a comparison between previous 2D fracture studies [e.g., *Li and Schmitt*, 1997] and the 3D models presented in this thesis. It is shown that the 3D models are consistent with the earlier 2D work, and that the 3D models confirm that borehole core fractures are primarily related to the in-situ crustal stress field. A concise summary of the effects of in situ stress, Poisson's ratio and core stub length is given. This chapter ends with a discussion of how the 3D models can be modified in future work.

Appendix 1 explains the database of 'base' stress solutions that was developed during this thesis. The list of files associated with this database is given in Table A1.1.

Appendix 2 gives an overview of the MATLAB^{TM} codes that were written to trace fractures in 3D. The organization of the codes and the user interface within the codes are given, so that users can easily use the codes.

Appendix 3 is a text version of fracture tracing codes written in MATLAB^{TM}. A digital copy of all the data base files and fracture tracing codes is also supplied as an attachment to this thesis and is ready to run under the MATLAB^{TM} R2010a environment.

Chapter 2

Background: Stress concentrations and A Review of Stress Determination Methods[1]

2.1 Motivation

Crustal stresses are generated by gravitational loading, thermal expansion, pore fluid diffusion, elevation differences, and, of course, tectonic deformation. As such, crustal stress can tell us a great deal about dynamic processes within the Earth particularly with regards to plate tectonics where to a large degree we still do not fully understand what exactly drives or impedes plate motions or even movement along large faults. Stress states lead to the ultimate failure of rock at many scales ranging from the largest earthquakes to the smallest micro seismic events and having better knowledge of stress states is crucial to understanding such seismicity. Finally, knowledge of in situ stress states has practical implications with regards to the stability and safety of underground workings and boreholes, and the capacity to carry out hydraulic stimulations for water or hydrocarbon recovery. With the rapid rise of enhanced recovery from low permeability 'tight' sands and shales by hydraulic fracturing methods, the interest in understanding and detecting stress states has grown rapidly in recent years.

The problem is that stress remains an elusive quantity to measure or even to constrain. The purpose of this thesis is to better understand drilling induced core

---

[1] A modified version of this chapter is in preparation for submission to *Tectonophysics*

9

fractures, as these fractures contain a great deal of information about the state of in situ stress, both qualitatively and quantitatively. This chapter provides some background information that motivates our study including a brief review of basic elasticity theory in order to provide a framework upon which later chapters will rely, a discussion of current knowledge of crustal stresses, a summary of alternative stress measurement techniques, and a review of the literature associated with drilling induced fractures.

2.2 Basic Theory

The literature on elasticity theory is vast with numerous textbooks at a variety of levels readily available, and only a small overview is necessary here to set the definitions. First, at a given point in the solid Earth and relative to an arbitrary reference frame, the stresses, or normalized forces in units of Pascals (1 Pa = 1 N/m^2) are distributed around an infinitesimal cube as shown in Figure 2.1. Two types of stresses are noted: those whose tractions are perpendicular to the face of the cube and called normal stresses and denoted with a σ symbol, and those whose tractions are parallel to the surface called shear stresses and denoted using a τ symbol.

The nine values apparent in Figure 2.1 define a stress tensor σ that may be written in normal matrix format as:

$$\sigma = \begin{bmatrix} \sigma_{xx} & \tau_{xy} & \tau_{xz} \\ \tau_{yx} & \sigma_{yy} & \tau_{yz} \\ \tau_{zx} & \tau_{zy} & \sigma_{zz} \end{bmatrix} \qquad (2.1)$$

The first subscript represents the plane upon which the given stress acts and the second indicates the direction of the associated traction.

It needs to be noted that this is a symmetric matrix with, for example, $\tau_{yx} = \tau_{xy}$. This is a 2nd order stress tensor. The values of components of the stress tensor will change if the co-ordinate frame is rotated although the tensor essentially does not change. This is understood by analogy to a first order tensor that we normally call a vector with three components that values of which change depending again upon which co-ordinate system is employed. The transformation is affected by

$$\sigma' = A\sigma A^T \qquad\qquad (2.2)$$
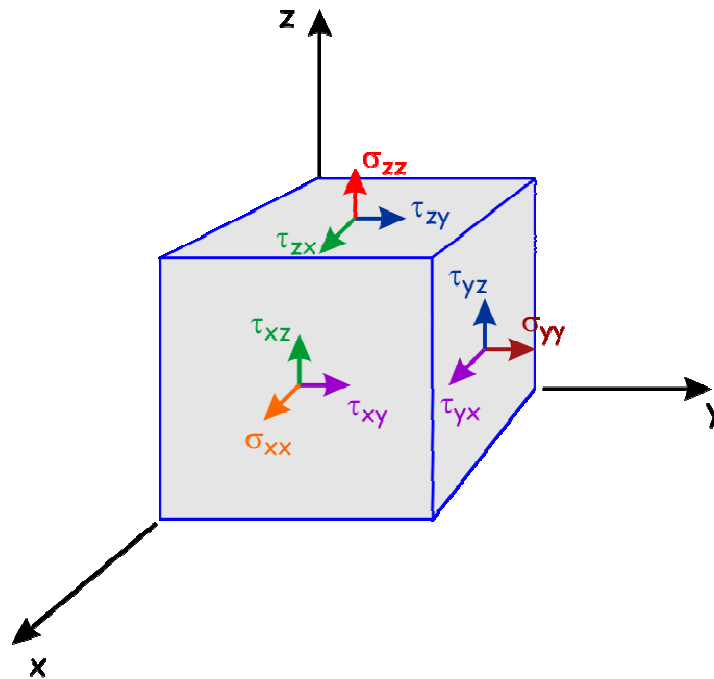
Figure 2.1: Complete stress state on infinitesimal cube of solid material in arbitrary *x-y-z* co-ordinate system with σ and τ representing normal and shear stresses, respectively. Stress sign convention shown with tensile normal stresses given positive sign is that used in usual engineering or physics studies and is employed in this thesis. In the geosciences and geotechnical engineering fields compressive normal stresses are taken with positive sign. Figure used courtesy of D.R. Schmitt.

where the rotation matrix A

$$A = \begin{bmatrix} a_{xx'} & a_{xy'} & a_{xz'} \\ a_{y'x} & a_{yy'} & a_{yz'} \\ a_{z'x} & a_{z'y} & a_{zz'} \end{bmatrix} \qquad (2.3)$$

is composed of the direction cosines a_{ij} between the original x-y-z and new x'-y'-z' co-ordinate frames.
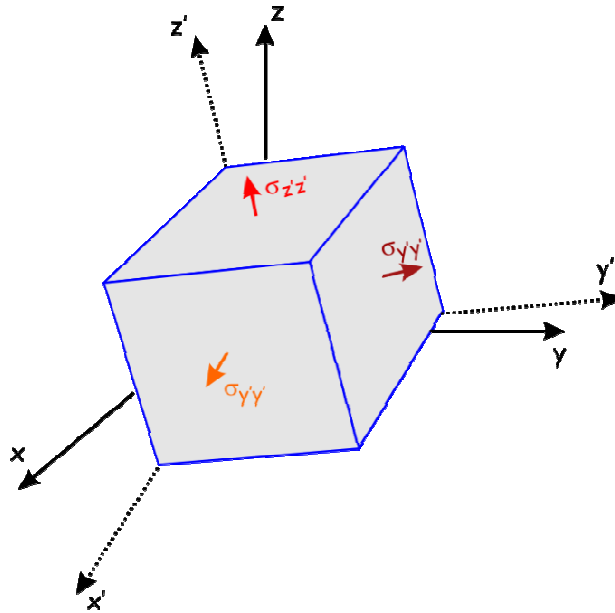
Figure 2.2: Rotation of the arbitrary co-ordinate frame *x-y-z* into the principal co-ordinate frame *x'-y'-z'* within which all the shear stresses vanish leaving only the three principal stresses. Figure used courtesy of D.R. Schmitt

Consequently, one may find a principal co-ordinate frame *x'-y'-z'* where all of the shear stresses vanish leaving only the three principal normal stresses with the rotated tensor appearing as:

$$\sigma' = \begin{bmatrix} \sigma_{x'x'} & 0 & 0 \\ 0 & \sigma_{y'y'} & 0 \\ 0 & 0 & \sigma_{z'z'} \end{bmatrix} \qquad (2.4)$$

This is also illustrated in figure 2.2. While there appears to be only three components in σ' it must be remembered that the directions of these stresses are known. This requires knowledge of three angles and such that six independent values must be obtained as exists more directly with σ.

A change in the stress state results in changes in both the volume and shape of an object. Briefly, a hypothetical fibre running through the material will undergo a change in length as the object deforms; this is referred to as a normal strain. A shear strain describes changes in the angles between two originally perpendicular fibres. For small strains, the strain tensor ε is

$$\varepsilon(x,y,z) = \begin{bmatrix} \varepsilon_{xx} & \varepsilon_{xy} & \varepsilon_{xz} \\ \varepsilon_{yx} & \varepsilon_{yy} & \varepsilon_{yz} \\ \varepsilon_{zx} & \varepsilon_{zy} & \varepsilon_{zz} \end{bmatrix} = \begin{bmatrix} \dfrac{\partial u_x}{\partial x} & \dfrac{1}{2}\left(\dfrac{\partial u_x}{\partial y} + \dfrac{\partial u_y}{\partial x}\right) & \dfrac{1}{2}\left(\dfrac{\partial u_x}{\partial z} + \dfrac{\partial u_z}{\partial x}\right) \\ \dfrac{1}{2}\left(\dfrac{\partial u_y}{\partial x} + \dfrac{\partial u_x}{\partial y}\right) & \dfrac{\partial u_y}{\partial y} & \dfrac{1}{2}\left(\dfrac{\partial u_y}{\partial z} + \dfrac{\partial u_z}{\partial y}\right) \\ \dfrac{1}{2}\left(\dfrac{\partial u_z}{\partial x} + \dfrac{\partial u_x}{\partial z}\right) & \dfrac{1}{2}\left(\dfrac{\partial u_z}{\partial y} + \dfrac{\partial u_y}{\partial z}\right) & \dfrac{\partial u_z}{\partial z} \end{bmatrix} \quad (2.5)$$

Where the displacement vector *u(x,y,z)* has the three components [u_x, u_y, u_z]. A principal strain tensor, too, may be found and in an isotropic material will align with the principal stresses. This strain tensor is symmetric. The reader should take care to note that the 'engineering strain' is also often employed with, for illustration, $\gamma_{xy} = 2\varepsilon_{xy}$ for a shear strains and $\gamma_{xx} = \varepsilon_{xx}$ for the normal strains. The advantage of engineering strains is that their value is that of the actual deformation that for shear strains is a small angle.

For the conditions of isotropic linear elasticity assumed in this thesis, stresses and strains are related to one another via Hooke's Law which may be written in a convenient Voigt matrix form as

$$
\begin{bmatrix} \varepsilon_{xx} \\ \varepsilon_{yy} \\ \varepsilon_{zz} \\ 2\varepsilon_{yz} \\ 2\varepsilon_{zx} \\ 2\varepsilon_{xy} \end{bmatrix} = \begin{bmatrix} \varepsilon_{xx} \\ \varepsilon_{yy} \\ \varepsilon_{zz} \\ \gamma_{yz} \\ \gamma_{zx} \\ \gamma_{xy} \end{bmatrix} = \frac{1}{E} \begin{bmatrix} 1 & -\upsilon & -\upsilon & 0 & 0 & 0 \\ -\upsilon & 1 & -\upsilon & 0 & 0 & 0 \\ -\upsilon & -\upsilon & 1 & 0 & 0 & 0 \\ 0 & 0 & 0 & 2(1+\upsilon) & 0 & 0 \\ 0 & 0 & 0 & 0 & 2(1+\upsilon) & 0 \\ 0 & 0 & 0 & 0 & 0 & 2(1+\upsilon) \end{bmatrix} \begin{bmatrix} \sigma_{xx} \\ \sigma_{yy} \\ \sigma_{zz} \\ \tau_{yz} \\ \tau_{zx} \\ \tau_{xy} \end{bmatrix} \qquad (2.6)
$$

Only two constants appear in the above. The first is the modulus of elasticity or Young's modulus E and the second is Poisson's ratio. These are the only elastic parameters that are needed to define the stress-strain behaviour of an isotropic linearly elastic material; these will be needed in later chapters. Examination of Equation 2.6 shows that for a given applied stress, the greater the value of E (a scalar), the smaller the strains. Further, larger the value of υ, the greater the shear strains. It will be seen later that while E can scale with the stresses linearly, υ will have an important control on the distributions of stresses near the borehole and it requires a special consideration of each υ employed.

Even though carried out briefly, this section has laid out the basic ideas necessary for the study of stress and strain relationships. The next section will introduce the concept of stress concentrations using an example of a long borehole.

2.3 Stress Concentrations
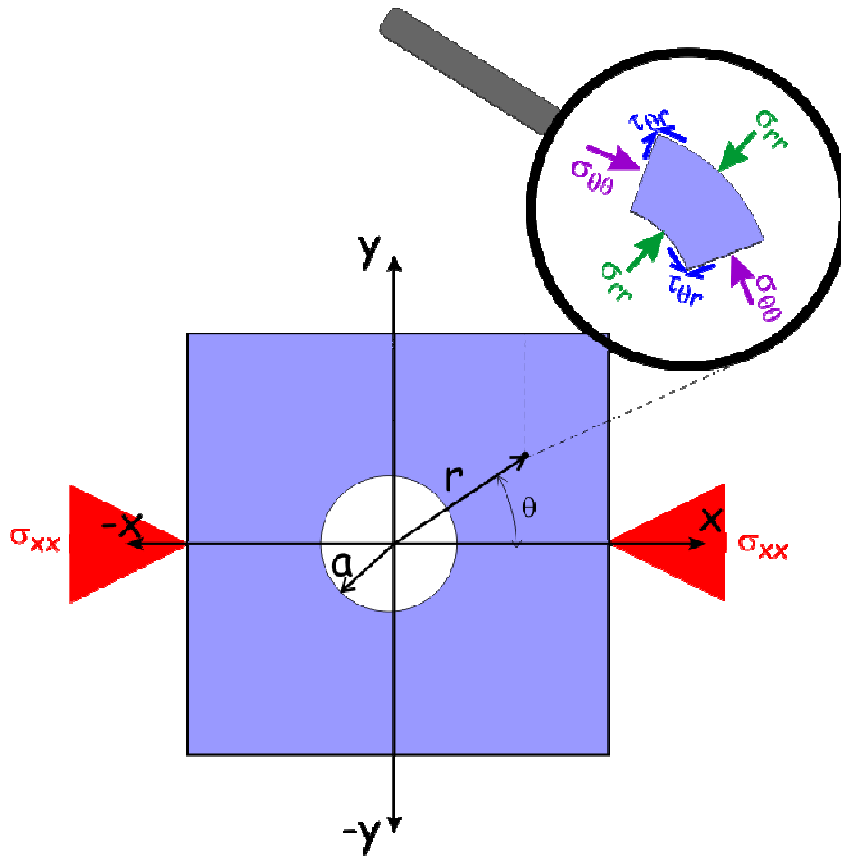
Figure 2.3: Geometry of Kirsch's [1898] solution for the stress concentrations due to a hole in a plate. Cylindrical element at location (r,θ) is magnified to show the cylindrical stresses acting on it. Figure used courtesy of D.R. Schmitt.

Within a homogeneous Earth we do not expect large and rapid stress gradients. This situation changes drastically, however, once some kind of cavity such as a tunnel, a mine drift, or a borehole is introduced. This cavity is said to 'concentrate' the pre-existing stresses. Such stress concentrations can lead to failure of stressed objects and consequently are of great interest in fields such as mechanical engineering where many objects must have holes [e.g., *Edwards*, 1951; *Pilkey, et al.*, 2008] even at the nanometer scale [*Ou, et al.*, 2009]. Later, this thesis focuses on the stress concentrations near the bottom of a borehole containing a core stub

15

that grows as coring continues. Here, however, we give a simpler example of stress concentrations for the simplest case of a circular hole of radius *a* in a horizontal plate subject to principal 'far-field' stress σ_{xx}. At a distance r from the hole axis and at azimuth θ measured with respect to the x-axis (Figure 2.3), the hole redistributes the stresses in its vicinity to maintain equilibrium according the classic 1898 solution of *Kirsch* [1898] with

$$\sigma_{rr} = \frac{\sigma_{xx}}{2}\left(1 - \frac{a^2}{r^2}\right) + \frac{\sigma_{xx}}{2}\left(1 + \frac{3a^4}{r^4} - \frac{4a^2}{r^2}\right)\cos(2\theta) \qquad (2.7)$$

$$\sigma_{\theta\theta} = \frac{\sigma_{xx}}{2}\left(1 + \frac{a^2}{r^2}\right) + \frac{\sigma_{xx}}{2}\left(1 + \frac{3a^4}{r^4}\right)\cos(2\theta) \qquad (2.8)$$

$$\tau_{\theta r} = -\frac{\sigma_{xx}}{2}\left(1 - \frac{3a^4}{r^4} + \frac{2a^2}{r^2}\right)\sin(2\theta) \qquad (2.9)$$

Where σ_{rr}, $\sigma_{\theta\theta}$ are the radial and azimuthal normal stresses and $\tau_{r\theta}$ is the shear stress generated by the applied far-field stress σ_{xx} a radial distance r from the axis of the hole of radius a at the cylindrical co-ordinates *(r, θ)*.

These stress concentrations can show some interesting patterns (Figure 2.4). For example, if σ_{xx} is compressional, a pure hoop tension $\sigma_{\theta\theta} = -\sigma_{xx}$ is generated at points on the hole in the direction of σ_{xx} (i.e. θ = 0° and 180°) but perpendicular to this (i.e, at θ = 90° and 270°) the hoop stress is amplified to $\sigma_{\theta\theta} = 3\sigma_{xx}$. Kirsh's [1898] equations have long been applied in the geosciences to understand borehole stability [*Bell and Gough*, 1979], hydraulic fracture initiation [*Hubbert and Willis*, 1957] and mine stability [e.g., *Li and Wang*, 2008].

The equations above are relatively straightforward; a simple analytic solution exists to find these stress concentrations. Figure 2.5 illustrates the stress distribution in the same geometry as in Figure 2.4, but with hydraulic pressure in
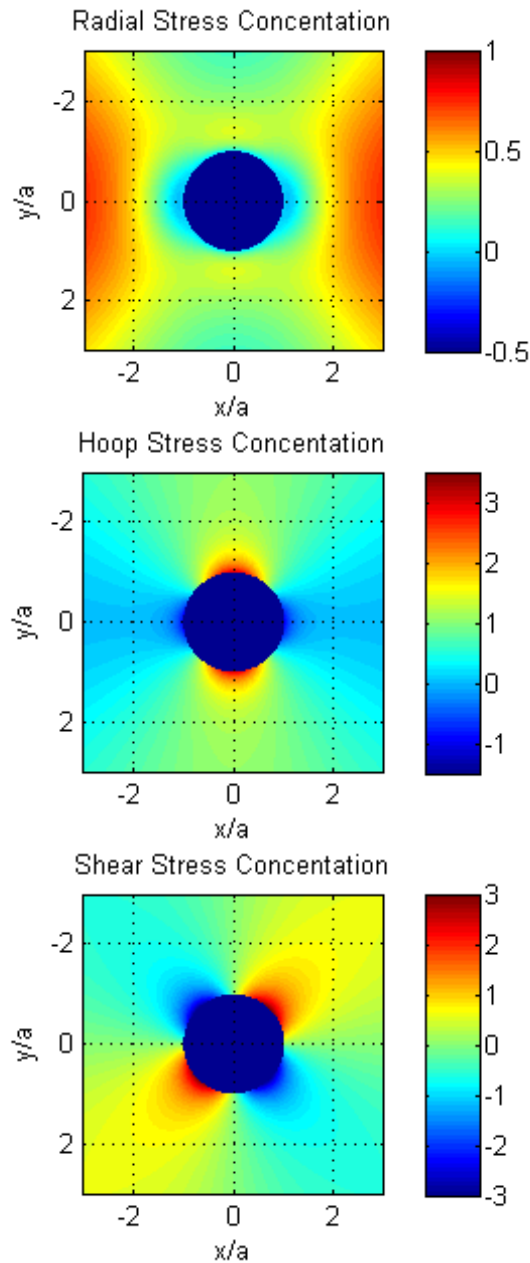
Figure 2.4: Illustration of the distribution of the stress concentrations in the vicinity of the hole in a plate subject to a far field compressive stress σ_{xx}. The hole is empty and supports no stress. The stress magnitudes shown are normalized with respect to the magnitude of the far-field applied stress σ_{xx}. Pure tension is reckoned negative in this figure. Figure used courtesy of D.R. Schmitt.
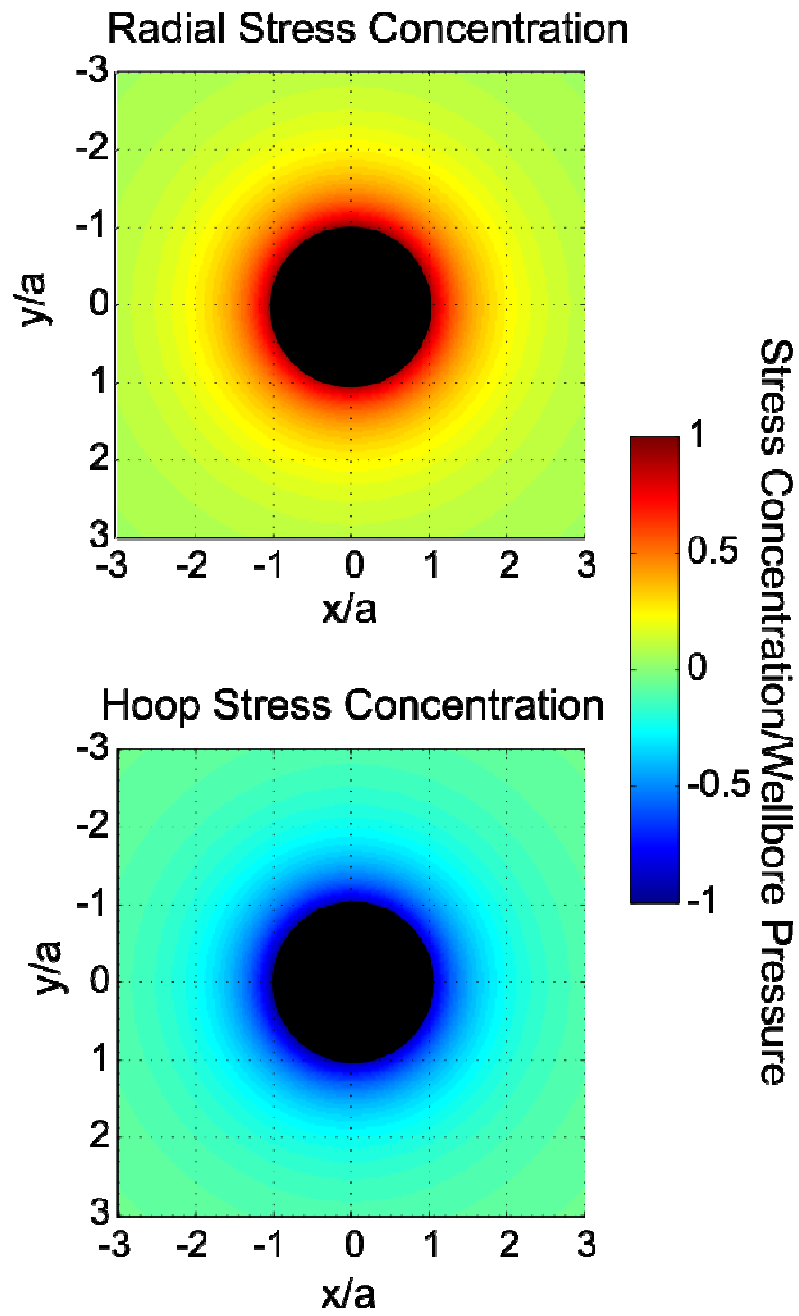
Figure 2.5: Illustration of the stress concentrations generated in the vicinity of a hole in a plate subject to an internal pressure P_w. Figure used courtesy of D.R. Schmitt.

the hole instead of far field stress σ_{xx}.

The Kirsch equations are, however, derived under 2D plane conditions and as shown in Equation 2.7-2.9, can only provide stress and displacement values with that plane. An ideal borehole is drilled in the 3D Earth, however, and out of plane normal and shear stresses also exist as illustrated for the general case of a long cylindrical cavity of radius *a* whose axis is arbitrarily oriented with respect to the principal stress state in the earth. Figure 2.6 shows two Cartesian co-ordinate frames with x-y-z having z aligned with the vertical and with x'-y'-z' aligned with the three principal stresses [$\sigma_{x'x'}$, $\sigma_{y'y'}$, $\sigma_{z'z'}$], respectively. The x-y-z frame is conveniently chosen such that borehole axis lies on the x-z plane. Following *Hiramatsu and Oka [1962]*, the *y*-axis passes through the origin perpendicular to the borehole axis that tilts at an angle ϕ relative to the *x*-axis. The third cylindrical r-θ–ζ co-ordinate frame is borehole centric with the ζ and borehole axes co-incident.

In terms of the three far-field principal stresses [$\sigma_{x'x'}$, $\sigma_{y'y'}$, $\sigma_{z'z'}$] and the direction cosines a_{ij} between x-y-z and x'-y'-z', the borehole centric stresses are conditions [*Edwards*, 1951; *Fairhurst*, 1964; *Hiramatsu and Oka*, 1962]

$$\sigma_r = \alpha_1 \left(1 - \frac{a^2}{r^2}\right) + \alpha_2 \left(1 - 4\frac{a^2}{r^2} + 3\frac{a^4}{r^4}\right)cos2\theta + \alpha_3 \left(1 - 4\frac{a^2}{r^2} + 3\frac{a^4}{r^4}\right)sin2\theta \qquad (2.10)$$

$$\sigma_\theta = \alpha_1 \left(1 + \frac{a^2}{r^2}\right) + \alpha_2 \left(-1 - 3\frac{a^4}{r^4}\right)cos2\theta + \alpha_3 \left(-1 - 3\frac{a^4}{r^4}\right)sin2\theta \qquad (2.11)$$

$$\sigma_\zeta = \beta_1 - 2v(\alpha_2 \frac{a^2}{r^2}cos2\theta - \alpha_3 \frac{a^2}{r^2}sin2\theta) \qquad (2.12)$$

$$\tau_{\theta\zeta} = \gamma_1 \left(1 + \frac{a^2}{r^2}\right)cos\theta + \gamma_2 \left(1 + \frac{a^2}{r^2}\right)sin\theta \qquad (2.13)$$

$$\tau_{r\zeta} = \gamma_1 \left(1 - \frac{a^2}{r^2}\right)sin\theta - \gamma_2 \left(1 - \frac{a^2}{r^2}\right)cos\theta \qquad (2.14)$$

$$\tau_{\theta r} = \alpha_2 \left(-1 - 2\frac{a^2}{r^2} + 3\frac{a^4}{r^4}\right) sin2\theta + \alpha_3 \left(1 + 2\frac{a^2}{r^2} - 3\frac{a^4}{r^4}\right) cos2\theta \tag{2.15}$$

where the coefficients include the geometrical rotations and principal stress information:

$$\alpha_1 = \frac{1}{2}\{(a_{11}^2 sin^2\phi + a_{12}^2 + a_{13}^2 cos^2\phi - 2a_{13}a_{11}sin\phi cos\phi)\sigma_{x'x'} +$$
$$(a_{21}^2 sin^2\phi + a_{22}^2 + a_{23}^2 cos^2\phi - 2a_{23}a_{21}sin\phi cos\phi)\sigma_{y'y'} + (a_{31}^2 sin^2\phi + a_{32}^2 +$$
$$a_{33}^2 cos^2\phi - 2a_{33}a_{31}sin\phi cos\phi)\sigma_{z'z'}\} \tag{2.16}$$

$$\alpha_2 = \frac{1}{2}\{(-a_{11}^2 sin^2\phi + a_{12}^2 - a_{13}^2 cos\phi + 2a_{13}a_{11}sin\phi cos\phi)\sigma_{x'x'} +$$
$$(-a_{21}^2 sin^2\phi + a_{22}^2 - a_{23}^2 cos^2\phi + 2a_{23}a_{21}sin\phi cos\phi)\sigma_{y'y'} + (-a_{31}^2 sin^2\phi +$$
$$a_{32}^2 - a_{33}^2 cos^2\phi + 2a_{33}a_{31}sin\phi cos\phi)\sigma_{z'z'}\} \tag{2.17}$$

$$\alpha_3 = a_{12}a_{13}cos\phi - a_{11}a_{12}sin\phi)\sigma_{x'x'} + (a_{22}a_{23}cos\phi - a_{22}a_{21}sin\phi)\sigma_{y'y'} +$$
$$+(a_{32}a_{33}cos\phi - a_{32}a_{31}sin\phi)\sigma_{z'z'} \tag{2.18}$$

$$\beta_1 = (a_{11}^2 cos^2\phi + a_{13}^2 sin^2\phi + 2a_{13}a_{11}sin\phi cos\phi)\sigma_{x'x'} + (a_{21}^2 cos^2\phi +$$
$$a_{23}^2 sin^2\phi + 2a_{23}a_{21}sin\phi cos\phi)\sigma_{y'y'} +$$
$$(a_{31}^2 cos^2\phi + a_{33}^2 sin^2\phi + a_{33}a_{31}sin\phi cos\phi)\sigma_{z'z'} \tag{2.19}$$

$$\gamma_1 = \{-a_{11}^2 sin\phi cos\phi + a_{13}^2 sin\phi cos\phi + a_{13}a_{11}(cos^2\phi - sin^2\phi)\}\sigma_{x'x'} +$$
$$\{-a_{21}^2 sin\phi cos\phi + a_{23}^2 sin\phi cos\phi + a_{23}a_{21}(cos^2\phi - sin^2\phi)\}\sigma_{y'y'} +$$
$$\{-a_{31}^2 sin\phi cos\phi + a_{33}^2 sin\phi cos\phi + a_{33}a_{31}(cos^2\phi - sin^2\phi)\}\sigma_{z'z'} \tag{2.20}$$

$$\gamma_2 =$$
$$(-a_{12}a_{13}sin\phi - a_{11}a_{12}cos\phi)\sigma_{x'x'} + (-a_{21}a_{23}sin\phi - a_{11}a_{12}cos\phi)\sigma_{y'y'} +$$
$$(-a_{32}a_{33}sin\phi - a_{31}a_{32}cos\phi)\sigma_{z'z'} \tag{2.21}$$

The reader should be aware that sign errors in the above have propagated through the literature, but *Fjaer et al.* [2008] have pointed out that the *Hiramatsu and Oka* [1962] equations are correct.
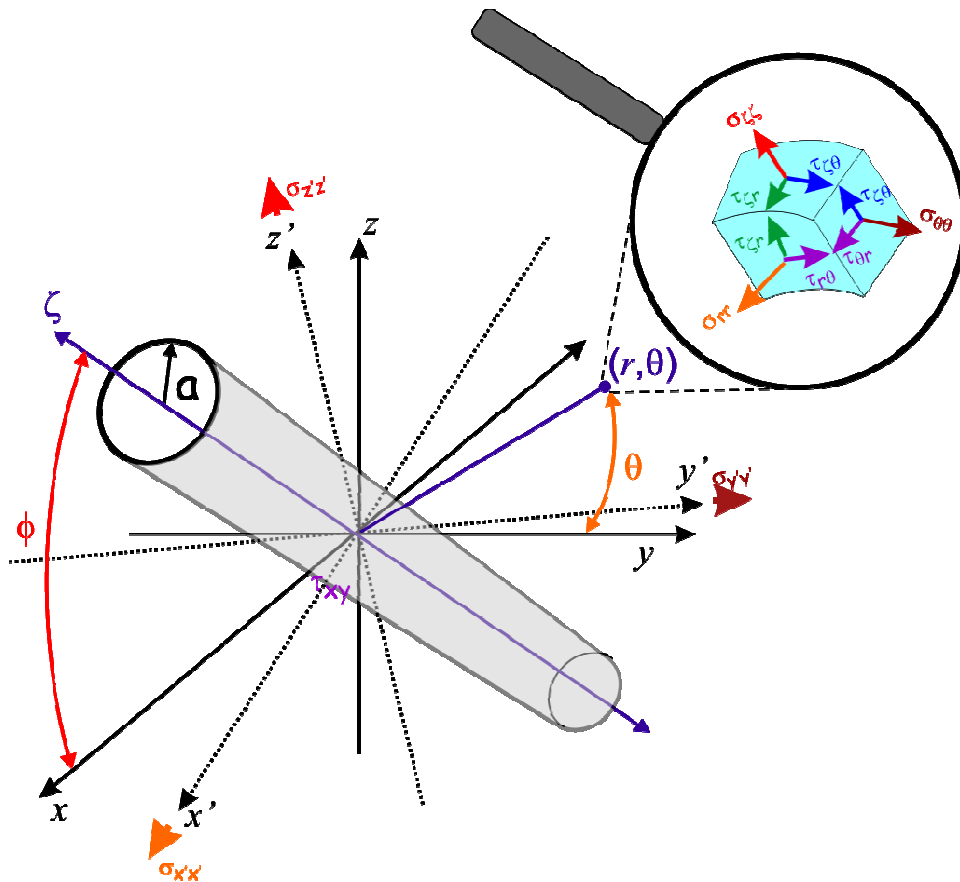
Figure 2.6: Co-ordinate frames and borehole centric stresses for the problem of an arbitrarily oriented borehole. Figure used courtesy of D.R. Schmitt.

The equations admit significant simplification at the borehole wall with r = a. (ζ) axis coincides with a principal stress (e.g., [*Cornet*, 1993; *Leeman and Hayes*, 1966]. In many cases it is assumed that the borehole is vertical (i.e. $\phi = \pi/2$) and Equation 2.10-2.15 reduces to:

$$\sigma_{\theta\theta} = \frac{\sigma_{xx}+\sigma_{yy}}{2}\left(1+\frac{a^2}{r^2}\right) - \frac{\sigma_{xx}-\sigma_{yy}}{2}\left(1+3\frac{a^4}{r^4}\right)\cos(2\theta) - \tau_{xy}\left(1+3\frac{a^4}{r^4}\right)\sin(2\theta)$$

$$(2.22)$$

$$\sigma_{\zeta\zeta} = \sigma_{zz} - \upsilon\{2(\sigma_{xx}+\sigma_{yy})\frac{a^2}{r^2}\cos(2\theta) + 4\tau_{xy}\frac{a^2}{r^2}\sin(2\theta)\} \qquad (2.23)$$

$$\sigma_{rr} = \frac{\sigma_{xx}+\sigma_{yy}}{2}\left(1-\frac{a^2}{r^2}\right) + \frac{\sigma_{xx}-\sigma_{yy}}{2}\left(1+3\frac{a^4}{r^4}-\frac{4a^2}{r^2}\right)\cos(2\theta) + \tau_{xy}\left(1+3\frac{a^4}{r^4}-\right.$$
$$\left.\frac{4a^2}{r^2}\right)\sin(2\theta) \qquad (2.24)$$

$$\sigma_{r\zeta} = (\tau_{xz}\cos(\theta) + \tau_{yz}\cos(\theta))(1+\frac{a^2}{r^2}) \qquad (2.25)$$

$$\sigma_{\theta\zeta} = (-\tau_{xz}\sin(\theta) - \tau_{yz}\cos(\theta))(1+\frac{a^2}{r^2}) \qquad (2.26)$$

$$\sigma_{r\theta} = \tau_{xy}\left(\left(1+2\frac{a^2}{r^2}-3\frac{a^4}{r^4}\right)\cos(2\theta) - \frac{\sigma_{xx}-\sigma_{yy}}{2}\left(1+2\frac{a^2}{r^2}-3\frac{a^4}{r^4}\right)\sin(2\theta) \quad (2.27)$$

One further consideration is that a real borehole in the Earth, however, is usually filled with some kind of drilling fluid be it water or dense muds. As with all fluids the pressure in the mud column will increase with depth. This fluid pressure P_w (here taken with positive sign) is a boundary condition on the wellbore wall that generates an axisymmetric stress field within the solid material $r \geq a$

$$\sigma_{rr} = P_w\frac{a^2}{r^2} \qquad (2.28)$$

$$\sigma_{\theta\theta} = -P_w\frac{a^2}{r^2} \qquad (2.29)$$

Upon examination it shows that a maximum tensile stress hoop stress $\sigma_{\theta\theta} = -P_w$ is generated immediately at the borehole wall with r = a. These formulas derive

from Lamé's solution for the stress concentrations in a long hollow cylinder (see Eqn. 44 and 45 of *Timoshenko and Goodier* [1970]).

The above stress concentrations are primarily static in nature, but both temperature and pore fluid pressure diffusion result in a stress field that is temporarily varied. Analytic solutions exist but as these depend critically on the boundary conditions and material properties (that may also be temperature or pore pressure sensitive) and a wide variety of situations can be addressed. In both problems, a diffusional equation must be solved. The solutions are analogous to one another to the point that both can share the same Figure 2.7. As the potential situations that can be solved are vast, we present here only two illustrative simple cases.

The first example is provided by *Stephens and Voight* [1982] who adapted *Ritchie and Sakakura's* [1956] thermo-elastic solutions for a hollow cylinder to study the stress concentrations at the borehole wall due to the application of a temperature T_w. It consists of a temperature gradient $\Delta T = T_w - T_\infty$ where T_∞ is both the initial uniform temperature of the system prior to perturbation and undisturbed temperature in the far-field of the borehole. Away from $r = a$ the solution depends on time as the temperature changes due to thermal diffusion, but immediately at the borehole wall the stresses are time independent as long as the temperature at the wellbore wall remains constant:

$$\sigma_{\theta\theta}(r = a) = \frac{\alpha E \Delta T}{1 - v} \qquad (2.30)$$

$$\sigma_{rr}(r = a) = 0 \qquad (2.31)$$

where α is the coefficient of thermal expansion. Increasing the temperature at $r = a$ effects a compressive hoop stress $\sigma_{\theta\theta}$ and *vice versa*. Although such thermal

effects are usually ignored, examination of Equation 2.30 shows that relatively large stresses are generated by modest changes in temperature (Figure 2.7). For a typical quartz-rich granite with E ~ 70 GPa a cooling of the wellbore wall by only 10° would generate a tensile stress $\sigma_{\theta\theta} = -22.4$ MPa, values that are easily of the order of the material's tensile strength. Indeed, *Wu et al. [2007]* employ temperature variations to control fracture propagation in hollow cylinders of Plexiglas.

Poro-elastic solutions for the stresses induced due to pore pressure diffusion are derived analogously [*Haimson and Fairhurst*, 1967; *Rice and Cleary*, 1976; *Schmitt and Zoback*, 1993]. For example, the hoop stress generated at *r = a* due to an instantaneous pressure change *ΔP = P$_w$ - P$_o$* is given by

$$\sigma_{\theta\theta}(r = a) = -\Delta P(1 - 2\eta) \qquad (2.32)$$

with

$$\eta = \frac{1}{2}(1 - \frac{K_d}{K_s})\frac{1-2v}{1-v} \qquad (2.33)$$

where *K$_d$* and *K$_s$* are the drained (or dry frame) and rock mineral moduli, respectively. The term *1 – K$_d$/K$_s$* is often called the Biot effective stress co-efficient.

The analogy between the thermal and fluid diffusion solutions is readily apparent in Figure 2.7, both of which are able to share the same figure.

Examination of these equations shows that pressurized fluid in the borehole generates a purely tensional, axisymmetric, hoop stress. Although in this thesis we ignore the effects of fluid pressure, it is important to the review of other stress measurements techniques. Note that the effect of fluid pressure on drilling induced fractures has been somewhat investigated [*Li and Schmitt*, 1997b; *Runzan*
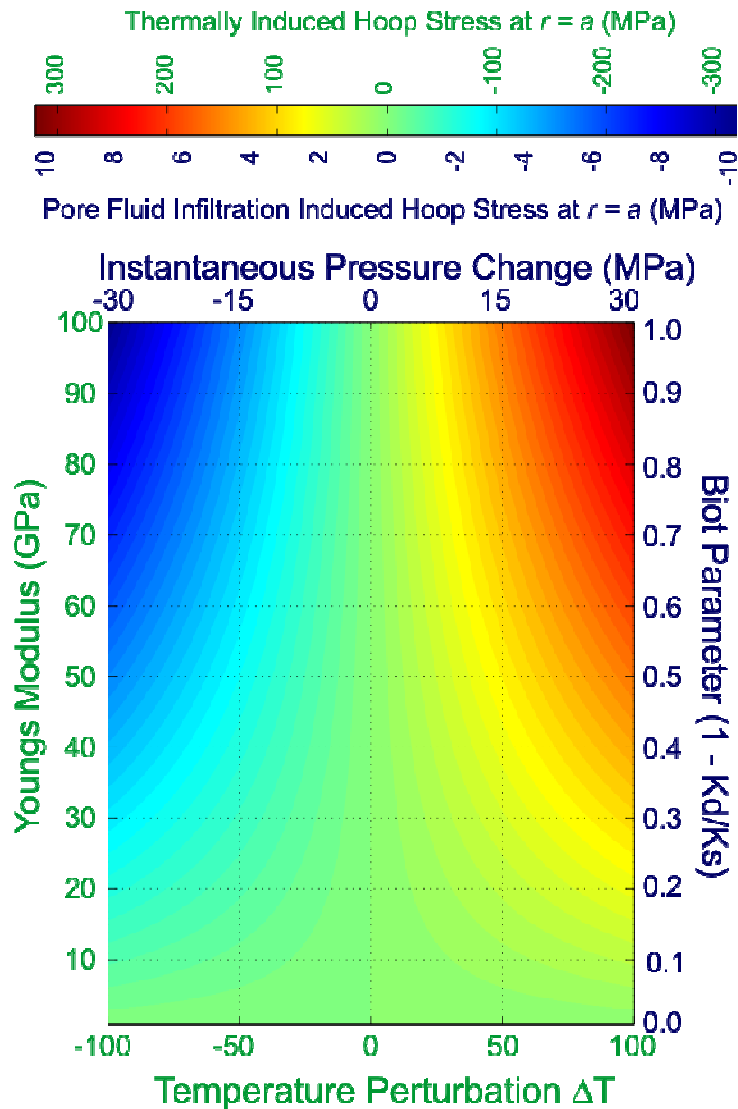
Figure 2.7: Illustration of the magnitudes of the hoop stresses generated at the borehole wall r = a for a poroelastic material of υ = 0.25 and as a function of the material's Biot parameter $1 - K_d/K_s$ and an instantaneous pressure change ΔP according to Equation 2.32, and of the magnitudes of the hoop stresses generated at the borehole wall $r = a$ for a material with $α = 8 \times 10^{-6}/°C$ and υ = 0.25 as a function of the material's Young's modulus E and the temperature perturbation ΔT according to Equation 2.30.   Tension is reckoned negative. Figure used courtesy of D.R. Schmitt.

and Schmitt, 2001], further work is necessary.

The above equations assume an isotropic and linearly elastic rock mass; and their examination reveals that, except for υ, the material properties are absent. However, real rock is usually much more complex [e.g., *Giovanni*, 1969] and solutions that consider the anisotropy of the rock mass [*Amadei*, 1983; *Fairhurst*, 1964] or time dependencies due to viscoelastic [*Wawersik and Stone*, 1989], poroelastic [*Abousleiman and Chen*, 2010; *Detournay and Cheng*, 1988; *Rice and Cleary*, 1976; *Schmitt and Zoback*, 1993], nonlinear elasticity [*Chin, et al.*, 2000; *Haimson and Tharp*, 1974; *Mahtab and Goodman*, 1968; *Meyer and Jacot*, 2001; *Mitaim and Detournay*, 2004; *Nawrocki*, 2010; *Santarelli, et al.*, 1986] and chemical [*Roshan and Rahman*, 2011] effects have been developed. The problems of stresses near long cavities is still of current interest with recent applications of conformal mapping techniques applied to differing cross sections [*Aadnoy and Angellolsen*, 1995; *Exadaktylos, et al.*, 2003]. However, nearly all stress analyses to date employ the simpler elastic solutions. The reader is referred to *Fjaer et al.,* [2008] for a comprehensive overview of these problems that includes details of the equations used in a variety of cases.

It must be noted that the geometry of a long cylindrical borehole is relatively symmetric and hence amendable to analytic solution. The bottom hole geometry being studied here is much less symmetric. Analytic solutions for such complicated problems cannot normally be solved without the use of numerical methods, and this is what will be employed in later chapters.

2.4 Rock Failure Criteria

It is important to briefly discuss how materials in general, and rocks in particularly fail; this information is obviously crucial to the interpretation of the drilling induced fractures.

By far, the most prevalent mode of failure in the Earth, which in nature is almost always in compression, is referred to as shear failure. Shear failure is most simply described using Mohr-Coulomb frictional failure theory described in many textbooks [*Jaeger et al.*, 2007]. The geometry of the failure is described in Figure 2.8 and the criteria states that shear failure occurs when

$$\tau = \sigma\mu + C \tag{2.34}$$

where μ is called the co-efficient of internal friction and C is the 'cohesion' in units of stress. The internal friction μ will control the angle with respect to σ_{max} at which shear failure will occur.
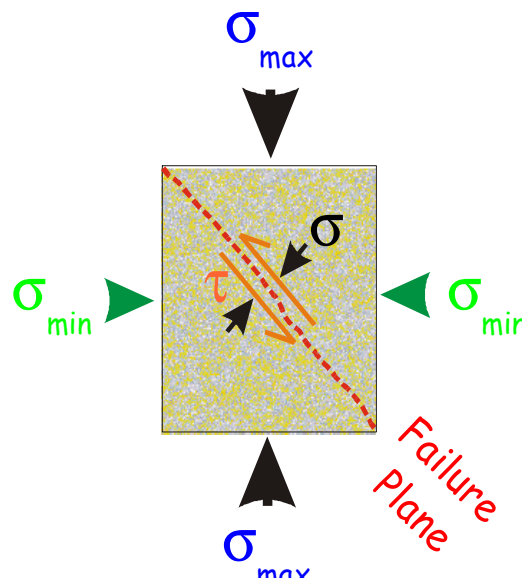
Figure 2.8: Geometry for the Mohr-Coulomb failure criteria. A mass of rock is subject to maximum and minimum compressive principal stresses σ_{max} and σ_{min}, respectively and these generate on the incipient failure plane normal and shear stresses σ and τ, respectively. Figure used courtesy of D.R. Schmitt.

However, drilling induced core fractures do not appear to be shear fractures; they are generated under conditions of pure tensile stress that are generated by the geometry at the borehole bottom while the core remains attached to the rock mass. As noted, such stress states are exceedingly rare in nature. In this case, a very simple criterion can be applied that states that tensile (pulling apart) failure will occur if the most tensile (least compressive) principal stress exceeds the 'tensile strength' T_o of the material. In such a case the tensile fracture will open in the direction of this tensile stress.

While we mostly consider shear and tensile failure in the analyses in this thesis, it is worth mentioning more recent developments with regards to compaction bands. These are highly localized zones observed in porous sandstones characterized by overall densification and micro crack damage to the mineral grains. That they do not display any shear offset suggests they 'close' to perpendicular to the greatest compression [*Mollema and Antonellini*, 1996] with loss of volume and hence can be called anti-mode I failure.

2.5 Crustal Stress States

When working with stresses in the Earth, we often assume that the direction of one of the principal stresses in the earth is vertical because the surface of the solid Earth is essentially a free boundary and because the stress generating acceleration of gravity *g* is directed downwards. As such, this principal stress is here denoted as *SV* will be expected to have a depth *h* and density ρ dependent magnitude:

$$SV(h) = -\int_0^h \rho(h)g\,dh \qquad (2.35)$$

where again the negative value arises due to the selection of the stress sign convention under the assumption that both *g* and *h* are positive numbers with the compression increasing with depth. By default, the other two principal stresses in the Earth must be directed horizontally and here we will denote them as SH and Sh to indicate the greatest and least horizontal principal compressions. SV may be estimated relatively easily if appropriate knowledge of the density overlying the point in question is known. The two horizontal stresses are not so readily found as they result from combinations of tectonic forces, induction from lateral constraint on the vertically stressed material, thermal anomalies, and fluid flow, just to name a few. Here we will assume for sake of a reference condition in this thesis that the virgin stress tensor in the earth will take the form of

$$S = \begin{bmatrix} SH & 0 & 0 \\ 0 & Sh & 0 \\ 0 & 0 & SV \end{bmatrix} \tag{2.36}$$

with *SH, Sh,* and *SV* aligned with the *x, y,* and *z* axes, respectively. Later in the thesis, it is these three principal 'far-field' stresses that will be applied to the finite element models.

The relative magnitudes of these three stresses to one another strongly controls the motion of faults in the earth and hence earthquakes and seismicity. These relative relationships are so critical to faulting theory applied by geophysicists and structural geologists that they serve as reference stress states and are introduced here to prepare for later discussion. A different kind of fault motion results from three different combinations of these stresses, and according to the pioneering developments of Anderson at the turn of the last century [see *Kanamori and Brodsky*, 2004]. These three reference states are referred to as:

29

- Normal or extensional faulting regime: SV > SH > Sh
- Thrust faulting regime: SH > Sh > SV
- Strike Slip faulting regime: SH > SV > Sh

As will be seen, it is often difficult to obtain truly quantitative measures of the complete or even the partial stress tensor (Equation 2.36) including directions. That said, however, knowledge of what faulting environment exists is still important.

2.6 Review of Stress Measurement Techniques

Stress is somewhat of an abstract concept and as a result measuring its direction and its magnitude within the Earth is not always straightforward. Another problem with trying to measure stress is that one must often physically reach the point in the Earth where the stress is to be measured, and this process alone is disruptive. Indeed, it will be seen that many stress indicators actually rely on the patterns produced by this disruption. The crustal stress measurement community is not necessarily large, but there is substantial literature and several good textbooks that outline stress measurement methods [e.g., *Amadei and Stephannson*, 1997; *Fjaer, et al.*, 2008; *Jaeger, et al.*, 2007; *Zang and Stephannson*, ; *Zoback*, 2007]. As such, we provide only a listing of methods used to indicate, estimate, or measure stress, with greater focus on those related to drilling induced fractures. These are organized on the basis of different classes.

2.6.1 Geological/Geophysical Indicators
- Igneous dyke or sill orientations: This concept is based on the assumption that a fluid driven fracture will open parallel to the

direction of the least compressive stress in the Earth. Consequently mapping 'recent' igneous dyke or sill orientations yields the direction of the least compressive stress [e.g., *Grasso, et al.*, 1991; *Gudmundsson*, 2006];

- Earthquake focal mechanisms: This relates back to the discussion of the classic Andersonian faulting regimes described above. Examination of earthquake records allow for constraint of the geometry of the faulting plane. It follows that if this orientation is known, then the type of fault has been determined and hence the Andersonian stress regime and its direction estimated. This is described in many seismological textbooks;

- Magma chamber and volcanic caldera orientations: Such features display a preferential alignment. For example, caldera collapses are usually elliptically shaped, not circular. This suggests some control of stress on their creation and this may be used to infer stress directions [*Paulsen and Wilson*, 2007; *Ruch and Walter*];

- Near surface features: The removal of rock due to quarrying or road construction can lead to stress relief features. Blast boreholes once revealed can display offsets [*Bell*, 1985] or axial fractures [*Pascal et al.*]. The floors of quarries can be subject to buckling fractures [*Adams*, 1982];

- Seismic anisotropy: Crack-like pore space, at any scale, is highly sensitive to the state of stress applied to the rock. For example, a rock containing randomly oriented cracks might be elastically isotropic until a uniaxial stress is applied to the material. This stress will preferentially close those cracks with planes perpendicular to the stress direction and consequently make the rock anisotropic [e.g., *Pyraknolte et al.*, 1990]. One manifestation

31

of this is that the seismic velocities become anisotropic (i.e. change with direction of propagation through the material) and if this can be sensed by transmission or reflection. The literature on this topic is large but some recent papers include *Vilhelm et al. [2010]*

2.6.2 Stress Relief Techniques

These methods all rely on measuring the small displacement or strains induced by perturbing the geometry of an object. That is, the material must vary its shape in response to a change in its geometrical boundaries due the redistribution of stresses. In the context of the geosciences, this mostly refers to shallow borehole or cores studies. These include various techniques to measure the stress relief deformation near a slot cut into a stressed rock mass [*Corthesy et al.*, 1999], various 'overcoring' methods [*Leite et al. 2010*], and laser interferometric based hole drilling techniques [*Schmitt et al.*, 2006]. The difficulty with these methods is that small strains or displacements must be measured causing some technical complexity and rock is a notoriously ill-behaved heterogeneous material and small flaws can significantly influence the results. These methods are used primarily in mining and geotechnical studies.

There are two variations on this theme that are worth mentioning as they are carried out on cores retrieved from the borehole.

The first method employs the concept that rocks, like many advanced materials, retain some 'memory' of the stresses they had experienced. The Kaiser effect [*Kaiser*, 1950; *Li and Nordlund*, 1993] involves monitoring of acoustic emissions as a material is stressed. This method presumes that no new crack damage is initiated in the sample, with the result that there are no acoustic emissions detected, until the samples is stressed past its original in situ stress state at which

point new damage, and acoustic emissions occur. *Yamamoto* [2009] uses similar ideas but by carefully measuring strains during reloading of a rock sample to estimate stress magnitudes.

The second method is called 'Anelastic Strain Recovery' (ASR) [*Engelder*, 1984; *Lin et al.*, 2006; *Matsuki*, 2008; *Matsuki and Takeuchi*, 1993; *Wolter and Berckhemer*, 1989]. The underlying premise of this technique is that rocks are viscoelastic materials. As such, their deformation is time-dependent; and as the initial stress relaxes, the sample creeps in response. As such, workers monitor the creep behaviour of the core with time immediately upon recovery from the earth. The 3D deformation is then inverted via a model of viscoelastic behaviour to provide an estimate of the stress directions and magnitudes.

2.7 Borehole Geophysics

As noted earlier, it is often not so much the stress that is measured directly, but rather its manifestations in a perturbed Earth. The stress concentrations as shown by *Kirsch's* [1898] solutions above illustrate this well. The only way for us to directly sample in the Earth is by creating a cavity. This cavity must concentrate the stresses as shown in Figure 2.4; the patterns of the disruption are what can be measured. These stress concentrations amplify the virgin in situ stresses and produce substantive anisotropy of the elastic properties or can lead to different kinds of failure of the borehole. The latter are of particularly economic concern as unstable borehole conditions can be costly to drilling operations.

Anisotropy: As noted earlier, cracks are highly sensitive to the stresses acting perpendicular to their plane. Heuristically, the greater the compression normal to

the crack plane, the more the crack will close. The greater the crack closure the stiffer the material becomes. Consequently, this pressure-dependent crack porosity is manifest as a substantial nonlinear elastic response in most rocks. This nonlinear behaviour has long been known from the earliest measurements of rock deformation [*Adams and Williamson*, 1923; *Zisman*, 1933] and was attributed by these early workers to this progressive closure of what we today would call microcrack porosity. One implication of this is that application of anisotropic stress states to a rock mass produces elastic anisotropy in the rock. For example, a greater compression along one axis than another will result in greater crack closure and hence stiffness in that same direction. [e.g., *Holt, et al.*, 1993; *Johnson and Rasolofosaon*, 1996; *Majmudar and Behringer*, 2005; *Rathore, et al.*, 1995; *Zheng*, 2000] and various approaches have been taken to evaluate this nonlinearity using higher order elastic constants [e.g., *Sinha and Winkler*, 1999] or by closure of the porosity [*Ciz and Shapiro*, 2009].

As noted earlier, the borehole cavity will concentrate the stresses in the Earth according to Kirsch and produce a series of quite anisotropic stresses around the wellbore. The variation in stresses circumferentially around the borehole induces variations in the elastic properties around the borehole as observed by *Winkler*, [1996] and Schmitt et al. These stress-dependent properties can be measured in a number of different ways by direct measurement of velocity (Figure 2.9) [*Balland and Renaud*, 2009; *Winkler*, 2005; *Winkler and D'Angelo*, 2006]. The differences in shear wave speeds at different azimuths around the wellbore as detected by a dipole sonic logging tool [*Sun and Prioul*, 2010*; Cengiz, et al.*, 1994; *Mueller, et al.*, 1994; *Winkler, et al.*, 1998; *Bose, et al.*, 2007; *Sinha, et al.*, 2000; *Ashraf Mohammed and Younane*, 2008; *Barton*, 2006; *Iturrino, et al.*, 2005; *Plona, et al.*,
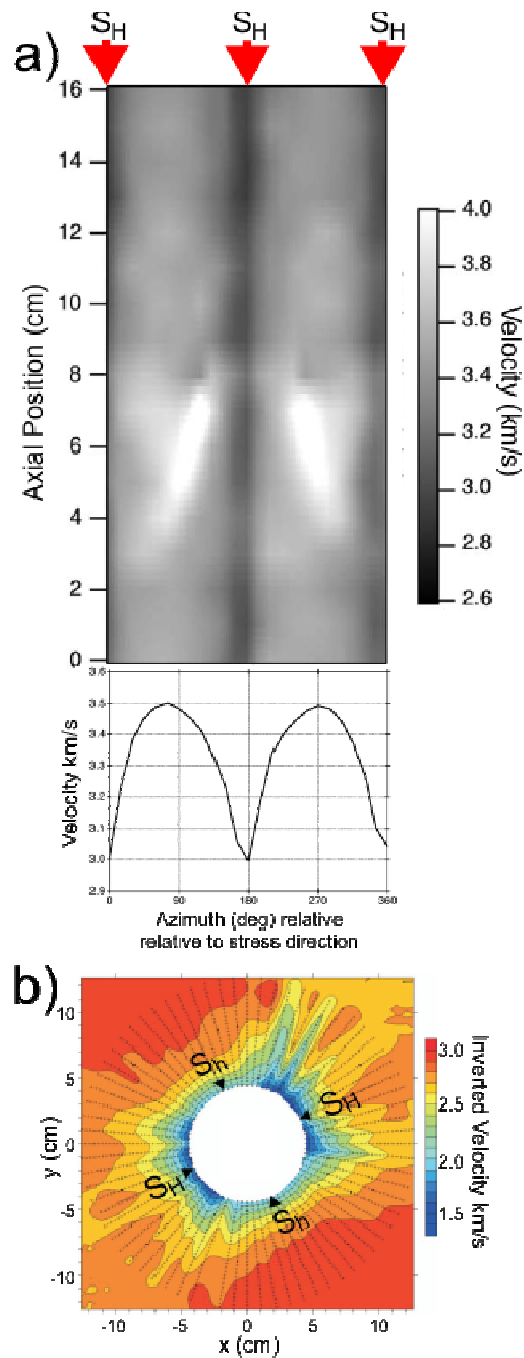
Figure 2.9: Examples of stress induced velocity variations in the vicinity of a borehole. a) Unwrapped image (top panel) of the apparent P-wave velocity parallel to the borehole axis as imaged along a laboratory test borehole subject to a compression SH of 10 MPa parallel to azimuths of $\theta = 0°$ and 180° and the corresponding average velocity (bottom panel) at each azimuth (adapted from [*Winkler and D'Angelo*, 2006]). Red arrows mark the azimuths at which the greatest compression is applied externally. b) Plan view looking down along the borehole axis of inverted velocities obtained along a number of differing radii (from [*Balland and Renaud*, 2009]). All figures used here are courtesy of the Society of Exploration Geophysicists according to their reasonable use policy.

35

2007], and by dispersion analysis of the guided Stoneley and flexural wave modes detected during sonic logging.

2.8 Hydraulic Fracturing

An artificial hydraulic fracture is created by rapidly pressurizing a sealed section of a wellbore until the in situ stresses and the rock strength is overcome and a fracture propagates away from the borehole (Figure 2.10). The fracture will continue to extend away into the geological formation; the fracture essentially increases the effective surface area of the borehole and allows much larger volumes of fluid to be extracted. Because the fluid pressures involved must overcome the stresses and the material strength in order to initiate, propagate, and remain 'open', the pressurization histories contain a great deal of information on the in situ state of stress.

A detailed description of a hydraulic fracturing stress measurement procedure is given by *Haimson and Cornet* [2003] and *Zoback* [2007] and only a brief outline is given here. Indeed, a simplified discussion of the pressurization record obtained is provided that illustrates only the essential elements of a record and ignores its finer details, the interpretation of which is beyond the scope of this thesis [*Gjonnes et al.*, 1998; *Hayashi and Haimson*, 1991; *Ito et al.*, 1999; *Nelson et al.*, 2007]. In open-hole (i.e. uncased) boreholes, a typical hydraulic fracturing test (Figure 2.10) begins with sealing of an interval along the borehole with two packers. Here, for the purposes of illustration the ideal case hydraulic fracturing from a borehole drilled parallel to the vertical stress into a linearly elastic, nonporous material with tensile strength T_o is considered. A simplified and

36

hypothetical pressurization record illustrates the process (Figure 2.11) with three pressurization cycles.
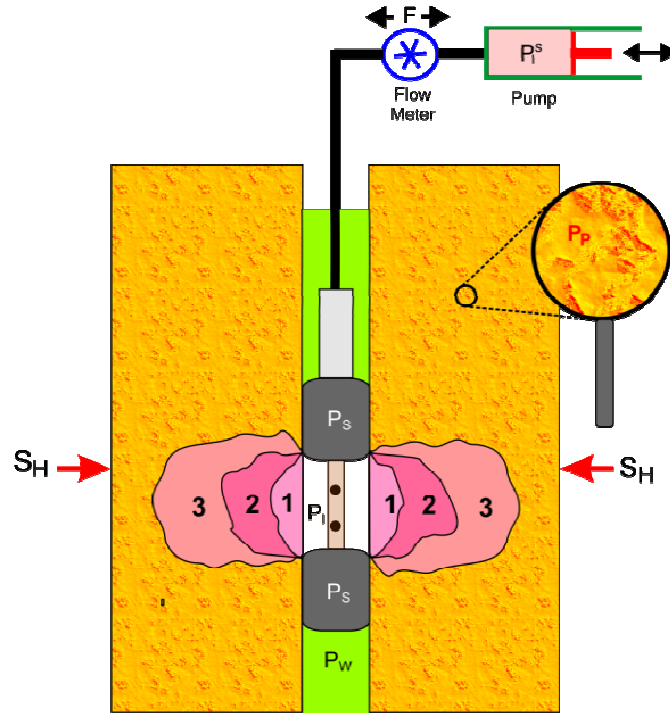
Figure 2.10: Outline of the principal components of a hydraulic fracturing stress measurement. An interval along the borehole is isolated by two inflatable packers to pressure P_S. The pressure in the interval P_I is then increased from ambient well bore pressure P_W by pumping fluid in. The interval pump pressure at the surface is P_I^S and the fluid flow rate F into and out of the interval is measured by the flow meter. The induced fracture extends successively with each of three P_I pressurization cycles in the direction of SH and opens against Sh. The pore pressure in the formation is P_P. Figure used courtesy of D.R. Schmitt.

In the first cycle, the interval is first rapidly pressurized from that ambient P_o until a rapid drop in the interval pressure P_I occurs even if pumping to the interval continues; the maximum value of P_I is called the break-down pressure P_B. The drastic reduction in pressure results from the abrupt increase in the interval volume due to the incipient opening of the fracture.

At this point the pumping ceases and the interval is 'shut-in'; P_I then relaxes to an equilibrium pressure P_{SI}. Although heterogeneities in the rock mass may locally divert it, once it is away from the borehole stress concentrations the fracture will open in the direction of the least compressive stress [*Hubbert and Willis*, 1957;
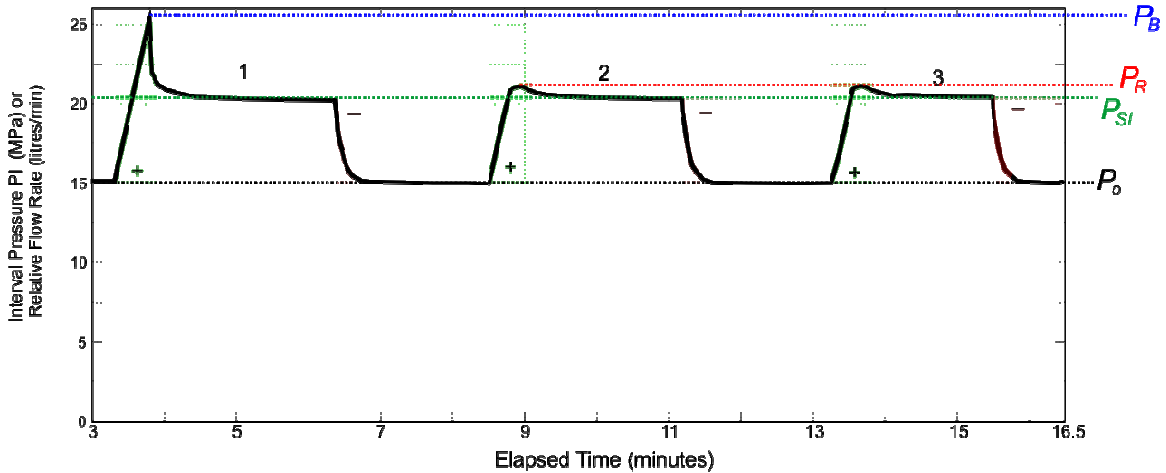
Figure 2.11: Illustration of a typical hydraulic fracturing (micro-frac) stress measurement. Green and red areas represent the flow rates into and out of the interval, these are each individually shifted with respect to the pressurization curve but are scaled appropriately. PB – break-down pressure, PR – reopening pressure, PSI – shut in pressure, Po – ambient wellbore pressure. Derived from data obtained at the ANDRILL SMS 2007 drilling project (Schmitt et al, unpublished).

Murdoch, 1995; *Warren and Smith*, 1985] although this may be complicated by horizontal fractures that intersect the borehole [e.g., *Evans, et al.*, 1988]. Hence, once the fracture exists, it can remain jacked open as long as the interval pressure P_{SI} is at least equal to the minimum compression which is Sh for strike-slip and normal faulting and SV for thrust faulting regimes.

After an appropriate equilibration, the interval pressure is released and decays back to the ambient borehole pressure prior to the experiment. The excess fluid in the interval will flow back to the surface reservoirs.

The cycle is repeated a number of times. On the second cycle the pressure increases until the already created fracture reopens. Again a rapid drop in the pressure accompanies the increased volume, but the interval pressure P_R at which this occurs is smaller than P_B because the rocks tensile strength no longer needs to be overcome. Some authors have suggested that the difference $P_B - P_R$ gives a useful value for T_o.

As already noted, P_{SI} gives a reliable quantitative measure of the minimum compression in the Earth. In addition, however, P_B and to some extent P_R contain information on the stress concentrations immediately at the borehole wall ($r = a$). For the simple case being studied, the incipient fracture initiation occurs when the P_I-induced $\sigma_{\theta\theta}$ tension (Equation 2.37) overcomes both T_o and the concentrations of the SH and Sh; this will occur at the SH azimuths ($\theta = 0^o$ and 180°). This knowledge too allows the stress directions to be found from oriented images of the borehole. Consequently, at breakdown ($P_I = P_B$) and where $P_{SI} = Sh$ the maximum horizontal compression is

$$SH = 3Sh + T_0 - P_B \qquad (2.37)$$

Equation 2.37 of course is the simplest 'break down' equation that can be written and has many deficiencies. It does not include, for example, the thermoelastic (Equation 2.30-2.31) or the poroelastic (Equation 2.32-2.33) induced stresses, or the effects of local pore pressure P_P on failure. The reader may find derivations of the appropriate corrections in numerous contributions [e.g., *Schmitt and Zoback*, 1993]. The values of SH so determined, however, are taken to be uncertain

39

because often even if one could presume to know exactly the physics operating during creation of the fracture leading to breakdown [e.g., *Golshani and Tran-Cong*, 2009], obtaining the appropriate physical properties needed is difficult and often only estimates can be made.

2.9 Borehole Breakouts and Drilling Induced Fractures

2.9.1 Borehole Breakouts

Bell and Gough [*Bell and Gough*, 1979; *Gough and Bell*, 1981] first observed, using oriented calliper logging information, that the cross-sections of many deep boreholes in Alberta were preferentially elongated in a NW-SE direction. They surmised on the basis of *Kirsch's* [1898] solutions (Equation 2.7-2.9) that those azimuths around a borehole subject to the maximum concentrated azimuthal compression $\sigma_{\theta\theta}$ occurred at the angles $\pi/2$ from the maximum far-field compression SH (Figure 2.12 (a)).

Consequently, they suggested that the azimuth of these shear fractures provided clues to the directions of the stresses within the earth. This was supported by additional field measurements [e.g., *Plumb and Hickman*, 1985]. Today, borehole breakout analyses account for a large majority of the data on in situ stress states.

A few photographs of borehole breakouts, or similar features, are shown in Figure 2.13 as well as one example of the cross section of a wellbore mapped by the travel times of ultrasonic pulses from a borehole televiewer log.

The actual mechanisms of the formation of the borehole breakouts were not entirely understood. Without this understanding, it is impossible to use the breakouts for any quantitative estimation of stress magnitudes; a number of
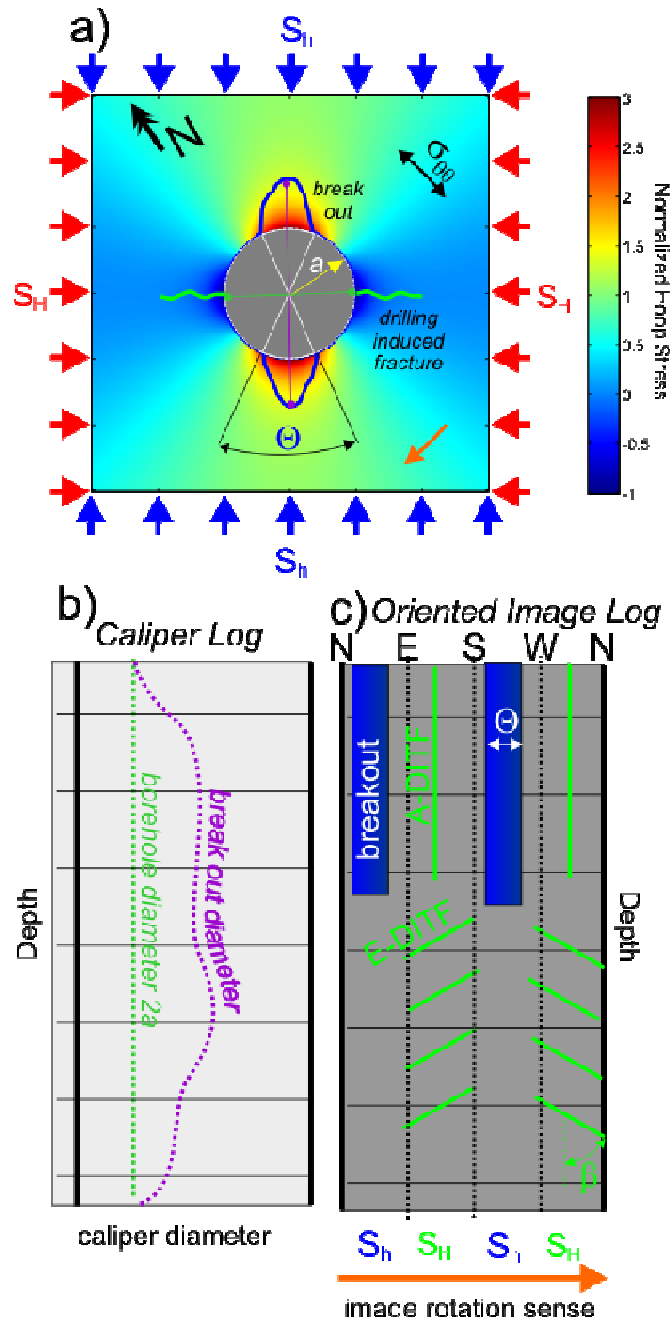
Figure 2.12: Cartoons of a) stress induced borehole deformation with the corresponding b) oriented calliper log (e.g., dipmeter), and c) oriented image log. Both axial (A-DITF) and en-echelon (E-DITF) drilling induced tensile fractures (green) and borehole breakouts (blue) are parallel and perpendicular to the SH springline, respectively. Figure used courtesy of D.R. Schmitt.

41
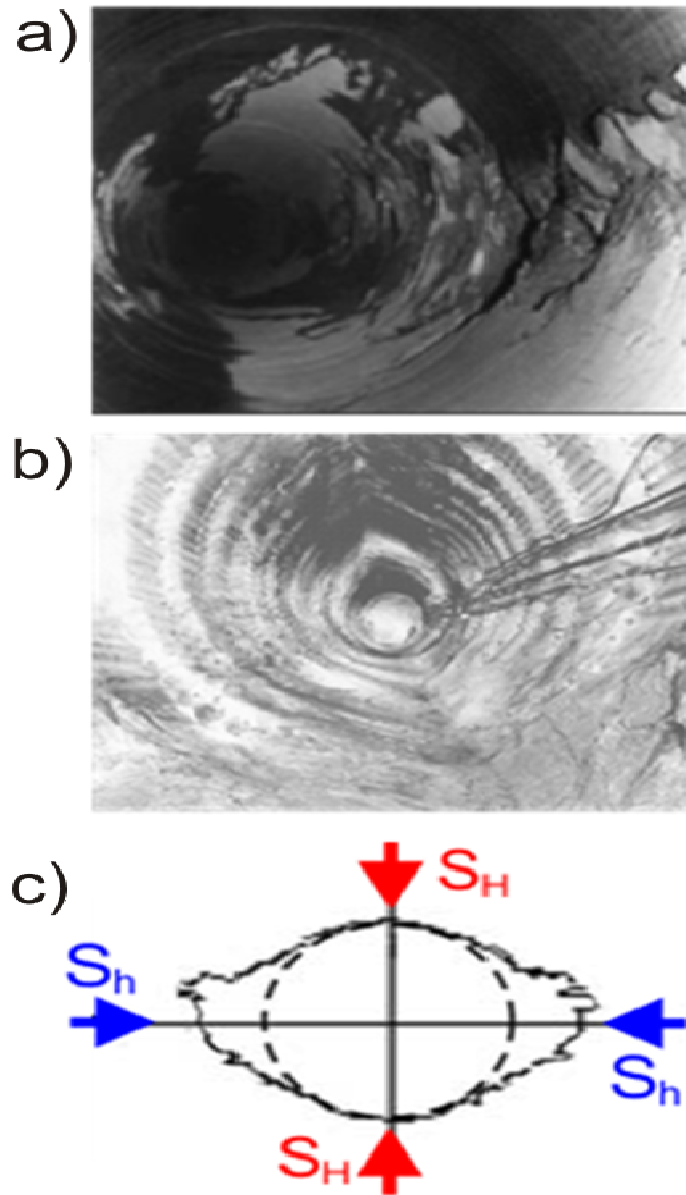
Figure 2.13: Photographs of borehole breakouts. a) downhole borehole breakouts in carbonate. [*Asquith and Krygowski*, 2004]. Figure used courtesy of American Association of Petroleum Geologists according to their reasonable use policy. b) extensive breakout formation around a circular tunnel excavated in granite (after [*Martin, et al.*, 1997], Figure used with permission of Elsevier Limited). c) cross-section shape of a break out in a Hawaiin basalt flows (after [*Morin and Wilkens*, 2005], Figure used courtesy of American Geophysical Union according to their reasonable use policy).

studies undertook to study the stress concentrations using analytic [*Cheatham*, 1993; *Exadaktylos, et al.*, 2003; *Mastin*, 1988] or numerical [*Zheng, et al.*, 1989] methods as well as various failure modes [*Al-Ajmi and Zimmerman*, 2006; *Detournay and Roegiers*, 1986; *Guenot*, 1989; *Tokar*, 1990; *Zoback, et al.*, 1985]. The literature is large and the reader may first want to consult the reviews of the topic within both *Germanovich and Dyskin* [2000] and *Haimson* [2007].

Indeed, borehole breakouts can be produced in a number of ways that are summarized in photographs taken from different laboratory tests in a variety of

rock types and a polymer epoxy. Figure 2.14(a) is a classic dog-eared breakout observed in sufficiently stiff and brittle rocks. In this case, the breakouts are produced by small extensile buckling similar to those seen in Figure 2.13(a) that continuously grows. Such a progressive failure mechanism, too, was observed in the growth of the large 'breakout', the progressive growth of which was monitored by *Martin et al.,* [1997] in Figure 2.13(c).

In contrast, shear failure may dominate breakout growth in some softer rocks. *Haimson* [2007], for example, noted the growth of dilatant shear cracks symmetrical to the Sh springline in tests on a Cordova Cream limestone; similar features may be apparent in hollow cylinder tests in Berea sandstone subject to an uniform state of radial confining stress [*Ewy and Cook*, 1990] in Figure 2.14(b) although in this case their azimuth depends on the strength anisotropy of the rock.

Compaction banding, too, appears to be responsible for some breakouts produced in highly porous and weak sandstones [*Bessinger, et al.*, 1997; *Dresen, et al.*, ; *Haimson*, 2007]. These unusual 'breakouts' rely on the removal of the sand grains

by flow of drilling fluid and produce remarkably linear fractures parallel to the SH springline (Figure 2.14(c)).

Finally, elasto-plastic deformations are likely in rocks subject to creep. An example of a laboratory tests on an epoxy ([*Tokar*, 1990] highlights the ellipse-like yield zone of deformation surrounding a hole in an epoxy block subject to a anisotropic stress state induced by compressing the epoxy block in the direction of the borehole axis with the two induced borehole-perpendicular principal stresses resulting from Poisson' ratio expansion against rigid boundaries (Figure 2.14(d)); as such the stress state is not completely known. The shape of this zone is in qualitative agreement with theoretical predictions that incorporate a Mohr-Coulomb friction law [e.g., *Detournay*, 1986] and this topic continues to receive attention with different failure mechanisms applied [e.g., *Li and Aubertin*, 2009; *Zhou, et al. 2010*]

As noted, true breakouts will lengthen the borehole axis in the direction of the Sh springline while remaining at the original bit diameter gauge 2a in the directions perpendicular to this (Figure 2.12(a)). A variety of different kinds of oriented logging tools including oriented callipers (i.e. dipmeters), electrical resistivity imagers, and ultrasonic borehole televiewers are usually used to locate and interpret breakouts (see *Hurley [2004]* and *Pöppelreiter, et al., [2010]* for technical descriptions of the operation of these instruments). More recently, advances in optical imaging technology have allowed the high resolution optical televiewers to be developed but their use is limited to air or clean water filled boreholes [e.g., *Williams and Johnson*, 2004], and to date there are few reports of their use in breakout analysis.
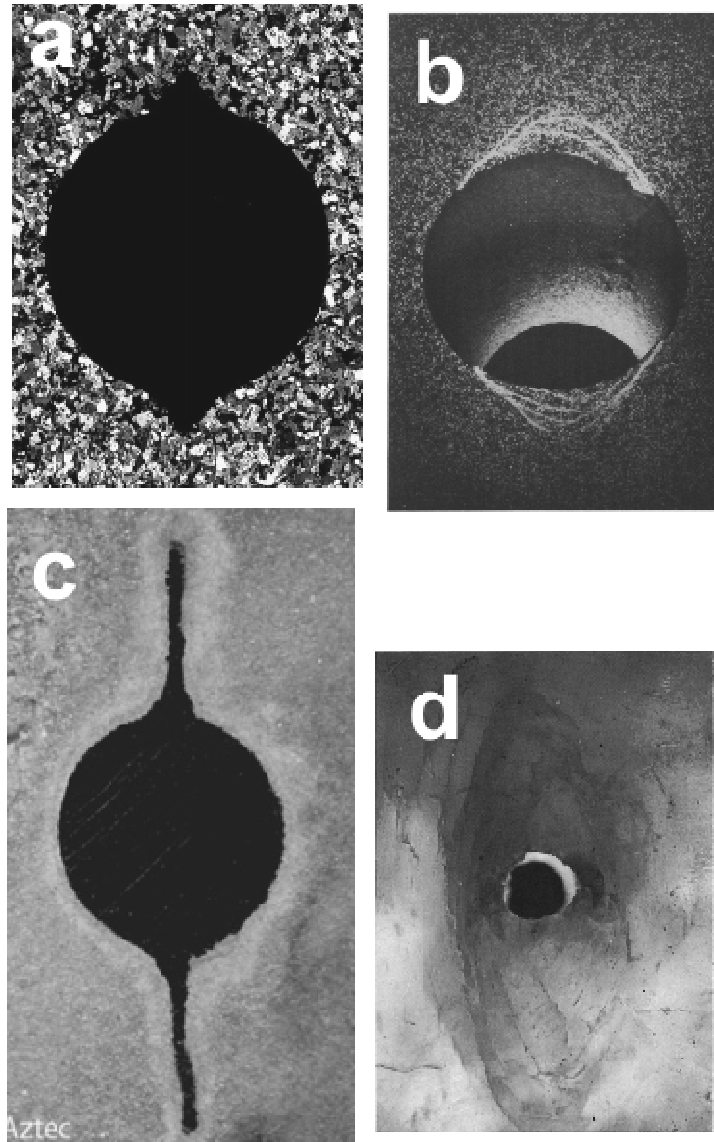
Figure 2.14: Examples of laboratory created break outs from vertical boreholes a) in a Westerley granite cube subject to Sh = 50 MPa, SV = 60 MPa, SH = 190 MPa [*Haimson*, 2007], Figure used with permission of Elsevier Limited. b) in an anisotropic Berea sandstone hollow cylinder subject to an external confining pressure of 75 MPa [*Ewy and Cook*, 1990], Figure used with permission of Elsevier Limited. c) in a porous Aztec sandstone subject to Sh = 20 MPa, SV = 30 MPa, SH = 45 MPa, [*Haimson*, 2007], Figure used with permission of Elsevier Limited. d) a heated clear epoxy subject to a triaxial state of stress (stress values unknown) [*Tokar*, 1990]. Figure used with permission of Elsevier Limited. In a) and c) the SH is perpendicular to the springline of the breakouts.

Briefly, oriented callipers have four or more extendable arms that press against the borehole wall and hence provide measures of the borehole diameter at a number of azimuths. The inclination and orientation of the tool is usually provided by a combination of north sensing magnetometers, gyroscopes, and accelerometers. If breakouts exist, the feet of one pair often become ensnared in the breakout gutters. These arms consequently measure at a more or less consistent azimuth a diameter greater than the original bit gauge while the second orthogonal pair remains at the bit gauge (Figure 2.12(b)). Hence, such tools provide both a measure of the depth of a pair of breakouts and their orientation that falling along the Sh springline provides information on the horizontal stress directions.

Imaging tools, in contrast, provide a great deal more information about the state of the borehole wall. These tools provide a 360º view of the borehole wall rock (Figure 2.12(c)) that allow for additional measurements such as the breakout width Θ to be estimated. This information has been used to constrain the magnitudes of the horizontal stresses by various authors [e.g., *Zoback et al.*, 2003].

Borehole breakouts are not the only type of stress induced damage seen on the walls of boreholes; a variety of drilling induced tensile fractures (DITF) are also seen. The simplest of these are axial A-DITF with more complex sets appearing in an en-echelon or chevron pattern (E-DITF). The axial and en-echelon fractures are interpreted to occur under conditions in which the principal stresses are aligned or oblique to the borehole axis, respectively. In some cases, they could be inadvertent hydraulic fractures produced by the wellbore static or transient (e.g., swabbing) pressure of the drilling fluids much as described above for hydraulic fracture initiation [*Aadnoy*, 1990]. They could also result from thermal disturbances caused by cooler temperatures of the drilling fluid or they could

result from concentrated tensional stress at the borehole wall according to Kirsch's solutions above [*Brudy and Zoback*, 1999]. Although these appear to be tensile features and they appear at those azimuths in tension along the borehole wall, they have also been interpreted as natural fractures that have slipped due to the tension and been referred to as drilling-enhanced fractures [e.g., *Barton, et al.*, 2009; *Barton and Zoback*, 2002]. Regardless, these fractures provide the direction of SH and may provide information to constrain stress magnitudes [*Aadnoy*, 1990; *Brudy and Zoback*, 1993; *Djurhuus and Aadnoy*, 2003; *Hayashi et al.*, 2003; *Nelson et al.*, 2005; *Okabe, et al.*, 1998; *Peska and Zoback*, 1995; *Valley and Evans*, 2009] if the wellbore fluid pressures and temperatures are known in a manner analogous to the use of hydraulic fracture data. Interpretation of the E-DITF requires that the angle β of their trace with respect to the borehole axis be measurable [*Aadnoy and Bell*, 1998].

Morin [1990] observed oval shaped fractures on the borehole wall (Figure 2.15(d)) that they interpreted based on an analytical analysis to be produced by a combination of the farfield and thermal stress concentrations. Similar fractures were recently reported in image logs from the Coso geothermal field, Nevada [*Davatzes and Hickman*, 2010].

2.9.2 Drilling Induced Core Fractures

The main topic of this thesis is the occurrence of 'drilling induced core fractures'. These are artificial fractures created during coring operations and the types of core fractures observed (Figure 2.16 and Figure 2.17) have been classified [*Hakala*, 1999; *Kulander, et al.*, 1990; *Venet, et al.*, 1990] as ranging from convex through flat to concave, the axial symmetry of which suggests relatively uniform horizontal stresses, and saddle-shaped through to petal-centreline that asymmetry of which indicates anisotropic far-field stresses (Figure 1.2).

47
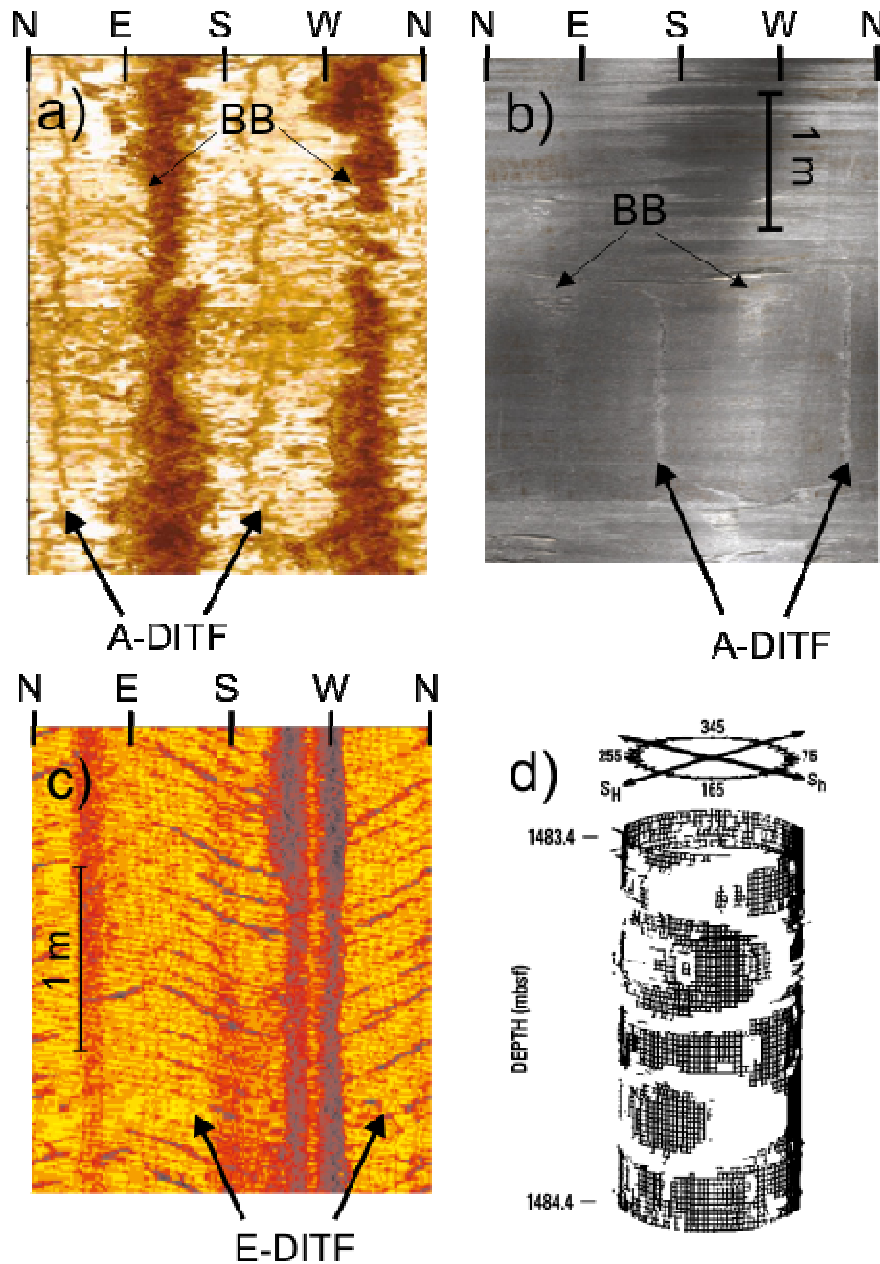
Figure 2.15: Examples of drilling induced tensile fractures (DITF) and borehole breakouts (BB) from a) an ultrasonic borehole televiewer image containing both axial A-DITF and borehole breakouts (after [*Zoback, et al.*, 2003]). b) optical televiewer image of axial A-DITF with incipient breakouts after [*Lucier, et al.*, 2009]. c) transverse en-echelon E-DITF observed in electrical image log (after [*Valley and Evans*, 2009]). d) oval fractures observed in ultrasonic televiewer images in basalt (after [*Morin and Wilkens*, 2005]).
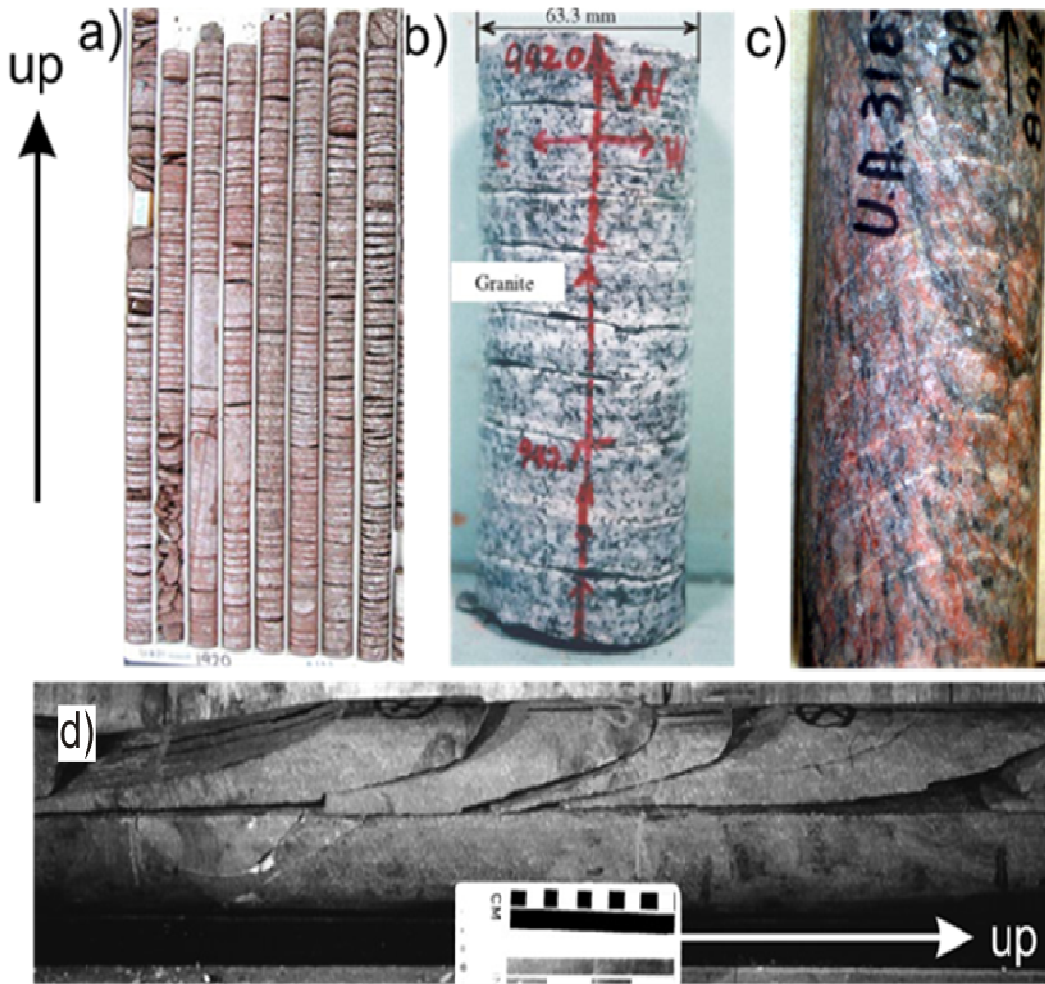
Figure 2.16: Examples of drilling induced core fracture phenomena. a) series of flat core discs along length of core (after [*Bunger*, 2010], Figure used with permission of Springer). b) series of uniformly spaced concave saddle shaped discs from a depth of 942 m from a vertical borehole at Sakuma, Shizuoka prefecture, Japan (from [*Kang, et al.*, 2006], Figure used with permission of Elsevier Limited). c) petal fractures in metamorphic rock from the Canadian shield in Alberta. Figure used courtesy of D.R. Schmitt. d) series of petal-centreline fractures in West Texas limestone core (from [*Lacazette*, 2009], Figure used courtesy of American Association of Petroleum Geologists according to their reasonable use policy).
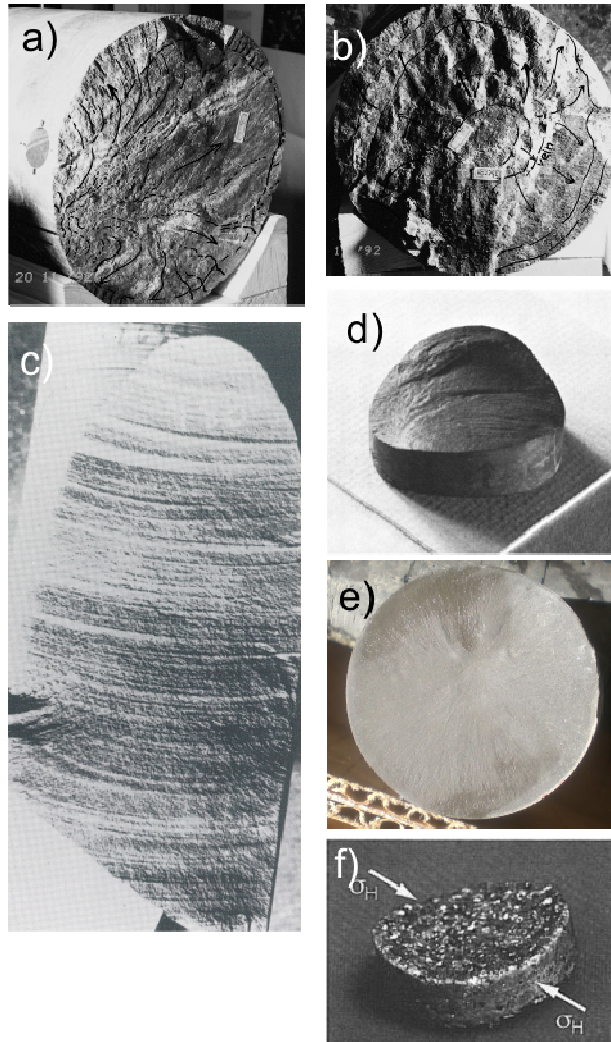
Figure 2.17: Examples of drilling induced core fracture surfaces showing the tensile nature. a) disc fracture initiating from core edge [*Bankwitz and Bankwitz*, 1997]. Figure used with permission of Springer. b) disc fracture initiating from core axis [*Bankwitz and Bankwitz*, 1997]. Figure used with permission of Springer. c) petal-centreline fracture initating at core edge [*Kulander, et al.*, 1990]. Figure used courtesy of American Association of Petroleum Geologists according to their reasonable use policy. d) convex saddle shaped core disk (from [*Paillet and Kim*, 1987], Figure used courtesy of American Geophysical Union according to their reasonable use policy). e) weakly concave disc fracture with fracture initiation point near centre of core in brittle shale. Photo courtesy of D.R. Schmitt. f) concave saddle shaped disc produced in laboratory experiments (from[*Song and Haimson*, 1999], Figure used with permission of American Rock Mechanics Association).

Despite the fact that rocks are complex materials, such fractures are remarkably uniform along a core in both spacing and shape as may be seen in the example photographs of Figure 2.16. Additional excellent examples of a variety of thicknesses of core disks may be found in *Lim and Martin* [2010]. Further, the morphology of these fractures seems to show that they are purely tensile features; this is supported by fractographic analyses of the fracture surfaces [*Bankwitz and Bankwitz*, 1997; 2000; *Kulander, et al.*, 1990] (Figure 2.17). *Li and Schmitt* [1998] demonstrated that the point of fracture initiation, too, was an important additional piece of information. As the state of stress in the Earth must almost always be compressive, the fact that such tensile fractures exist suggests that they must be produced by concentration of the stresses by the geometry at the bottom of the borehole. In many cases, particularly where borehole stability is an issue and fractures may be the only information available on the in situ state of stress; understanding the relationships between of their shapes and spacing has been a goal of many workers.

The stress concentrations at the bottomhole and near the core stub are not as easily obtained as the axisymmeric stresses away from any ends of a long borehole as discussed earlier. The asymmetric and three dimensional bottomhole cannot be described in simple closed form equations [e.g., *Coates and Yu*, 1970], and aside from some empirical measurements [*Galle and Wilhoit*, 1962], numerical approaches have been the method of choice in attempting to better understand stress concentrations. *Hocking [1976]* provides a comprehensive review of the experimental and numerical work up to that time. Since then, the problem has received continued attention with application to failure and damage at the ends of tunnels [e.g., *Diederichs, et al.*, 2004; *Eberhardt*, 2001; *Ito, et al.*, 1998; *Rumzan and Schmitt*, 2001] and boreholes and for overcoring techniques

[*Kang, et al.*, 2006; *Wang and Wong*, 1987]. However, much of the focus of the overcoring/undercoring community lies in finding sets of experimental geometry-dependent stress concentration factors and the work is usually not directly transferrable to the study of core damage.

Before continuing, it is useful to better define the geometry of drilling induced core fractures (DICF). Different types of coring bits are used for various purposes in the petroleum, mining, and nuclear waste industries (Figure 2.18). The bit essentially grinds away the material around the central stub or pedestal of the core materials. The shape and width of the cut out slot, or kerf, of course depends on the type of coring bit employed, and this must influence the final distribution of the stresses. Further, as might be inferred by the photographs of Figure 2.16, the core fractures are more or less uniformly spaced; and this suggests that the core stub length will also influence stress concentrations.

This geometry is more complex than a simple flat ended borehole and of course workers have been forced towards numerical approaches in attempting to understand such fractures, with the finite element method being applied in most of these studies [*Dyke*, 1989; *Hakala*, 1999; *Kaga, et al.*, 2003; *Li and Schmitt*, 1997a; b; 1998; *Lim and Martin*, 2010; *Lim, et al.*, 2006; *Matsuki, et al.*, 2003; 2004; *Sugawara, et al.*, 1978; *Venet*, 1993; *Venet, et al.*, 1990]. One exception is the study of *Gorodov et al.*, [2006] who used a discrete particle approach to look at the damage produced in a core stub of granular material during coring. Experimental studies of such fractures remain quite limited [*Jaeger and Cook*, 1963; *Obert and Stephenson*, 1965].

One issue in attempting to predict what form the DICF will take is that the criteria for both fracture initiation and propagation are not necessarily well understood.
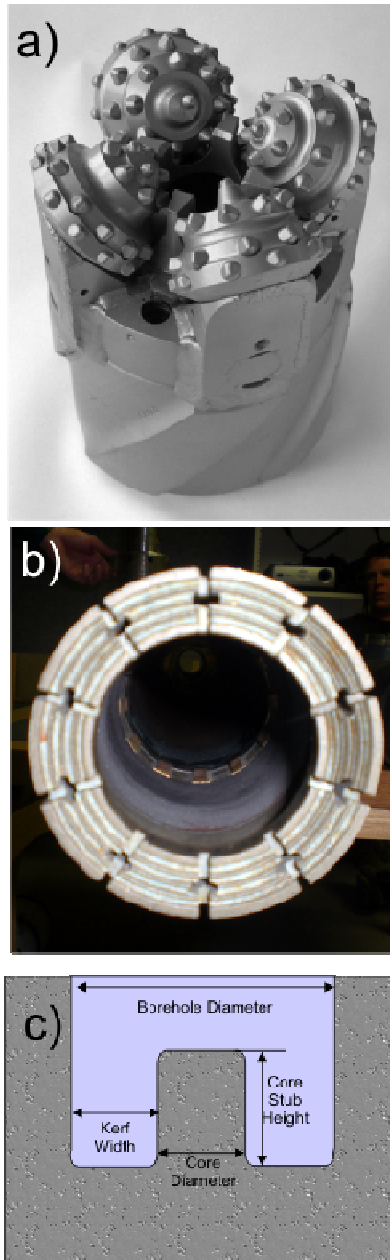
Figure 2.18: Types of coring bits: a) Rotary tri-cone bit produces 58.7mm diameter core (photo used courtesy of Integrated Ocean Drilling Program according to their reasonable use policy b) Typical PQ dimension diamond impregnated coring bit with 85.09mm diameter core. Photo courtesy of D.R. Schmitt. c) Side view through the borehole bottom.

This topic will be reviewed again in later chapters as it is an important issue with regards to the developments in this thesis. However, it is instructive to look at what kinds of criteria have been employed. *Dyke* [1989] attempted to localize the fracture trajectory on the basis of strain energy arguments. *Li and Schmitt* [1998] carried out 3D FEM models on a variety of core stub geometries and used a simple maximum tensile stress failure criterion to both initiate and propagate the tensional fractures. This approach was also adapted by *Hakala* [1999]. *Matsuki et al.*, [2004] carried out extensive finite element modelling for a variety of HQ core stub lengths subject to general states of farfield stresses and under a set of reasonable assumptions on the uniformity and direction of stress within the stub, and they were able to develop a set of 'critical tensile stress' criteria that allow estimation of the full stress field. Most recently, *Lim and Martin* [2010] applied a fracture mechanics approach that yields disk surfaces in agreement with field observations. And finally, *Bunger* [2010] has applied the *Matsuki et al's*, [2004] criterion for statistical evaluation of a large number of core disks from a South African borehole.

Taken together, the best approach is to combine as many different methods as possible to obtain a clearer picture of what the state of stress should be, good examples of this approach with regards to stress determination in ocean drilling are demonstrated at the Kumano forearc off Japan is given by *Lin et al* [2010a] and at the Chelungpu fault, Taiwan [*Haimson*, 2010; *Haimson, et al.*, 2010; *Lin, et al.*, 2010b; *Zhang and Roegiers*, 2010]

The work here builds on these earlier studies. A long term goal of this research will be to add to the toolbox of methods available to researchers wanting to measure in situ stresses. The thesis begins with new calculations based on those of *Li and Schmitt* [1998] using more modern computational capabilities. This

provides for us a much more densely sampled model than was previously possible. More importantly, however, this thesis explores a methodology to calculate the propagation of DICF fully in three dimensions. This is a significant step past the 2D tracing of *Li and Schmitt* [1998]. The results show a great deal of detail in the 3D structure of the fracture shapes; and this may lead to improved estimates of in situ stress. Towards the end, a new and rapid program that forward calculates the fracture morphologies for a variety of stress states is implemented.

2.10 References

Aadnoy, B. S. (1990), In-situ stress directions from borehole fracture traces, *Journal of Petroleum Science and Engineering*, 4, 143-153.

Aadnoy, B. S., and F. Angellolsen (1995), Some Effects of Ellipticity on the Fracturing and Collapse Behavior of a Borehole, *Int. J. Rock Mech. Min. Sci.*, *32*, 621-627.

Aadnoy, B. S., and J. S. Bell (1998), Classification of drilling induced fractures and their relationship to in situ stress directions, *The Log Analyst*, 27-42.

Abousleiman, Y. N., and S. L. Chen (2010), Poromechanics Response of an Inclined Borehole Subject to in-Situ Stress and Finite Length Fluid Discharge, *Journal of Mechanics of Materials and Structures*, *5*, 47-66.

Adams, J. (1982), Stress-Relief Buckles in the Mcfarland Quarry, Ottawa, *Can. J. Earth Sci.*, *19*, 1883-1887.

Adams, L. H., and E. D. Williamson (1923), On the compressibility of minerals and rocks at high pressures, *Journal of the Franklin Institute*, *195*, 475-529.

Al-Ajmi, A. M., and R. W. Zimmerman (2006), Stability analysis of vertical boreholes using the Mogi-Coulomb failure criterion, *International Journal of Rock Mechanics and Mining Sciences*, *43*, 1200-1211.

Amadei, B. (1983), *Rock anisotropy and the theory of stress measurements*, 478 pp., Springer-Verlag, Berlin.

Amadei, B., and O. Stephannson (1997), *Rock stress and its measurement*, 490 pp., Chapman and Hall, New York.

Ashraf Mohammed, A.-T., and N. A. Younane (2008), Acoustic Measurement and Calibration of In Situ Stress Anisotropy Around a Wellbore, in *SPE Annual Technical Conference and Exhibition*, edited, Society of Petroleum Engineers, Denver, Colorado, USA.

Asquith, G., and D. Krygowski (2004), *Basic well log analysis* 244 pp., AAPG, Tulsa.

Balland, C., J. Morel, G. Armand, and W. Pettitt (2009), Ultrasonic velocity survey in Callovo-Oxfordian argillaceous rock during shaft excavation, *International Journal of Rock Mechanics and Mining Sciences*, *46*, 69-79.

Balland, C., and V. Renaud (2009), High-resolution velocity field imaging around a borehole: Excavation-damaged zone characterization, *Geophysics*, *74*, E223-E232.

Bankwitz, P., and E. Bankwitz (1997), Fractographic features on joints in KTB drill cores as indicators of the contemporary stress orientation, *Geol. Rundsch.*, *86*, S34-S44.

Bankwitz, P., and E. Bankwitz (2000), Drilling-induced fracturing processes and the evidence for the in situ stress field (KTB drilling site, NE Bavaria), *Neues Jahrbuch Fur Geologie Und Palaontologie-Abhandlungen*, *218*, 85-127.

Barton, C., D. Moos, and K. Tezuka (2009), Geomechanical wellbore imaging: Implications for reservoir fracture permeability, *AAPG Bull.*, *93*, 1551-1569.

Barton, C. A., and M. D. Zoback (2002), Discrimination of natural fractures from drilling-induced wellbore failures in wellbore image data-implications for reservoir permeability, *Spe Reservoir Evaluation & Engineering*, *5*, 249-254.

Barton, N. (2006), Rock stress, pore pressure, borehole stability and sonic logging, in *Rock Quality, Seismic Velocity, Attenuation and Anisotropy*, edited, pp. 295-322, Taylor & Francis, New York.

Batista, M. (2010), On the stress concentration around a hole in an infinite plate subject to a uniform load at infinity, *International Journal of Mechanical Sciences*, *53*, 254-261.

Bell, J. S. (1985), Offset Boreholes in the Rocky Mountains of Alberta, Canada, *Geology*, *13*, 734-737.

Bell, J. S., and D. I. Gough (1979), Northeast-Southwest Compressive Stress in Alberta - Evidence from Oil-Wells, *Earth Planet. Sci. Lett.*, *45*, 475-482.

Bessinger, B. A., Z. Liu, N. G. W. Cook, and L. R. Myer (1997), A new fracturing mechanism for granular media, *Geophys. Res. Lett.*, *24*, 2605-2608.

Bose, S., B. K. Sinha, S. Sunaga, T. Endo, and H. P. Valero (2007), Anisotropy processing without matched cross-dipole transmitters, *SEG Technical Program Expanded Abstracts*, *26*, 114-118.

Brudy, M., and M. D. Zoback (1993), Compressive and Tensile Failure of Boreholes Arbitrarily-Inclined to Principal Stress Axes - Application to the Ktb Boreholes, Germany, *Int. J. Rock Mech. Min. Sci.*, *30*, 1035-1038.

Brudy, M., and M. D. Zoback (1999), Drilling-induced tensile wall-fractures: implications for determination of in-situ stress orientation and magnitude, *International Journal of Rock Mechanics and Mining Sciences*, *36*, 191-215.

Bunger, A. P. (2010), Stochastic Analysis of Core Discing for Estimation of In Situ Stress, *Rock Mech. Rock Eng.*, *43*, 275-286.

Cengiz, E., K. Klaas, W. Marty, B. Austin, and K. Michael (1994), Dipole shear anisotropy logging, *SEG Technical Program Expanded Abstracts*, *13*, 1139-1142.

Cheatham, J. B. (1993), A New Hypothesis to Explain Stability of Borehole Breakouts, *Int. J. Rock Mech. Min. Sci.*, *30*, 1095-1101.

Chin, L. Y., R. Raghavan, and L. K. Thomas (2000), Fully Coupled Analysis of Well Responses in Stress-Sensitive Reservoirs, *SPE Reservoir Evaluation & Engineering*, *3*.

Christiansson, R. (2006), The latest developments for in-situ rock stress measuring techniques, paper presented at In-Situ Rock Stress, Taylor & Francis, Trondheim, June 19-21.

Ciz, R., and S. A. Shapiro (2009), Stress-dependent anisotropy in transversely isotropic rocks: Comparison between theory and laboratory experiment on shale, *Geophysics*, *74*, D7-D12.

Coates, D. F., and Y. S. Yu (1970), A Note on Stress Concentrations at End of a Cylindrical Hole, *International Journal of Rock Mechanics and Mining Sciences*, *7*, 583-588.

Cornet, F. H. (1993), 12. Stresses in Rock and Rock Masses: Principles, Practice, and Projects, in *Comprehensive Rock Engineering*, edited by J. A. Hudson, pp. 297-327, Pergamon Press, Oxford.

Corthesy, R., G. He, D. E. Gill, and M. H. Leite (1999), A stress calculation model for the 3D borehole slotter, *International Journal of Rock Mechanics and Mining Sciences*, *36*, 493-508.

Davatzes, N., and S. H. Hickman (2010), Stress, fracture, and fluid-flow analysis using acoustic and electrical image logs in hot fractured granites of the Coso geothermal field, California, U.S.A., in *Dipmeter and borehole image log technology*, edited by M. Pöppelreiter, C. Garcia-Carballido and M. Kraaijveld, pp. 259-293, American Association of Petroleum Geologists, Tulsa.

Detournay, E. (1986), An Approximate Statical Solution of the Elastoplastic Interface for the Problem of Galin with a Cohesive-Frictional Material, *International Journal of Solids and Structures*, *22*, 1435-1454.

Detournay, E., and A. H. D. Cheng (1988), Poroelastic Response of a Borehole in a Non-Hydrostatic Stress-Field, *International Journal of Rock Mechanics and Mining Sciences & Geomechanics Abstracts*, *25*, 171-182.

Detournay, E., and J. C. Roegiers (1986), Well Bore Breakouts and Insitu Stress - Comment, *Journal of Geophysical Research-Solid Earth and Planets*, *91*, 14161-14162.

Diederichs, M. S., P. K. Kaiser, and E. Eberhardt (2004), Damage initiation and propagation in hard rock during tunnelling and the influence of near-face stress rotation, *International Journal of Rock Mechanics and Mining Sciences*, *41*, 785-812.

Djurhuus, J., and B. S. Aadnoy (2003), In situ,stress state from inversion of fracturing data from oil wells and borehole image logs, *Journal of Petroleum Science and Engineering*, *38*, 121-130.

Dresen, G., S. Stanchits, and E. Rybacki Borehole breakout evolution through acoustic emission location analysis, *International Journal of Rock Mechanics and Mining Sciences*, *47*, 426-435.

Dyke, C. (Ed.) (1989), *Core disking: its potential as an indicator of principal stress directions*, 1057-1064 pp., Balkema, Rotterdam.

Eberhardt, E. (2001), Numerical modelling of three-dimension stress rotation ahead of an advancing tunnel face, *International Journal of Rock Mechanics and Mining Sciences*, *38*, 499-518.

Edwards, R. H. (1951), Stress Concentrations around Spheroidal Inclusions and Cavities, *J. Appl. Mech.-Trans. ASME*, *18*, 19-30.

Engelder, T. (1984), The Time-Dependent Strain Relaxation of Algerie Granite, *International Journal of Rock Mechanics and Mining Sciences*, *21*, 63-73.

Evans, K. F., C. H. Scholz, and T. Engelder (1988), An Analysis of Horizontal Fracture Initiation During Hydrofrac Stress Measurements in Granite at North-Conway, New-Hampshire, *Geophysical Journal-Oxford*, *93*, 251-264.

Ewy, R. T., and N. G. W. Cook (1990), Deformation and Fracture around Cylindrical Openings in Rock .1. Observations and Analysis of Deformations, *Int. J. Rock Mech. Min. Sci.*, *27*, 387-407.

Exadaktylos, G. E., P. A. Liolios, and M. C. Stavropoulou (2003), A semi-analytical elastic stress-displacement solution for notched circular openings in rocks, *International Journal of Solids and Structures*, *40*, 1165-1187.

Fairhurst, C. (1964), Measurement of in situ rock stresses with particular reference to hydraulic fracturing, *Felsmechanik und Ingenieurgeologie*, *2*, 129-147.

Fjaer, E., R. Holt, P. Horsrud, A. Raaen, and R. Risnes (2008), *Petroleum related rock mechanics*, 2nd ed., 491 pp., Elsevier, Amsterdam.

Galle, E. M., and J. C. Wilhoit (1962), Stresses around a Wellbore Due to Internal Pressure and Unequal Principal Geostatic Stresses, *Society of Petroleum Engineers Journal*, *2*, 145-155.

Germanovich, L. N., and A. V. Dyskin (2000), Fracture mechanisms and instability of openings in compression, *International Journal of Rock Mechanics and Mining Sciences*, *37*, 263-284.

Giovanni, B. (1969), Some Constitutive Equations For Rock Materials, in *The 11th U.S. Symposium on Rock Mechanics (USRMS)*, edited, American Institute of Mining, Metallurgical, and Petroleum Engineers Inc. Permission to Distribute - American Rock Mechanics Association, Berkeley, CA.

Gjonnes, M., A. Cruz, P. Horsrud, and R. M. Holt (1998), Leak-off tests for horizontal stress determination?, *Journal of Petroleum Science and Engineering*, *20*, 63-71.

Golshani, A., and T. Tran-Cong (2009), Energy analysis of hydraulic fracturing, *KSCE J. Civ. Eng.*, *13*, 219-224.

Gorodkov, S., L. Li, and R. Holt (2006), Stress path during coring: A discrete particle modelling approach, in *In-Situ Rock Stress*, edited, pp. 541-549, Taylor & Francis.

Gough, D. I., and J. S. Bell (1981), Stress Orientations from Oil-Well Fractures in Alberta and Texas, *Can. J. Earth Sci.*, *18*, 638-645.

Grasso, M., A. Pezzino, C. D. Reuther, R. Lanza, and M. Miletto (1991), Late Cretaceous and Recent Tectonic Stress Orientations Recorded by Basalt Dykes at Capo-Passero (Southeastern Sicily), *Tectonophysics*, *185*, 247-259.

Gudmundsson, A. (2006), How local stresses control magma-chamber ruptures, dyke injections, and eruptions in composite volcanoes, *Earth-Sci. Rev.*, *79*, 1-31.

Guenot, A. (1989), Borehole Breakouts and Stress-Fields, *Int. J. Rock Mech. Min. Sci.*, *26*, 185-195.

Haimson, B. (2007), Micromechanisms of borehole instability leading to breakouts in rocks, *International Journal of Rock Mechanics and Mining Sciences*, *44*, 157-173.

Haimson, B. (2010), Reply to Discussion by J. Zhang and J-C Roegiers on the paper "Integrating borehole breakout dimensions, strength criteria, and leak-off test results, to constrain the state of stress across the Chelungpu Fault, Taiwan" by Bezalel Haimson, Weiren Lin, Haruyuki Oku, Jih-Hao Hung, Sheng-Rong Song, published in Tectonophysics, vol. 482, p. 65-72, 2010, *Tectonophysics*, *492*, 299-301.

Haimson, B., and C. Fairhurst (1967), Initiation and Extension of Hydraulic Fractures in Rocks, *J. Pet. Technol.*, *7*, 310-318.

Haimson, B., and M. Lee (1995), Estimating deep in situ stresses from borehole breakouts and core disking - experimental results in granite, paper presented at Proceedings of the International Workshop on Rock Stress Measurement at Great Depth: 8th International Congress on Rock Mechanics, Tokyo.

Haimson, B., W. R. Lin, H. Oku, J. H. Hung, and S. R. Song (2010), Integrating borehole-breakout dimensions, strength criteria, and leak-off test results, to constrain the state of stress across the Chelungpu Fault, Taiwan, *Tectonophysics*, *482*, 65-72.

Haimson, B. C., and F. H. Cornet (2003), ISRM suggested methods for rock stress estimation - Part 3: hydraulic fracturing (HF) and/or hydraulic testing of pre-existing fractures (HTPF), *International Journal of Rock Mechanics and Mining Sciences*, *40*, 1011-1020.

Haimson, B. C., and T. M. Tharp (1974), Stresses Around Boreholes in Bilinear Elastic Rock, *Society of Petroleum Engineers Journal*, *14*, 145-151.

Hakala, M. (1999), Numerical study of the core disk fracturing and interpretation of the in situ state of stress, in *Ninth International Congress on Rock Mechanics, Vols 1 & 2*, edited by G. Vouille and P. Berest, pp. 1149-1153, A a Balkema Publishers, Leiden.

Hayashi, K., and B. C. Haimson (1991), Characteristics of Shut-in Curves in Hydraulic Fracturing Stress Measurements and Determination of Insitu Minimum Compressive Stress, *Journal of Geophysical Research-Solid Earth*, *96*, 18311-18321.

Hayashi, K., N. Kimura, and K. Toshiki (2003), Effect of thermal stress on drilling-induced tensile fractures under a variety of far field stress state, in *Rock Stress*, edited by K. Sugawara, Y. Obara and A. Sato, pp. 295-300, A a Balkema Publishers, Leiden.

Hiramatsu, Y., and Y. Oka (1962), Stress around a shaft or level excavated in ground with a three-dimensional stress state, *Mem. Fac. Engng Kyoto Univ. Part I.*, *24*, 56-76.

Hocking, G. (1976), 3-Dimensional Elastic Stress Distribution around Flat End of a Cylindrical Cavity, *International Journal of Rock Mechanics and Mining Sciences*, *13*, 331-337.

Holt, R., A. Skjaerstein, and P. Storemyr (1993), Acoustic anisotropy of deteriorated soapstone from the Nidaros Cathedral, Trondheim, Norway, *Can. J. Expl. Geophysics*, *29*, 18-30.

Hubbert, M. K., and D. G. Willis (1957), Mechanics of Hydraulic Fracturing, *Transactions of the American Institute of Mining and Metallurgical Engineers*, *210*, 153-163.

Hurley, N. (2004), Borehole images, in *Basic Well Log Analysis*, edited by G. Asquith and D. Krygowski, pp. 151-163, American Association of Petroleum Geologists, Tulsa.

Ito, T., K. Evans, K. Kawai, and K. Hayashi (1999), Hydraulic fracture reopening pressure and the estimation of maximum horizontal stress, *International Journal of Rock Mechanics and Mining Sciences*, *36*, 811-825.

Ito, T., K. Kurosawa, and K. Hayashi (1998), Stress concentration at the bottom of a borehole and its effect on borehole breakout formation, *Rock Mech. Rock Eng.*, *31*, 153-168.

Iturrino, G. J., D. Goldberg, H. Glassman, D. Patterson, Y. F. Sun, G. Guerin, and S. Haggas (2005), Shear-wave anisotropy from dipole shear logs in oceanic crustal environments, in *Petrophysical Properties of Crystalline Rocks*, edited by P. K. Harvey, T. S. Brewer, P. A. Pezard and V. A. Petrov, pp. 117-131.

Jaeger, J., N. Cook, and R. Zimmerman (2007), *Fundamentals of rock mechanics*, 488 pp., Wiley-Blackwell, New York.

Jaeger, J. C., and N. G. W. Cook (1963), Pinching-Off and Disking of Rocks, *Journal of Geophysical Research*, *68*, 1759-&.

Johnson, P. A., and P. N. J. Rasolofosaon (1996), Nonlinear elasticity and stress-induced anisotropy in rock, *J. Geophys. Res.-Solid Earth*, *101*, 3113-3124.

Kaga, N., K. Matsuki, and K. Sakaguchi (2003), The in situ stress states associated with core discing estimated by analysis of principal tensile stress, *International Journal of Rock Mechanics and Mining Sciences*, *40*, 653-665.

Kaiser, J. (1950), Untersuchung über das Auftreten von Geräuschen beim Zugversuch, Thesis Dr.-Ing. , 152 pp, Universität München (TUM).

Kanamori, H., and E. E. Brodsky (2004), The physics of earthquakes, *Rep. Prog. Phys.*, *67*, 1429-1496.

Kang, S. S., Y. Ishiguro, and Y. Obara (2006), Evaluation of core disking rock stress and tensile strength via the compact conical-ended borehole overcoring technique, *International Journal of Rock Mechanics and Mining Sciences*, *43*, 1226-1240.

Kirsch, G. (1898), Die Theorie der Elastizitat und die Bedurfnisse der Festigkeitslehre, *Zeit Verein Deutsch Ing*, *42*, 797-807.

Kulander, B. R. D., L. Stuart, and J. Billy (1990), *Fractured core analysis; interpretation, logging, and use of natural and induced fractures in core*, 88 pp., American Association of Petroleum Geologists, Tulsa.

Lacazette, A. (Ed.) (2009), *Distinguishing natural from induced tensile fractures in image logs*, 2nd ed., American Association of Petroleum Geologists, Tulsa.

Leeman, E., and D. Hayes (1966), A technique for determining the complete state of stress in rock using a single borehole, paper presented at Proceedings 1st Congress International Society of Rock Mechanics, Lisbon.

Leite, M. H., V. Boivin, and R. Corthesy (2010), Stress calculation methods for overcoring techniques in heterogeneous rocks, *International Journal of Rock Mechanics and Mining Sciences*, *47*, 1180-1192.

Li, C., and E. Nordlund (1993), Experimental-Verification of the Kaiser Effect in Rocks, *Rock Mech. Rock Eng.*, *26*, 333-351.

Li, L., and M. Aubertin (2009), An elastoplastic evaluation of the stress state around cylindrical openings based on a closed multiaxial yield surface, *International Journal for Numerical and Analytical Methods in Geomechanics*, *33*, 193-213.

Li, S. C., and M. B. Wang (2008), Elastic analysis of stress-displacement field for a lined circular tunnel at great depth due to ground loads and internal pressure, *Tunn. Undergr. Space Technol.*, *23*, 609-617.

Li, Y. Y., and D. R. Schmitt (1997a), Effects of Poisson's ratio and core stub length on bottomhole stress concentrations, *International Journal of Rock Mechanics and Mining Sciences*, *34*, 761-773.

Li, Y. Y., and D. R. Schmitt (1997b), Well-bore bottom stress concentration and induced core fractures, *Aapg Bulletin-American Association of Petroleum Geologists*, *81*, 1909-1925.

Li, Y. Y., and D. R. Schmitt (1998), Drilling-induced core fractures and in situ stress, *Journal of Geophysical Research-Solid Earth*, *103*, 5225-5239.

Lim, S., and C. Martin (2010), Core disking and its relationship with stress magnitude for Lac du, *International Journal of Rock Mechanics and Mining Sciences*, *47*, 254-264.

Lim, S., C. Martin, and R. Christiansson (2006), Estimating in-situ stress magnitudes from core disking, paper presented at International Symposium on In-Situ Rock Stress, Taylor & Francis, Trondheim, June 19-21.

Lin, W. R., M. L. Doan, J. C. Moore, L. McNeill, T. B. Byrne, T. Ito, D. Saffer, M. Conin, M. Kinoshita, Y. Sanada, K. T. Moe, E. Araki, H. Tobin, D. Boutt, Y. Kano, N. W. Hayman, P. Flemings, G. J. Huftile, D. Cukur, C. Buret, A. M. Schleicher, N. Efimenko, K. Kawabata, D. M. Buchs, S. J. Jiang, K. Kameo, K. Horiguchi, T. Wiersberg, A. Kopf, K. Kitada, N. Eguchi, S. Toczko, K. Takahashi, and Y. Kido (2010a), Present-day principal horizontal stress orientations in the Kumano forearc basin of the southwest Japan subduction zone determined from IODP NanTroSEIZE drilling Site C0009, *Geophys. Res. Lett.*, *37*.

Lin, W. R., M. Kwasniewski, T. Imamura, and K. Matsuki (2006), Determination of three-dimensional in situ stresses from anelastic strain recovery measurement of cores at great depth, *Tectonophysics*, *426*, 221-238.

Lin, W. R., E. C. Yeh, J. H. Hung, B. Haimson, and T. Hirono (2010b), Localized rotation of principal stress around faults and fractures determined from borehole breakouts in hole B of the Taiwan Chelungpu-fault Drilling Project (TCDP), *Tectonophysics*, *482*, 82-91.

Lucier, A. M., M. D. Zoback, V. Heesakkers, Z. Reches, and S. K. Murphy (2009), Constraining the far-field in situ stress state near a deep South African gold mine, *International Journal of Rock Mechanics and Mining Sciences*, *46*, 555-567.

Mahtab, M. A., and R. E. Goodman (1968), Stresses Around Wellbores in Nonlinear Rock, *8*.

Majmudar, T. S., and R. P. Behringer (2005), Contact force measurements and stress-induced anisotropy in granular materials, *Nature*, *435*, 1079-1082.

Martin, C. D., R. S. Read, and J. B. Martino (1997), Observations of brittle failure around a circular test tunnel, *International Journal of Rock Mechanics and Mining Sciences*, *34*, 1065-1073.

Mastin, L. (1988), Effect of Borehole Deviation on Breakout Orientations, *Journal of Geophysical Research-Solid Earth and Planets*, *93*, 9187-9195.

Matsuki, K. (2008), Anelastic strain recovery compliance of rocks and its application to in situ stress measurement, *International Journal of Rock Mechanics and Mining Sciences*, *45*, 952-965.

Matsuki, K., N. Kaga, T. Yokoyama, and N. Tsuda (2003), Determination of three-dimensional directions of in situ stress from core discing, in *Rock Stress*, edited by K. Sugawara, Y. Obara and A. Sato, pp. 237-243.

Matsuki, K., N. Kaga, T. Yokoyama, and N. Tsuda (2004), Determination of three dimensional in situ stress from core discing based on analysis of principal tensile stress, *International Journal of Rock Mechanics and Mining Sciences*, *41*, 1167-1190.

Matsuki, K., and K. Takeuchi (1993), 3-Dimensional in-Situ Stress Determination by Anelastic Strain Recovery of a Rock Core, *Int. J. Rock Mech. Min. Sci.*, *30*, 1019-1022.

Meyer, B., and H. Jacot (2001), Impact of stress-dependent Young's moduli on hydraulic fracture modeling, in *DC Rocks 2001, The 38th U.S. Symposium*

on Rock Mechanics (USRMS), edited, Swets & Zeitlinger Lisse, Permission to Distribute - American Rock Mechanics Association, Washington D.C.

Mitaim, S., and E. Detournay (2004), Damage around a cylindrical opening in a brittle rock mass, *International Journal of Rock Mechanics and Mining Sciences*, *41*, 1447-1457.

Mollema, P. N., and M. A. Antonellini (1996), Compaction bands: A structural analog for anti-mode I cracks in aeolian sandstone, *Tectonophysics*, *267*, 209-228.

Morin, R. H. (1990), Information on Stress Conditions in the Oceanic-Crust from Oval Fractures in a Deep Borehole, *Geophys. Res. Lett.*, *17*, 1311-1314.

Morin, R. H., and R. H. Wilkens (2005), Structure and stress state of Hawaiian island basalts penetrated by the Hawaii Scientific Drilling Project deep core hole, *Journal of Geophysical Research-Solid Earth*, *110*.

Mueller, M. C., A. J. Boyd, and C. Esmersoy (1994), Case studies of the dipole shear anisotropy log, *SEG Technical Program Expanded Abstracts*, *13*, 1143-1146.

Murdoch, L. C. (1995), Forms of Hydraulic Fractures Created During a Field-Test in Overconsolidated Glacial Drift, *Quarterly Journal of Engineering Geology*, *28*, 23-35.

Nawrocki, P. (2010), CRITICAL WELLBORE PRESSURES USING DIFFERENT ROCK FAILURE CRITERIA, in *ISRM International Symposium - 6th Asian Rock Mechanics Symposium*, edited, 2010, Central

Board of Irrigation and Power (CBIP) and International Society for Rock Mechanics (ISRM), New Delhi, India.

Nelson, E. J., S. T. Chipperfield, R. R. Hillis, J. Gilbert, J. McGowen, and S. D. Mildren (2007), The relationship between closure pressures from fluid injection tests and the minimum principal stress in strong rocks, *International Journal of Rock Mechanics and Mining Sciences*, *44*, 787-801.

Nelson, E. J., J. J. Meyer, R. R. Hillis, and S. D. Mildren (2005), Transverse drilling-induced tensile fractures in the West Tuna area, Gippsland Basin, Australia: implications for the in situ stress regime, *International Journal of Rock Mechanics and Mining Sciences*, *42*, 361-371.

Obert, L., and D. Stephenson (1965), Stress conditions under which core disking occurs, *Society of Mechanical Engineers Transactions*, *323*, 227-235.

Okabe, T., K. Hayashi, N. Shinohara, and S. Takasugi (1998), Inversion of drilling-induced tensile fracture data obtained from a single inclined borehole, *International Journal of Rock Mechanics and Mining Sciences*, *35*, 747-758.

Ou, Z. Y., G. F. Wang, and T. J. Wang (2009), An analytical solution for the elastic fields near spheroidal nano-inclusions, *Acta Mech. Sin.*, *25*, 821-830.

Paillet, F. L., and K. Kim (1987), Character and Distribution of Borehole Breakouts and Their Relationship to Insitu Stresses in Deep Columbia River Basalts, *Journal of Geophysical Research-Solid Earth and Planets*, *92*, 6223-6234.

Pascal, C., D. Roberts, and R. H. Gabrielsen Tectonic significance of present-day stress relief phenomena in formerly glaciated regions, *J. Geol. Soc.*, *167*, 363-371.

Paulsen, T., and T. Wilson (2007), Elongate summit calderas as Neogene paleostress indicators in Antarctica. Short Research Paper 072.

Peska, P., and M. D. Zoback (1995), Compressive and Tensile Failure of Inclined Well Bores and Determination of in-Situ Stress and Rock Strength, *Journal of Geophysical Research-Solid Earth*, *100*, 12791-12811.

Pilkey, W., D. Pilkey, and R. Peterson (2008), *Peterson's Stress Concentration Factors*, 3rd ed., 560 pp., Wiley, New York.

Plona, T., H. P. Valero, S. Bose, J. Walsh, E. Wielemaker, and P. Saldungaray (2007), Reliable small-percentage azimuthal anisotropy evaluation from a new wireline cross-dipole sonic tool: Field Examples from US, Mexico and Ukraine, *SEG Technical Program Expanded Abstracts*, *26*, 328-332.

Plumb, R. A., and S. H. Hickman (1985), Stress-Induced Borehole Elongation - a Comparison between the 4-Arm Dipmeter and the Borehole Televiewer in the Auburn Geothermal Well, *Journal of Geophysical Research-Solid Earth and Planets*, *90*, 5513-5521.

Pöppelreiter, M., C. Garcia-Carballido, and M. Kraaijveld (2010), Borehole image log technology: Application across the exploration and production cycle, in *Dipmeter and borehole image log technology*, edited by M. Pöppelreiter, C. Garcia-Carballido and M. Kraaijveld, pp. 1-13, American Association of Petroleum Geologists, Tulsa.

Pyraknolte, L. J., L. R. Myer, and N. G. W. Cook (1990), Anisotropy in Seismic Velocities and Amplitudes from Multiple Parallel Fractures, *Journal of Geophysical Research-Solid Earth and Planets*, *95*, 11345-11358.

Rathore, J. S., E. Fjaer, R. M. Holt, and L. Renlie (1995), P-Wave and S-Wave Anisotropy of a Synthetic Sandstone with Controlled Crack Geometry, *Geophys. Prospect.*, *43*, 711-728.

Rice, J. R., and M. P. Cleary (1976), Some Basic Stress Diffusion Solutions for Fluid-Saturated Elastic Porous-Media with Compressible Constituents, *Reviews of Geophysics*, *14*, 227-241.

Ritchie, R. H., and A. Y. Sakakura (1956), Asymptotic Expansions of Solutions of the Heat Conduction Equation in Internally Bounded Cylindrical Geometry, *Journal of Applied Physics*, *27*, 1453-1459.

Roshan, H., and S. Rahman (2011), Analysis of Pore Pressure and Stress Distribution around a Wellbore Drilled in Chemically Active Elastoplastic Formations, *Rock Mech. Rock Eng.*, 1-12.

Ruch, J., and T. R. Walter (2010), Relationship between the InSAR-measured uplift, the structural framework, and the present-day stress field at Lazufre volcanic area, central Andes, *Tectonophysics*, *492*, 133-140.

Rumzan, I., and D. R. Schmitt (2001), The influence of well bore fluid pressure on drilling penetration rates and stress dependent strength, in *Rock Mechanics in the National Interest, Vols 1 and 2*, edited by D. Elsworth, J. P. Tinucci and K. A. Heasley, pp. 911-917, A a Balkema Publishers, Leiden.

Santarelli, F. J., E. T. Brown, and V. Maury (1986), Analysis of Borehole Stresses Using Pressure-Dependent, Linear Elasticity, *Int. J. Rock Mech. Min. Sci.*, *23*, 445-449.

Schmitt, D. R., M. S. Diallo, and F. Weichman (2006), Quantitative determination of stress by inversion of speckle interferometer fringe patterns: experimental laboratory tests, *Geophys. J. Int.*, *167*, 1425-1438.

Schmitt, D. R., and M. D. Zoback (1993), Infiltration Effects in the Tensile Rupture of Thin-Walled Cylinders of Glass and Granite - Implications for the Hydraulic Fracturing Breakdown Equation, *Int. J. Rock Mech. Min. Sci.*, *30*, 289-303.

Sinha, B. K., M. R. Kane, and B. Frignet (2000), Dipole dispersion crossover and sonic logs in a limestone reservoir, *Geophysics*, *65*, 390-407.

Sinha, B. K., and K. W. Winkler (1999), Formation nonlinear constants from sonic measurements at two borehole pressures, *Geophysics*, *64*, 1890-1900.

Song, I., and B. Haimson (1999), Core disking in Westerley granite and its potential use for in situ stress estimation, paper presented at Rock Mechanics for Industry: Proceedings of the 37th U.S. Rock Mechanics Symposium, Balkema, Vail, CO.

Stephens, G., and B. Voight (1982), Hydraulic Fracturing Theory for Conditions of Thermal-Stress, *International Journal of Rock Mechanics and Mining Sciences*, *19*, 279-284.

Sugawara, K., Y. Kemeoka, T. Saito, Y. Oka, and Y. Hiramatsu (1978), A study on core disking of rock, *J. Jpn. Assoc. Min.*, *94*, 19-25.

Sun, H. T., and R. Prioul (2010), Relating shear sonic anisotropy directions to stress in deviated wells, *Geophysics*, *75*, D57-D67.

Timoshenko, S., and J. Goodier (1970), *Theory of Elasticity, 3rd Edition*, 3rd ed., 567 pp., McGraw-Hill, New York.

Tokar, G. (1990), Experimental-Analysis of the Elastoplastic Zone Surrounding a Borehole in a Specimen of Rock-Like Material under Multiaxial Pressure, *Eng. Fract. Mech.*, *35*, 879.

Valley, B., and K. F. Evans (2009), Stress orientation to 5 km depth in the basement below Basel (Switzerland) from borehole failure analysis, *Swiss J. Geosci.*, *102*, 467-480.

Venet, V. (1993), Contribution to the Optimizing of Core Drilling by Modeling the initiation of discing, *Revue De L Institut Francais Du Petrole*, *48*, 15-42.

Venet, V., J. P. Henry, F. J. Santarelli, and V. Maury (1990), Modelisation du discage pour l'estimation des contraintes in situ a grande profondeur, paper presented at Rock at Great Depth: Rock Mechanics and Rock Physics at Great Depth, Balkema, Pau, August 28-31, 1989.

Vilhelm, J., V. Rudajev, R. Zivor, T. Lokajicek, and Z. Pros (2010), Influence of crack distribution of rocks on P-wave velocity anisotropy - a laboratory and field scale study, *Geophys. Prospect.*, *58*, 1099-1110.

Wang, Y., and T. F. Wong (1987), Finite-Element Analysis of 2 Overcoring Techniques for Insitu Stress Measurement, *Int. J. Rock Mech. Min. Sci.*, *24*, 41-52.

Warren, W. E., and C. W. Smith (1985), Insitu Stress Estimates from Hydraulic Fracturing and Direct Observation of Crack Orientation, *Journal of Geophysical Research-Solid Earth and Planets*, *90*, 6829-6839.

Wawersik, W. R., and C. M. Stone (1989), A characterization of pressure records in inelastic rock demonstrated by hydraulic fracturing measurements in salt, *Int. J. Rock Mech. Min. Sci.*, *26*, 613-627.

Williams, J. H., and C. D. Johnson (2004), Acoustic and optical borehole-wall imaging for fractured-rock aquifer studies, *J. Appl. Geophys.*, *55*, 151-159.

Wilson, T., and T. Paulsen (2000), Brittle deformation patterns of CRP-2/2A, Victoria Land Basin, Antarctica, *Terra Antartica*, *7*, 287-298.

Winkler, K. W. (1996), Azimuthal velocity variations caused by borehole stress concentrations, *J. Geophys. Res.-Solid Earth*, *101*, 8615-8621.

Winkler, K. W. (2005), Borehole damage indicator from stress-induced velocity variations, *Geophysics*, *70*, F11-F16.

Winkler, K. W., and R. D'Angelo (2006), Ultrasonic borehole velocity imaging, *Geophysics*, *71*, F25-F30.

Winkler, K. W., B. K. Sinha, and T. J. Plona (1998), Effects of borehole stress concentrations on dipole anisotropy measurements, *Geophysics*, *63*, 11-17.

Wolter, K. E., and H. Berckhemer (1989), Time-Dependent Strain Recovery of Cores from the Ktb - Deep Drill Hole, *Rock Mech. Rock Eng.*, *22*, 273-287.

Wu, R., L. N. Germanovich, P. E. Van Dyke, and R. P. Lowell (2007), Thermal technique for controlling hydraulic fractures, *Journal of Geophysical Research-Solid Earth*, *112*.

Yamamoto, K. (2009), A theory of rock core-based methods for in-situ stress measurement, *Earth Planets Space*, *61*, 1143-1161.

Zang, A., and O. Stephannson (2010), *Stress field in the earth's crust*, 322 pp., Springer, Amsterdam.

Zhang, J. C., and J. C. Roegiers (2010), Discussion on "Integrating borehole-breakout dimensions, strength criteria, and leak-off test results, to constrain the state of stress across the Chelungpu Fault, Taiwan", *Tectonophysics*, *492*, 295-298.

Zheng, Z. (2000), Seismic anisotropy due to stress-induced cracks, *International Journal of Rock Mechanics and Mining Sciences*, *37*, 39-49.

Zheng, Z. Q., J. Kemeny, and N. G. W. Cook (1989), Analysis of Borehole Breakouts, *Journal of Geophysical Research-Solid Earth and Planets*, *94*, 7171-7182.

Zhou, X. P., X. R. Bao, M. H. Yu, and Q. Xie (2010), Triaxial stress state of cylindrical openings for rocks modeled by elastoplasticity and strength criterion, *Theor. Appl. Fract. Mech.*, *53*, 65-73.

Zisman, W. A. (1933), Compressibility and anisotropy of rocks at and near the earths surface, *Proceedings of the National Academy of Sciences of the United States of America*, *19*, 666-679.

Zoback, M. D. (2007), *Reservoir Geomechanics*, Cambridge University Press, Cambridge.

Zoback, M. D., C. A. Barton, M. Brudy, D. A. Castillo, T. Finkbeiner, B. R. Grollimund, D. B. Moos, P. Peska, C. D. Ward, and D. J. Wiprut (2003), Determination of stress orientation and magnitude in deep wells,

International Journal of Rock Mechanics and Mining Sciences, *40*, 1049-1076.

Zoback, M. D., D. Moos, L. Mastin, and R. N. Anderson (1985), Well Bore Breakouts and Insitu Stress, *Journal of Geophysical Research-Solid Earth and Planets*, *90*, 5523-5530.

Chapter 3

Numerical Modeling

3.1 Introduction

In this thesis, three-dimensional numerical models are used to investigate the development of drilling-induced borehole core fractures. This chapter describes the numerical modeling procedure employed in this study. Two steps are used in the numerical solution.

First, the finite element package ANSYS$^{\text{TM}}$ is used to numerically calculate the stress states expected at the bottom of a borehole during coring operations. An extensive set of numerical 'basis' solutions of the stress distributions for a variety of bottom hole core stub geometries and for a range of Poisson's ratios under both an isolated vertical and horizontal stress is archived. These basis solutions may readily be superposed to reproduce any combination of SV-SH-Sh stress states (where SV is the vertical stress, SH is the maximum horizontal stress and Sh is the minimum horizontal stress as discussed in Chapter 2) to study a range of crustal stress conditions.

The second step involves calculation of fracturing of the borehole core as a result of the stress distribution. The computed stress field from ANSYS$^{\text{TM}}$ is imported into MATLAB$^{\text{TM}}$ and a strategy is then developed to propagate a tensile fracture

through this stress state in order to construct the predicted drilling induced fracture surface.

In this chapter, the geometry of the problem is first outlined. This is followed by a detailed description of the numerical methodology used for: (1) calculating the stress distribution in the vicinity of the borehole bottom; and, (2) propagating fractures through the core stub. Comparison of the computed stress field from step (1) with analytic solutions for key stress states demonstrates the numerical accuracy of the model results.

3.2 Borehole geometry used in models

This study considers a vertical cylindrical borehole in a volume of rock that is under three mutually orthogonal in-situ stresses SV, SH, and Sh, as shown in Figure 3.1.

The cylindrical borehole is drilled using a rotating diamond drilling bit (Figure 3.2). The drill bit cores the hole, yielding a core stub within the centre of the borehole and corresponding circular bottom cut, referred to as the kerf in drilling parlance. It is important to note that there are many different geometries and sizes of core bits. As shown in Chapter 2, mining industry wireline core bits tend to have a much smaller kerf width relative to the core stub diameter. Petroleum industry rotary bits may have larger kerf to core radii ratios. As such, the modeling here was selected not so much to model any one particular bit geometry, but to provide insight into the problem of drilling induced core fractures. More
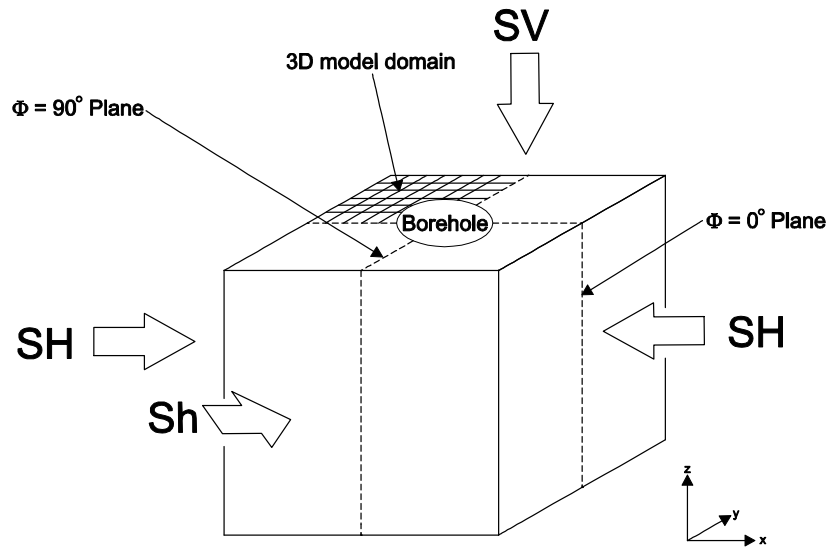
Figure 3.1: Regional in-situ stresses around a vertical borehole
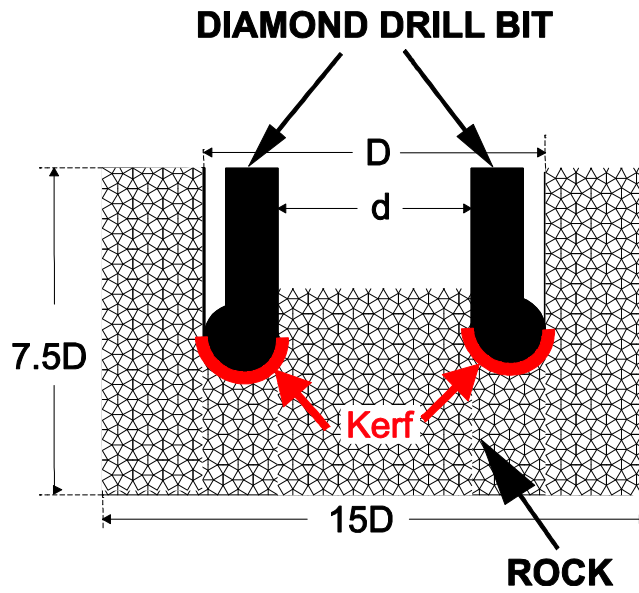
Figure 3.2: Drilling demonstration
(Not to scale)

detailed future work may require that specific bit geometries be considered should one wish to carry out quantitative analysis of the observed core fractures.

As the borehole is drilled, stress concentrations occur near the bottom of the borehole, which can lead to the formation of fractures within the core stub. The goal of this study is to understand the three-dimensional distribution of stress in the vicinity of the borehole and to infer possible fracture geometries within the core stub. Future work could also look at fractures within the borehole walls.

Owing to symmetry of the borehole and of the applied stresses, it is only necessary to model one quadrant around the borehole (Figure 3.1). The model geometry is shown in detail in Figure 3.3a and follows that used by *Li and Schmitt* [1997b; 1998]. A Cartesian coordinate system is defined in which the origin is located at symmetry axis (vertical axis at the centre of the core) and is at the same height as the bottom of the drill bit. The two vertical planes that pass through the centre of the borehole are symmetry planes. They are identified by their orientation with respect to the direction of maximum horizontal stress (SH). The $\Phi = 0°$ plane is parallel to SH and the $\Phi = 90°$ is perpendicular to SH (i.e., parallel to Sh).

Units of dimension are arbitrary as linear elasticity is assumed, and thus the geometry may be scaled relative to the model. In this study, distance units are reported relative to the diameter of the borehole (D) and diameter of the core (d). The full 3D model domain ranges 7.5D in x, y, z directions. Hence, the outside
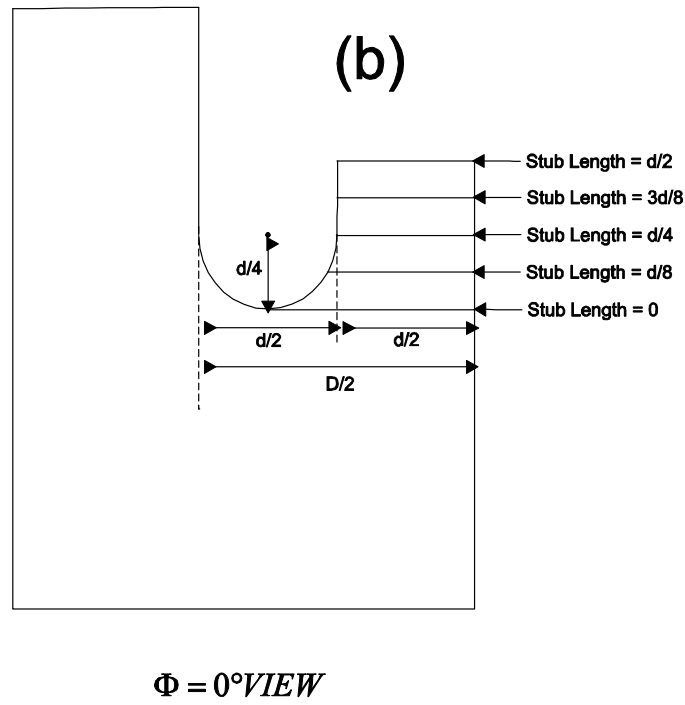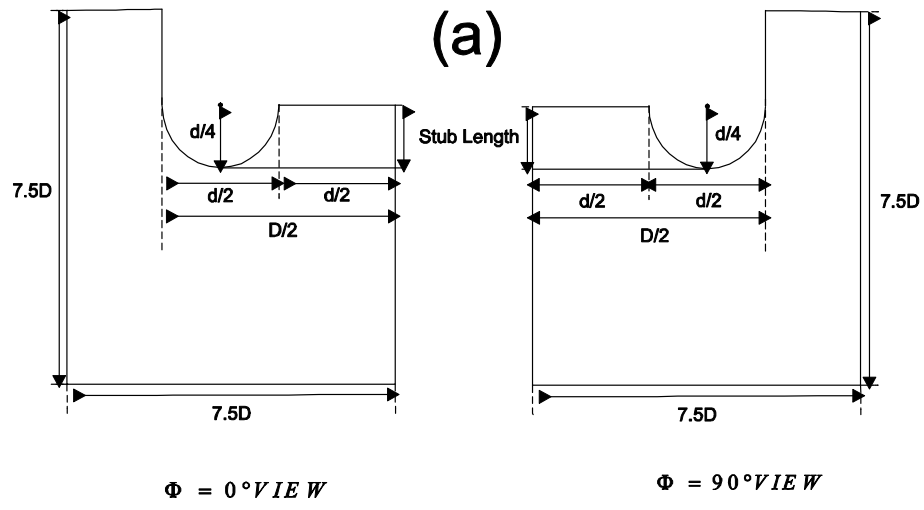
Figure 3.3: (a) Symmetry plane profiles. (b) Model geometry with variations in stub length. (Note: these 2 drawings are not scaled)

model boundaries are a minimum of 15 times the borehole radius away from the borehole itself, in order to avoid model edge effects in the vicinity of the borehole. The drill bit is a half-circular shape with a radius of d/4 for a total kerf width of d/2, while the radius of the borehole is D/2 and the radius of the core is d/2.

Earlier work has shown that the length of the core stub (L) is important to the distribution of the stresses [*Li and Schmitt*, 1997b], and therefore stress patterns within the core study may change as the borehole is drilled. The numerical models consider the static stress distribution for a given stub length and variations in stress during the drilling process are assessed by varying the core stub length (L) from 0 to d/2 (Figure 3.3b).

3.3 Numerical modeling of the 3D stress field around a borehole

This study uses the Finite Element Method (FEM) to calculate the stress distribution near the bottom of a borehole for the 3D model domain shown above. FEM is a widely used technique to solve partial differential equations numerically. It is particularly popular in fields such as mechanical engineering because it allows for the stress-strain distributions to be calculated for a wide variety of complex geometries. This is of course crucial in the design of solid components in order to obtain insight into how such objects might fail when subject to working conditions.

FEM is a well-established technique and there is little need to go into the details

as numerous textbooks exist [e.g., *Zienkiewicz, et al.,* 2005]. In addition, a variety of sophisticated commercial software programs are available that allow the FEM to be used by large groups of researchers. In particular, such software allows the problem geometry to be constructed more readily. The program ANSYS™ , available under license at the University of Alberta, was employed in the current study.

After *Zienkiewicz, et al.,* (2005), the typical FEM methodology proceeds by the five steps that will be described in more details in the following pages:

1. Problem definition in terms of the differential equations to be solved.
2. Selection of the type of finite elements to be used.
3. Construction of the finite element mesh upon which the calculations will proceed; this is usually the most labour intensive component.
4. Assignment of physical properties to model materials.
5. Definition of the appropriate stress and displacement boundary conditions to the model domain.

3.3.1 Governing equations

Mathematically speaking, the problem to be solved is a boundary value problem, in which the stresses in the vicinity of the borehole depend on the far-field in-situ crustal stresses (boundary conditions), the geometry of the bottom of the borehole and the assigned elastic properties of the rocks. The governing functions include strain-displacement relation functions, stress-strain relation functions (Hooke's Law), and equations of equilibrium (Newton's Law) that form a series of partial differential equations that need to be solved:

$$\bar{\bar{\tau}} = \lambda trace(\bar{\bar{\varepsilon}})I + 2G\bar{\bar{\varepsilon}} \qquad \text{(Hooke's Law)} \qquad (3.1)$$

$$\nabla^T \bar{\bar{\tau}} + \rho \underline{F} = \rho \frac{\partial^2 \underline{u}}{\partial t^2} \qquad \text{(Newton's Law)} \qquad (3.2)$$

$$\bar{\bar{\varepsilon}} = \frac{1}{2}\left[\nabla \underline{u} + (\nabla \underline{u})^T\right] \qquad \text{(Strain-displacement relation)} \qquad (3.3)$$

Where $\bar{\bar{\tau}}$ is the 2nd order stress tensor, $\bar{\bar{\varepsilon}}$ is the 2nd order strain tensor, λ is Lame's constant, G is the shear modulus, ρ is the material density, $\underline{F}$ is the body force, and $\underline{u}$ is the displacement. It should be noted that, in the models in this study, the density term does not have a significant effect on the solution, owing to the limited vertical height of the model domain, and thus for simplicity a density of zero is used. Therefore:

$$\nabla^T \bar{\bar{\tau}} = 0 \qquad (3.4)$$

The FEM method is used to numerically solve these equations by producing a set of linear algebraic equations for the unknown stresses and displacements at nodes within the finite element mesh.

3.3.2 Types of Elements Employed

In the FEM, the model domain is represented by a finite element mesh, composed of discrete 3D elements and associated nodes. The above equations are solved at nodes. The placement of the nodes depends on the element size and the type of element that is used. When constructing the model, it is important to choose an element type that will yield accurate results. In ANSYS $^{\text{TM}}$, there are two main

types of solid elements: hexahedron elements with nodes located at the vertices (Figure 3.4a) and tetrahedral elements, where nodes are located at both the vertices and in the middle of each edge (Figure 3.4b). In general, hexahedron elements give the most accurate solutions based on Finite Element theory and experience in real applications. The SOLID45 element in ANSYS^{TM}, which has 8 nodes (Figure 3.4a), was used in the modeling in this study. In constructing the models, it was important to design the FEM mesh such that the entire model geometry was composed of hexahedron elements. In some cases, the hexahedron elements may be degenerated to tetrahedral elements with nodes at the same position (as shown in Figure 3.4a tetrahedral option); the result is a less accurate numerical solution. In the models in this study, care was taken to ensure that there was no degeneration.

3.3.3 Finite Element Mesh

Once the model geometry is set (Figure 3.3), it must be appropriately meshed using the chosen hexahedron elements (Figure 3.4a) prior to the FEM calculations. This is a key aspect in the current problem, as the stress state must be well understood near the core stub in order to accurately resolve stress gradients that are crucial to the fracture propagation analysis. Figure 3.5 shows the mesh that yielded the most accurate solution for a stub length of 0.25d. Attention should be paid to the high density of elements near the bottom of the borehole and aspect ratio is less than 1:20. Table 3.1 gives the number of elements and nodes and the range of element sizes in the meshes that were developed for 5 different stub lengths.
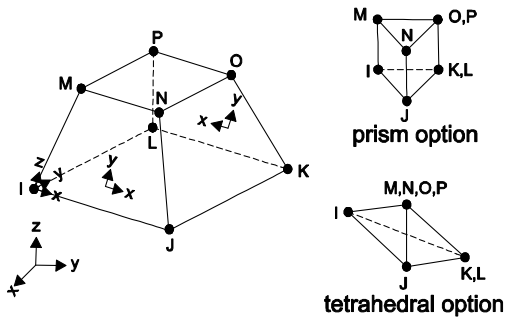
(a)
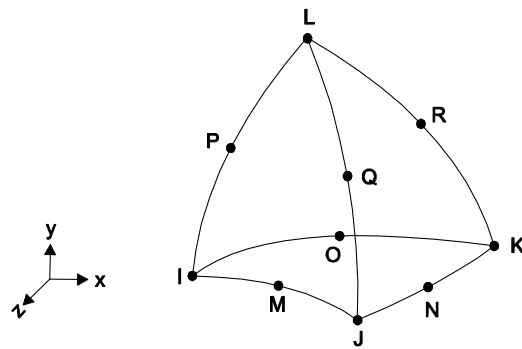
(b)

Figure 3.4: (a) Example of a hexahedron element (Solid45 Geometry in ANSYS[TM]). (b) Example of a tetrahedral element (Solid92 Geometry in ANSYS[TM])
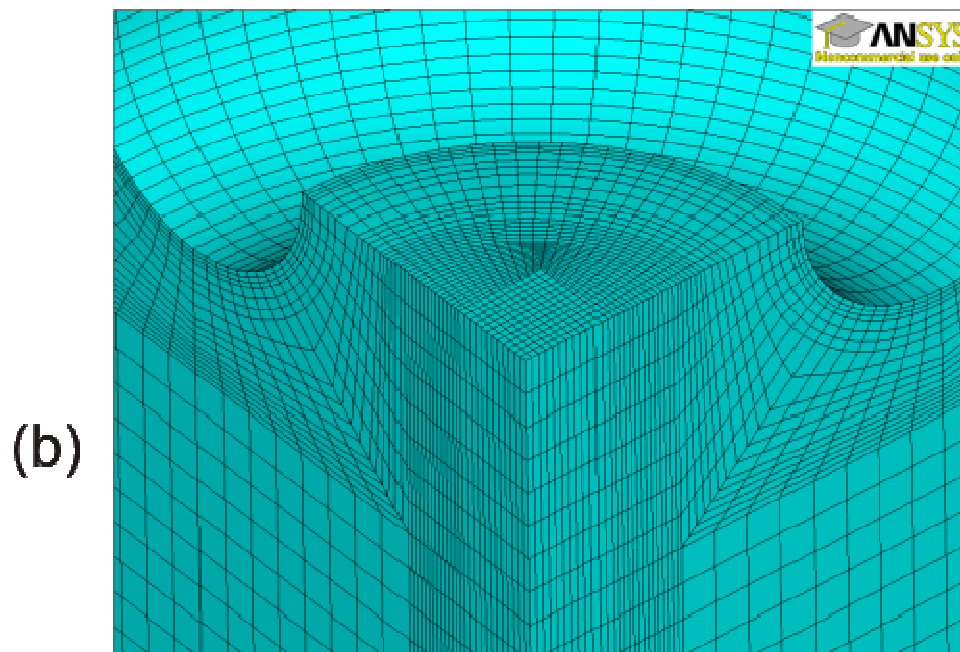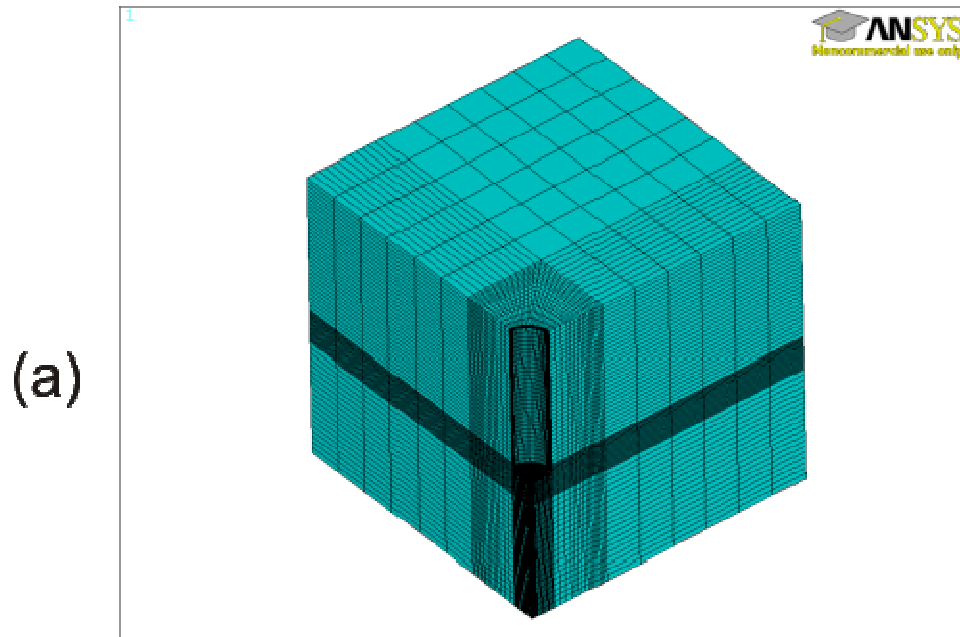
Figure 3.5: (a) Entire 3D FEM mesh for a stub length of 0.25d. The size of entire model domain is 7.5Dx7.5Dx7.5D. (b) FEM mesh at the bottom of borehole.

Table 3.1: Number of elements and nodes in the finite element mesh for different core stub lengths (note that d is the diameter of the core)

Stub Length	Number of Nodes	Number of Elements	Minimum Element Size	Maximum Element Size
0	130948	~124860	~0.025d X 0.025d X 0.044d	~1.75d X 1.75d X 0.3d
d/8	118008	~112060	~0.025d X 0.025d X 0.044d	~1.75d X 1.75d X 0.3d
d/4	118008	~112060	~0.025d X 0.025d X 0.044d	~1.75d X 1.75d X 0.3d
3d/8	123822	~117640	~0.025d X 0.025d X 0.044d	~1.75d X 1.75d X 0.3d
d/2	127698	~121360	~0.025d X 0.025d X 0.044d	~1.75d X 1.75d X 0.3d

3.3.4 Material properties

The solid material making up the borehole walls and the core stub is assumed to be homogeneous, linearly elastic, and isotropic. The elastic behaviour of the material is governed by the Young's modulus (E) and Poisson's ratio (υ). Briefly speaking, E, also known as the modulus of elasticity, is defined as the ratio of uniaxial stress to the resulting uniaxial strain. Poisson's ratio is the ratio between the negative of the radial to the axial strain when an object is subject to a uniaxial aligned principal stress. The literature on basic elasticity is vast and the reader is referred to *Zimmerman* et al. [2007] for further background information. Table 3.2 gives the range of density and elastic parameters (E, υ and G - the shear modulus) for typical rocks that make up the Earth's crust. Note that neither the density nor the shear modulus were used in the numerical models.

Table 3.2: Material properties of typical crustal material (after Turcotte & Schubert 2002)

	Density kg m^{-3}	E 10^9 Pa	G 10^9 Pa	υ
Sedimentary rocks				
Shale	2100 - 2700	10 - 70	10 – 30	0.1 - 0.2
Sandstone	1900 - 2500	10 - 60	4 – 20	0.1 - 0.3
Limestone	1600 -2700	50 - 80	20 – 30	0.15 - 0.3
Dolomite	2700 - 2850	50 - 90	20 – 640	0.1 - 0.4
Metamorphic rocks				
Gneiss	2600 - 2850	40 - 60	20- 30	0.15 - 0.25
Amphibole	2800 - 3150		50 – 100	0.4
Marble	2670 - 2750	30 - 80	20 - 35	0.2 - 0.3
Igneous rocks				
Basalt	2950	60 - 80	25 - 35	0.2 - 0.25
Granite	2650	40 - 70	20 - 30	0.2 - 0.25
Diabase	2900	80 - 110	30 - 45	0.25
Gabbro	2950	60 - 100	20 - 35	0.15 - 0.2
Diorite	2800	60 - 80	30 - 35	0.25 - 0.3
Pyroxenite	3250	100	40	
Anorthosite	2640 - 2920	83	35	0.25
Granodiorite	2700	70	30	0.25

Both E and υ are important to the calculation of the state of stress near the bottom of the borehole. First, the magnitude of the stresses generated will be controlled by ratio between the applied stress (i.e., each of SV (vertical overburden pressure), SH (maximum horizontal stress) and Sh (minimum horizontal stress)) and the value of E. The larger this ratio, the higher the strains induced, as discussed by *Li and Schmitt* [1997a]. Hence, for the purposes of modeling of stress distributions, and under the assumption of linear elasticity, it is the scaling of this ratio that is important for determining failure. As such, it is possible to carry out the problem in a scaled fashion with regards to both E and the spatial dimensions. For the numerical calculations, E = 10 GPa was used, but results are reported using scaled values (see Section 3.3.6).

The same is not true for Poisson's ratio, which, together with the actual borehole geometry, does have a control on the distribution of the stresses within the body [*Li and Schmitt*, 1997a]. This requires that separate solutions be calculated for each value of υ. Here, models were calculated for five values of Poisson's ratio: 0.05, 0.15, 0.25, 0.35, and 0.45.

3.3.5 Boundary conditions

Boundary conditions are applied to each of the boundaries of the model (Figure 3.6). On three faces of the model, stress boundary conditions are used, in which the assigned stresses reflect in-situ stresses within the crust. Assigned stresses are perpendicular to the boundary and correspond to the vertical overburden pressure (SV) on the upper boundary of the model, and two components of horizontal stress (SH and Sh) on the vertical planes outside the borehole region. It is

assumed that stresses on each of these boundaries are uniform. On the remaining two vertical boundaries of the model domain (the $\Phi = 0°$ and $\Phi = 90°$ planes), a symmetry boundary condition is used, in which nodes along this boundary can only move within this plane during deformation. This reflects the fact that these two boundaries correspond to planes of symmetry for the borehole. The final boundary condition is applied to the bottom surface of the model, which is the constrained plane. Here, nodes are restricted from moving in the vertical direction. Table 3.3 gives the boundary condition parameters used in the numerical models.
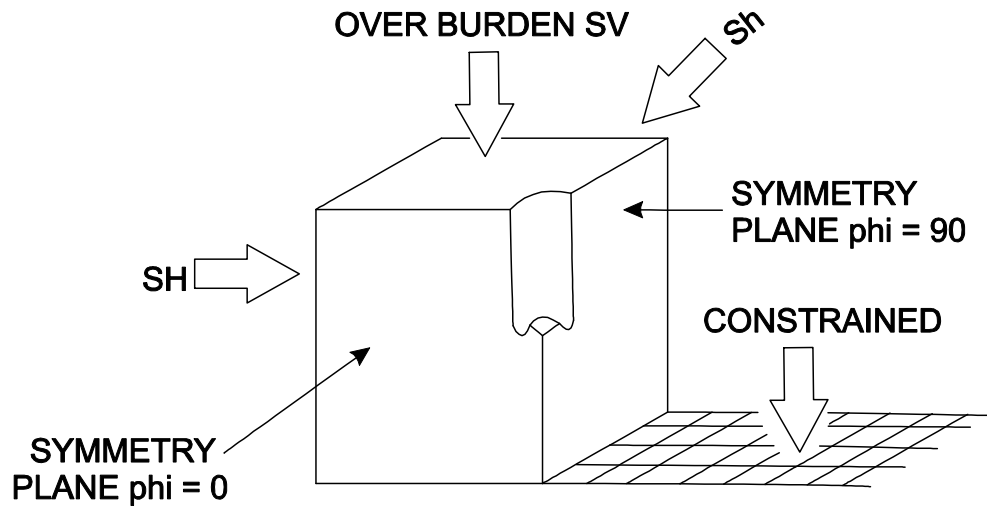
Figure 3.6: Boundary conditions for the numerical model

For the initial conditions, an unstressed state (no strain) is assumed. It is also assumed that there is small strain during deformation processing, which is reasonable through comparison of the magnitude of Young's modulus and in situ stress. This is important when using ANSYS^{TM} because if there is large deformation, a multi-step load must be applied.

Table 3.3: Boundary conditions using in numerical models (note that D is the diameter of the borehole and UX, UY, UZ represent the displacement along x, y, z directions, respectively)

Location	Description	Boundary Condition Type	Value Used For Generating Base Models
Z = 3.75D	SV - Overburden stress	Stress #1	20 MPa
Z = -7.5D	SH - Maximum horizontal stress	Stress #2	20 MPa
Y = 7.5D	Sh - Minimum horizontal stress	Stress #3	20 MPa
X = 0	Φ = 90° plane	Symmetry #1	UX = 0
Y = 0	Φ = 0° plane	Symmetry #2	UY = 0
Z = -3.75D	Bottom plane	Constrained	UZ = 0

3.3.6 Computational Procedure

The general procedure for calculating the stress distribution in the 3D numerical model is given in Figure 3.7.

Previous work has shown that variations in the relative magnitudes of SV, SH and Sh are the main control on the core fracture geometry [*Li and Schmitt*, 1997b]. Here, a range of crustal stress states are explored. A variety of stress states can be quickly reconstructed by linear superposition of the individual solutions for an applied vertical stress (SV) and two horizontal applied stresses (Sh and SH).
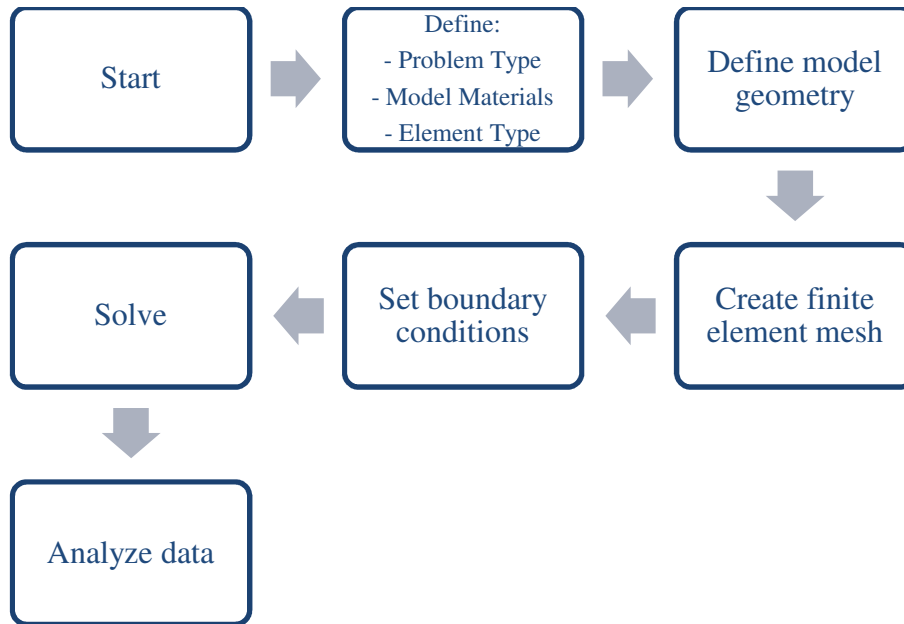
Figure 3.7: Flowchart showing stress field computations in ANSYS™.

These are called 'base' solutions in tensor form V, H, and h that exist at the set of nodal points $(x_i,\ y_i,\ z_i)$ of the mesh employed.

The stress field for a single vertical stress, V $(L,\ \upsilon,\ x_i,\ y_i,\ z_i)$, and horizontal stresses, H $(L,\ \upsilon,\ x_i,\ y_i,\ z_i)$ and h $(L,\ \upsilon,\ x_i,\ y_i,\ z_i)$ were computed using ANSYS™, where L is the stub length, υ is the Poisson's ratio, and $x_i,\ y_i,\ z_i$ stand for coordinate number.

During the calculation of the individual components, a single stress (SV, SH or Sh) of 20 MPa was applied at the model boundary, while setting the other two stresses

to zero. As previously noted, the stress field depends on the ratio between the applied stress and Young's modulus. In this study, a Young's modulus of E = 10 GPa was used, giving a σ/E ratio of R = 1/500. There is nothing special about this ratio, but as shown below, in later superposition, the appropriate scaling factors need to be employed.

The individual basis solutions can be superposed to yield any crustal stress field:

$$\sigma_{total} = aV + bH + ch \qquad (3.5)$$

where a, b, and c are scalar values of the appropriately scaled applied stresses. If one wishes, for example, to have particular (scalar) far field stresses SV, SH, and Sh applied, then within equation (3.5) a, b, c respectively represents:

$$a = \frac{1}{R}\frac{SV}{E_m} \qquad (3.6)$$

$$b = \frac{1}{R}\frac{SH}{E_m} \qquad (3.7)$$

$$c = \frac{1}{R}\frac{Sh}{E_m} \qquad (3.8)$$

where R is the σ/E ratio for the FEM basis solutions (1/500 in the current study) and E_m is the Young's modulus of the material under study. Such superposition is valid, as the medium is considered to be linearly elastic and isotropic and, a, b and c can be any positive number which depends on the values of applied stress (SV, SH or Sh) and E_m that are of interest. This approach, which uses already calculated stress base solution V, H, and h, allows for a rapid systematic exploration of the 3D stress field for a variety of in situ stress conditions.

Base solutions were obtained for the three applied stress states (SV, SH, Sh) for five values of the Poisson's ratio and five different stub lengths, for a total of 75 different model calculations. All models were run using ANSYS^{TM} (version 12) in a Microsoft Windows XP Professional environment (Version 2002, Service Pace 3) on a computer with a 3.00GHz Intel® Core™2 Duo CPU and 3.25 GB of RAM. In general, each base solution took about 15 minutes to run in ANSYS^{TM} and produced approximately 10 MB of information. The individual base solutions were saved in data files, which are provided as an electronic supplement to this thesis. Table A1.1 in Appendix 1 gives the name of the data files corresponding to each base solution. A program was written in MATLAB^{TM} to read the base solutions and carry out the superposition, based on the user's desired values of SV, SH and Sh.

Note that the results in this thesis are reported non-dimensionally. All distances have been divided by d, the borehole core radius. As shown in previous work [e.g., *Li and Schmitt*, 1998], only the relative magnitudes of SV, SH and Sh matter. Thus, the reported stresses are normalized by the value of the largest boundary stress for each case under consideration.
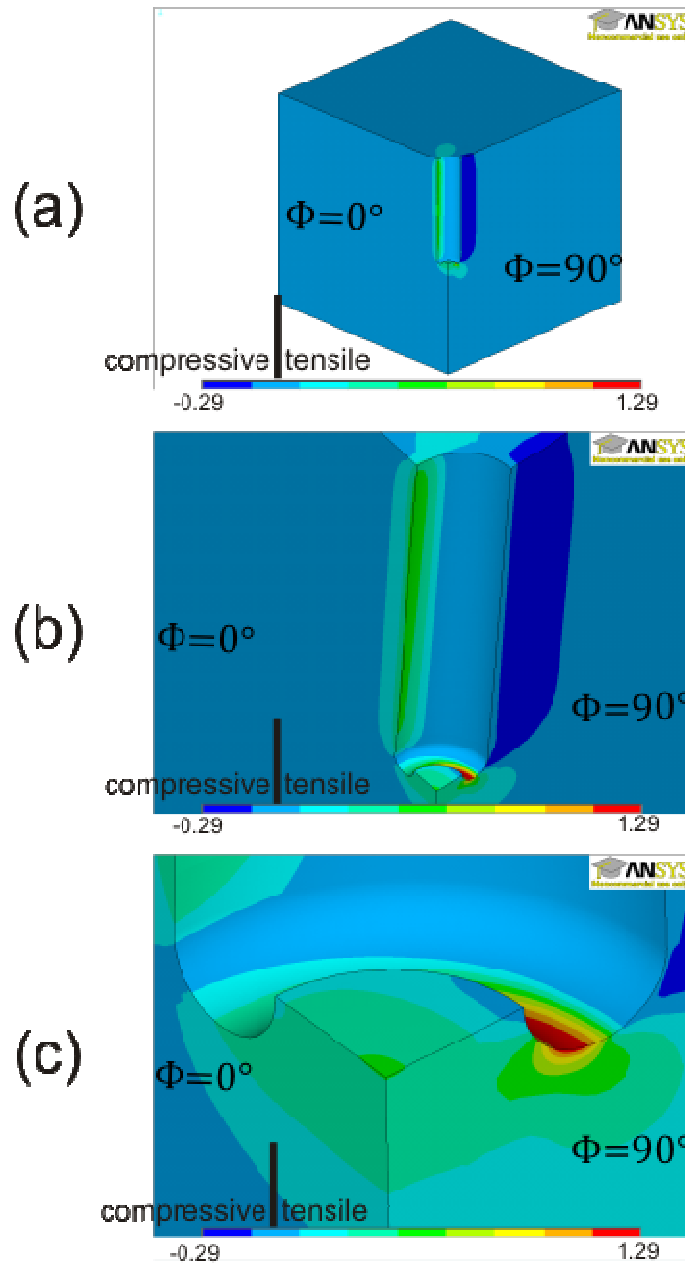
Figure 3.8: Stress field calculated for SV:SH:Sh=1:0.5:0, Poisson's ratio is 0.25 and stub length is 0.25d. (a) Entire model domain showing the uniform stress state in the far field. (b) Stress field for the borehole. Note the stress concentration at the Φ=0° and Φ=90° planes. (c) Stress field at the bottom of the borehole demonstrating large values of tensile stress.

3.4 Accuracy of the computed stress field

Figure 3.8 in the previous page shows an example of the stress field calculated using the superposition approach for a non-dimensional stress condition of SV:SH:Sh = 1:0.5:0, Poisson's ratio (υ) of 0.25 and the stub length of d/4. This figure shows the first principle stress (i.e., least compressive stress). The stress values in this plot are normalized and can be converted into actual stress values by multiplying by the desired SV. This plot clearly shows the spatial variations in stress. Away from the borehole (Figure 3.8a), stresses are equal to the in-situ stress in both magnitude and direction, as expected. The presence of the borehole perturbs the in-situ stress, and in particular produces areas where the rocks experience tensile stress, although all boundary stresses are compressive. Well above the bottom of the borehole, stresses primarily vary in the horizontal direction, with maximum values of compressive and tensional stress observed along the $\Phi = 0°$ and $\Phi = 90°$ planes, respectively (Figure 3.8b). These are discussed in more detail in the next section. The strongest variations in stress are seen in the vicinity of the bottom of the borehole (Figure 3.8c). Here, stresses vary in three-dimension, and exhibit the largest values of tensile stress. These tensile stresses are inferred to give rise to fractures.

Before calculating the expected fracture trajectories, it is critical to assess the accuracy of the computed stress field. In this thesis, three different tests were used: (1) the Kirsch test (see also Chapter 2), (2) the 110 test; and (3) symmetry tests. These are presented in the following sections, with an example of test results for one model. These tests were also applied to many other models in order to ensure

accuracy. They were particularly important in developing a suitable finite element mesh for the stress calculations, especially the 110 test.

3.4.1 Kirsch test

Unfortunately, no analytic solution exists for the 3D stress field in the vicinity of the bottom of a borehole with a core stub so there are no ready comparisons that may be made to calibrate the finite element model. However, as discussed in Chapter 2, Kirsch [1898] derived expressions for the hoop stress around a circular hole in a 2D plate with given far field principal stresses σ_1 and σ_2:

$$\tau_{\theta\theta} = (\sigma_1^\infty + \sigma_2^\infty) - 2(\sigma_1^\infty - \sigma_2^\infty)\cos 2\theta \qquad (3.9)$$

Where $\tau_{\theta\theta}$ represents the hoop stress, σ_1^∞ is one principal stress in far field, and σ_2^∞ is the other one, θ is angle used to indicate the location around hoop. This equation predicts the hoop stress variation along the circular hole boundary. Particularly for the case when one principal stress in far field is zero, the ratio of the maximum hoop stress ($\theta=0°$) and minimum hoop stress ($\theta=90°$) could be (+1):(-3), where "+" means tensile, "-" means compressive. This equation has long been used to provide theoretical measures of the stress concentrations around boreholes and has been applied to many stress related phenomena such as hydraulic fracturing [*Haimson and Cornet*, 2003; *Hubbert and Willis*, 1957; *Schmitt and Zoback*, 1989] and borehole breakout analyses [*Bell and Gough*, 1979; *Zoback, et al.*, 1985].

This 2D solution can be compared to the 3D model results within horizontal planes at distances sufficiently removed from the bottom of the model borehole

such that any complicating 3D effects may be ignored. Figure 3.9 compares the computed stresses around the borehole wall with the analytic result at different heights above the bottom of the borehole (distances reported in terms of D, the diameter of the borehole) for the stress model shown in Figure 3.8, where θ=0° corresponding to Φ=0°, $\sigma_1^\infty = 0.5$, $\sigma_2^\infty = 0$. The largest values of compressional stress are observed at Φ = 90° (3 times larger than the maximum tensile stress) and the largest tensional stresses are found at Φ = 0°. The computed stresses are within 5% of the *Kirsch* [1898] solution for horizontal planes that are more than 3D above the borehole bottom. Closer to the bottom of the borehole, the effect of the borehole bases becomes important and the tress concentrations are no longer two-dimensional (see also Figure 3.8).
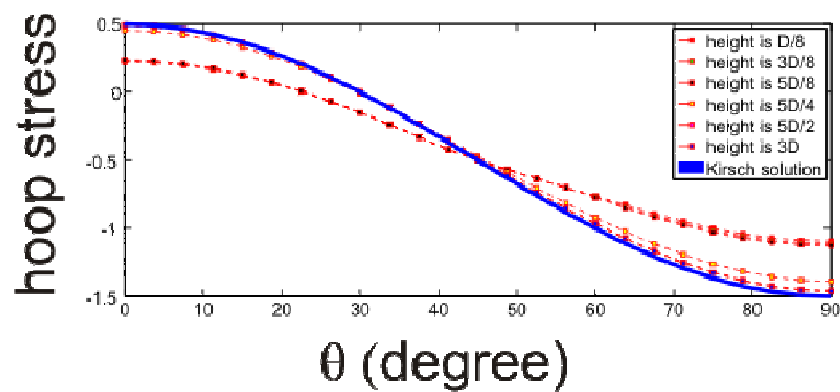
Figure 3.9: Variation in stress (normalized hoop stress) around the borehole walls at various distances from the bottom of the borehole. At longer distances, model results are in good agreement with the analytic 2D Kirsch solution.

3.4.2 The 110 test

This test examines the stresses on the vertical symmetry planes of the model domain (the Φ = 0° and Φ = 90° planes). On these two planes, it is expected that

two principal stresses should be parallel to the plane and the third principle stress should be perpendicular to the plane, using the following argument:

- We can designate a small penny-shaped element to be located on symmetry plane and parallel to this symmetry plane. Based on Cauchy's 1st law, the traction on the left side of this element must be equal to the right side of the element because equilibrium is required to make system stable.

- Since the element is located on symmetry plane, the left side of the element must be in the same situation as the right side of the element, i.e., mirror symmetry.

- Therefore, traction must be perpendicular to the element, and of course this must be a case in which no shear stress exists, so it has to be one of the principal stresses. Consequently, the other two principal stresses must be parallel to the element.

The stress field in Figure 3.8 was analyzed for the orientation of the stress field along the $\Phi = 0°$ and $\Phi = 90°$ planes. Along each plane, the eigenvectors of the 3D stress field were calculated. On the basis of the above arguments, it is expected that the projection on the symmetry plane of two eigenvectors should have a magnitude of 1 (i.e., lie in the symmetry plane), and the projection on symmetry plane of the other eigenvector should have a value of 0. Therefore this was called the "110 test". Note that this test was developed for the current research, but could be applied to other studies that use a symmetry boundary condition.
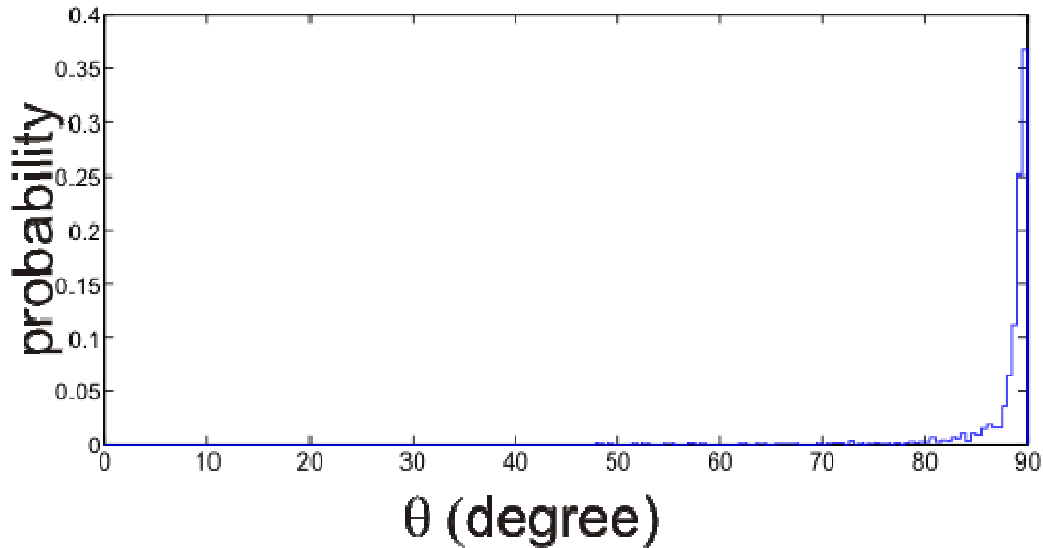
Figure 3.10: Probability distribution of the orientation of third eigenvector of the stress field at nodes on the $\Phi = 90°$ plane

The 110 test predicts that the third eigenvector should have an angle of 90° with respect to the symmetry plane. Figure 3.10 shows the probability distribution in the angle of the third eigenvector for all nodes in the $\Phi = 90°$ plane for the model in Figure 3.8. This figure shows that over 85% of the nodes have eigenvectors at angles of > 87°, and over 98% nodes are have an angle larger than 80°. A similar distribution is observed for the $\Phi = 0°$ plane. The small variations in the angle from 90° are due to error of the numerical calculation. Overall, this test shows that the computed stress field is in excellent agreement with that expected.

3.4.3 Symmetry test

The final test involves looking at the computed stress fields for situations in which there is an isotropic horizontal stress (SH = Sh). In this case, it is expected that

103

any vertical plane containing the Z axis should have the same stress distribution (i.e., axial symmetry). To illustrate this, a model was calculated for the case SV:SH:Sh = 1:0.5:0.5, Poisson's ratio (υ) of 0.25 and stub length of d/4. Figure 3.11 shows the projection of the two principal stresses on several vertical planes through this model. The orientation of the plane is defined by its angle (Φ) with respect to the direction of SH. The computed orientation and magnitude of two principal stresses are the same for each plane, demonstrating that the results are numerically accurate.

3.5 Numerical method for fracture tracing

Using the three tests described above, a finite element mesh was constructed that could be used to accurately calculate the 3D stresses in the vicinity of the borehole. Base solutions (V, H, h) were computed using ANSYS$^{\text{TM}}$. These results were then imported into MATLAB$^{\text{TM}}$ to carry out superposition and track the growth of a tensile fracture for a range of in-situ stress states, Poisson's ratio and stub lengths.

3.5.1 Tensile fracture model

The fracture propagation model used in this study builds on the algorithm used by *Li and Schmitt* [1997] for a 2D case. Based on the observations of real core fractures, *Li and Schmitt* [1997] assumed that the drilling induced core fractures were formed under a purely tensional stress. A fracture initiates once the tension
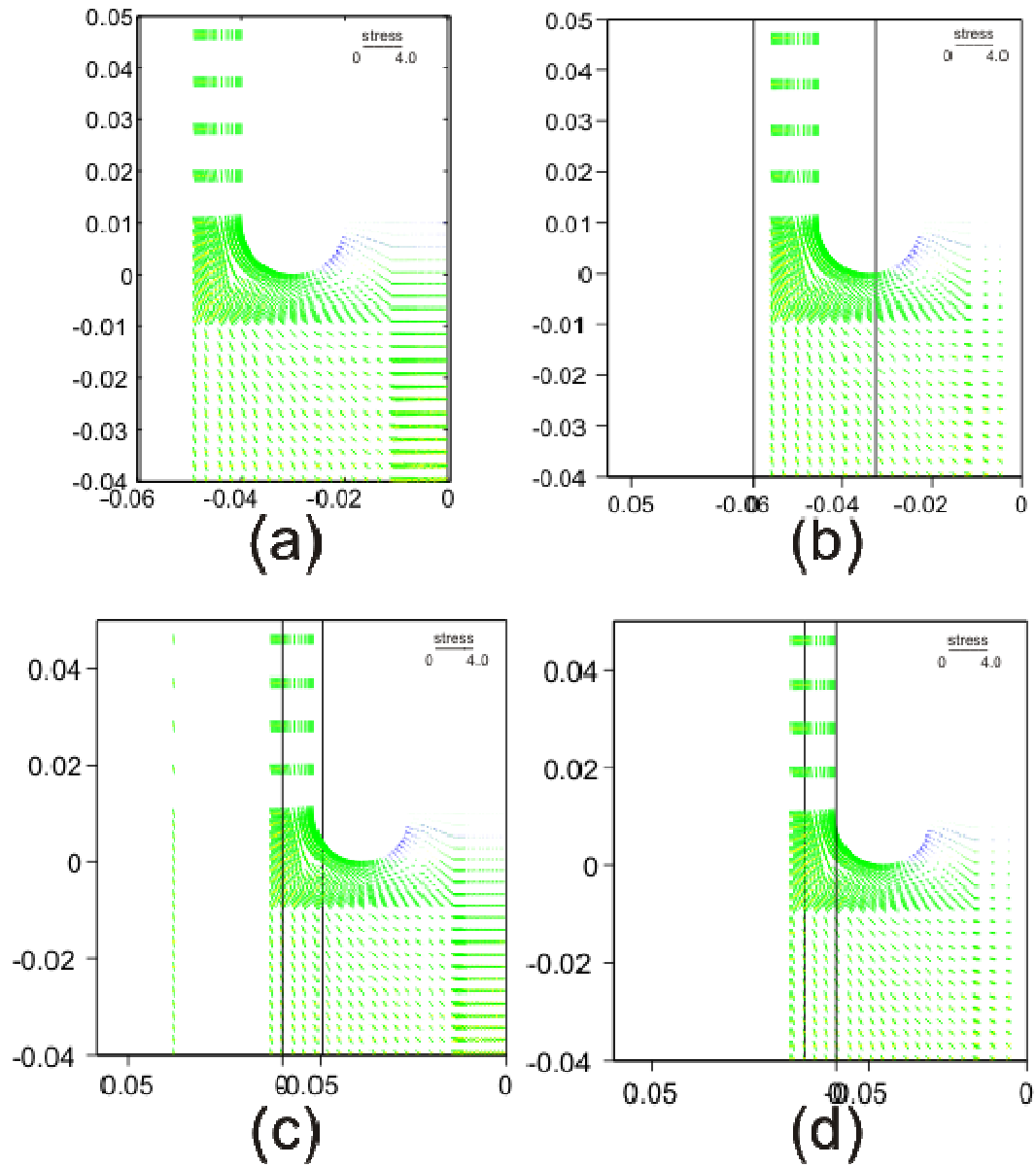
Figure 3.11: Projection of two principal stresses within vertical planes through the borehole for a model with SH = Sh. (a) $\Phi = 0°$ plane; (b) $\Phi = 30°$ plane; (c) $\Phi = 45°$ plane; (d) $\Phi = 60°$ plane. Note that the blue represents the tensile stress, and the green represents the compressive stress.

exceeds the material's tensile strength and the fracture opens perpendicularly to the direction of this stress as a Mode I crack. Deciding where the fracture initiates and how the fracture will then propagate is not necessarily straightforward. *Li and Schmitt* [1997] developed a simple approach to model such fracture propagation in 2D along the $\Phi = 0°$ and $\Phi = 90°$ planes of a full 3D stress model. Within each 2D plane, the fracture initiation point was taken to simply be the point subject to the greatest principal tensile stress, and the tensile fracture opened perpendicular to this principal stress direction. This idea is similar to the maximum tensile stress criterion employed to predict fracture trajectories [*Viola and Piva*, 1984] or the maximum circumferential stress criterion [*Erdgodan and Sih*, 1963]. *Li and Schmitt* [1997] then propagated the fracture perpendicular to the tensile stress direction to the first edge of the element in which the fracture has initiated. At the intersection of the 'crack' projection and the element face, the 3D stress state was determined and a new set of principle stresses found. The fracture trajectory was then modified by the direction of the greatest tension at this point and the process repeated with projection of this new segment again to the next element edge. The fracturing process is expected to cease once no purely tensional stress is found, although they allowed the calculation to proceed even through fully compressive zones for purposes of illustration.

There is much to criticize though with this procedure. First, this is essentially a static calculation that ignores any inertia gained by the medium upon conversion of potential strain energy to dynamic kinetic energy [*Berry*, 1960]. Second, the procedure does not admit that the creation of the fracture itself must result in a redistribution of the stresses. Various schemes have been developed to overcome this problem nearly all of which require re-meshing of the model and defining new contact surfaces in order to effect realistic fracture trajectories [e.g., *Shahani*

and Fasakhodi, 2009] or by having the strength of those elements intersected by a fracture vanish [e.g., *Beissel, et al.*, 1998]. That said, however, there remains much that is unknown and recently in a review of this topic [*Pook*, 2010] stated that *"At the present state of the art the factors controlling the path taken by a propagating crack are not completely understood"*. The problem is further complicated by the more complex physical process of fracture within rocks themselves; as so called 'tensile' fractures retain considerable cohesion with no discrete open fracture even visible (see for example Figure 2.16(c)). Consequently, although it is realized that the approach to fracture propagation is flawed, this method still attempts to capture some of the essential physics that would be expected. Different failure criteria, such as those that use maximum strain energy, could be employed to the existing numerical data set. The greatest advantage of the current approach lies more in its ability to rapidly test many different stress conditions.

3.5.2 Tensile fracture propagation in 3D

In this thesis, an algorithm for calculating the full 3D tensile fracture propagation was developed based on the 2D approach of *Li and Schmitt* [1997]. Some substantial adaptations were required in order to account for the fact that the crack must now propagate as a surface in 3D, and the criteria for finding the loci of the fracture front must be found. The 2D problem was much simpler in that the crack was only a line and the propagation need only be controlled by the stress directions at a single point.
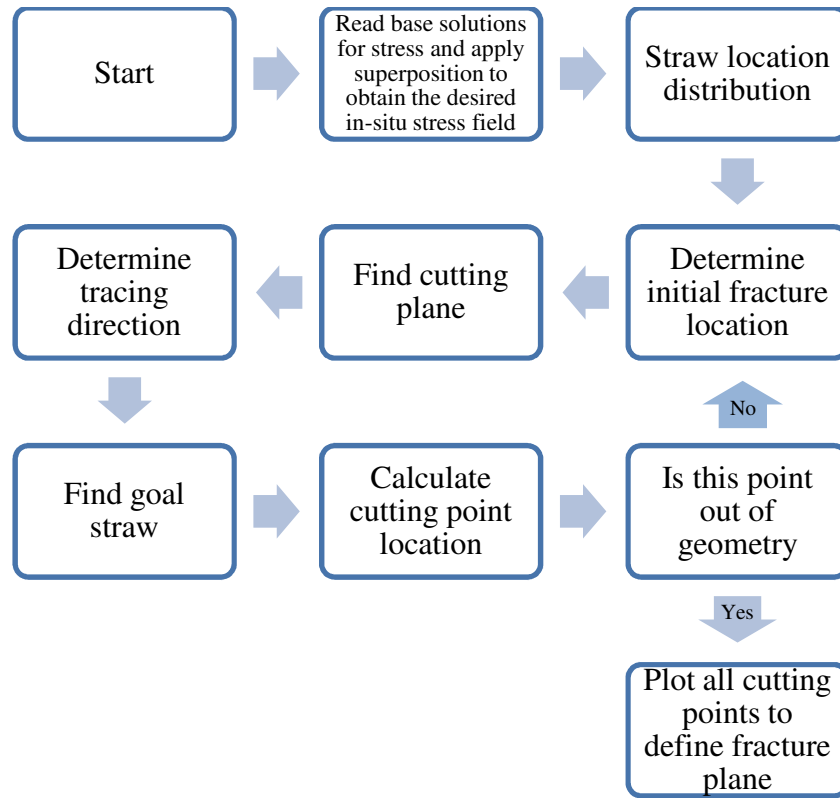
Figure 3.12: MATLAB$^{\text{TM}}$ flowchart for fracture tracing

The overall procedure used in the MATLAB$^{\text{TM}}$ codes is summarized in Figure 3.12 and follows the following steps:

1. Appropriately superpose the basis stress solutions to create the SV-SH-Sh compressive stress conditions desired. This is relatively easily done at each of the nodes (x_i , y_i , z_i) within the FEM mesh employed. The FEM mesh was designed with nodes aligned in vertically columns, with very small spacing between the nodes. Each column forms a "straw" that is used in the fracture tracing.

2. Search for the node with greatest principal tensile stress within the mesh. This location will be taken as the fracture initiation point.

3. Calculate the orientation of a plane that is normal to the direction of the tensional stress. This is taken as a cutting plane that extends outward from the node.

4. Extend this plane through the "straw forest" to locate the points where it intersects the two adjacent straws, as shown in step A in Figure 3.13.

5. The point of intersection is taken as the fracture point on the straw. The stress at the fracture point is taken to be that of the closest node on that straw. Owing to the close vertical spacing of nodes along the straw, it is believed that directly using the stress tensor at the nearest node will not introduce significant errors into the solution; future work could determine the stress solution at the fracture point through interpolation of the nearest nodes. Note that this straw should not fracture unless the tensile stress exceeds the strength of the material. However, in this initial implementation, it is assumed that the material has no tensile strength, and indeed the fracture is allowed to propagate according the minimum compressive stress criteria even if no tensile stress exists. Future developments could easily incorporate this.

6. At the fracture point, analyze the stress tensor and find the direction of least compressive stress and use this to extend the cutting plane to the next set of straws (step B in Figure 3.13).

7. Repeat steps A and B to continuously extend the fracture (Figure 3.13). In the current models, fractures terminate once they have broken all the way through the model. Strictly speaking, fractures should terminate once the tensile stress along the cutting plane is less
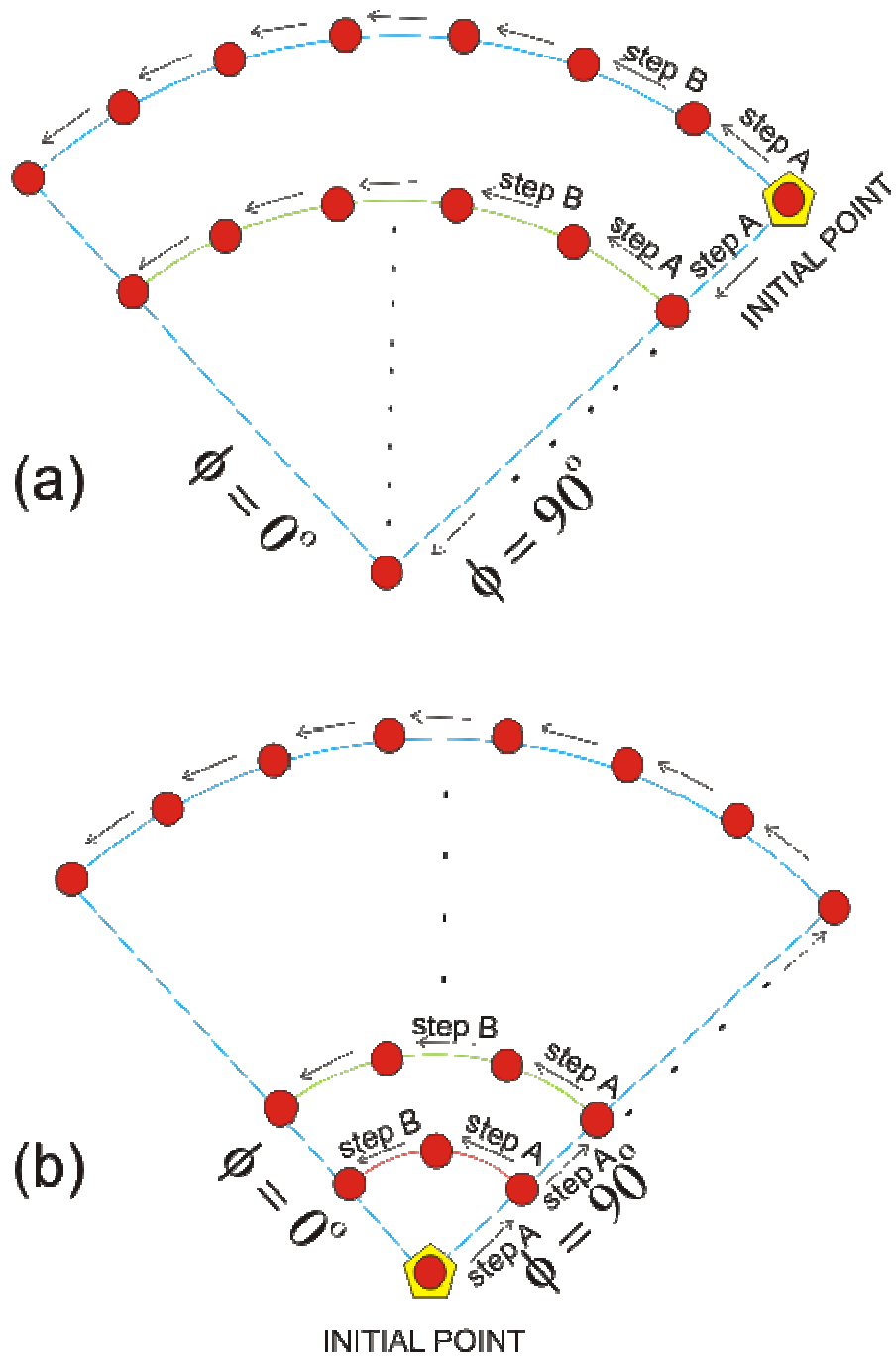
Figure 3.13: Numerical fracture tracing methods (top view). (a) Initial point located at kerf. (b) Initial point located on symmetry axis.
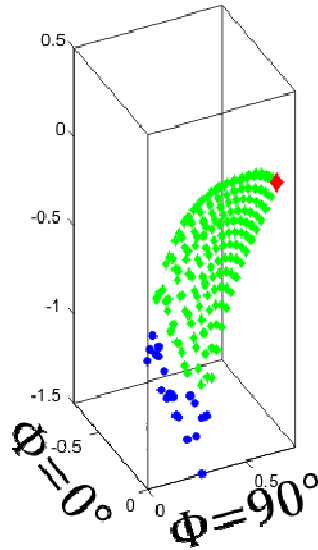
Figure 3.14: Demonstration of fracture tracing results

than the material strength. However, in this study, fractures propagate according to the direction of least compressive stress and therefore can enter a compressive zone (where all stresses are compressive).

8. Finally, all the fracture points (in both the tensile and compressive zones) can be plotted in 3D space to define the fracture surface.

As an example, Figure 3.14 shows the 3D fracture surface for the stress model shown in Figure 3.8. Here, SV:SH:Sh = 1:0.5:0, Posson's ratio (υ) is 0.25 and the stub length is d/4. The fracture initiation point is shown with a red diamond. The

fracture points are plotted using green to show where the fracture is in the tensile zone and in blue colour for the compressive zone. The transition between the two zones gives the approximate extent of a tensile fracture for a material with a low tensile strength.

The numerical techniques presented in this chapter provide an efficient way to rapidly calculate the 3D stress state near the bottom of a borehole and the resulting 3D fractures in the core stub. The next chapter explores how variations in the in-situ crustal strength, Poisson's ratio and core stub length affect the development of core fractures.

3.6 References

Beissel, S. R., G. R. Johnson, and C. H. Popelar (1998), An element-failure algorithm for dynamic crack propagation in general directions, *Eng. Fract. Mech.*, *61*, 407-425.

Bell, J. S., and D. I. Gough (1979), Northeast-Southwest Compressive Stress in Alberta - Evidence from Oil-Wells, *Earth Planet. Sci. Lett.*, *45*, 475-482.

Berry, J. P. (1960), Some Kinetic Considerations of the Griffith Criterion for Fracture .1. Equations of Motion at Constant Force, *J. Mech. Phys. Solids*, *8*, 194-206.

Erdgodan, F., and G. Sih (1963), On the crack extension in plates under plane loading and transverse shear, *J. Basic Eng., Trans. ASME, Series D*, *85*, 519-527.

Haimson, B. C., and F. H. Cornet (2003), ISRM suggested methods for rock stress estimation - Part 3: hydraulic fracturing (HF) and/or hydraulic testing of pre-existing fractures (HTPF), *International Journal of Rock Mechanics and Mining Sciences*, *40*, 1011-1020.

Hubbert, M. K., and D. G. Willis (1957), Mechanics of Hydraulic Fracturing, *Transactions of the American Institute of Mining and Metallurgical Engineers*, *210*, 153-163.

Jaeger, J., N. Cook, and R. Zimmerman (2007), *Fundamentals of rock mechanics*, Wiley-Blackwell, New York.

Li, Y. Y., and D. R. Schmitt (1997a), Effects of Poisson's ratio and core stub length on bottomhole stress concentrations, *International Journal of Rock Mechanics and Mining Sciences*, *34*, 761-773.

Li, Y. Y., and D. R. Schmitt (1997b), Well-bore bottom stress concentration and induced core fractures, *Aapg Bulletin-American Association of Petroleum Geologists*, *81*, 1909-1925.

Li, Y. Y., and D. R. Schmitt (1998), Drilling-induced core fractures and in situ stress, *Journal of Geophysical Research-Solid Earth*, *103*, 5225-5239.

Pook, L. P. (2010), Five decades of crack path research, *Eng. Fract. Mech.*, *77*, 1619-1630.

Schmitt, D. R., and M. D. Zoback (1989), Poroelastic Effects in the Determination of the Maximum Horizontal Principal Stress in Hydraulic Fracturing Tests - a Proposed Breakdown Equation Employing a Modified Effective Stress Relation for Tensile Failure, *Int. J. Rock Mech. Min. Sci.*, *26*, 499-506.

Shahani, A. R., and M. R. A. Fasakhodi (2009), Finite element analysis of dynamic crack propagation using remeshing technique, *Mater. Des.*, *30*, 1032-1041.

Turcotte, D.L. and Schubert, G. (2002), *Geodynamics, Second Edition,* Cambridge University Press, 456pp.

Viola, E., and A. Piva (1984), Crack paths in sheets of brittle material, *Eng. Fract. Mech.*, *19*, 1069-1084.

Zienkiewicz, O., R. Taylor, and J. Zhu (2005), *The Finite Element Method: Its Basis and Fundamentals, 6th Ed.*, Elsevier, Amsterdam.

Zoback, M. D., D. Moos, L. Mastin, and R. N. Anderson (1985), Well Bore Breakouts and Insitu Stress, *Journal of Geophysical Research-Solid Earth and Planets*, *90*, 5523-5530.

Chapter 4

3D Fracture Analysis

4.1 Introduction

In this chapter, the numerical modeling methodology outlined in Chapter 3 is applied to understand the development of fractures in borehole cores. In real cores, fractures are observed to have distinct morphologies and can be classified as petal, petal centreline, saddle and disc or cup (see Figure 1.2). Here, numerical models are used to understand the conditions under which each morphology is observed according to the numerical modeling. As described in Section 3.3.6, a set of base solutions (V, H, h) was developed for five core stub lengths and five values of Poisson's ratio. These base solutions can be superposed in order to generate any stress field around a borehole, for given values of the overburden stress (SV), maximum horizontal stress (SH), minimum horizontal stress (Sh), Poisson's ratio (υ) and core stub length (L). Within the 3D stress field, fractures in the core stub are assumed to initiate at the point of maximum tensile stress and propagate from this point through the stub along a direction perpendicular to the maximum tensile stress direction. Fracture trajectory is calculated based on the spatial variations in the orientation of the stress field.

The first set of models examines variations in the in-situ stress within the crust. Earlier studies of tensile fracture development in 2D [*Li and Schmitt*, 1998] have

shown that the crustal stress state exerts a dominant control on fracture morphology. The current study extends this work to full 3D models of the fracture surfaces that might be produced. Later in the chapter, variations in Poisson's ratio are tested in order to study the influence of rock elastic properties on fracturing. Finally, the influence of the core stub length is considered. This provides a way to examine how stresses in the core evolve during drilling and thus how fracturing may be affected.

4.2 Effect of in situ stress on fracture morphology

This section explore the development of tensile fractures for a range of in-situ crustal stress conditions (SV, SH, Sh). Before proceeding, some explanatory notes with regards to the model figures shown in this chapter are necessary. Figure 4.1a, for example, consists of two panels. The right panel shows the stress concentrations at the edge surfaces of the 3D finite element model, keeping in mind that symmetry considerations allow calculations to be carried out on only one quadrant. The colors shown are proportional to the value of the least compressive principal stress at each point on the surface of the model. The associated color bar at the bottom has been further delineated into the positive (tensile) and negative (compressional) stresses. The values associated with this color bar are normalized with respect to the absolute value of the greatest applied compression. For example, the maximum value in the color bar of Figure 4.1a is 0.12 which means that the maximum tensile stress generated has a magnitude about 12% that of the maximum applied compression, which is SV in this case. So if SV=20MPa, then the maximum tensile stress would be ~2.4 MPa.

In the left panel, the 3D fracture surface determined using the method given in Section 3.5.2 is shown with the geometry of the borehole left completely transparent. Distance units are normalized using d, the diameter of the borehole core. A depth of zero corresponds to the bottom of the borehole, and the directions parallel to SH and Sh are designated as the $\Phi = 0°$ and $\Phi = 90°$ planes respectively. On the fracture surface, each dot corresponds to the position of the cutting point on a vertical straw. The fracture initiation point is taken at the location of the global most tensile stress and is indicated by the red diamond symbol. It is assumed fractures may be initiated at any value of tensile stress, even those that are very small. In reality, most rocks have a finite tensile strength [*Zimmerman* et al., 2007] and will only undergo fracturing once this strength is exceeded. Furthermore, once the fracture is initiated, the fracture is propagated according to the least compressive stress criterion even if no tensile stress exists. To some degree, this may mimic the effects of fracture mechanics in which cohesion is lost behind the fracture front. The zones of tension and compression along this hypothetical fracture surface are distinguished by the green and blue colors, respectively. In the models, the fracture can reach a maximum depth of 3.75D below the bottom of the kerf.

The sections that follow are organized systematically in order to highlight various aspects of differing stress fields and how fractures evolve with changes in conditions. Broadly this includes:

1. A set that highlights stress concentrations under isotropic applied stress conditions beginning in the normal faulting regime (SV > SH = Sh) and transitioning through to a thrust faulting regime (SH = Sh > SV);

117

2. Individual explorations of the normal (SV > SH > Sh), the strike slip (SH > SV > Sh), and the thrust faulting regimes (SH > Sh > SV);

Although a large number of examples have been calculated and are shown here, the list above cannot be exhaustive and the reader is directed to employ the codes developed in Chapter 3 for specific cases of interest.

4.2.1 Isotropic horizontal stress (SH = Sh)

This set of models focuses on isotopic horizontal in-situ stress conditions (i.e., SH = Sh). The rock material in these models has a Poisson's ratio of 0.25 and the core stub length is 0.25d (where d is the diameter of the core). The following three sections illustrate cases where the overburden stress is more compressive, equal, or less compressive than the horizontal stress magnitude. For the isotropic horizontal stress situations, the initial fracture point is not a single point but a circle centred on the symmetry axis and parallel to horizontal plane. For convenience, only one point on this circle is marked as the initial point.

4.2.1.1 SV > SH = Sh

Figure 4.1 illustrates the case when overburden stress SV is more compressive than beginning horizontal stresses that are 80% that of SV and transitioning to a case where the horizontal stresses are only 10% of SV. This stress state falls within the normal faulting regime.

stub length is 0.25, Poisson's ratio is 0.25, SV:SH:Sh=a:b:c,b=c,a>b,a>c
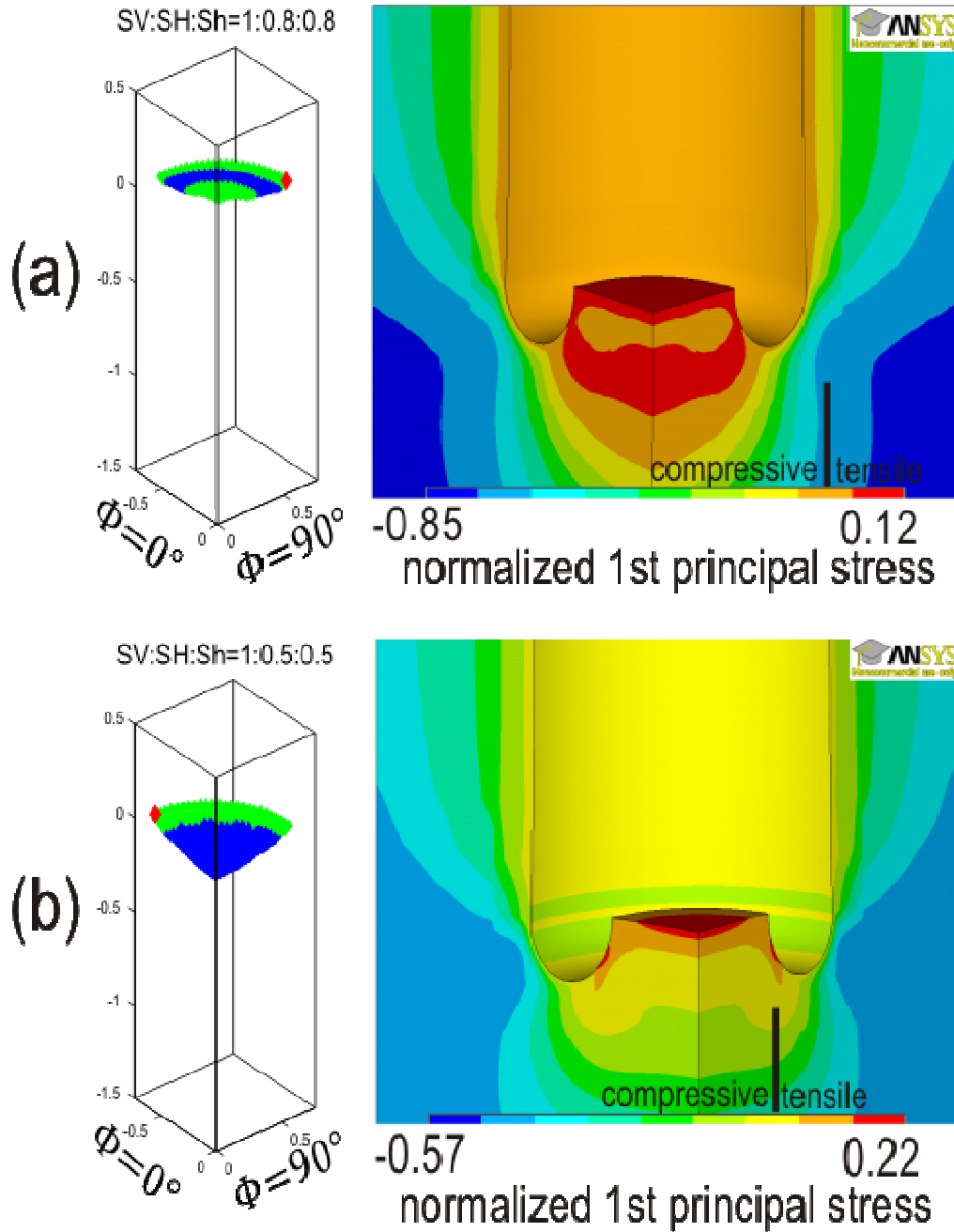
Figure 4.1: Plots of the fracture surface (left) and normalized stress (right) for variations in in-situ stress when SV>SH=Sh. (a) SV:SH:Sh = 1:0.8:0.8. (b) SV:SH:Sh = 1:0.5:0.5

119
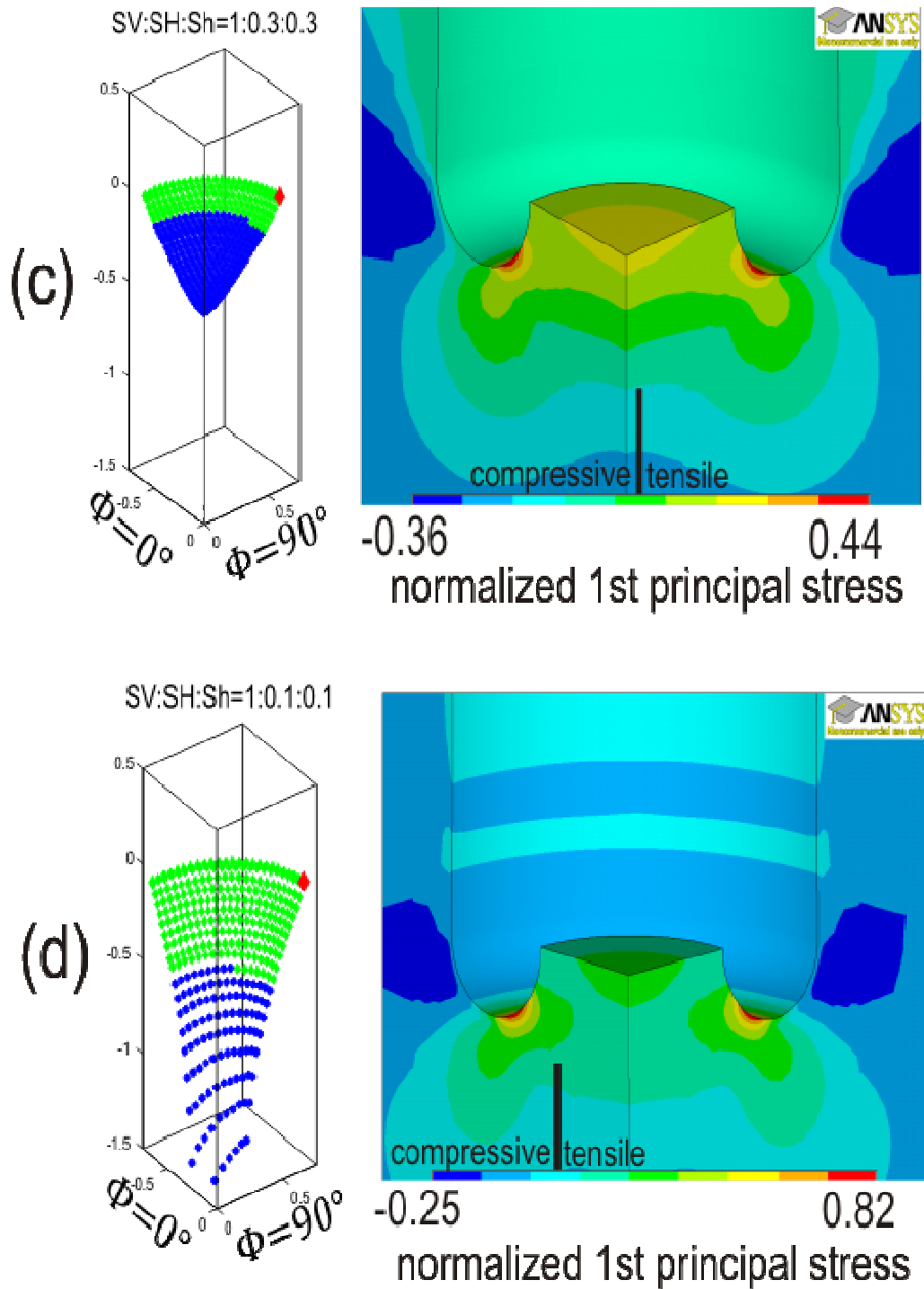
Figure 4.1 continued: (c) SV:SH:Sh = 1:0.3:0.3. (d) SV:SH:Sh = 1:0.1:0.1

The stress and fracture figures have symmetry properties due to the isotropy of the horizontal stress. When the horizontal stress magnitude is close to that for the overburden stress SV, the fracture surface is a flat disc shape, as shown in Figure 4.1a. As the horizontal stresses decrease, the fracture surface deepens, becoming increasingly concave such that the fracture is almost vase-like in shape (Figure 4.1d). Figure 4.1 further shows that the fracture initiation point is always on the inner kerf, and that the fracture presumably propagates into fully compressive zones (as indicated by the blue surface color on the fracture). This could indicate that such fractures may only break the outer portions of the core. Interestingly, the global maximum tension magnitude increases as the horizontal stresses decrease. For example, in Figure 4.1(a), it is about 12% of SV for SH = Sh = 0.8 SV but this increases to 82% when SH = Sh = 0.1SV. This suggests there is more possibility for fracture occurrence for smaller horizontal stresses.

It is also important to note that there are additional zones of tensile stress at the top of the core near the symmetry axis (e.g., Figure 4.1 (a) and (b)), which could lead to the development of additional fractures in these areas, although the magnitudes are relatively small.

4.2.1.2 SV = SH = Sh

The single panel of Figure 4.2 illustrates the case when overburden stress is equal to horizontal stress. The figure shows symmetry property as expected under the isotropic horizontal stress situation. The fracture shape looks like a flat disc but slightly bends upwards toward symmetry axis, i.e. it appears weakly convex. The initial point is located at the inner kerf, the global maximum tensile stress is about
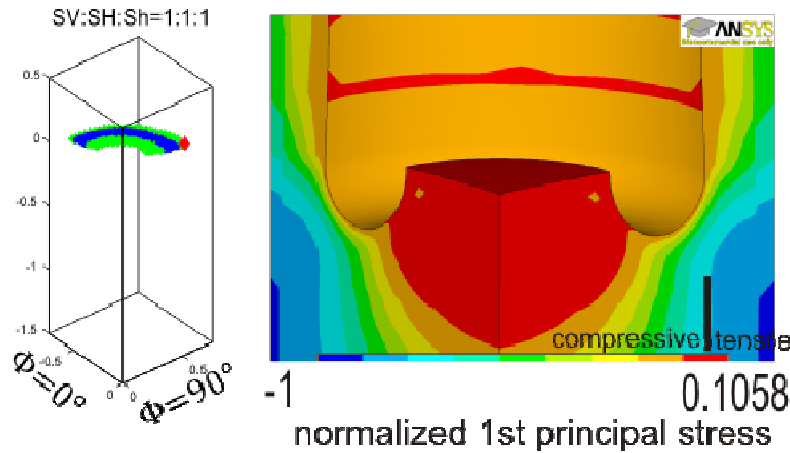
Figure 4.2: Plot of the fracture surface (left) and normalized stress (right) for the case SV=SH=Sh.

11% of SV; i.e, it is much smaller than in situ stress in magnitude. This suggests that a more fully isotropic state of stress will retard the formation of a fracture as the body is essentially in compression.

Tensile stress concentrations are also observed on the core top and borehole wall, so additional fractures may occur here.

4.2.1.3 SH = Sh > SV

Figure 4.3 (a-d) illustrates the case when overburden stress is smaller than the isotropic horizontal stresses, placing this into the thrust faulting regime. These figures have symmetry properties as expected, and the fracture shape is a flat disc for all values of overburden stress. The depth of the fracture initiation point does

deepen with decreasing SV. However, the fact that there is little difference between the fracture shapes could suggest that obtaining quantitative information about the stress state for this type of fracture will be difficult.

An important point is that the fracture initiation point is always located on the symmetry axis. The global maximum tensile stress at this point increases when the overburden stress decreases, for example, in figure 4.3(a), it is ~10% of SH with SV = 0.8, but in Figure 4.3(d), it is ~23% of SH with SV = 0.1. As such, the facts that the fracture begins in the centre of the core and that there is compression near its outside edges suggest that the fracture may never make it to the outside surface. This implies that one could have a highly damaged core but there may not be any indication of this by surface examination. One might need x-ray tomography to know in advance if the core had been damaged or not (see *Maury et al,* [1988] for an interesting example of an X-ray image of a core with a fracture only at its center).

The borehole walls also appear to be under a tensile stress, and thus may undergo fractures, although the tensile stress values are fairly low here.
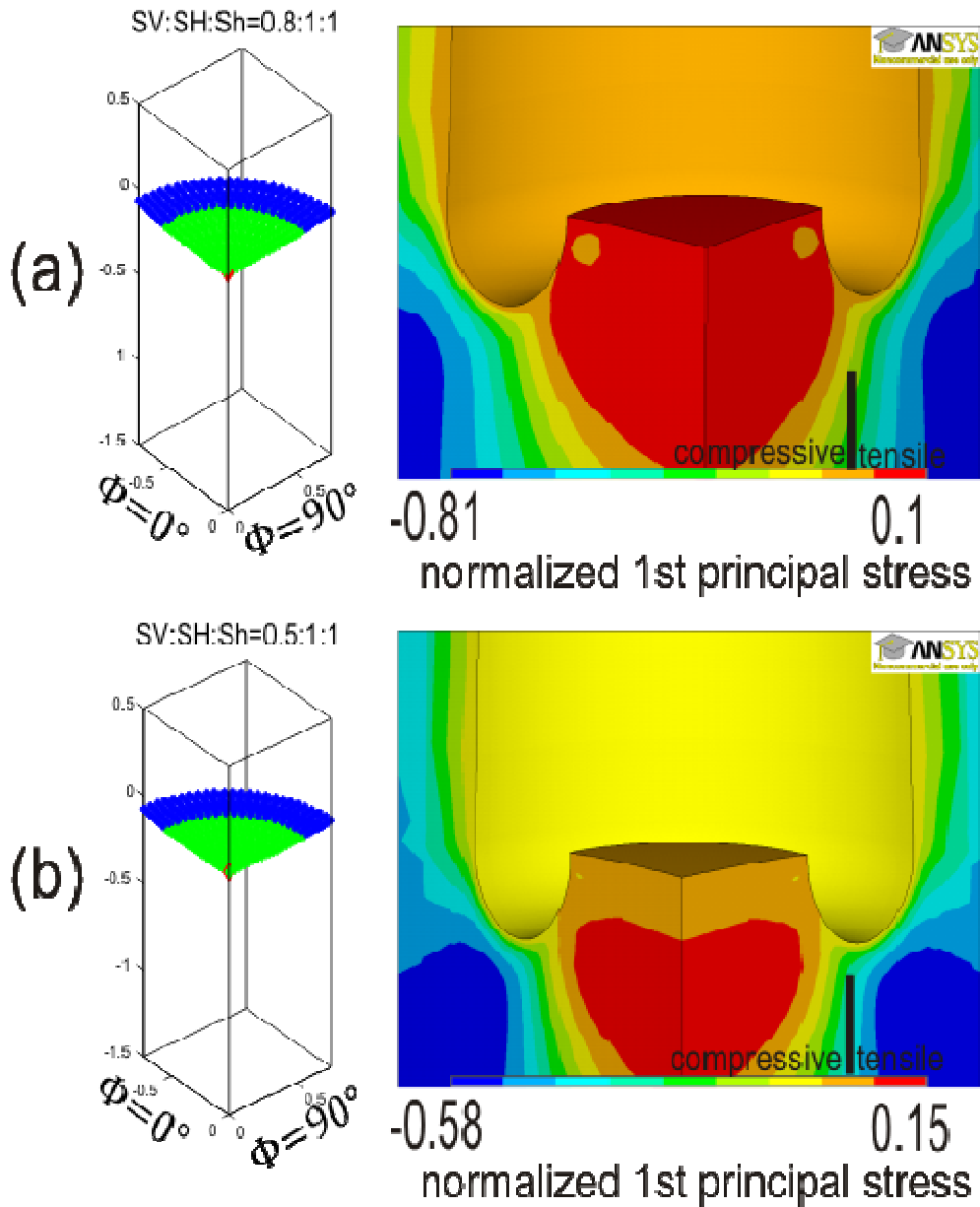
Figure 4.3: Plots of fracture surface (left) and normalized stress (right) for variations in in-situ stress when SV<SH and SV<Sh (a) SV:SH:Sh=0.8:1:1. (b) SV:SH:Sh=0.5:1:1.

Figure 4.3 continued: (c) SV:SH:Sh=0.3:1:1. (d) SV:SH:Sh=0.1:1:1.
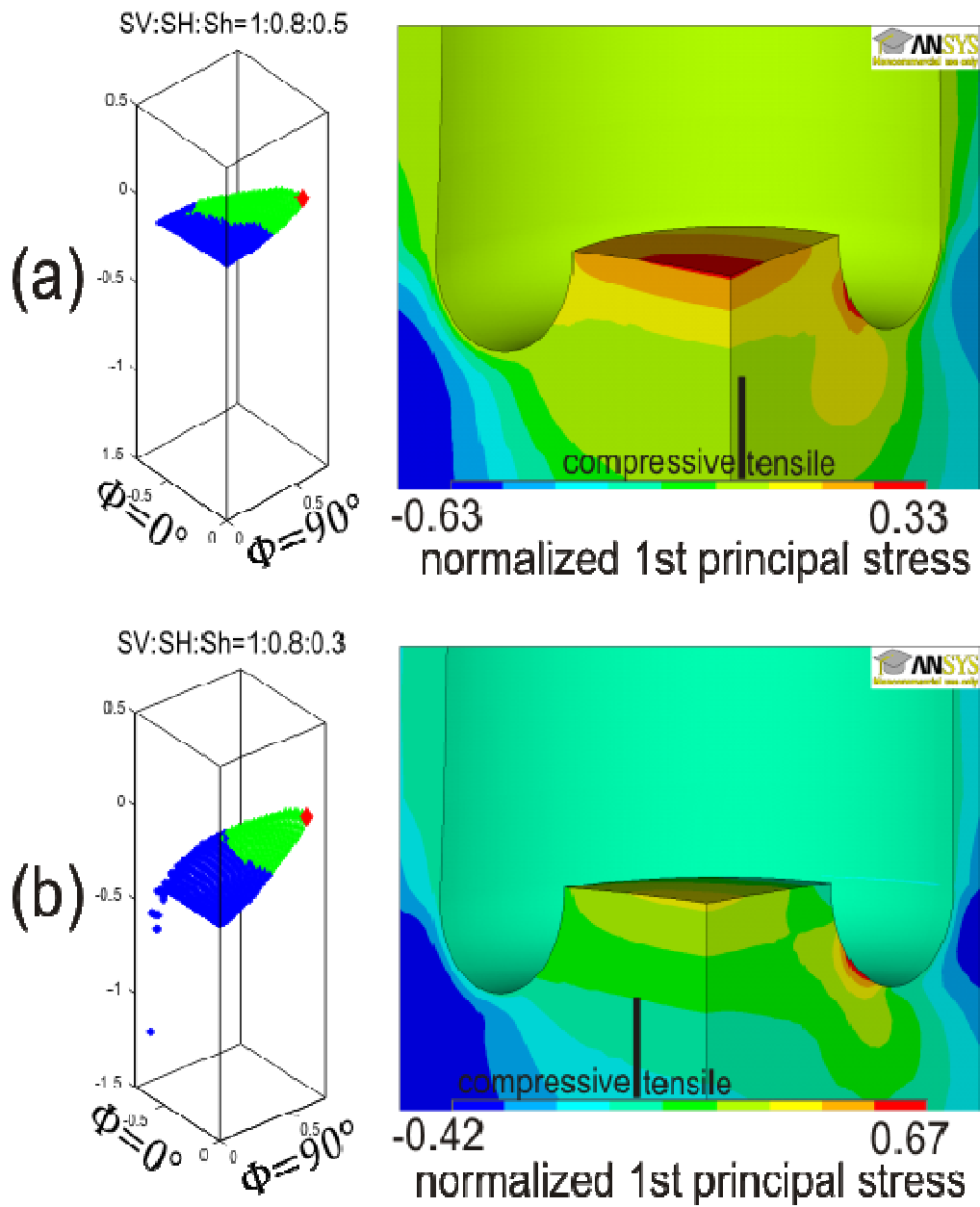
Figure 4.4: Plots of the fracture surface (left) and normalized stress (right) for variations in in-situ stress when SV>SH>Sh. (a) SV:SH:Sh=1:0.8:0.5. (b) SV:SH:Sh=1:0.8:0.3.
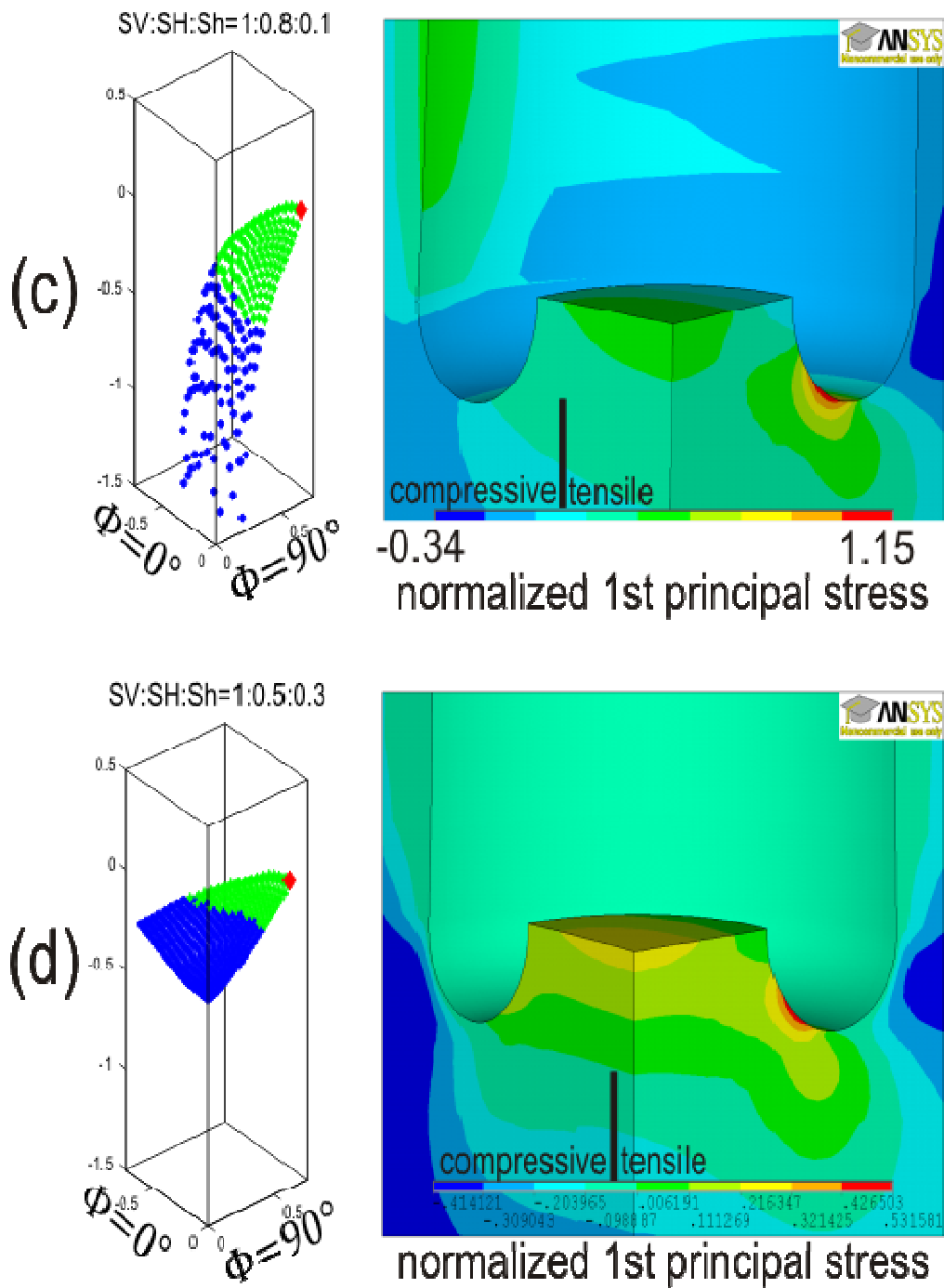
Figure 4.4 continued: (c) SV:SH:Sh=1:0.8:0.1. (d) SV:SH:Sh=1:0.5:0.3.
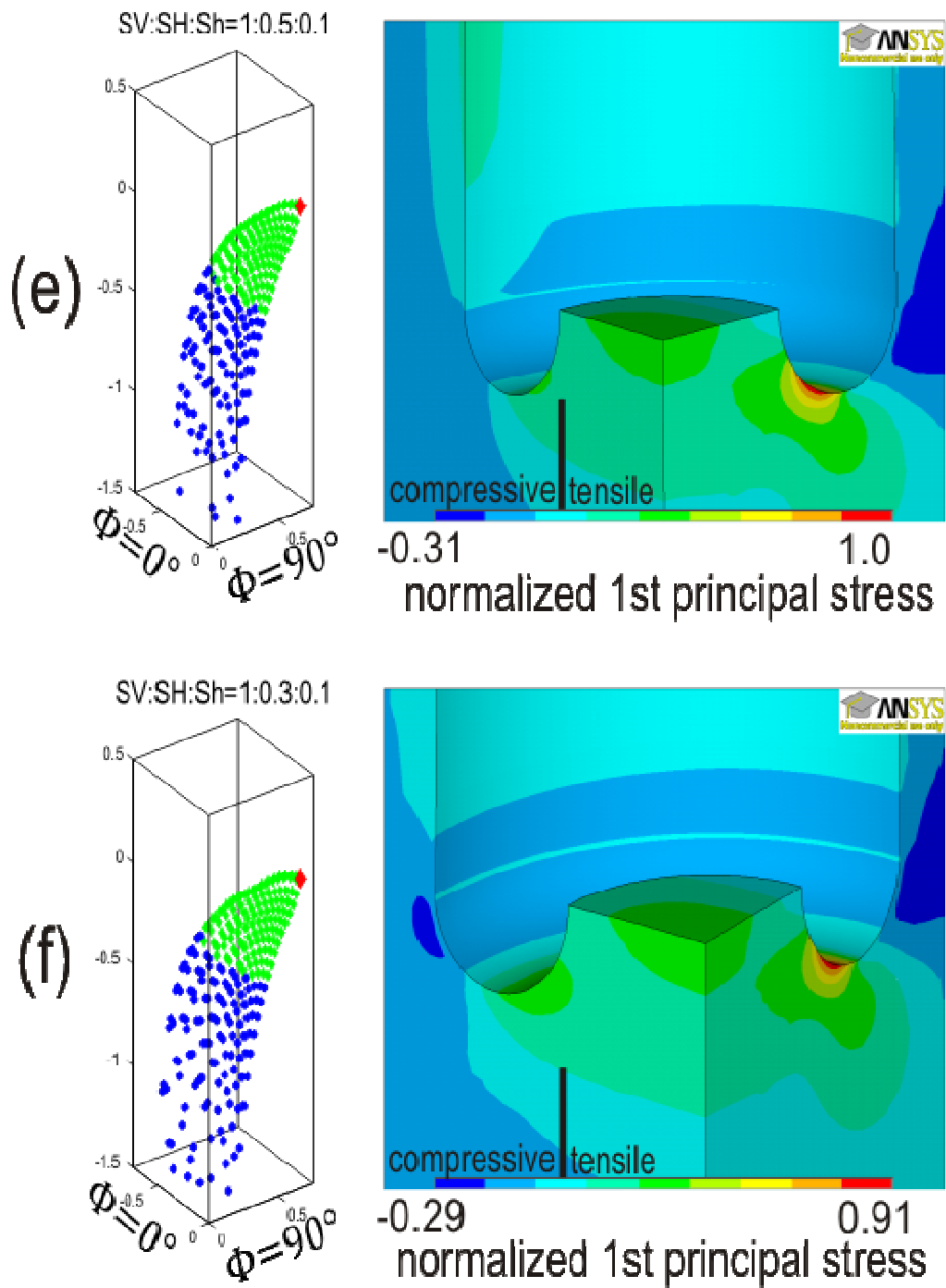
Figure 4.4 continued: (e) SV:SH:Sh=1:0.5:0.1. (f) SV:SH:Sh=1:0.3:0.1.

128
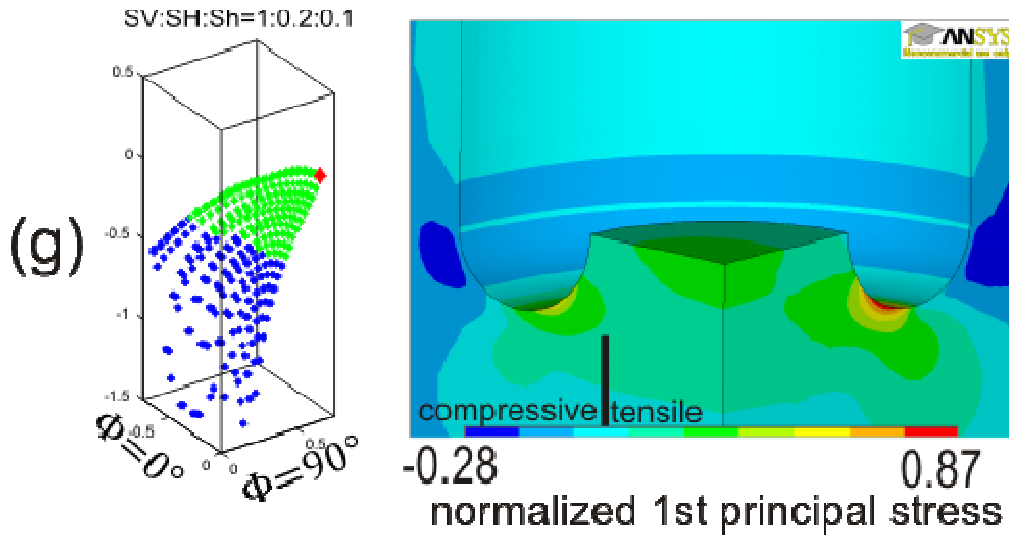
Figure 4.4 continued: (g) SV:SH:Sh=1:0.2:0.1.

4.2.2 Normal fault stress regime (SV > SH > Sh)

This set of models focuses on cases of anisotropic horizontal stress conditions in which the overburden stress is larger than both horizontal stresses. Consistent with the above section, the rock material in these models has a Poisson's ratio of 0.25 and the core stub length is 0.25d (where d is the diameter of the core).

Figure 4.4 (a-g) illustrates combinations for in situ stresses SV, SH, and Sh which are constrained in the condition SV > SH > Sh. In all models, the initial fracture point is located in the inner kerf at the $\Phi = 90°$ plane (i.e., pointing in the direction of the least horizontal compression Sh). For a given SV to SH ratio, the global maximum tensile stress increases as the minimum horizontal stress decreases. For example, in Figure 4.4(a), it is ~33% of SV with Sh = 0.5, but in

129

Figure 4.4(c), it is 115% of SV with Sh = 0.1. The global tensile stress also depends on the value of SH; as this becomes smaller and the horizontal stresses become less anisotropic, the tensile stress decreases. For example, in Figure 4.4(c) with SH: Sh = 0.8 : 0.1, the global maximum is 115%, whereas in Figure 4.4g when SH : Sh = 0.2 : 0.1, it is 87%. The global maximum tensile stress is important to understand the possibility of fracture opening. From above we can see that this value is influenced by not only the ratio of SV to SH, but also the ratio of SH to Sh, thus we predict that how possible the fracture will happen by some given in situ stress.

This in situ stress regime exhibits three fracture shapes. When the three stresses are comparable, a saddle is observed (Figure 4.4a, b, d) in which the middle is lower than the surrounding area. In this case, the fracture propagates through the core along an initially downward trajectory before flattening in the centre of the core. As the horizontal stresses become more anisotropic, petal shapes (Figures 4.4c, g) and petal-centreline shapes (Figures 4.4 e, f) occur. In both cases, the fracture follows a downward trajectory into the core, but are distinguished by the fracture trajectory and the distance between the fracture and $\Phi = 0^\circ$ symmetry plane. If the fracture is tangential to the $\Phi = 0^\circ$ plane and is close this axis, it is defined as petal-centreline fracture. Otherwise, it is defined as a petal fracture.

In the case of SV:SH:Sh = 1.0 : 0.8 : 0.5, a second maximum tensile region is observed in the centre of the core top (Figure 4.4a), so this may give rise to secondary fractures. In other cases, tensile stresses are also observed in the core top, but the magnitude is less than the tensile stress at the inner kerf.

4.2.3 Strike-slip fault stress regime (SH > SV > Sh)

This set of models focuses on the strike-slip fault stress regime in which the overburden stress is larger than the minimum horizontal in-situ stress but smaller than the maximum horizontal stress. Again, the rock material has a Poisson's ratio of 0.25 and the core stub length is 0.25d.

As shown in Figure 4.5, two types of fractures are observed for this stress regime. When the overburden stress is comparable with the minimum horizontal stress, as in Figure 4.5(a, b, d, f, g), a saddle shape is observed in which the middle is higher than surrounding. When the minimum horizontal stress is much smaller than the overburden stress, a petal-centreline shape occurs, as in Figure 4.5(c, e). However, unlike the case for the normal faulting regime, the strike of these fractures is not as well defined.

As with the normal faulting regime, the fracture initiation point in the strike-slip regime is always located on the inner kerf at $\Phi = 90°$ plane. The global maximum tensile stress increases as the minimum horizontal stress decreases for a given SH to SV ratio. For example, in Figure 4.5(a), it is ~28% of SH with Sh = 0.5, but in Figure 4.5(c), it is 104% of SH with Sh = 0.1. This means that fractures are more likely to be initiated for relative low values of Sh. In addition, the magnitude of global tensile stress decreases as the overburden stress decreases. For example, in Figure 4.5(g), it is 72% with SV = 0.2, but in Figure 4.5(c), it is 104% with SV = 0.8.
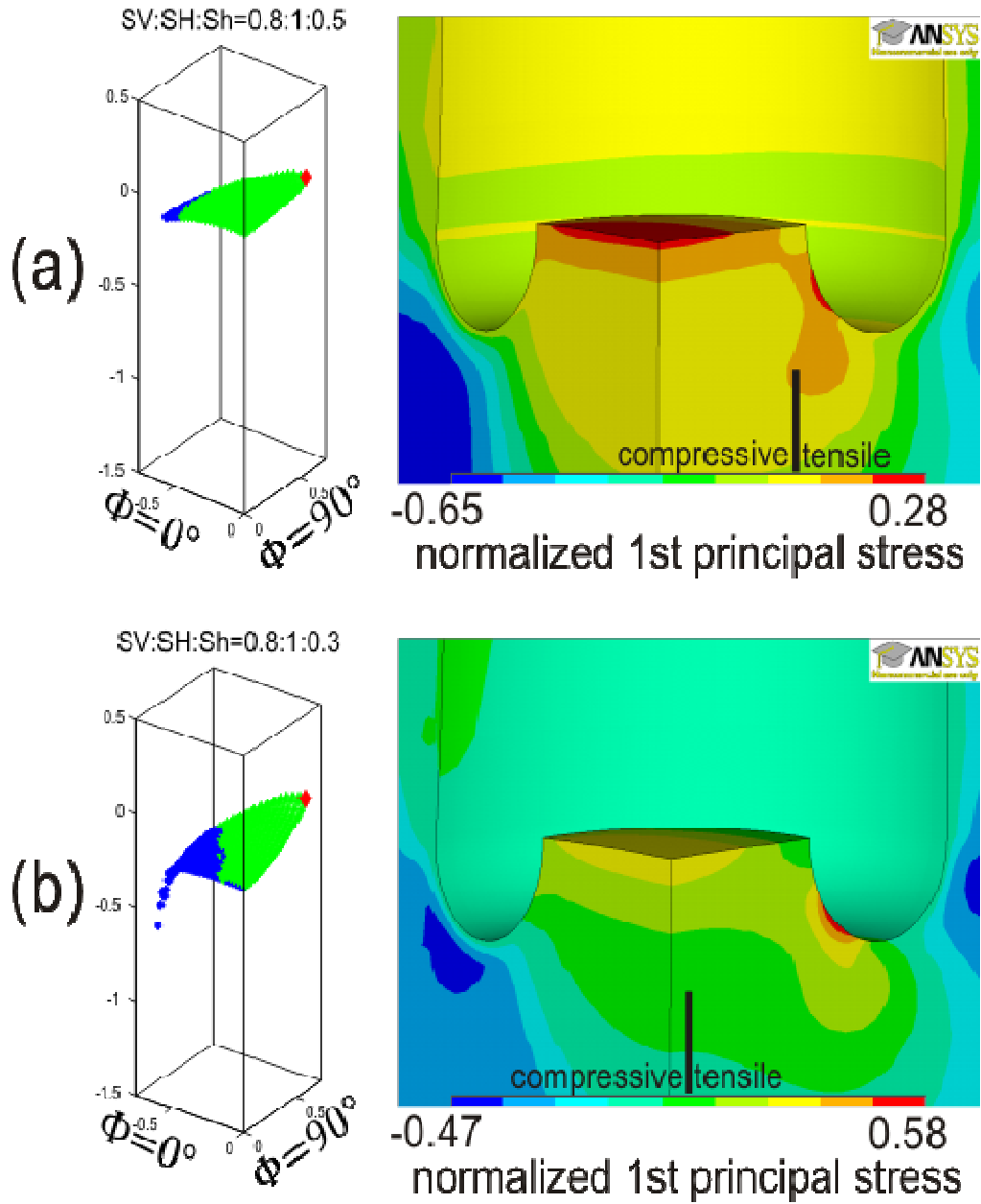
Figure 4.5: Plots of the fracture surface (left) and normalized stress (right) for variations in in-situ stress when SV<SH and SV>Sh (a) SV:SH:Sh=0.8:1:0.5 (b) SV:SH:Sh=0.8:1:0.3

**Figure 4.5 continued:** (c) SV:SH:Sh=0.8:1:0.1. (d) SV:SH:Sh=0.5:1:0.3.

133
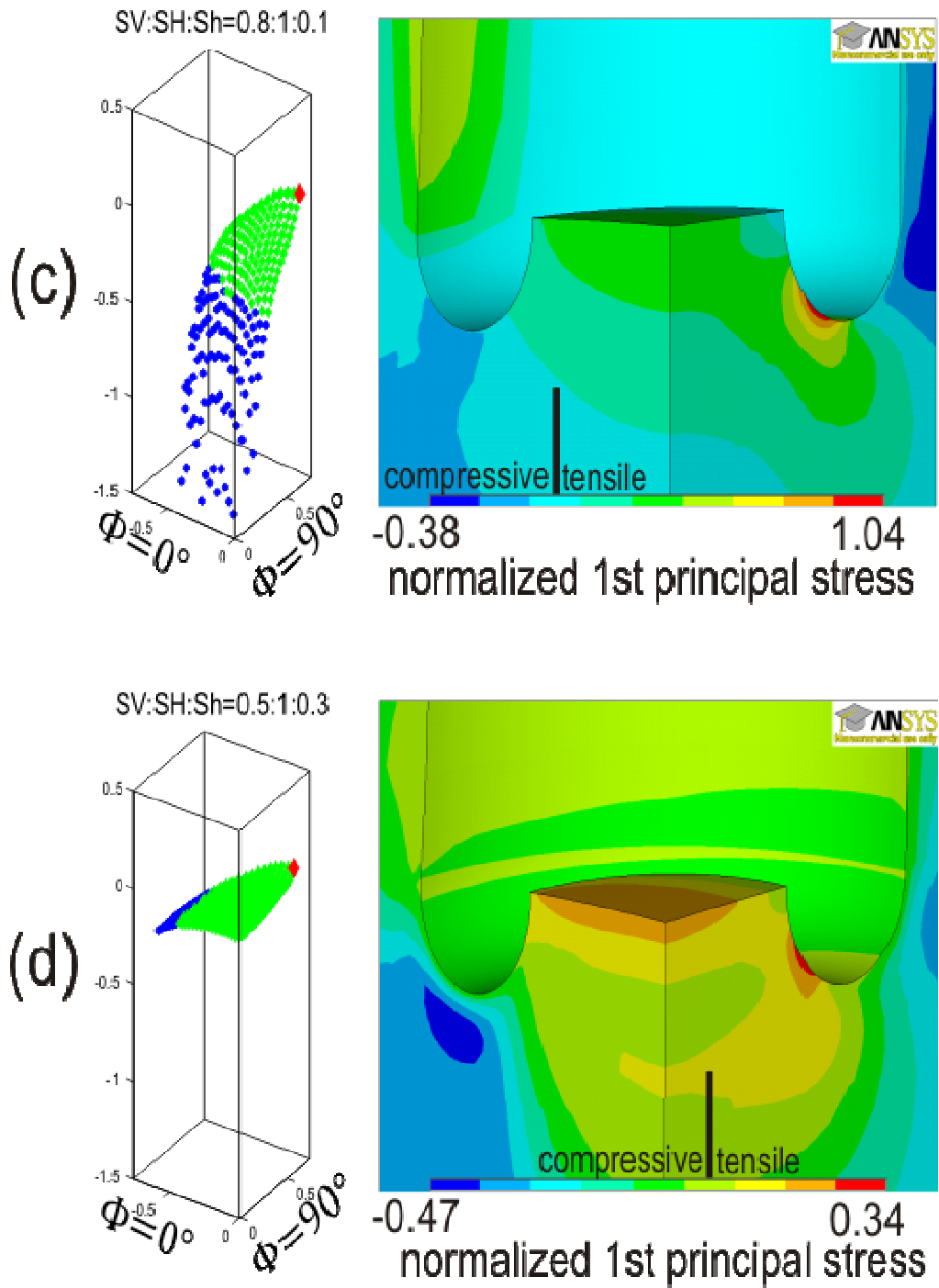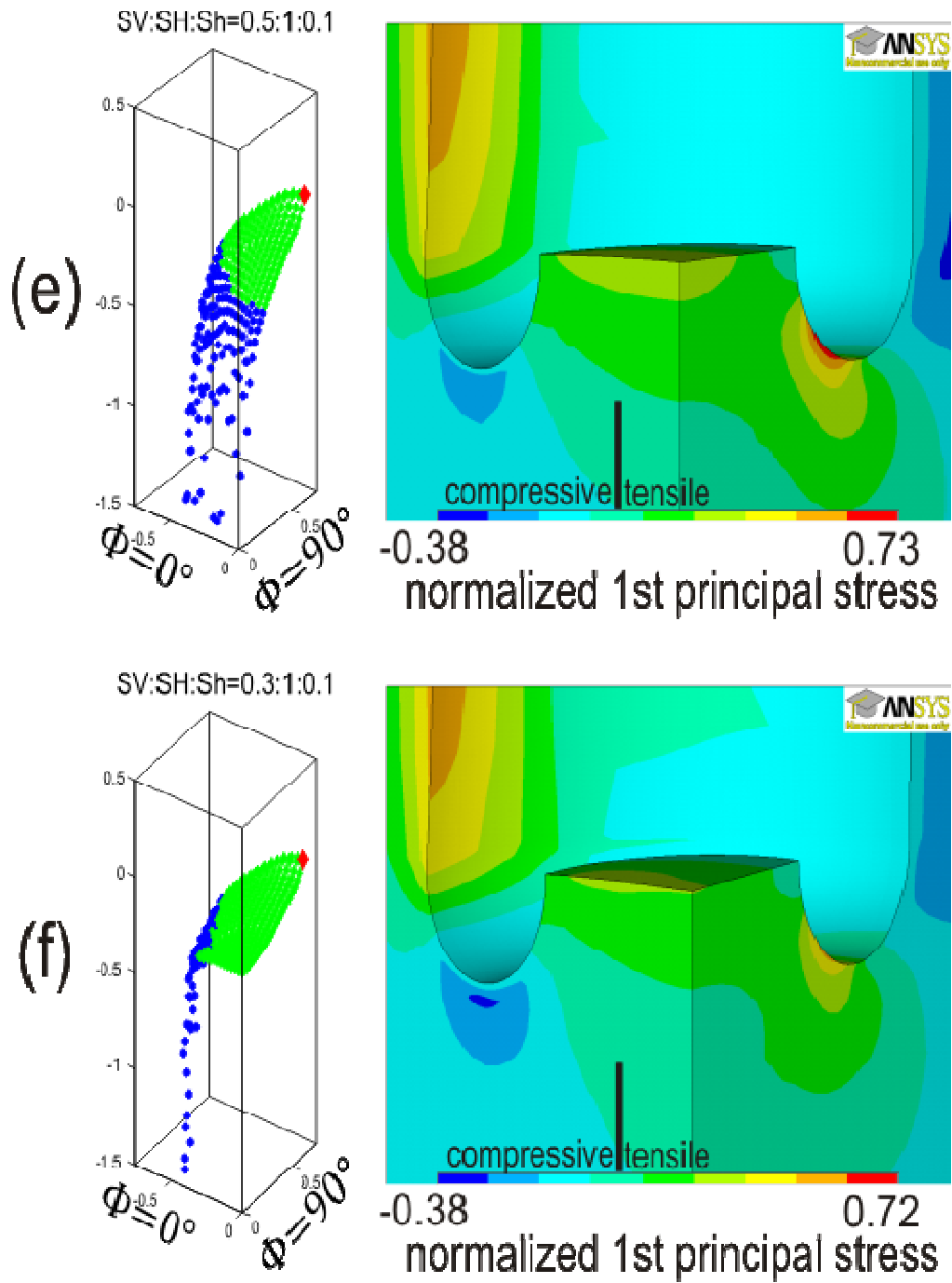
Figure 4.5 continued: (e) SV:SH:Sh=0.5:1:0.1. (f) SV:SH:Sh=0.3:1:0.1.
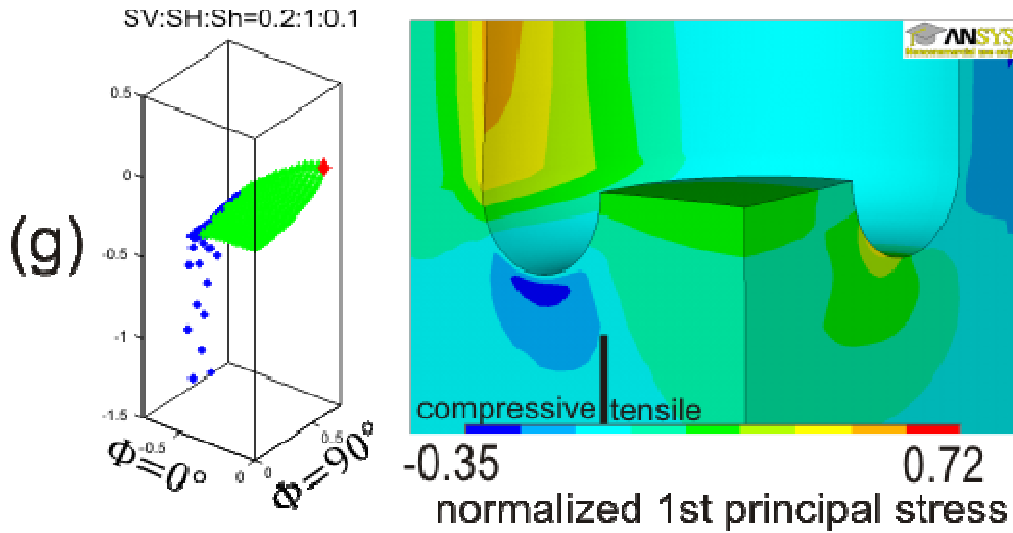
Figure 4.5 continued: (g) SV:SH:Sh=0.2:1:0.1.

In these models, other zones of tensile stress are observed at the top of the core (e.g., Figure 4.5 a,b,d) and in the wall of the borehole (e.g., Figure 4.5 c,e,f,g), which could lead to secondary fractures in these locations. In particular, significant tensile stress in the borehole wall is observed for the cases with Sh = 0.1, which suggests that significant fractures in the borehole wall may only be observed in rock with a low horizontal stress in one direction.

4.2.4 Thrust fault stress regime (SH > Sh > SV)

The final set of models investigates the thrust fault stress regime in which the overburden stress is smaller than both horizontal stresses. As in previous sections, the rock material has a Poisson's ratio of 0.25 and a core stub length of 0.25d.

As shown in Figure 4.6 (a-c), when both horizontal stresses are large (in this case SH : Sh = 1 : 0.8), a flat disc-shaped fracture occurs. This morphology is consistent with the nearly isotropic state of horizontal stress. As Sh decreases to 0.5 (Figure 4.6 d, e), the disc becomes curved near the edge of the core, producing a slight convex shape. Note that the curvature appears to be mostly confined to the regions where compressive stress occur, so it is unclear if these fractures would develop in real rocks. In all of these cases, the fracture initiation point occurs along the symmetry axis in the centre of the core.

For low values of both SV and Sh (Figure 4.6 f, g), the fracture initiation point shifts to the inner kerf on $\Phi = 90°$ plane. The fracture is curved and forms a saddle shape, which means we can expect the transform from disk to saddle if both horizontal stresses reach a very small value. The magnitude of tensile stress at the fracture initiation point is between 13% and 42% of SH. The magnitude of tensile stress increases for decreasing values of SV (e.g., SV=0.1, Figure 4.6 c, e, f, g) and low values of Sh (e.g., Sh = 0.2 in figure 4.6g).

Significant tensile stress is observed in the wall of the borehole when the overburden stress is very small, as in Figure 4.6(c, e, f, g) with SV = 0.1. Tensile stresses are also produced on the core top in Figure 4.6 a, b, d. Thus, secondary fractures may develop in these locations.
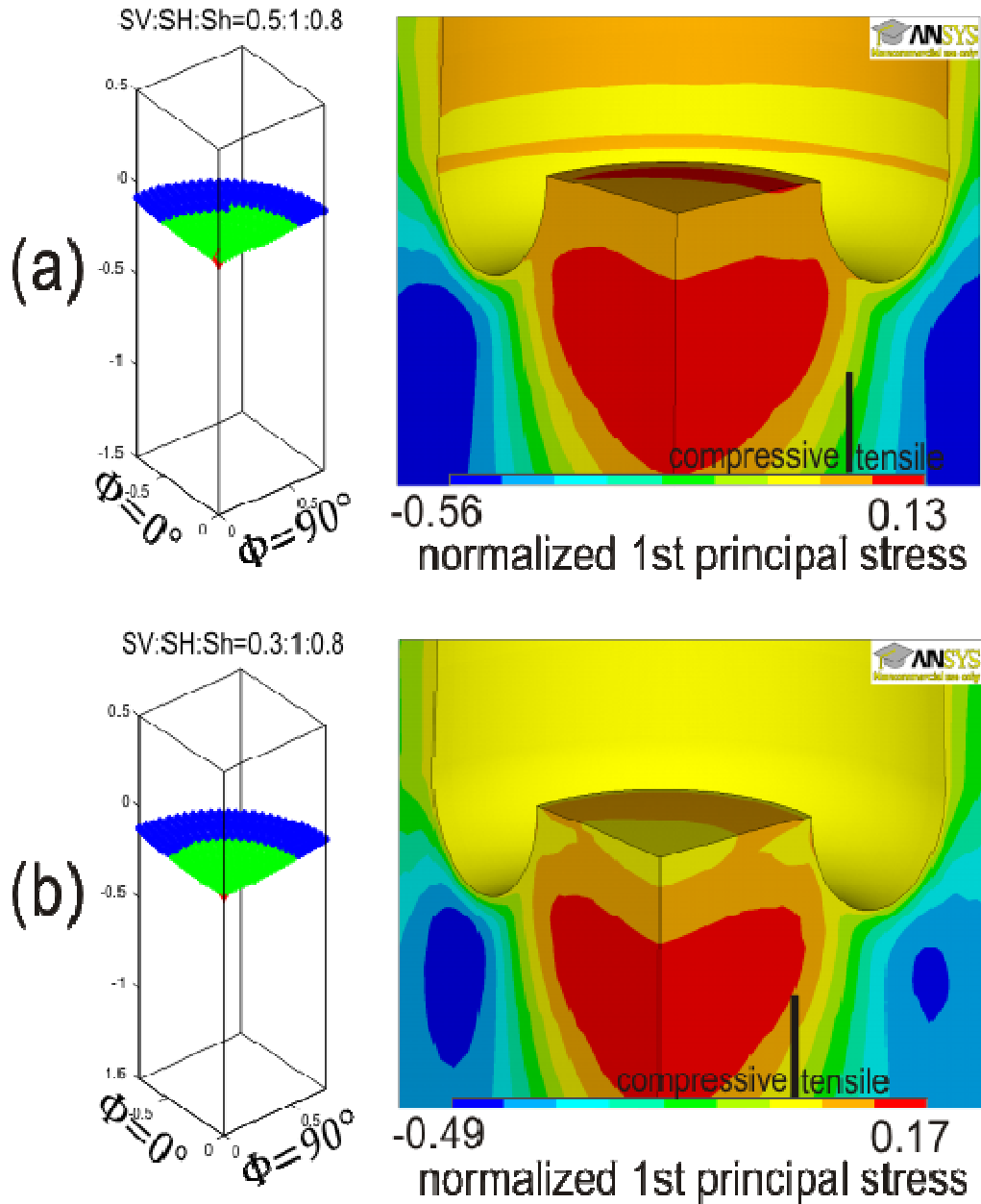
Figure 4.6: Plots of the fracture surface (left) and normalized stress (right) for variations in in-situ stress when SV<SH and SV<Sh. (a) SV:SH:Sh=0.5:1:0.8. (b) SV:SH:Sh=0.3:1:0.8.
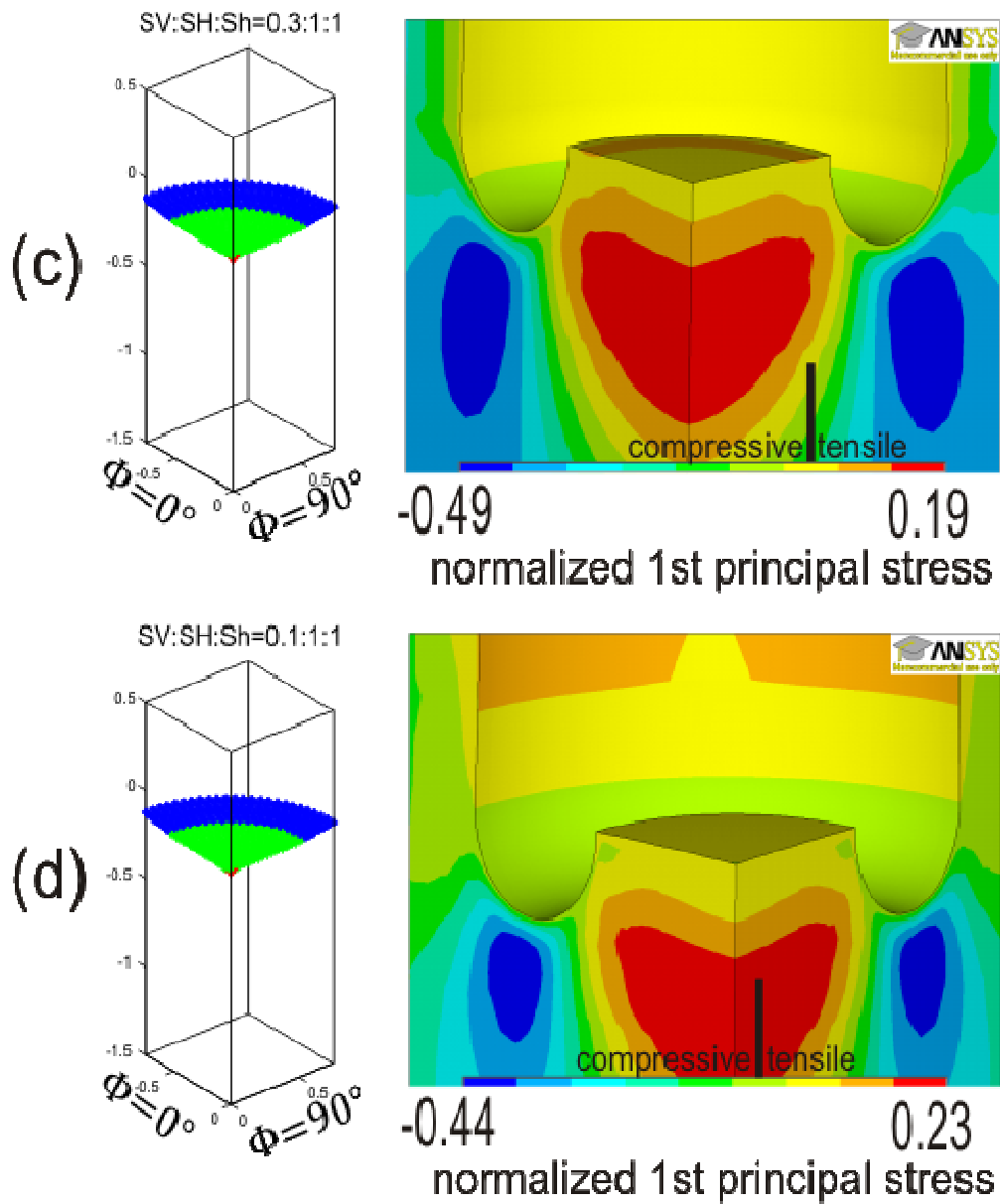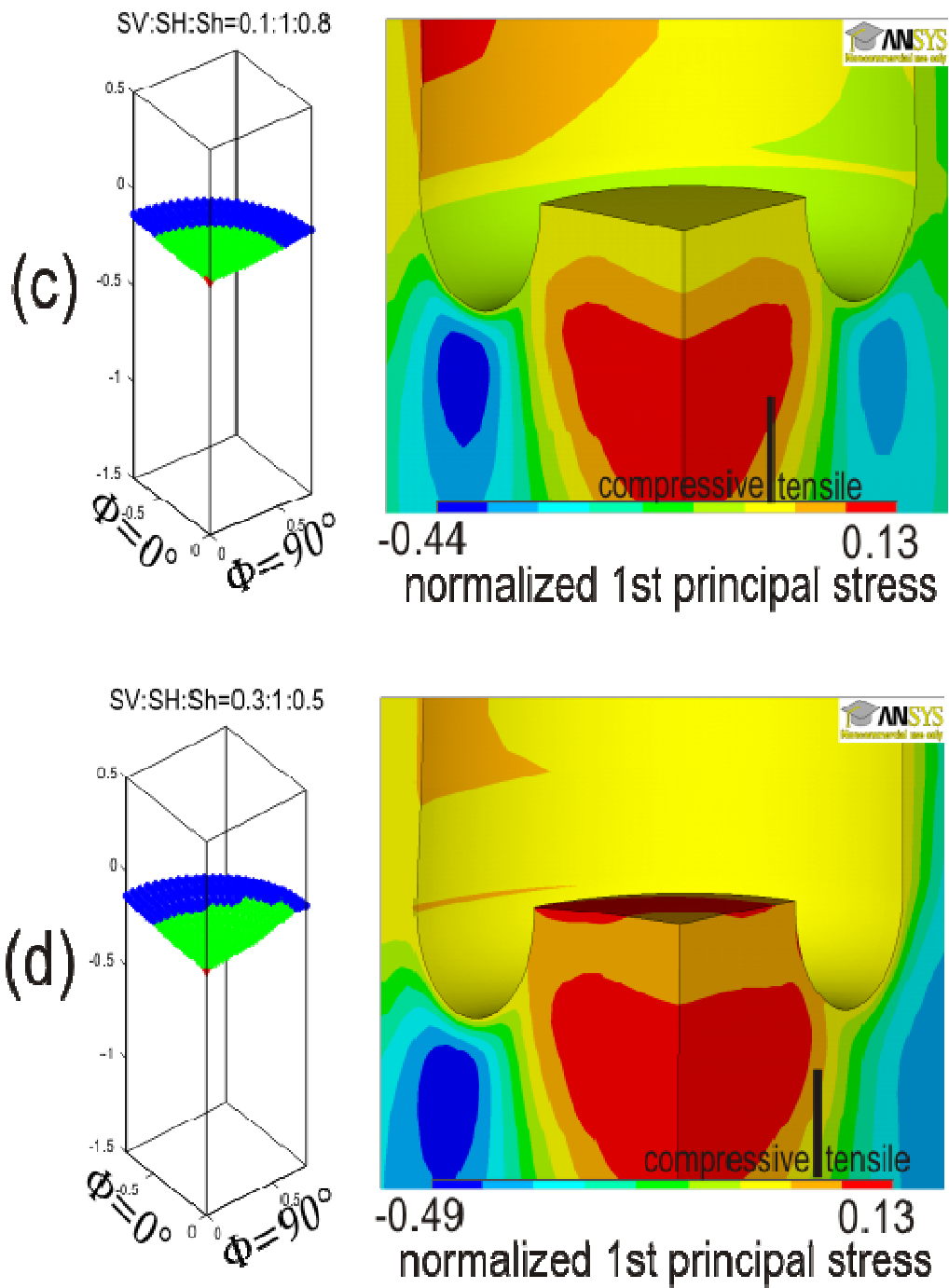
Figure 4.6 continued: (c) SV:SH:Sh=0.1:1:0.8. (d) SV:SH:Sh=0.3:1:0.5.
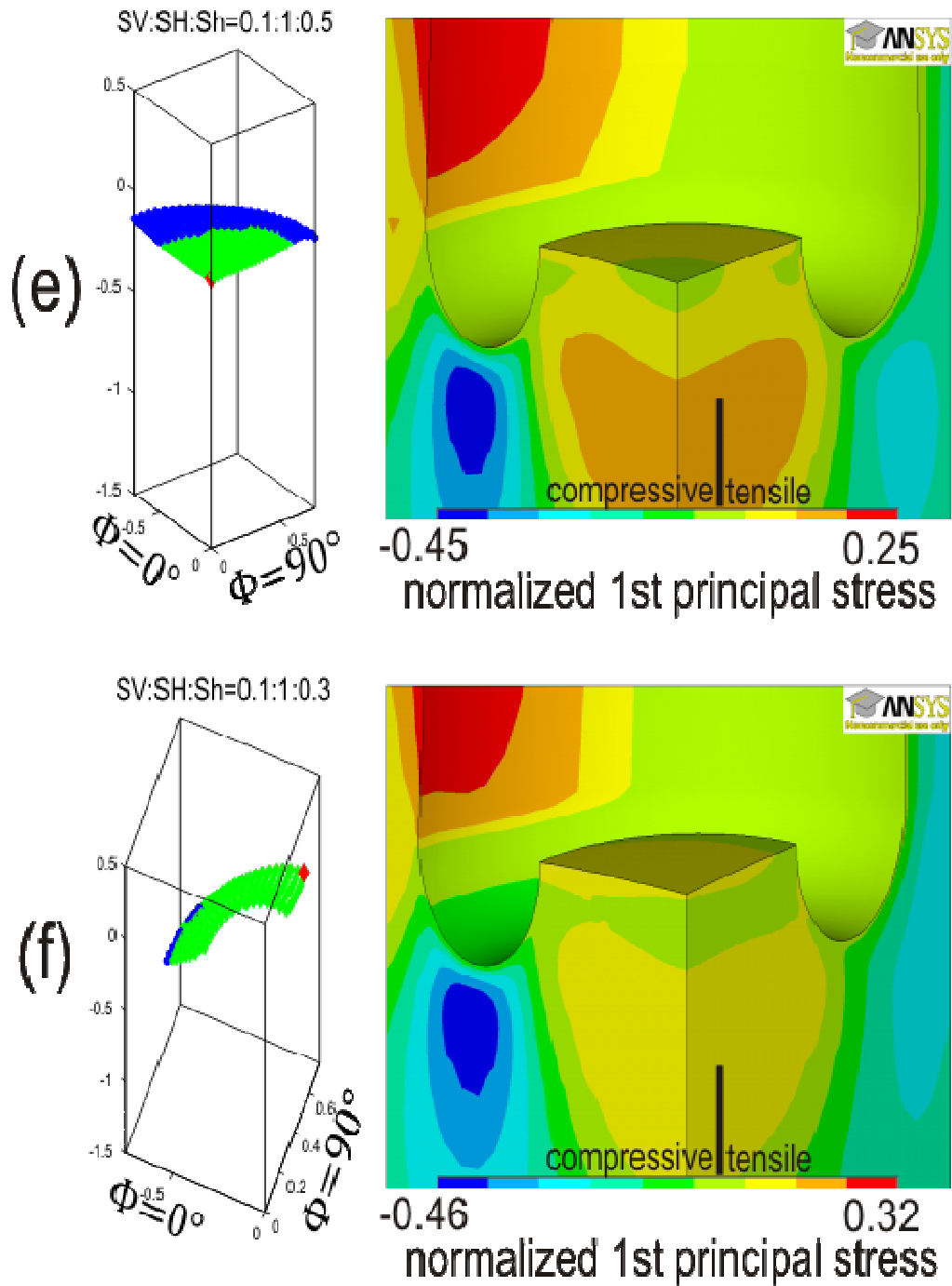
Figure 4.6 continued: (e) SV:SH:Sh=0.1:1:0.5. (f) SV:SH:Sh=0.1:1:0.3.
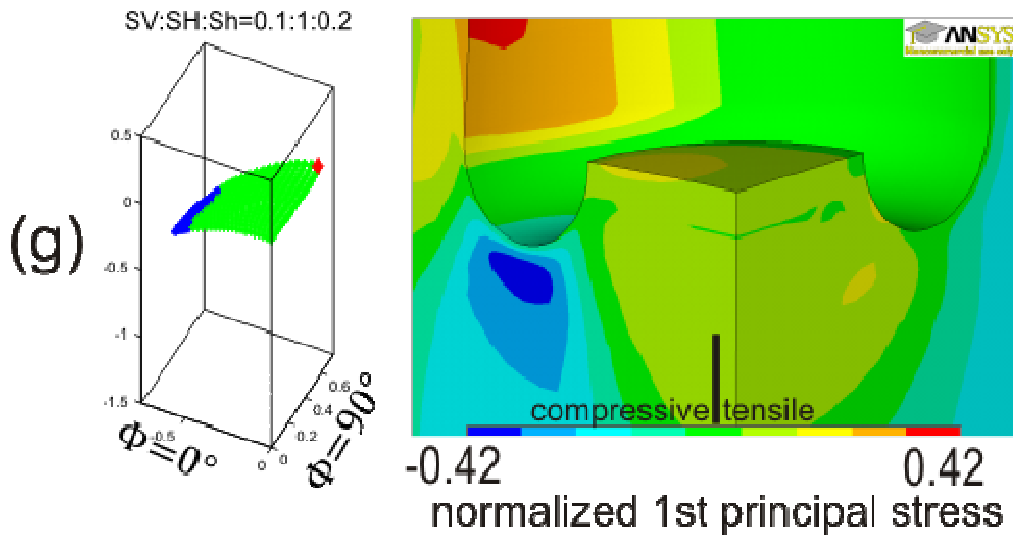
Figure 4.6 continued: (g) SV:SH:Sh=0.1:1:0.2.

4.2.5 Summary of the effect of in-situ stress

As shown above, a range of fracture morphologies was produced in the numerical models under various states of in-situ stress. The main types of fractures in the models are: disc, saddle, petal and petal-centreline. In some cases, the disc is not perfectly flat, but instead has edges that bend upward. Such symmetric concave disc fractures are often called cups. Overall, the modeled fractures appear to be consistent with fracture geometries observed in real cores. The only type of fracture not produced here are the core-edge fractures (see Figure 1.2), which may be due to a limitation of the numerical modeling method. This is discussed further in Chapter 5.

In the models, fractures develop through tensile failure within zones of stress concentration produced at the bottom of the borehole. The fracture trajectory

140

reflects the spatial variations in stress within the model core. Figure 4.7 summarizes the observed fracture morphology for the different states of in-situ stress examined above. This figure clearly shows that each fracture morphology tends to be observed under restricted in-situ stress conditions. The following general observations can be made:

(1) Disc shape (flat or cup) fractures usually are generated under:

- Isotropic horizontal stress;

- A thrust fault stress regime with relatively large minimum horizontal stress.

(2) Petal shape fractures are generated under a normal fault stress regime with extremely small minimum horizontal stress.

(3) Petal-centreline shape fractures occur in two cases:

- Normal fault stress regime with relatively small minimum horizontal stress, or when both horizontal stress are relative small;

- Strike-slip fault stress regime with relatively small minimum horizontal stress.

(4) Saddle fractures are usually generated in the following two cases:

- Normal fault stress regime where both horizontal stresses are not very small compared to the overburden stress

- Strike-slip fault stress regime where the minimum horizontal stress is only slightly smaller than the overburden stress.

- Thrust fault regime with small minimum horizontal stress.

It appears that the minimum horizontal stress has direct influence on fracture morphology. For a given ratio of SV/SH stress, the fracture shape evolves from petal to petal-centreline to saddle and then to disc with increasing minimum horizontal stress. Figure 4.7 shows that there is a strong relationship between fracture morphology and in-situ crustal stress and therefore observations of fracture shapes in borehole cores may be used to constrain the regional crustal stress field at the borehole site.

In addition to the fracture morphology, it is important to consider whether the stress concentrations are sufficient to generate tensile fractures and where such fractures will initiate. Figure 4.8 shows the normalized maximum tensile stress for different in situ stress conditions, using a stub length of 0.25d and Poisson's ratio of 0.25. Plots have been generated for the three different stress regimes. For the normal fault regime (Figure 4.8a), it is found that when Sh is relatively small, the global maximum tensile stress is located at the kerf and has a fairly large value. As Sh increases, the magnitude of tensile stress decreases, and the point of fracture initiation may shift to the core top, except in cases where SH is much smaller than SV.

For the strike slip fault regime (Figure 4.8b), the maximum tensile stress is located at the kerf when the horizontal stresses are anisotropic (SH is much larger than Sh), and the magnitude is fairly large and thus fractures may be expected to occur. As Sh increases, the maximum tensile stress at the kerf decreases and becomes comparable to the tensile stress at the core top. The magnitude of the stress is quite low, so it is unclear if a fracture would develop.
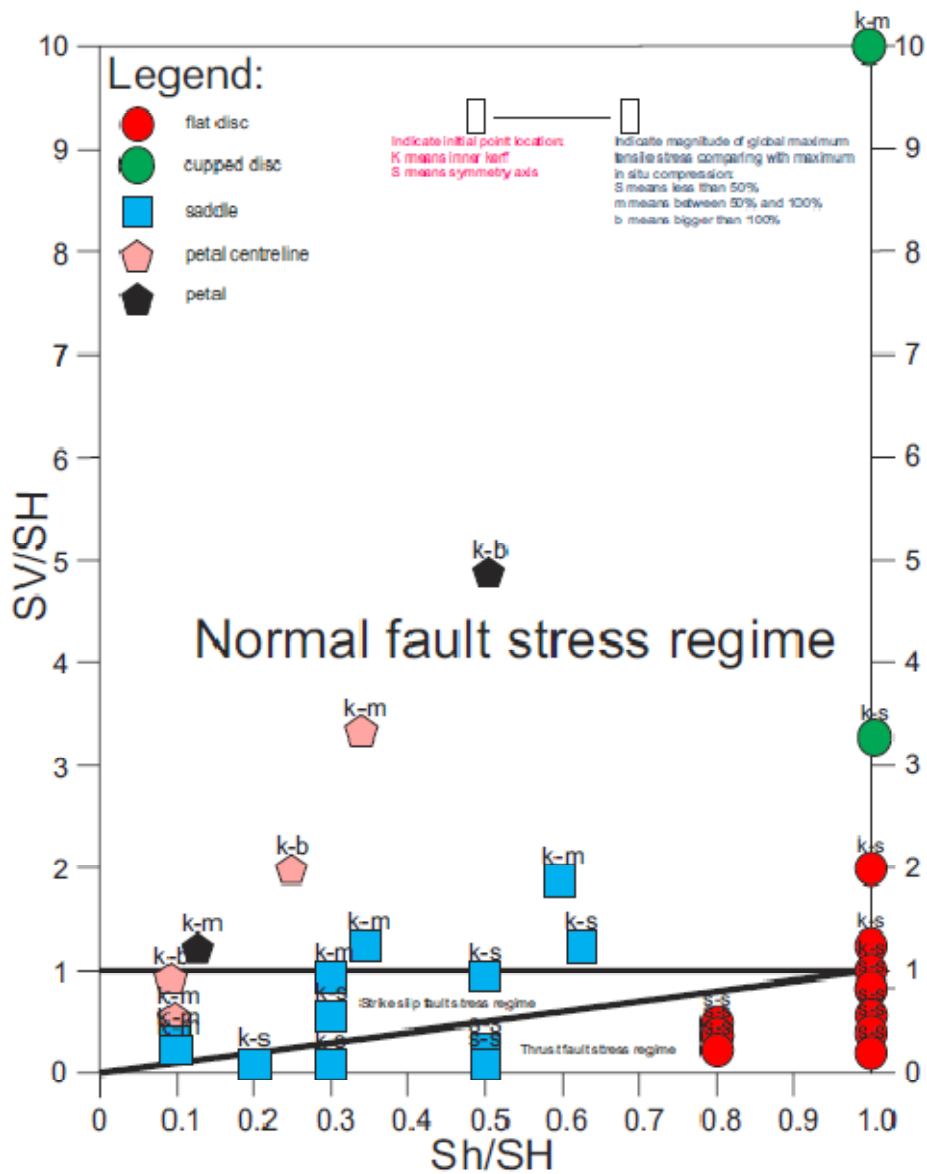
Figure 4.7: Summary plot showing fracture morphology, initiation point and magnitude of global maximum tensile stress. Note that solid black lines are used to separate the different stress regimes.
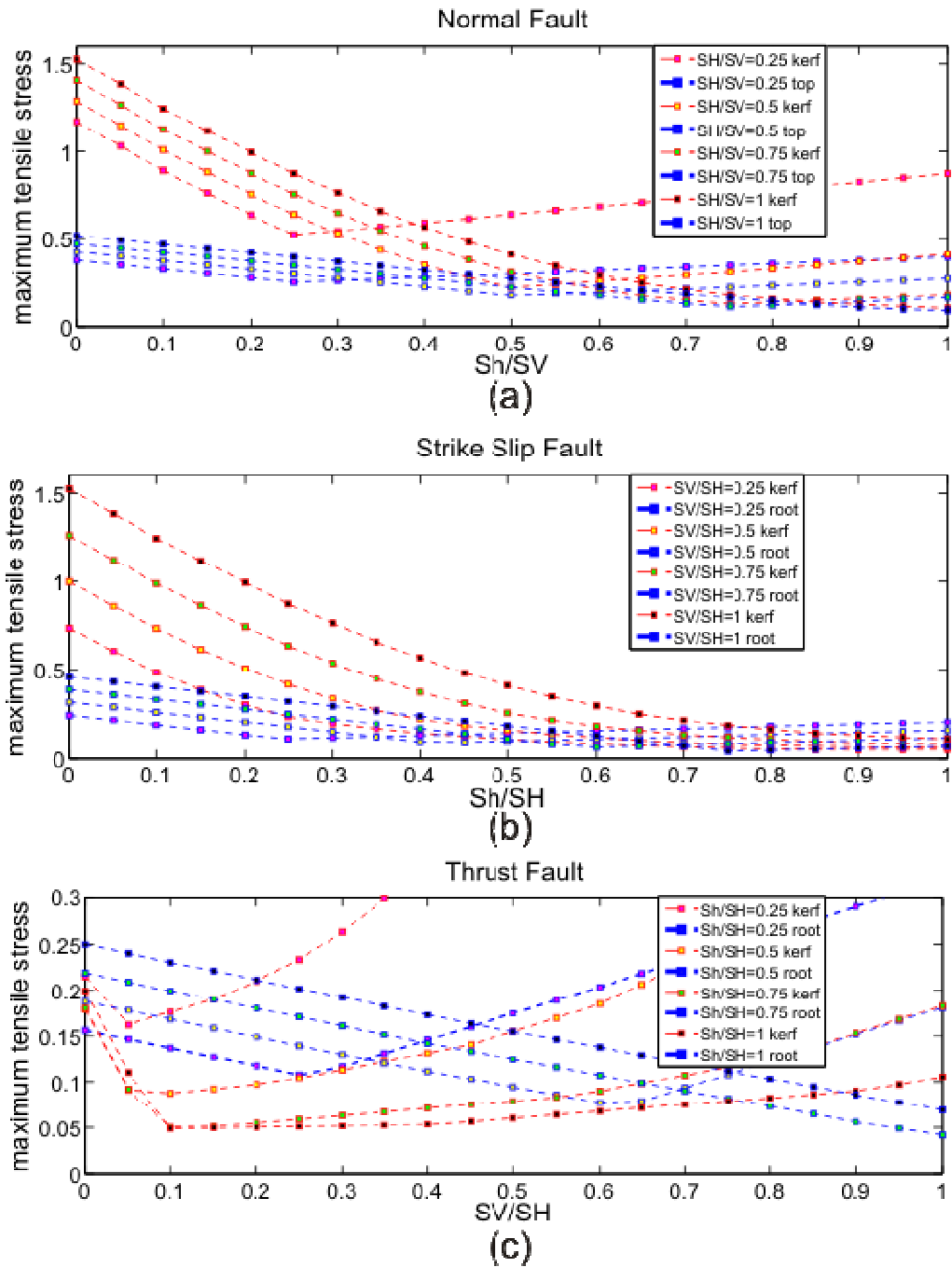
Figure 4.8: Variations in the magnitude of global maximum tensile stress in different stress regimes with a Poisson's ratio of 0.25 and a stub length of 0.25d. (a) Normal fault regime. (b) Strike slip fault regime. (c) Thrust fault regime.

For the thrust fault regime (Figure 4.8c), the maximum tensile stresses are relatively small for most models and therefore, it may be difficult to produce a fracture in this regime. The largest magnitudes of tensile stress are found for models with low Sh/SH and high SV/SH; in these cases fractures may initiate at the kerf. For other models, the plot shows that the maximum tensile stresses are either located at the kerf or at the root (i.e., in the centre of the core stub). If a fracture were to develop in the root, the fracture may not propagate through the whole core body and therefore may not be observable on the outer boundary surface of the core.

Overall, the models demonstrate that, for a range of crustal stress conditions, significant tensile stresses can be generated at the bottom of a borehole. Such stresses can produce tensile fractures. It appears that the fracture morphology is related to the in situ crustal stresses, and thus observations of core fracture may provide a way to constrain crustal stresses. However, it is also necessary to consider whether other parameters may also affect the fracturing process. In the following sections, variations in the elastic properties of the rock and changes in the Poisson's ratio and the core stub length are investigated.

4.3 Effect of Poisson's ratio on fracture morphology

This topic was first addressed by [*Li and Schmitt*, 1997]. Poisson's ratio is expected to have an influence on fracture morphology since the stress distribution can be changed by variations in Poisson's ratio. Table 3.2 shows that Poisson's ratio varies, depending on rock type; most rocks have a Poisson's ratio between 0.1 and 0.4.

Poisson's ratio is defined as the negative of the ratio of the transverse strain to the longitudinal strain, under the condition of uni-axial stress, that is, $v \equiv -\varepsilon 2/\varepsilon 1 = -\varepsilon 3/\varepsilon 1 = \lambda/2(\lambda + G)$, where λ and G are Lame's parameters. Poisson's ratio is typically a positive number (negative Poisson's ratios are not forbidden and indeed exist in many specially engineered materials), in which case a longitudinal compression would be accompanied by transverse expansion and vice versa.

Hooke's law can be used to simply illustrate the influence on stress by Poisson's ratio as follows:

$$\tau_{xx} = (\lambda + 2G)\varepsilon_{xx} + \lambda\varepsilon_{yy} + \lambda\varepsilon_{zz}, \tag{4.1}$$

$$\tau_{yy} = \lambda\varepsilon_{xx} + (\lambda + 2G)\lambda\varepsilon_{yy} + \lambda\varepsilon_{zz}, \tag{4.2}$$

$$\tau_{zz} = \lambda\varepsilon_{xx} + \lambda\varepsilon_{yy} + (\lambda + 2G)\lambda\varepsilon_{zz}, \tag{4.3}$$

$$\tau_{xy} = 2G\varepsilon_{xy}, \tag{4.4}$$

$$\tau_{xz} = 2G\varepsilon_{xz}, \tag{4.5}$$

$$\tau_{yz} = 2G\varepsilon_{yz}, \tag{4.6}$$

where τ is stress, ε is strain, λ and G are Lame's parameters. G is also called the shear modulus.

As shown by the equations, Lame's parameters have an influence on stress. Although many elastic parameters (such as bulk modulus, Young's modulus, Poisson's ratio, and shear modulus) can be defined for an isotropic material, only two of them are independent. This research focuses on variations in Young's

146

modulus E and Poisson's ratio υ. These are related to Lame's parameters by the following:

$$\lambda = E\,\frac{\upsilon}{(1+\upsilon)(1-2\upsilon)},\qquad\qquad (4.7)$$

$$G = \frac{E}{2(1+\upsilon)},\qquad\qquad (4.8)$$

where λ and G is Lame's parameters, E is Young's modulus, υ is Poisson's ratio.

It is clear that Poisson's ratio υ can influence stress distribution in a non-linear way within the body. Consequently, the principal stress direction will change as Poisson's ratio varies, which will affect fracture trajectories.   This section examines the influence of changes in Poisson's ratio on core fractures for a selected set of stress conditions. Values in Poisson's ratio of 0.05, 0.15, 0.25, 0.35 and 0.45 are considered; these span the range for typical crustal rocks (Table 3.2). In all of the cases, the core stub length is 0.25d is used (where d is the diameter of the core).

4.3.1 SV:SH:Sh = 1:0.5:0.5

This set of models focuses on the case of isotropic horizontal stress, using SV:SH:Sh = 1:0.5:0.5. Figure 4.9 illustrates how variations in Poisson's ratio affect fracture morphology. A concave disc fracture is generated in these situations with a small Poisson's ratio producing a flat disc shape within a
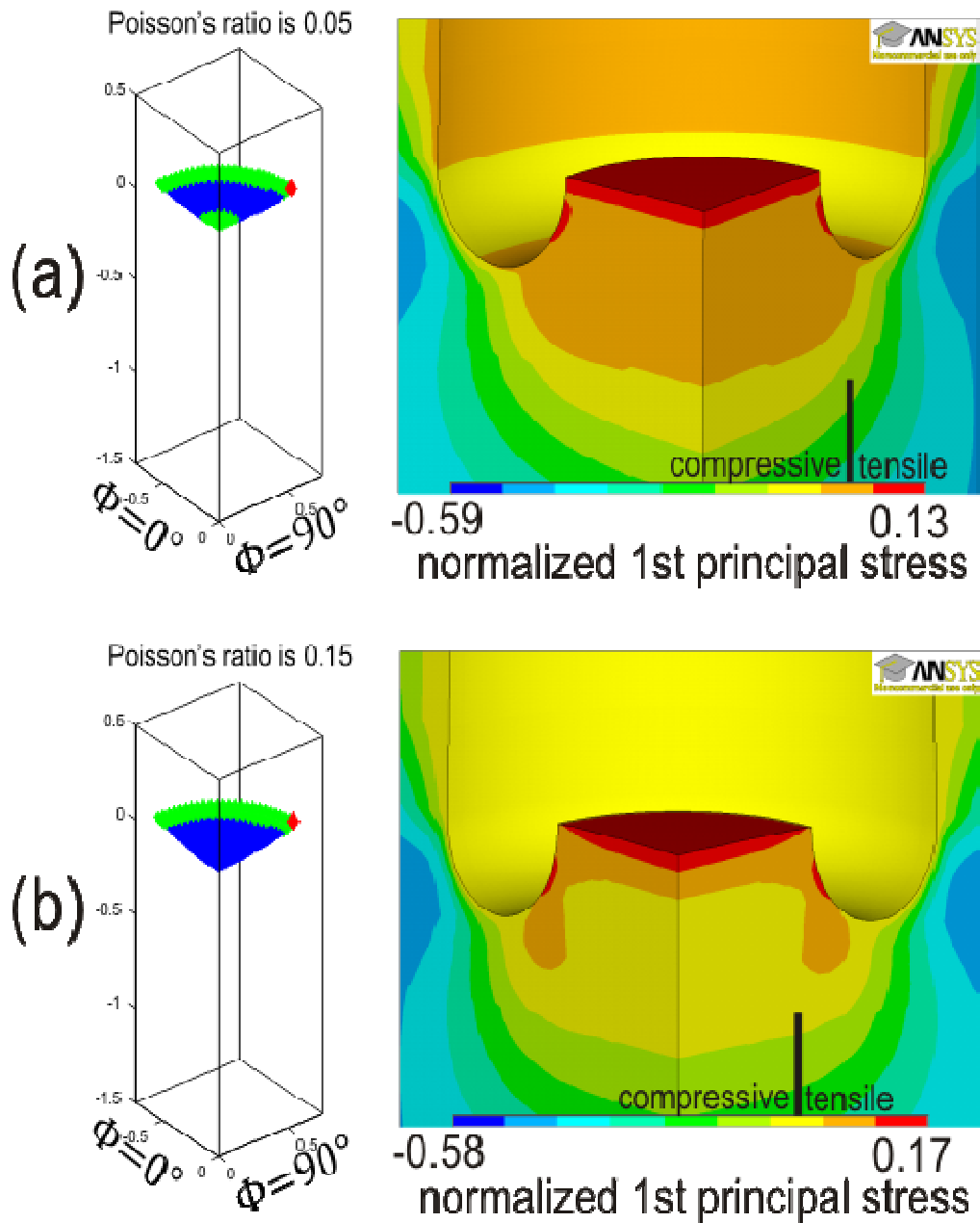
Figure 4.9: Plots of the fracture surface (left) and normalized stress (right) for variations in Poisson's ratio when SV:SH:Sh=1:0.5:0.5. (a) Poisson's ratio is 0.05 (b) Poisson's ratio is 0.15.
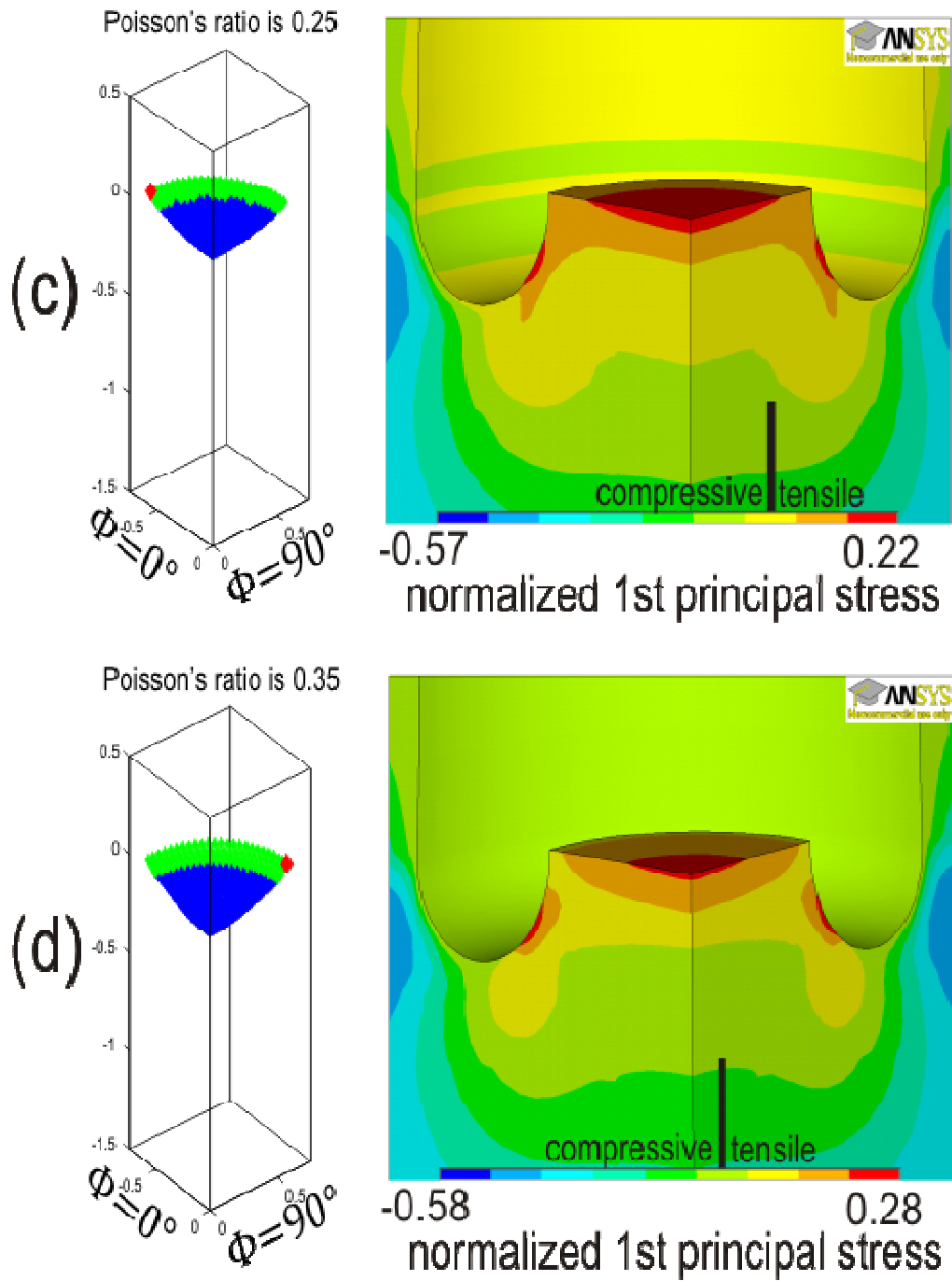
Figure 4.9 continued: (c) Poisson's ratio is 0.25. (d) Poisson's ratio is 0.35.
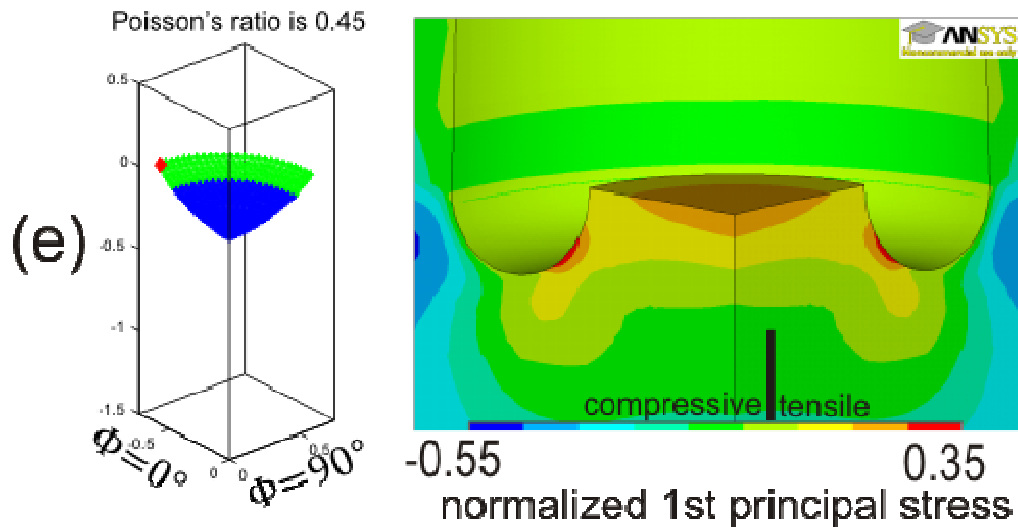
Figure 4.9 continued: (e) Poisson's ratio is 0.45.

relatively small zone of tension (Figure 4.9a). As Poisson's ratio increases, the stress directions change, producing increasingly deeper fractures. The magnitudes of the generated tensile stresses increase, as does the volume of the material put under tension. Further, the fracture surface enters a compression zone in the centre of the core, suggesting that the induced fracture may only exist at the core periphery in all of the cases.

These figures show that the initial point is always located at the inner kerf. Note that this is an isotropic horizontal situation, so the initial point is a circle rather than a single point. The global maximum tensile stress increases as Poisson's ratio increases, from 13% of SV when Poisson's ratio is 0.05 (Figure 4.9a) to 35% when Poisson's ratio is 0.45 (Figure 4.9e). Therefore, it is more likely that fracture will arise when material has a larger Poisson's ratio.

A strong local maximum tensile stress occurs on the core top at the symmetry axis in all cases. Secondary fractures may occur here.

4.3.2 SV:SH:Sh = 1:0.5:0.25

This set of models focuses on the case of a normal fault stress regime, with SV:SH:Sh = 1:0.5:0.25. Figure 4.10 illustrates how different Poisson's ratios influence fracture morphology. Two types of fracture shapes are observed: saddle and petal-centreline. When Poisson's ratio is relatively small, a saddle fracture is generated (Figure 4.10 a, b), where fractures are concave up in the middle and concave down at edge. On the other hand, petal-centreline shape fractures occur at a larger Poisson's ratio ($\upsilon > 0.15$ for this in-situ stress, as shown in Figure 4.10 c, d, e). For all cases, the initial fracture is located at the inner kerf on the $\Phi = 90°$ plane. The global maximum tensile stress increases as Poisson's ratio increases, from 39% of SV when Poisson's ratio is 0.05 to 91% when Poisson's ratio is 0.45. This means that there is a higher possibility for a fracture occurring for rocks with a larger Poisson's ratio.

In the centre of the core top, a local maximum tensile stress is observed which could produce a secondary fracture. However, its magnitude is about one third of the global maximum, and therefore it is unclear if it will be sufficient to break the rock.
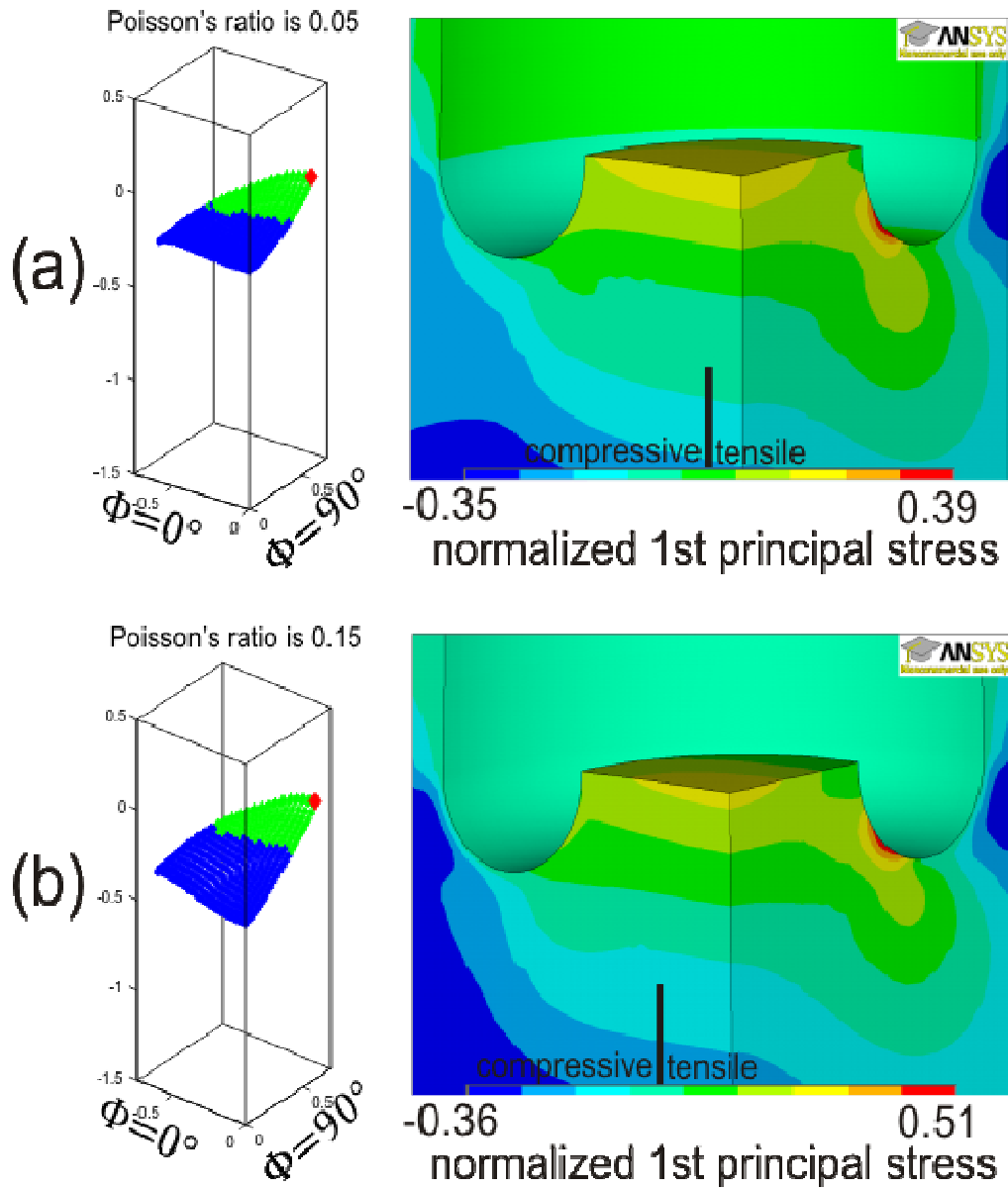
Figure 4.10: Plots of the fracture surface (left) and normalized stress (right) for variations in Poisson's ratio when SV:SH:Sh=1:0.5:0.25. (a) Poisson's ratio is 0.05. (b) Poisson's ratio is 0.15.
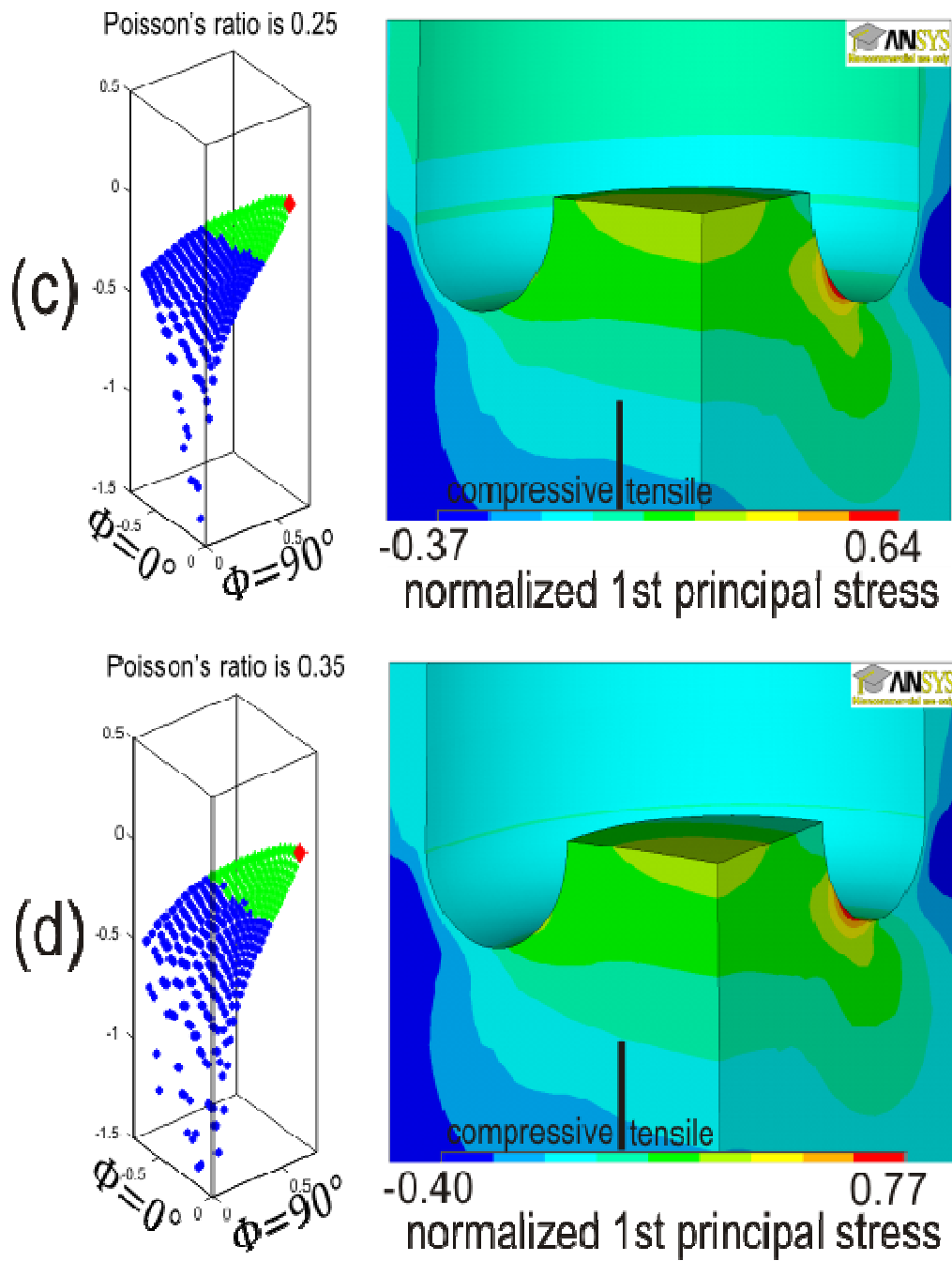
Figure 4.10 continued: (c) Poisson's ratio is 0.25. (d) Poisson's ratio is 0.35.

153
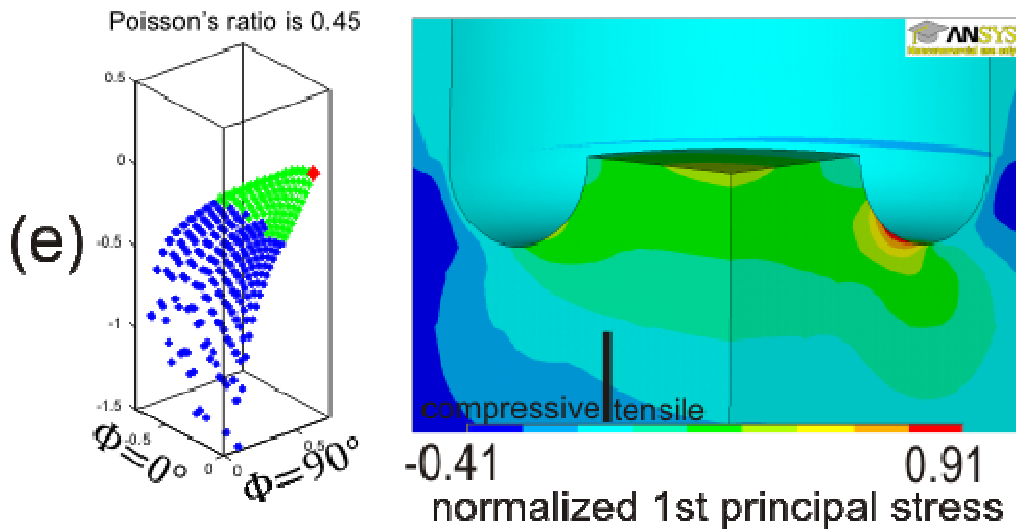
Figure 4.10 continued: (e) Poisson's ratio is 0.45.

4.3.3 SV:SH:Sh = 1:0.5:0

This set of models focuses on another normal fault stress regime case, with SV:SH:Sh = 1:0.5:0 (Figure 4.11). Here with all different values of Poisson's ratio, a petal shape fracture is generated; Poisson's ratio does not appear to have much influence on the fracture shape. However, the size of the tensile zone increases as Poisson's ratio increases, meaning that a larger volume of rock may be damaged if the rock has a high Poisson's ratio.

All fractures initiate on the inner kerf on the $\Phi = 90°$ plane, and the global maximum tensile stress increases with Poisson's ratio. When Poisson's ratio is 0.05, the maximum stress is 94% of SV and when Poisson's ratio is 0.45, it is 164%. It should be noted that the global greatest tensile stress is much larger than was observed for other states of in-situ stress (e.g., section 4.3.1 and 4.3.2) and
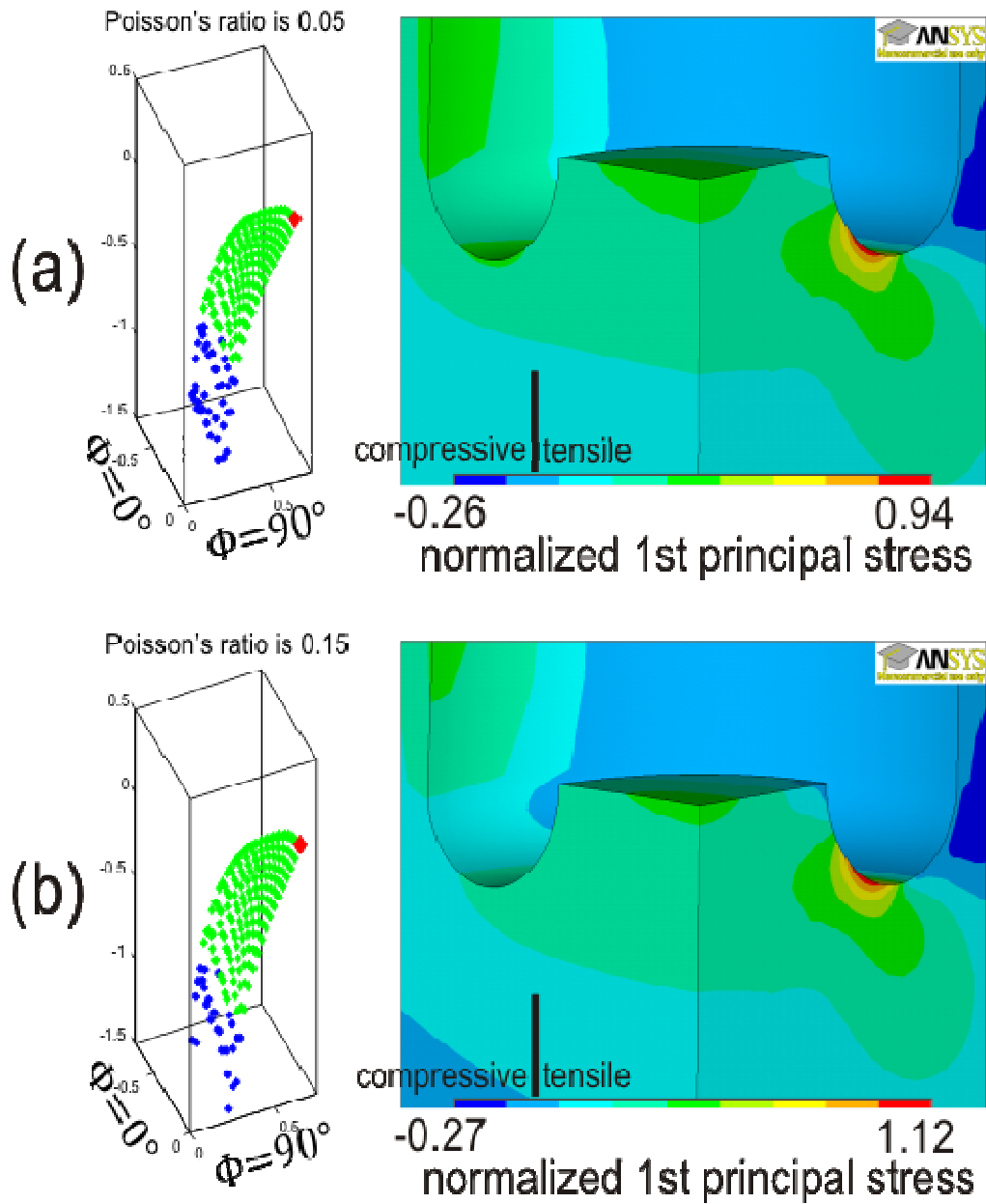
Figure 4.11: Plots of the fracture surface (left) and normalized stress (right) for variations in Poisson's ratio when SV:SH:Sh=1:0.5:0. (a) Poisson's ratio is 0.05. (b) Poisson's ratio is 0.15.
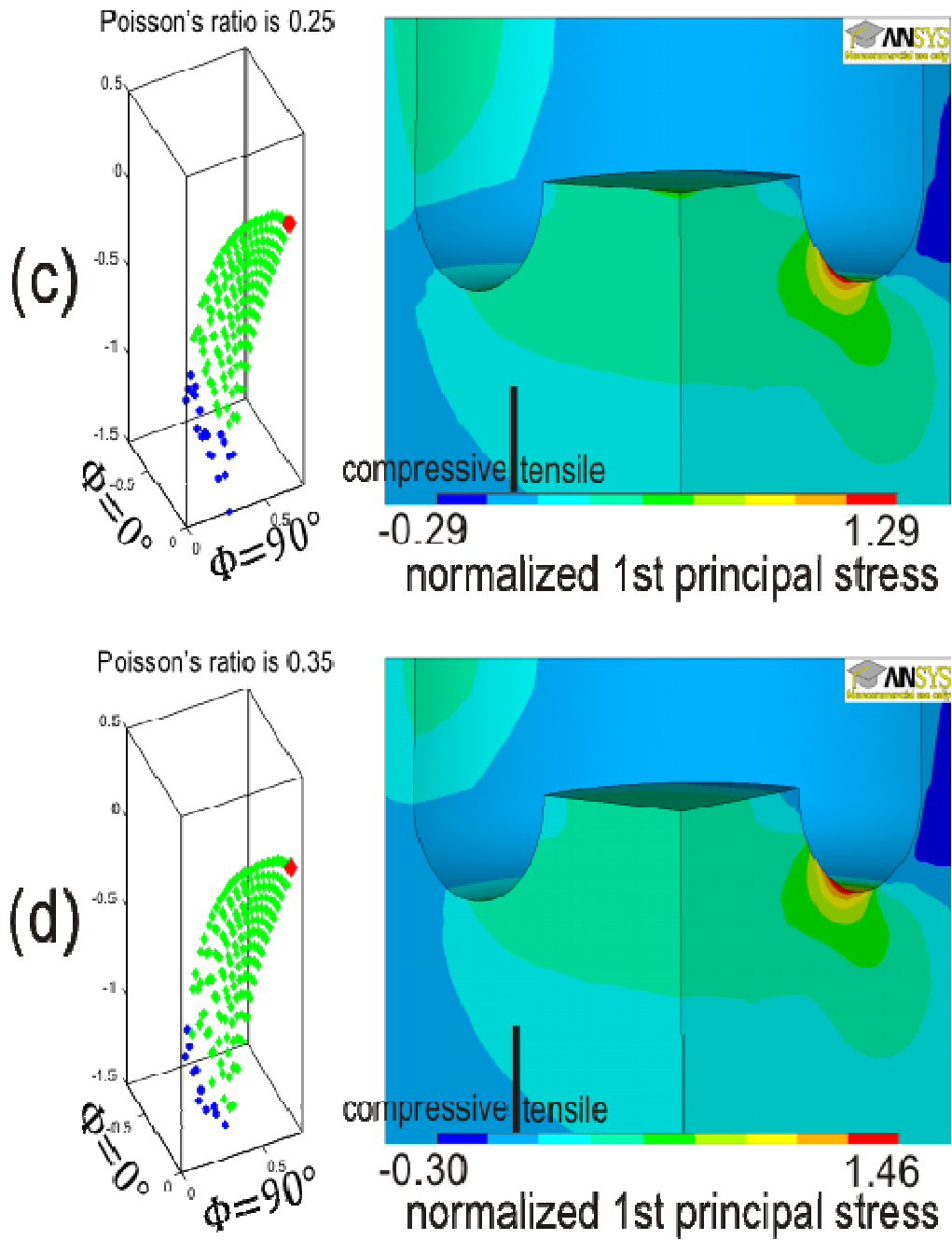
Figure 4.11 continued: (c) Poisson's ratio is 0.25. (d) Poisson's ratio is 0.35.
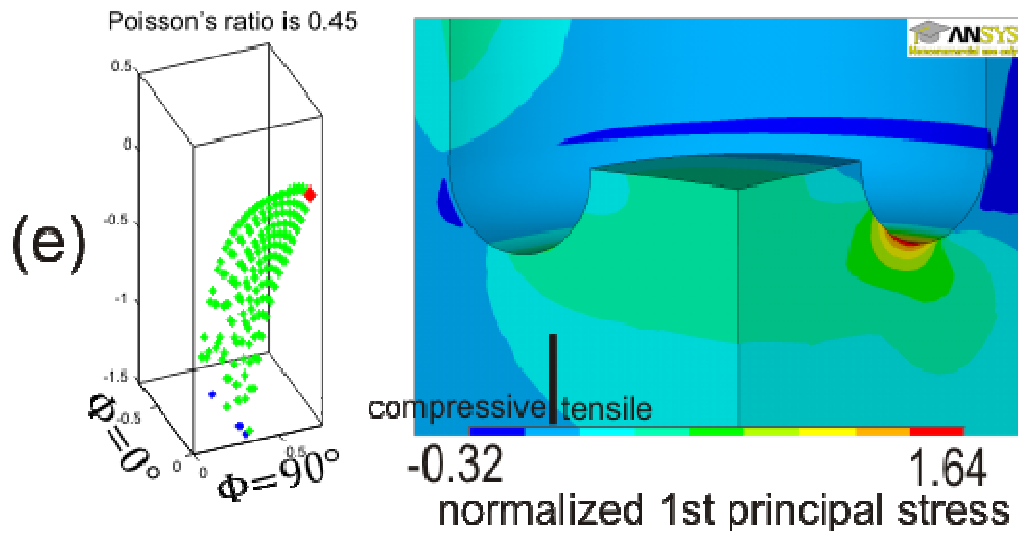
Figure 4.11 continued: (e) Poisson's ratio is 0.45

therefore fractures may initiate more easily in this situation.

There are also local regions of maximum tensile stress in both the core top and borehole wall, which may lead to the development of fractures in these two locations

4.3.4 SV:SH:Sh = 0.8:1:0.5

This set of models focuses on the case when SV:SH:Sh = 0.8:1:0.5, as an example of a strike-slip fault stress regime. Figure 4.12 illustrates the effect of the different Poisson's ratios on the stress distribution and fractures at near the bottom of the borehole.

The fractures have generally a saddle-shape appearance for Poison's ratios greater or equal to 0.15. The only exception is when Poisson's ratio is very small. In this case, the saddle shape fracture may bend upward to the symmetry axis, as shown in Figure 4.12(a) with Poisson's ratio is 0.05. It is also observed that the size of the tensile zone decreases slightly as Poisson's ratio increases.

For all Poisson's ratios, the fracture initiation point is located on the inner kerf at the $\Phi = 90°$ plane, and the global maximum tensile stress increases with increasing Poisson's ratio. The greatest tensile stress values range from 15% of SH for a Poisson's ratio of 0.05 to 43% with $\upsilon = 0.45$. The magnitude of maximum tensile stress is fairly low, meaning that it may be difficult to produce fractures in rocks that have an intrinsic tensile strength.

A second area of tensile stress is observed on the core top and it has a comparable magnitude to the global maximum tensile stress. Secondary fractures may be produced here.

Figure 4.12: Plots of the fracture surface (left) and normalized stress (right) for variations in Poisson's ratio when SV:SH:Sh=0.8:1:0.5. (a) Poisson's ratio is 0.05. (b) Poisson's ratio is 0.15.
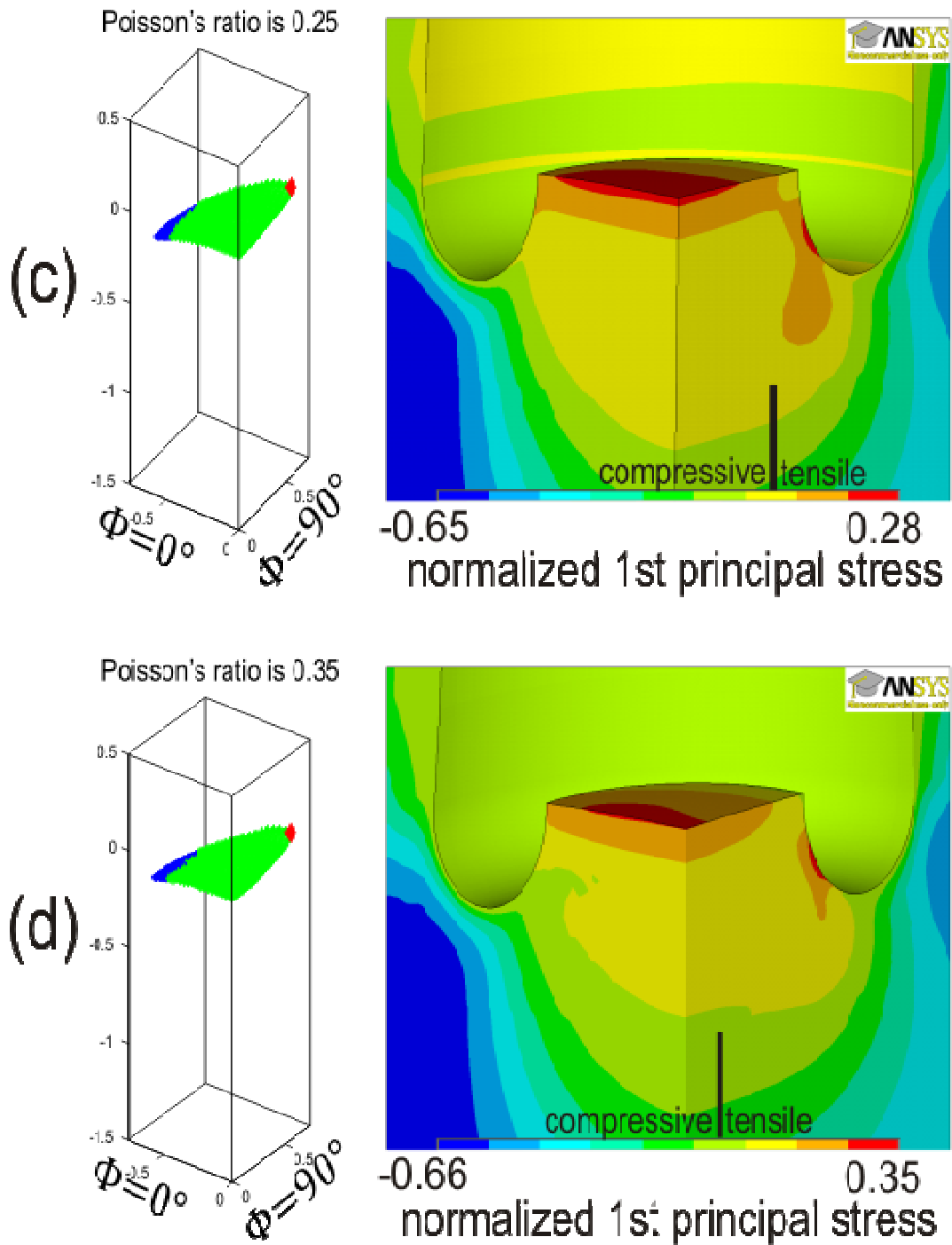
Figure 4.12 continued: (c) Poisson's ratio is 0.25. (d) Poisson's ratio is 0.35.

160
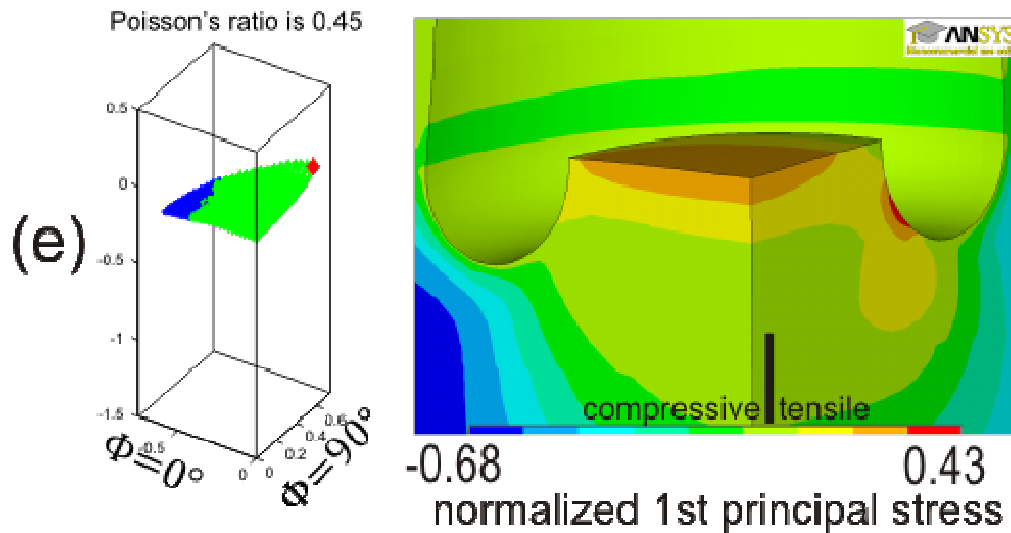
Figure 4.12 continued: (e) Poisson's ratio is 0.45.

4.3.5 SV:SH:Sh = 0.5:1:0.8

Finally, the effect of Poisson's ratio for a thrust fault stress regime was examined using SV:SH:Sh = 0.5:1:0.8. As shown in Figure 4.13, variations in Poisson's ratio have little effect on the stress field at the bottom of the borehole or the predicted fracture morphology, except when Poisson's ratio is 0.45. For $\upsilon < 0.45$, all fractures have a flat disc shape, with fractures initiating in the centre of the core, at the symmetry axis. At a Poisson's ratio of 0.45, the disc may bend up towards symmetry axis, and the initial fracture point is located at the inner kerf on the $\Phi = 90°$ plane (Figure 4.13e).

In contrast to the cases presented above, the global maximum tensile stress *decreases* with an increase in Poisson's ratio, from 16% of SH for $\upsilon = 0.05$ to 11% of SH for $\upsilon = 0.45$. Note that these are relatively low tensile stress values, and therefore it may be difficult to produce a fracture in a real rock. It is also observed

stub length is 0.25, SV:SH:Sh−0.5:1:0.8
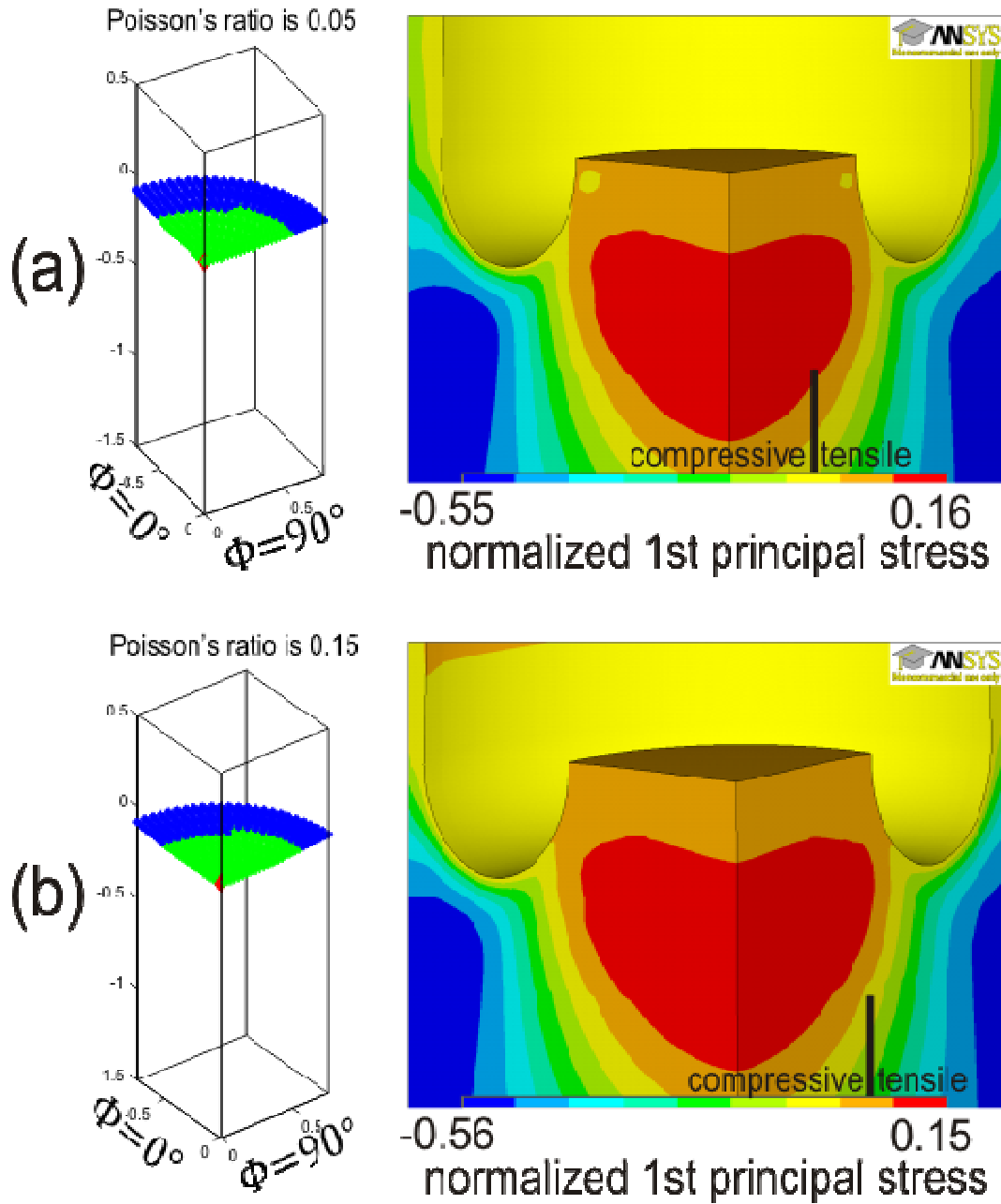
Figure 4.13: Plots of the fracture surface (left) and normalized stress (right) for variations in Poisson's ratio when SV:SH:Sh=0.5:1:0.8. (a) Poisson's ratio is 0.05. (b) Poisson's ratio is 0.15.
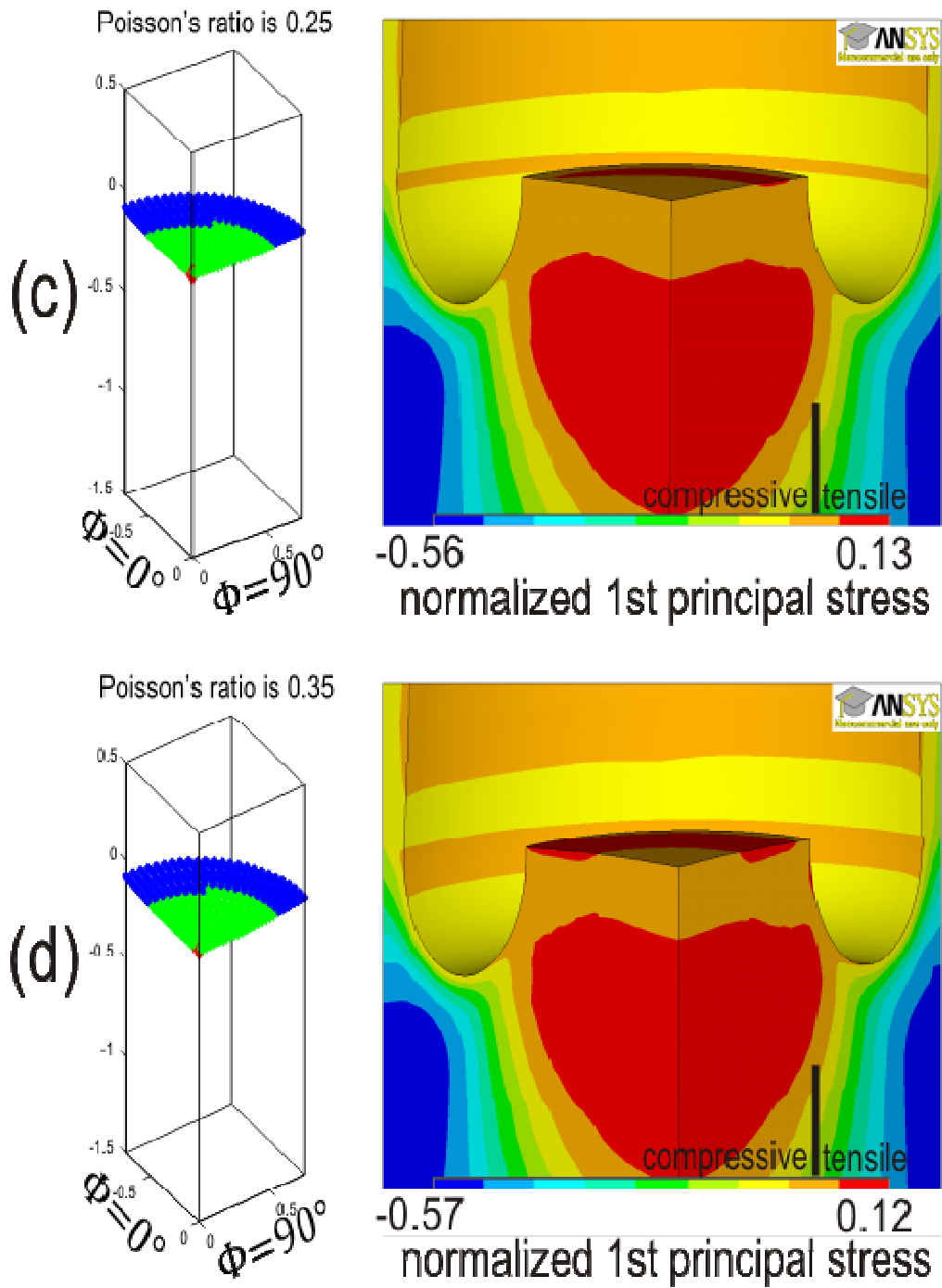
Figure 4.13 continued: (c) Poisson's ratio is 0.25. (d) Poisson's ratio is 0.35.
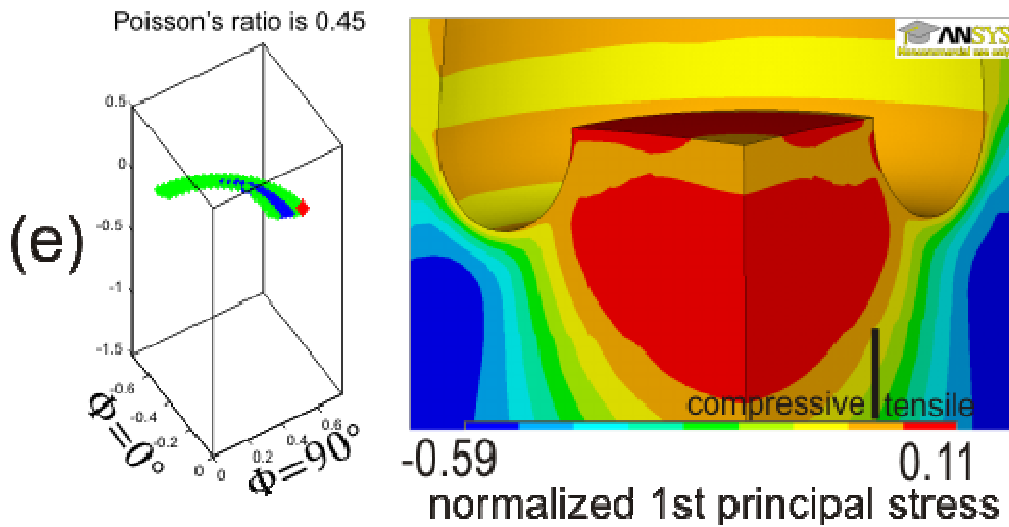
Figure 4.13 continued: (e) Poisson's ratio is 0.45.

that there is a region of local tensile stress can be observed on core top near edge of the core, which may produce secondary fractures.

4.3.6 Summary of the effect of Poisson's ratio

In the sections above, variations in Poisson's ratio were assessed for several in-situ stress situations and for a core stub length of 0.25d. In general, it was observed that Poisson's ratio has only a small influence on the morphology of fractures and that the location of fracture initiation was not strongly affected by changes in the Poisson's ratio. Further, as Poisson's ratio increases, the magnitude of global maximum tensile stress became larger, meaning that it is more likely that fractures will occur in rocks with a high Poisson's ratio. Figure 4.14 shows the relationship between maximum tensile stress for the three fault regimes, using
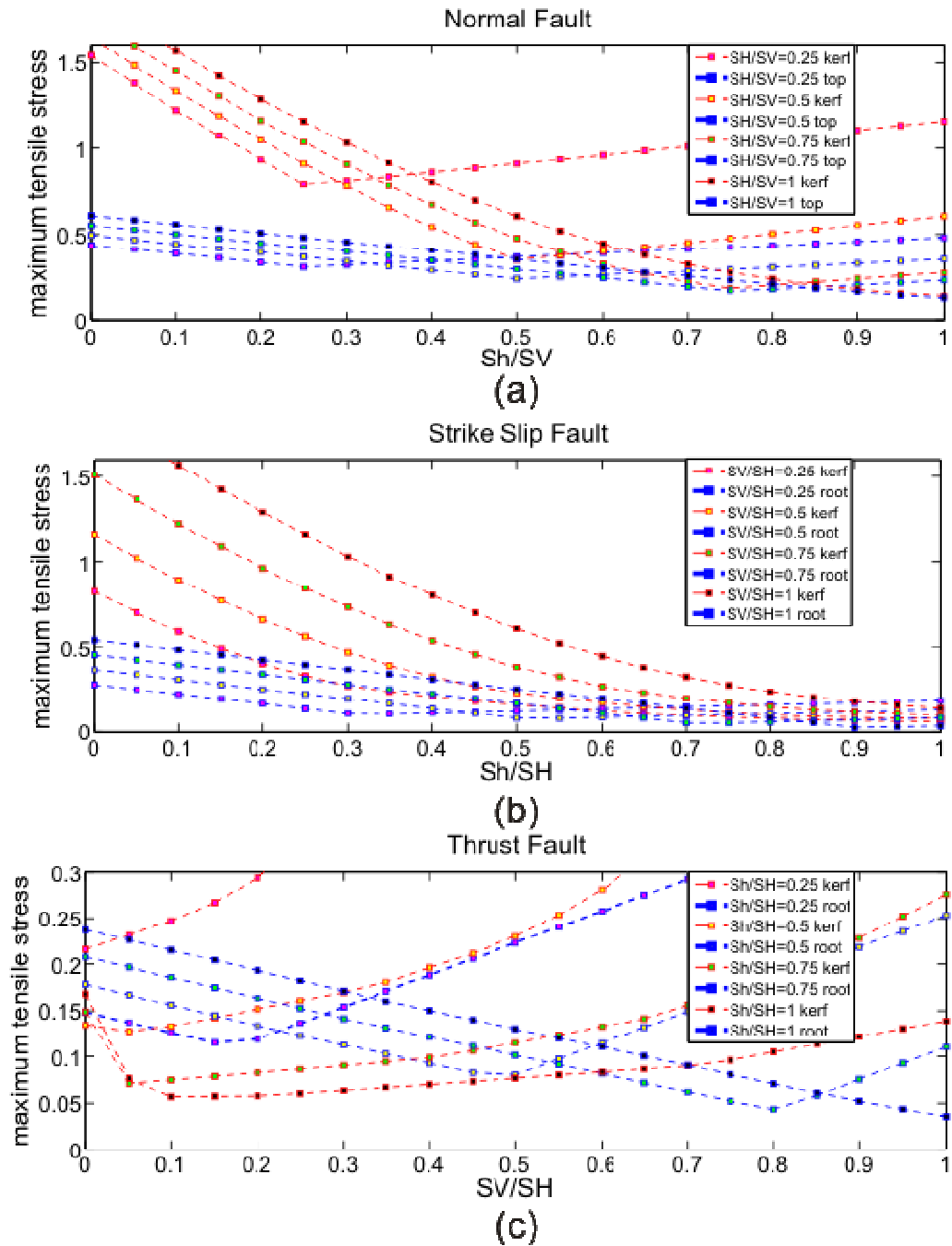
Figure 4.14: Variations in the magnitude of global maximum tensile stress in different stress regimes with a Poisson's ratio 0.45 and a stub length of 0.25d. (a) Normal fault regime. (b) Strike slip fault regime. (c) Thrust fault regime.

a Poisson's ratio of 0.45 and stub length of 0.25d. In general, these plots are similar to those generated for a Poisson's ratio of 0.25 (Figure 4.8), except that the magnitude of tensile stress is larger for a higher Poisson's ratio.

The two key exceptions to the observed trend are:

(1) The case of SV:SH:Sh = 1:0.5:0.25 (section 4.3.2) where fracture shapes changed from saddle-shaped to petal-centreline shape with increasing Poisson's ratio, and;

(2) The case of SV:SH:Sh = 0.5:1:0.8 (section 4.3.5) where the global maximum tensile stress decreased with increasing Poisson's ratio.

Excluding these two cases, these results suggest that fracture morphology is not strongly dependent on Poisson's ratio, meaning that different types of rocks should exhibit similar fracturing behaviour.

4.4 Effect of the core stub length on fracture morphology

In the numerical modeling in this study, the core stub length is defined as the distance between the bottom of the drilling bit and the top of the core. The core stub is generated during drilling process, as the drill bits carve into the intact rock at the bottom of the borehole. Therefore, the length of the core stub increases during drilling. A key question is whether the changing core stub length will result in changes in the stress distribution, and consequently affect the

development of drilling-induced fractures within the core stub. Previous work on 2D fractures has suggested that the stub length has a strong effect on stress distribution for small stubs, but once the core stub has grown sufficiently long, further increases in the length no longer have any effect [*Li and Schmitt*, 1997]. As such, this will have implications to the understanding of fracture spacing particularly with regards to the potential to extract semi-quantitative information about the stress states from the fracture spacing and morphologies.

The numerical models in this study are static, in that the length of the core stub is constant and the modeled stress field is therefore a "snapshot" at a given stub length. Insight into the evolution of the stress distribution during drilling can be gained using models of varying stub length. In this section, stub lengths of 0.0, 0.125d, 0.25d, 0.375d, and 0.5d are considered, where d is the diameter of the core. Five different in-situ stress states are investigated as examples, using a Poisson's ratio of 0.25 and a Young's modulus of 10 GPa for all models. For other combinations of parameters, readers are referred to the modeling codes described in Chapter 3. In the figure captions, it should be note that the stub length is given as a fraction of d (the diameter of the core).

4.4.1 SV:SH:Sh = 1:0.5:0.5

This set of models examines variation in core stub lengths for an in-situ stress of SV:SH:Sh = 1:0.5:0.5. The resulting fracture geometry and stress field are shown in Figure 4.15. All models develop disc-shaped fractures, as expected because the horizontal stress is isotropic. With an increase in the stub length, the fractures get
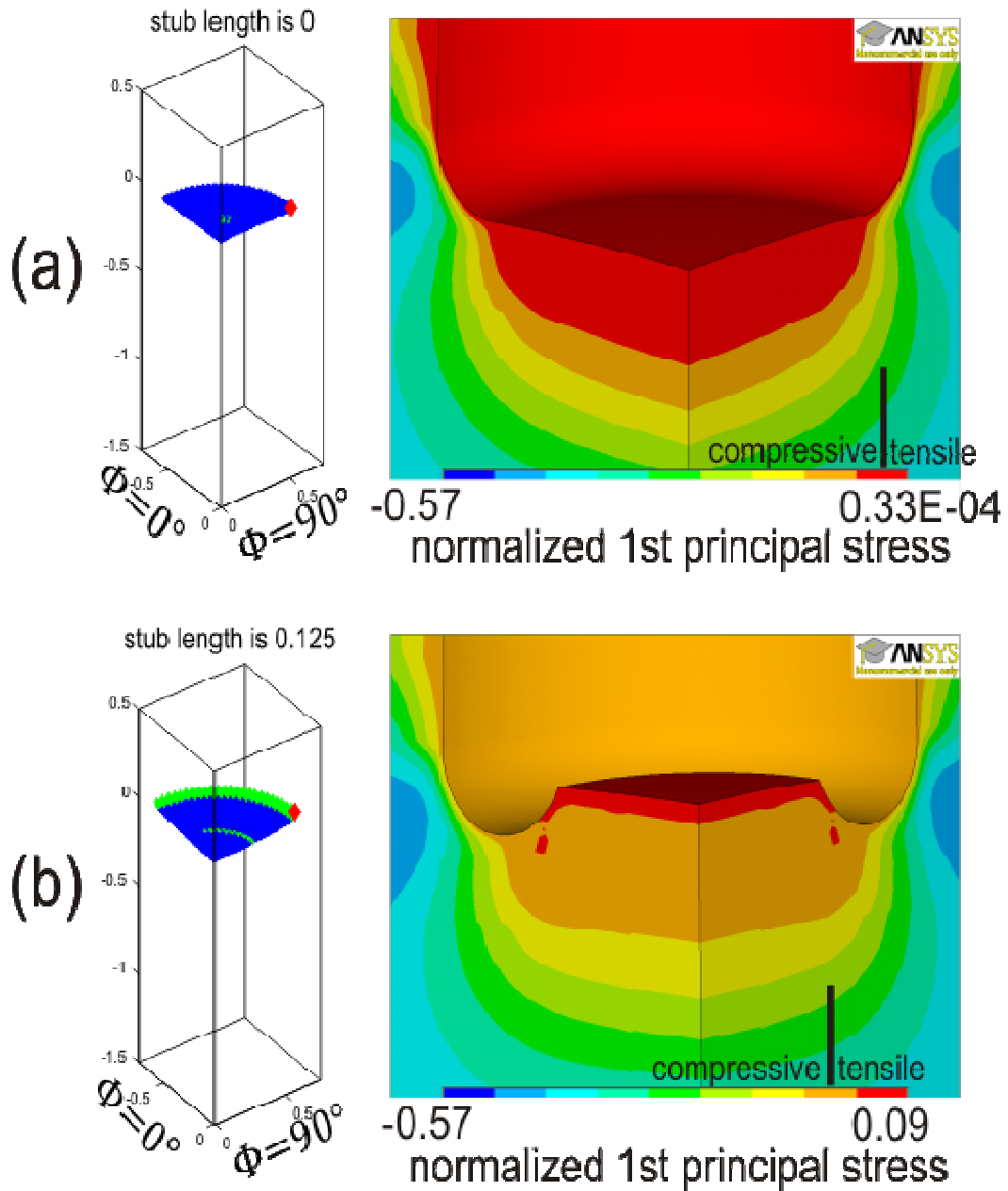
Figure 4.15: Plots of the fracture surface (left) and normalized stress (right) for variations in stub length when SV:SH:Sh=1:0.5:0.5. (a) Stub length is 0. (b) Stub length is 0.125d.

168

stub length is 0.25

compressive | tensile

-0.57   0.22
normalized 1st principal stress

stub length is 0.375

compressive | tensile

-0.57   0.30
normalized 1st principal stress
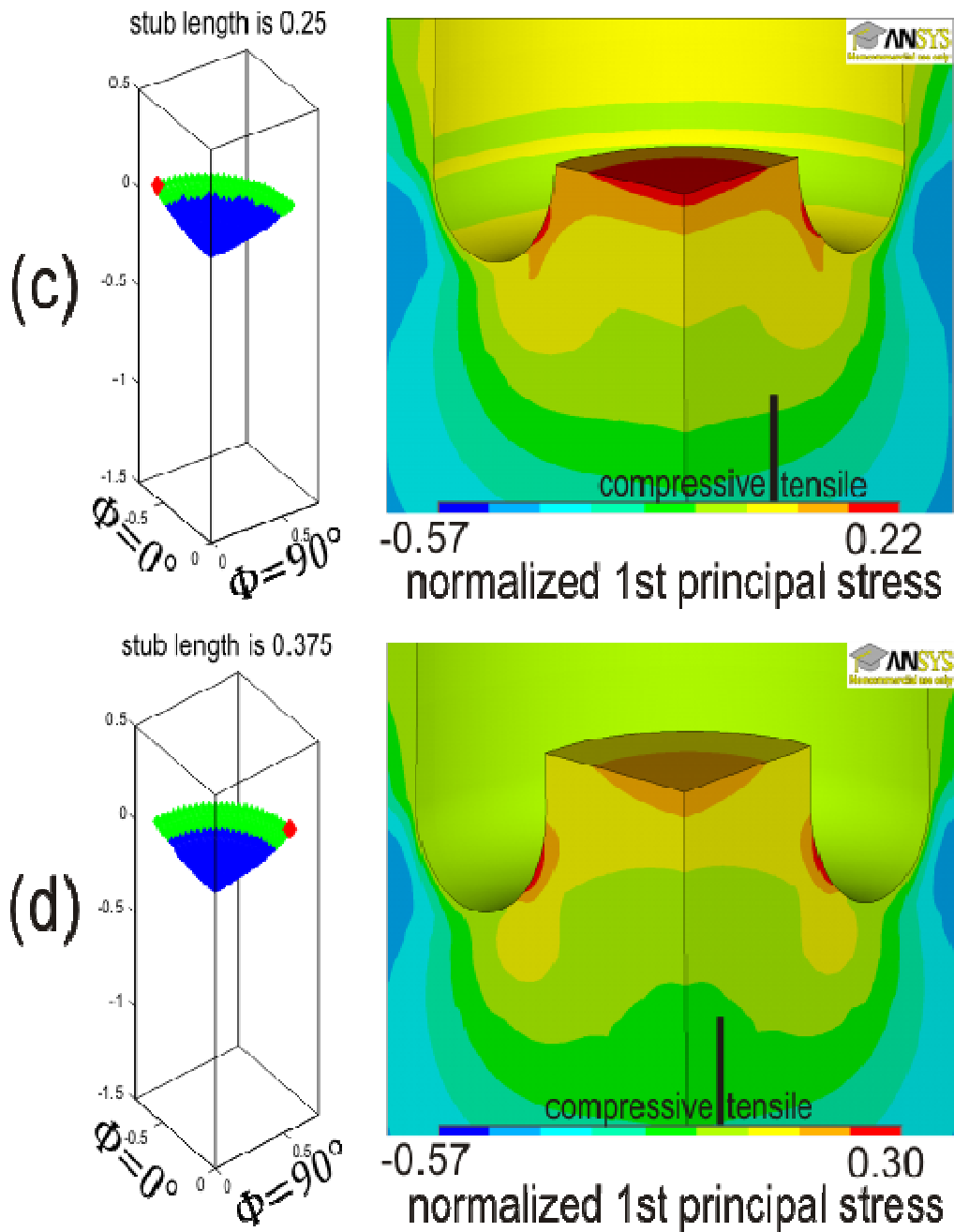
Figure 4.15 continued: (c) Stub length is 0.25d. (d) Stub length is 0.375d.

Figure 4.15 continued: (e) Stub length is 0.5d.

deeper on the edge, as can be seen by comparing Figures 4.15(a) and (e). For the longest stub length of 0.5d, a sudden jump in the fracture propagation direction a stub length of 0.375d (Figure 4.15d). It is likely that there is a deficiency in the fracture propagation modeling code here as at these locations more isotropic stresses are found and this makes it difficult for the fracture propagation code to proceed smoothly. As will be discussed in Chapter 5, this will be an issue for future improvements to the code.

For all models, fractures initiate on the inner kerf; note that this is an isotropic horizontal stress situation so the fracture initiation will occur on a circle rather than a single point. The global maximum tensile stress increases with increasing stub length. For a stub length of 0d (no stub), the maximum tensile stress is 0.003% of SV. It is highly unlikely at fractures would develop in this case; indeed, the computed fracture plane which is along the bottom of the borehole is nearly

170

entirely compressive. Maximum tensile stress increases from 9% of SV when the stub length is 0.125d to 33% of SV when the stub length is 0.5d, suggesting that it is more likely for fractures to develop for longer stub lengths.

For all cases, especially those with shorter stub lengths, a zone of tensile stress is observed in the centre of the core top. Secondary fractures may develop here.

4.4.2 SV:SH:Sh = 1:0.5:0.25

Figure 4.16 shows the effect of variations in core stub length for an in-situ stress of SV:SH:Sh = 1:0.5:0.25 (i.e., a normal faulting stress regime). For core stub lengths of 0.125d or greater, petal-centreline fractures are generations and the stub length does not have an obvious influence on the fracture shape. All fractures initiate on the inner kerf at the $\Phi = 90°$ plane, and the maximum tensile stress increases with core stub length, from 47% of SV for a stub length of 0.125d to 71% of SV for a stub length is 0.5d. For these models, a second region of tensile stress is observed in the centre of the core top, which may give rise to secondary fractures. Note that the magnitude of the tensile stress in this region decreases with increasing stub length, and therefore the secondary fractures are less likely for the longer stubs.

The model with a stub length of 0d is anomalous. It predicts that the fracture would follow a curved line along the $\Phi = 0°$ plane and that the fracture would initiate in the centre of the core top, at a maximum tensile stress of 27% of SV.

171
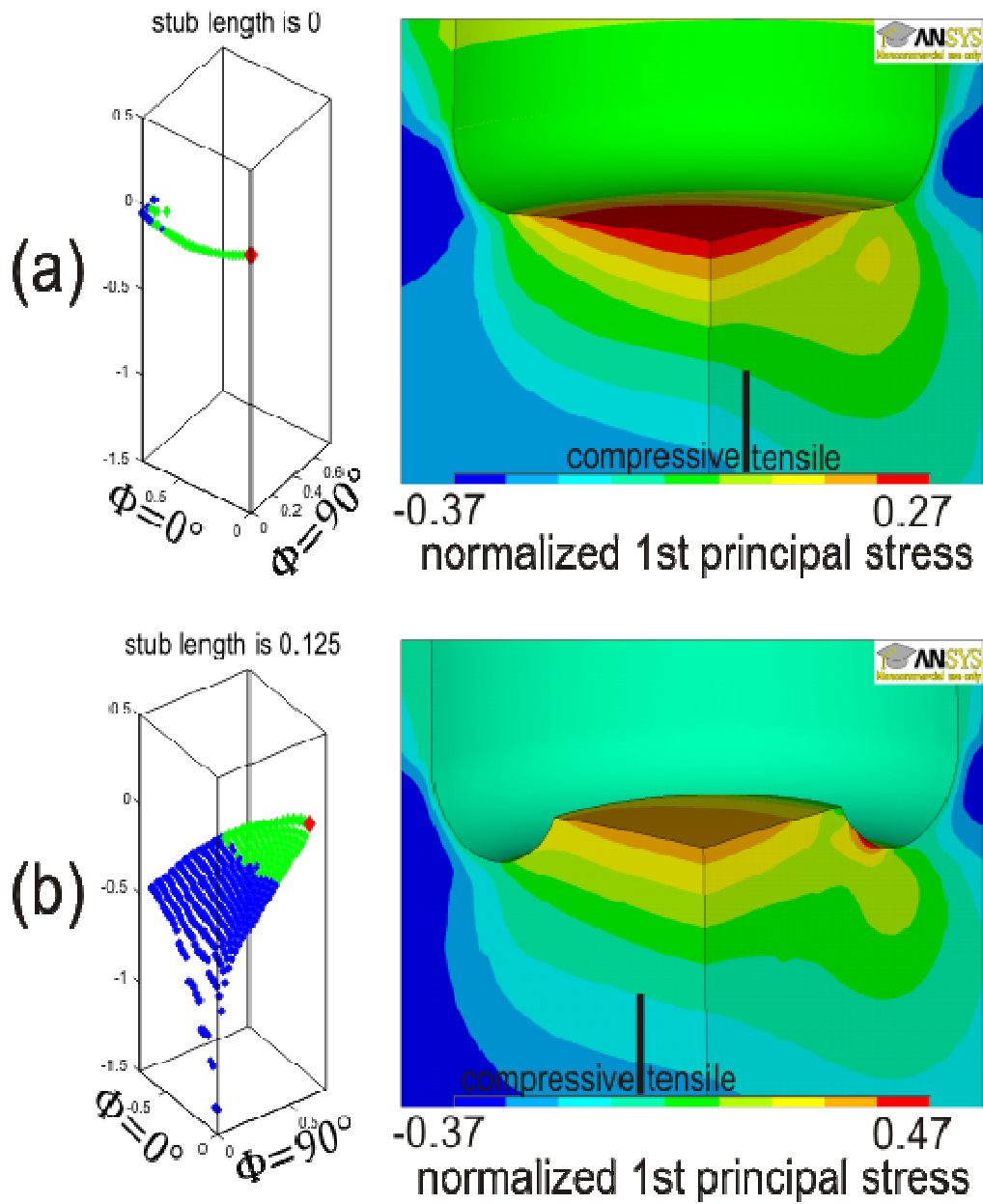
Figure 4.16: Plots of the fracture surface (left) and normalized stress (right) for variations in stub length when SV:SH:Sh=1:0.5:0.25. (a) Stub length is 0. (b) Stub length is 0.125d.
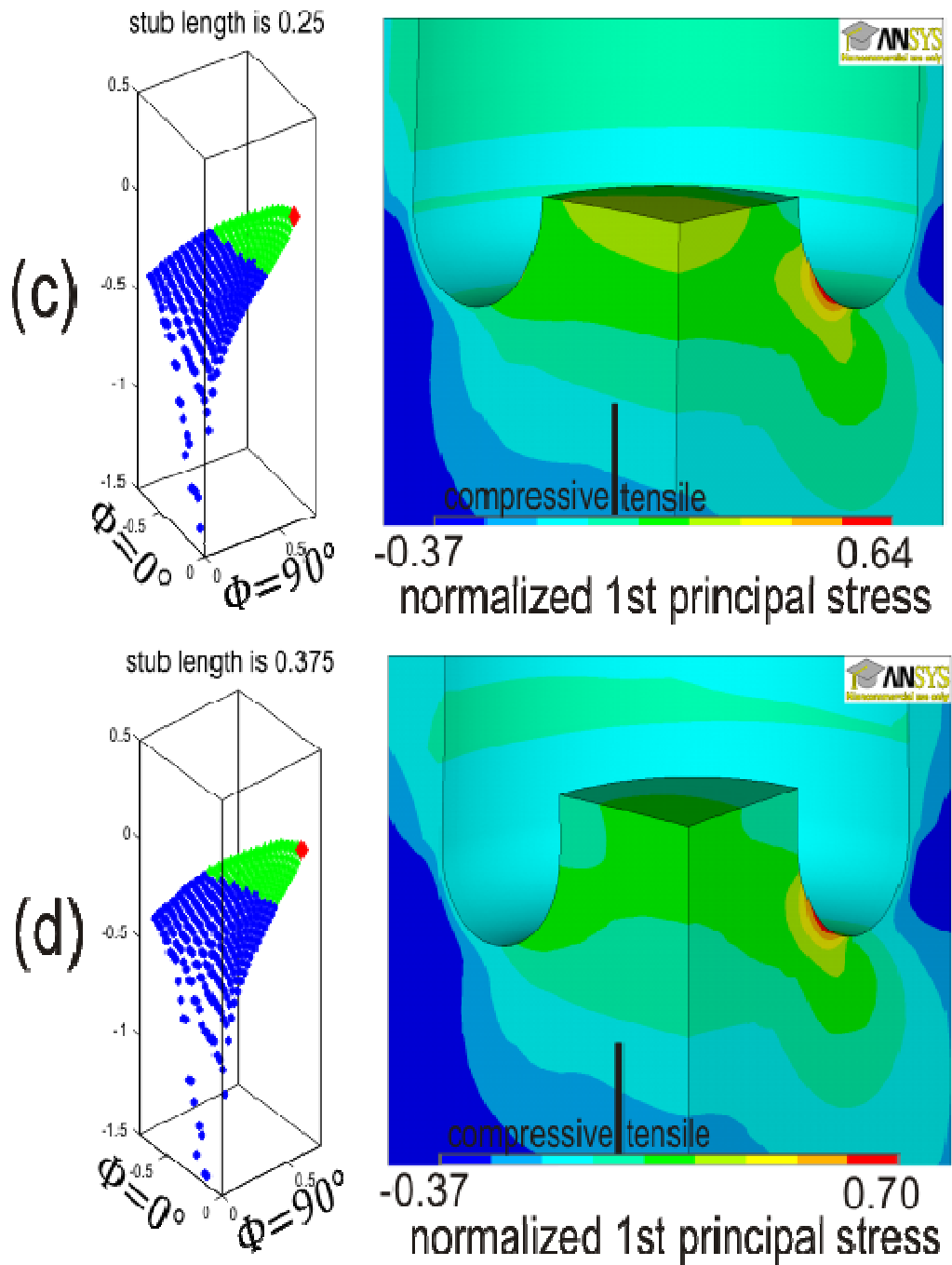
Figure 4.16 continued: (c) Stub length is 0.25d. (d) Stub length is 0.375d.
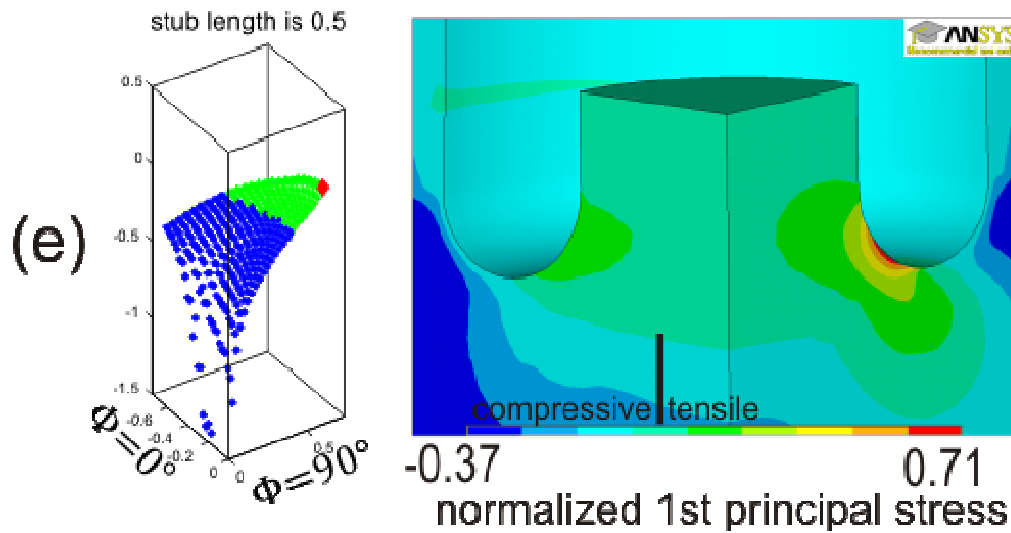
Figure 4.16 continued: (e) Stub length is 0.5d.

The shape of the fracture indicates that the direction of maximum tensile stress is horizontal, and therefore fractures will open in a vertical direction. Because the numerical modeling method uses vertical straws to calculate the fracture trajectory, the vertical fracture will not cut the adjacent straws, and it is not possible to trace the fracture development. This is a limitation of the current models and, as discussed in Chapter 5, may be resolved by using horizontal straws; this is left for future research.

4.4.3 SV:SH:Sh = 1:0.5:0

This set of models considers the normal faulting stress regime with SV:SH:Sh = 1:0.5:0. Figure 4.17 shows the model results for the five different stub lengths. For stub lengths of 0.125d or greater, fractures initiate on the inner kerf at the Φ = 90° plane and a petal-shaped fracture is produced. The fracture shape does not

change significantly as the stub length increases, but the maximum tensile stress at the point of fracture initiation is larger for longer core stubs; it increases from 109% of SV to 133% of SV as the stub length changes from 0.125d to 0.5d. In all these cases, tensile stress is also observed in the centre of the core top and in the borehole wall at the $\Phi = 0°$ plane, which may give rise to secondary fractures. In both regions, stresses appear to decrease with increasing stub length.

As observed in the previous section, the model with a stub length of 0d exhibits a different behaviour, with a curved fracture along the $\Phi = 0°$ plane, which initiated in the centre of the core at a tensile stress of 62% of SV. Again, this geometry likely reflects a deficiency in the modeling approach and should be examined in more detail in future studies.

4.4.4 SV:SH:Sh = 0.8:1:0.5

The effect of stub length on fractures generated in the strike-slip faulting regime was examined using SV:SH:Sh = 0.8:1:0.5. As shown in Figure 4.18a, when the stub length is 0d, extremely small tensile stresses are produced at the bottom of the borehole and in the walls. A maximum value 0.037% of SH is found at the inner kerf on the $\Phi = 90°$ plane and the predicted fracture is a disk shape along the bottom of the borehole at a tiny depth, with the fracture plane entirely in the compressive regime. Owing to the extremely low tensile stresses in this model, it is unlikely that a fracture would be produced.

As the stub length increases to 0.125d, the point of maximum tensile stress shifts
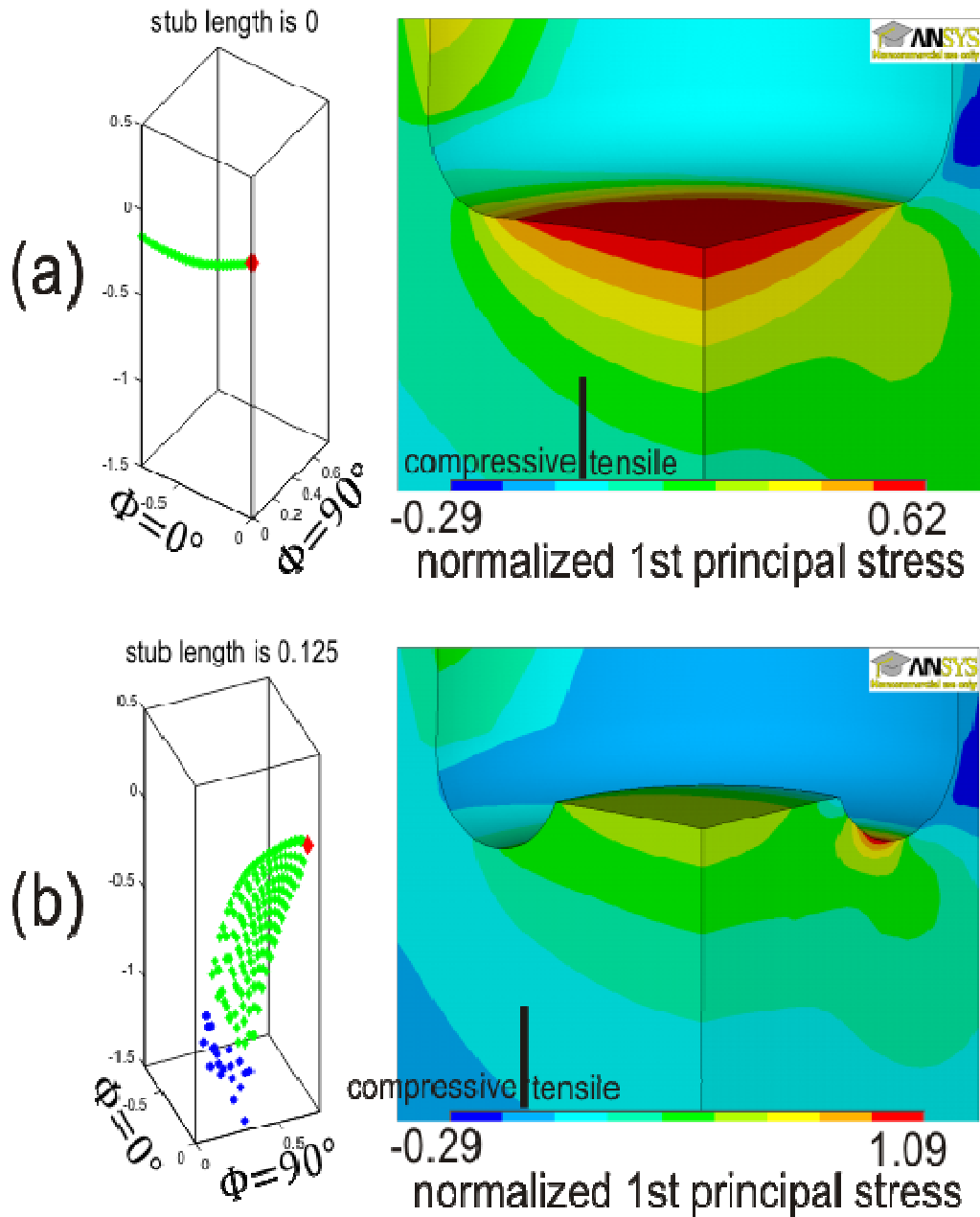
Figure 4.17: Plots of the fracture surface (left) and normalized stress (right) for variations in stub length when SV:SH:Sh=1:0.5:0. (a) Stub length is 0. (b) Stub length is 0.125d.

176
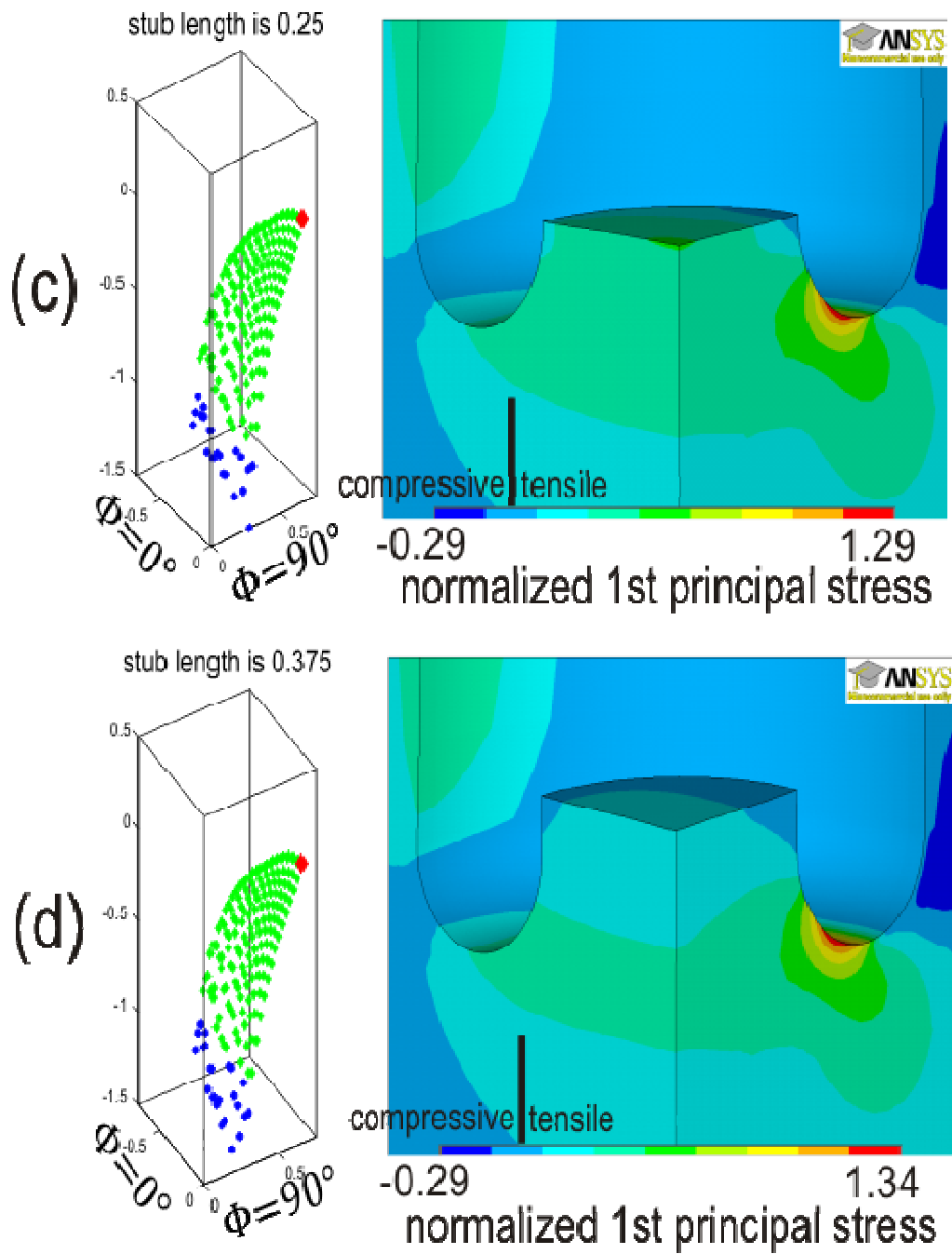
Figure 4.17 continued: (c) Stub length is 0.25d. (d) Stub length is 0.375d.
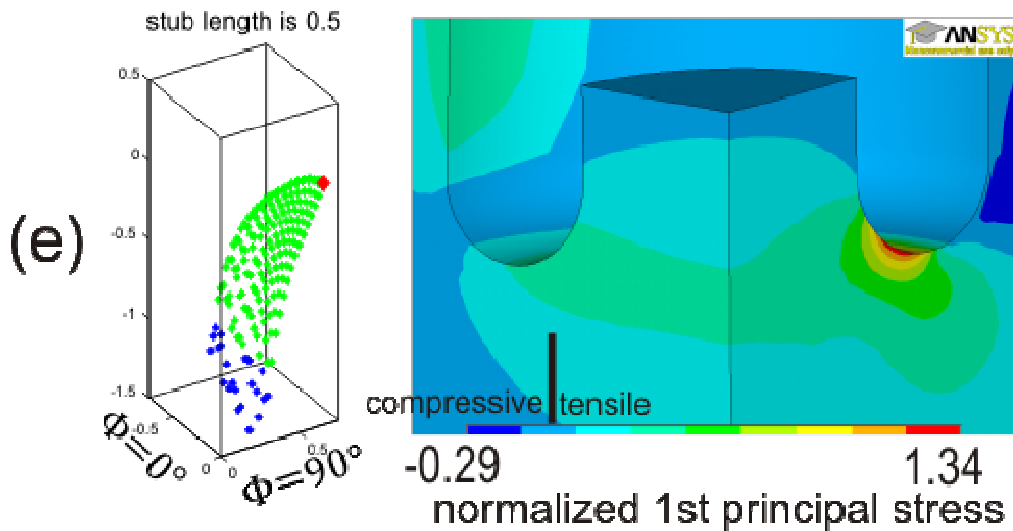
Figure 4.17 continued: (e) Stub length is 0.5d.

to the inner kerf at the $\Phi = 0°$ plane (Figure 4.18b), where a value of 16% of SH is found. The stress distribution in this model predicts that the fracture plane would propagate vertically. Since the modeling code uses vertical straws to determine fracture propagation, it appears that it is not possible to calculate the fracture plane for this case; only the point of fracture initiation is determined. This case should be examined more carefully in future work.

For stub lengths of 0.25d and greater, the fracture calculations appear to be well-behaved (Figure 4.18c, d, e). In all these models, fractures initiate in the inner kerf at the $\Phi = 90°$ plane, and fractures have a convex saddle shape. The fracture geometry is similar among all models, but there are variations in the magnitude of the stress on the fracture plane. At the point of fracture initiation, the maximum tensile stress increases with lengthening core stubs, from 28% of SH for a 0.25d length to 46% of SH for a 0.5d length. In addition, at stub lengths of 0.25d and
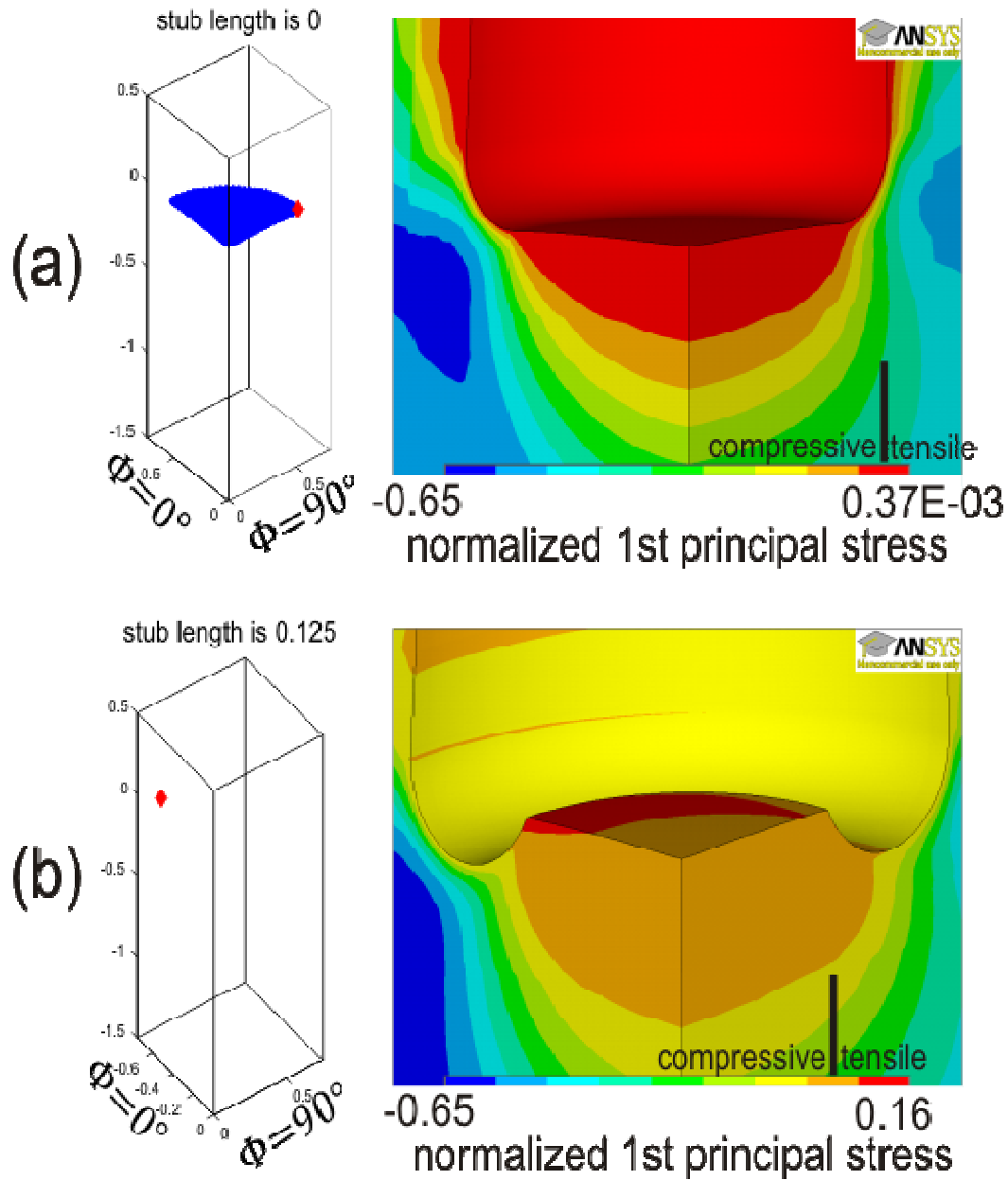
Figure 4.18: Plots of the fracture surface (left) and normalized stress (right) for variations in stub length when SV:SH:Sh=0.8:1:0.5. (a) Stub length is 0. (b) Stub length is 0.125d.

179
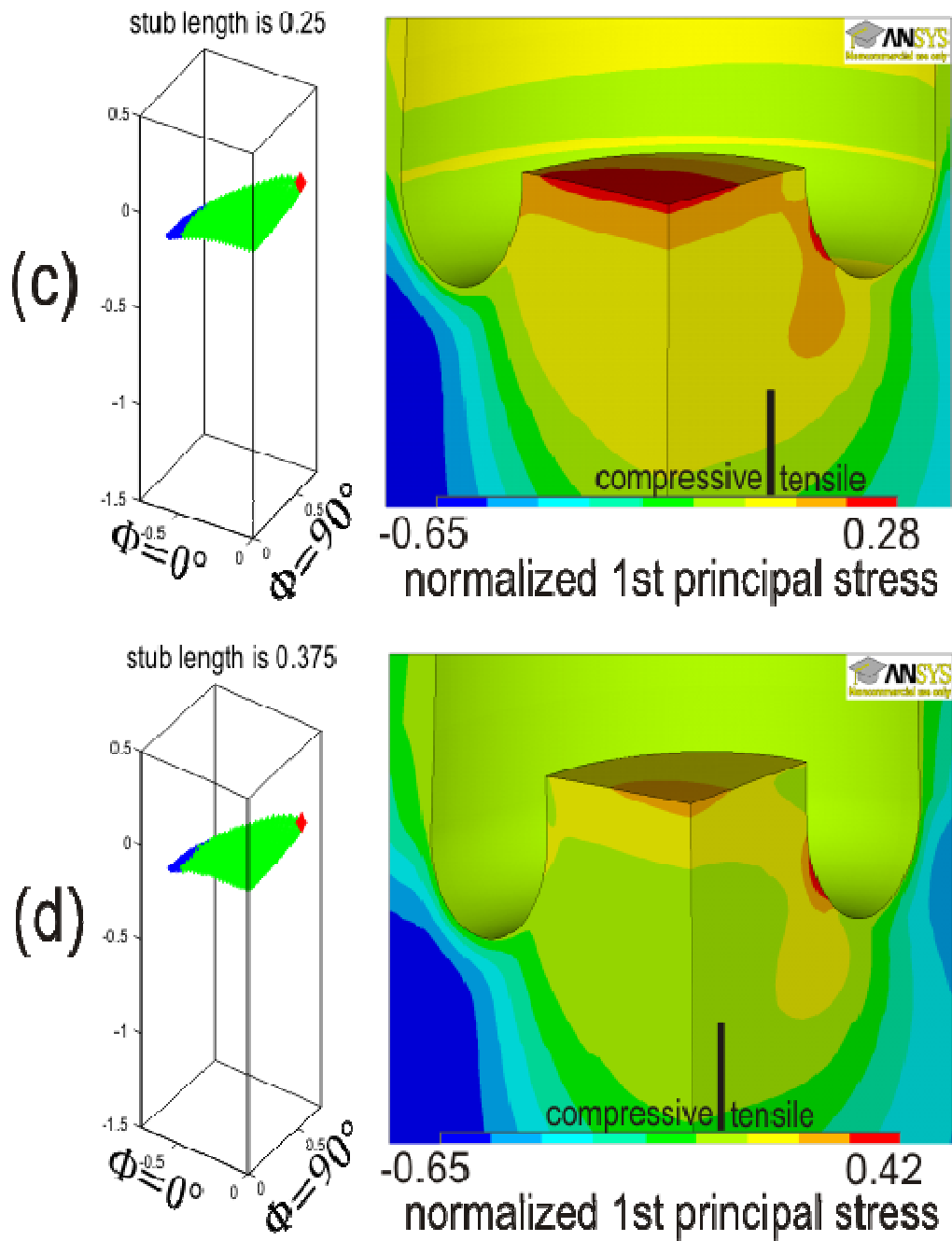
Figure 4.18 continued: (c) Stub length is 0.25d. (d) Stub length is 0.375d.
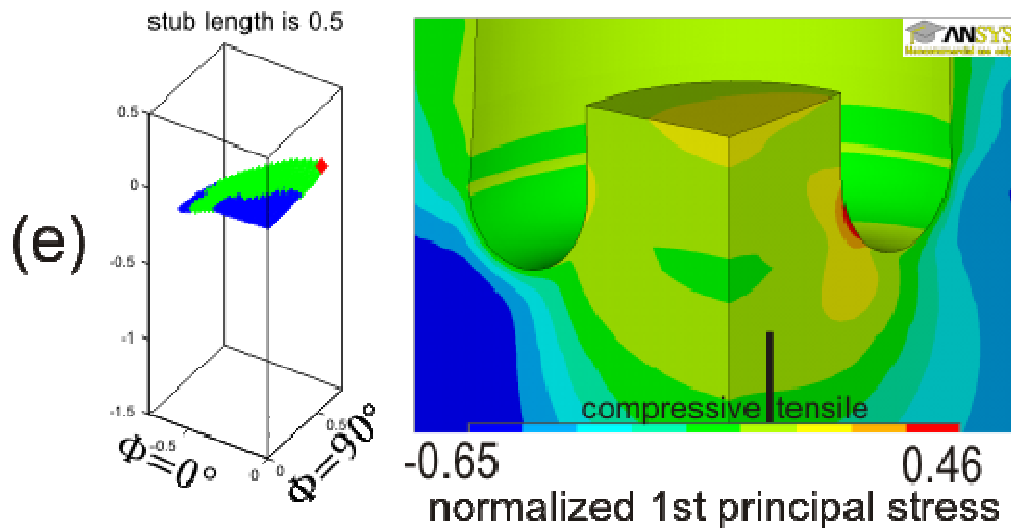
Figure 4.18 continued: (e) Stub length is 0.5d.

0.375d, the majority of the fracture plane is under tensile stress, but at a stub length of 0.5d, the fracture plane enters the compressive zone in the centre of the core stub.

For the latter three stub lengths, tensile stresses are also observed in the centre of the core top, with the magnitude decreasing with larger stubs. Secondary fractures may be produced here.

4.4.5 SV:SH:Sh = 0.5:1:0.8

The final set of models examines the variations in stub length for SV:SH:Sh =0.5:1:0.8, i.e., a thrust faulting stress regime. The results are plotted in Figure 4.19. Unlike the previous models, it appears that the stub length does affect the fracture morphology. At stub lengths of 0.125d and 0.25d, fractures appear to be

flat discs, but become more saddle-shaped at stub lengths of 0.375d and 0.5d. Note that the case with a no stub (length = 0d) also predicts a disc shape, but the maximum tensile stress is extremely small (0.0015% of SH) and the fracture propagates within the compressive regime, so it is expected that fractures would not be produced in real rocks. This model will not be considered further.

As seen previously, the magnitude of maximum tensile stress becomes larger as the core stub length increases; at a length of 0.125d, it is 12% of SH, whereas at a length of 0.5d, it is 27% of SH. However, for this in-situ stress state, the point of initiation varies with changes in stub length. For lengths of 0.375d and 0.5d, fractures initiate on the inner kerf at the $\Phi = 90°$ plane. For a length of 0.25d, the fracture initiates within the core at the symmetry axis. For a length of 0.125d, the fracture initiation point is located within the core stub, as a point that is close to (but NOT exactly in) the inner kerf at the $\Phi = 0°$ plane. A possible explanation for this behaviour is that the stress field can be changed by core stub length, thus the location of global maximum tensile stress also be changed due to variations in the stress field distribution.

For all cases, a weak local maximum tensile stress is observed in the centre of the core top, which may lead to secondary fractures.
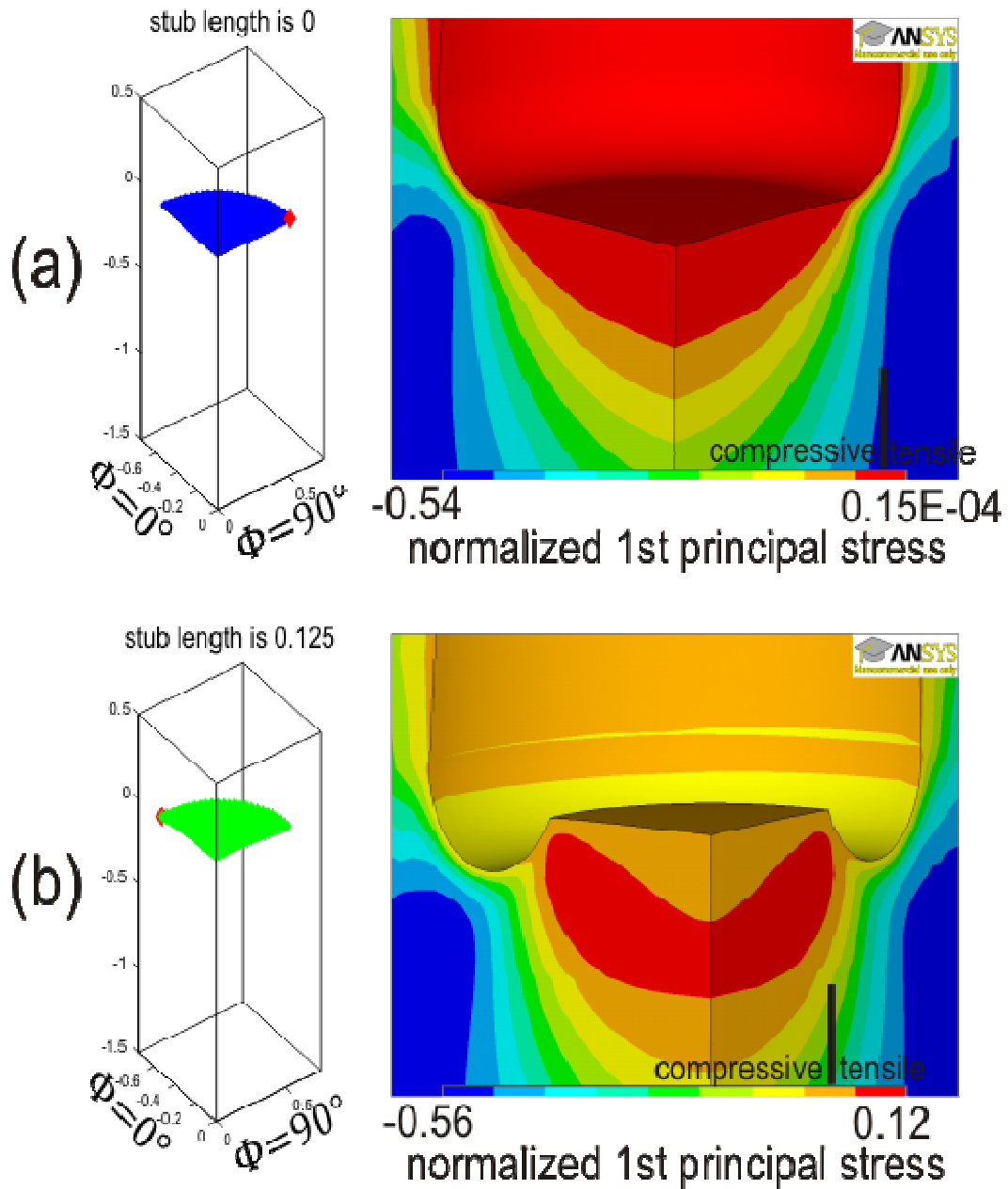
Figure 4.19: Plots of the fracture surface (left) and normalized stress (right) for variations in stub length when SV:SH:Sh=0.5:1:0.8. (a) Stub length is 0. (b) Stub length is 0.125d.
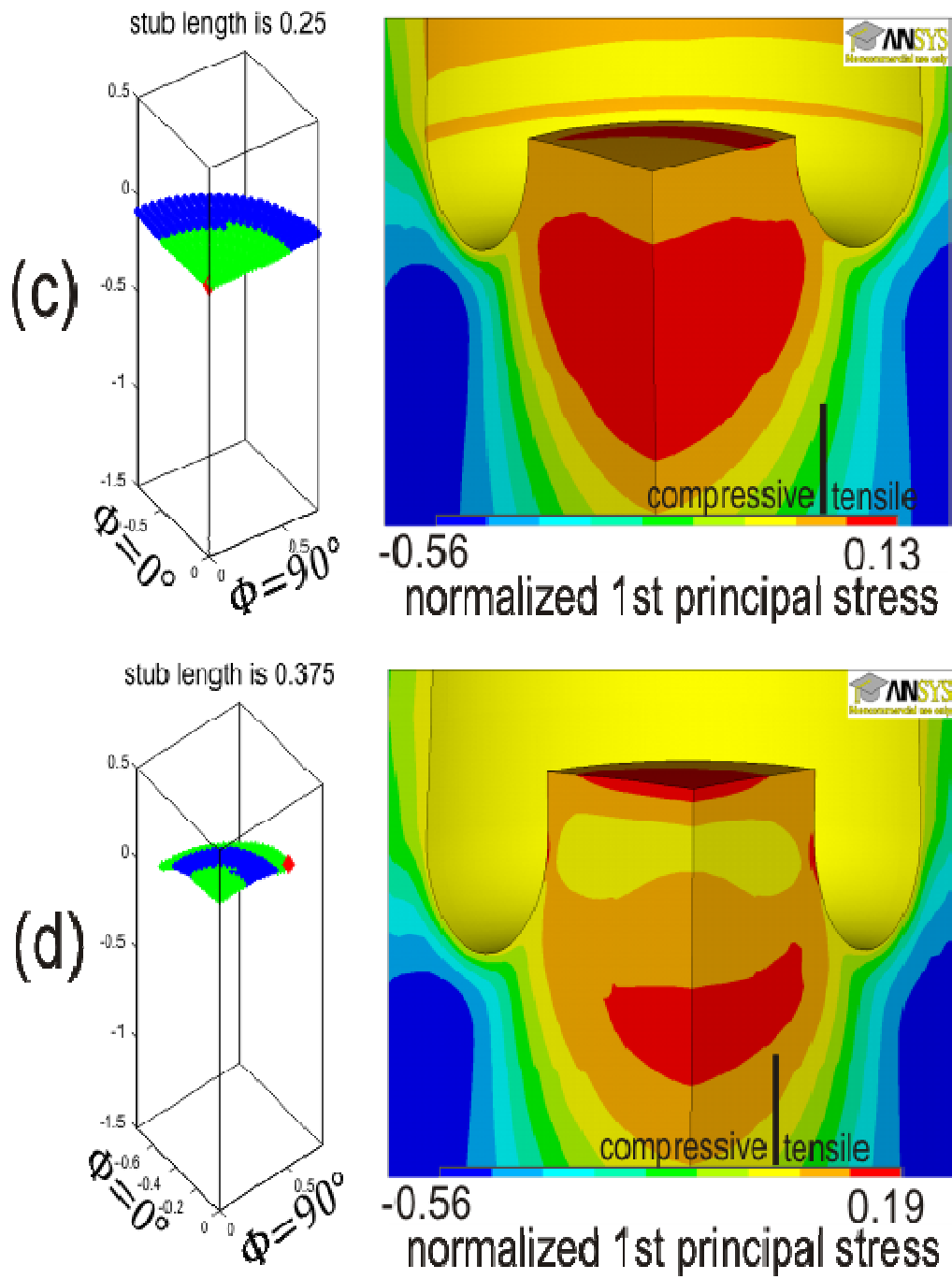
Figure 4.19 continued: (c) Stub length is 0.25d. (d) Stub length is 0.375d.
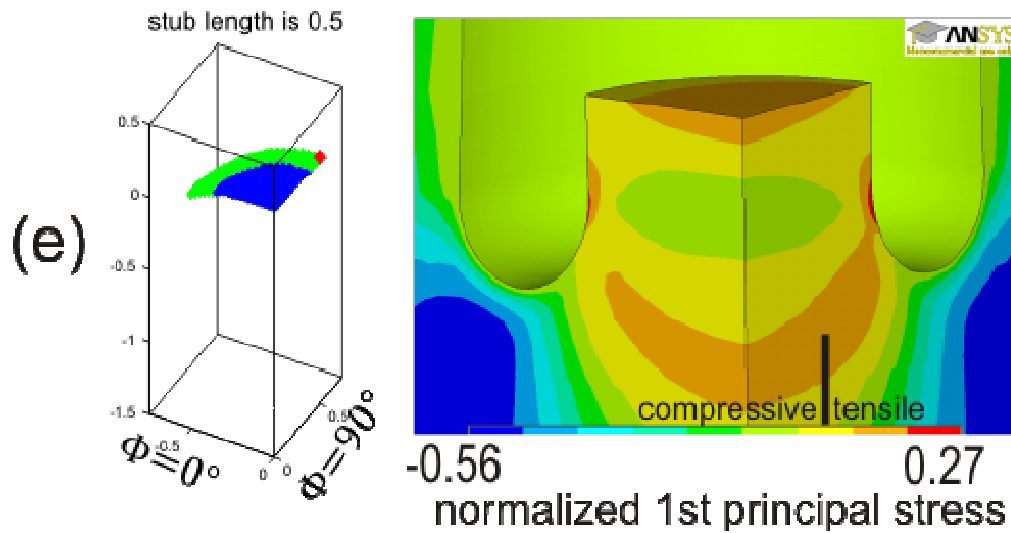
Figure 4.19 continued: (e) Stub length is 0.5d.

4.4.6 Summary of the effect of stub length

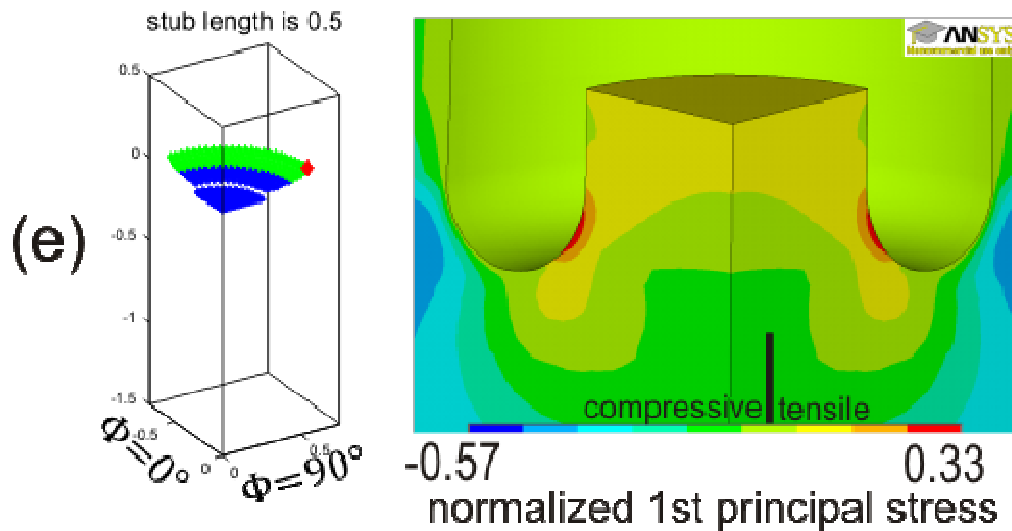In general, for the in situ stress cases examined, it appears that for stub lengths of 0.25d or greater, the predicted fractures are similar, in terms of their morphology and initiation point. The only exception to this is the thrust faulting stress regime in which the model with a stub length of 0.25d was a disk fracture that initiated at the core centre, whereas the models with a longer stub length were saddle-shaped fractures that initiated at the inner kerf. In all cases, an increase in stub length produced an increase in maximum tensile stress, and thus a higher likelihood of fracture development. The maximum tensile stress for a stub length of 0.5d and Poisson's ratio of 0.25 is shown in Figure 4.20 for a variety of crustal stress conditions. The plots for the normal fault and strike slip fault regimes are similar to those generated with a stub length of 0.25d (Figure 4.8), but with slightly larger maximum tensile stress values for the longer stub length. For the thrust fault regime (Figure 4.20c), the longer stub length produces much larger stresses in the

kerf region, and therefore a longer stub may be required for tensile fractures to develop in this stress regime.

Models with no core stub (length of 0d) exhibit anomalous behaviour. For these cases, either flat disk fractures in the borehole bottom or vertical fractures are predicted; note that the vertical fractures are not properly traced by the current modeling approach. However, for most of these models, the maximum tensile stress is quite small and the fractures propagate through the compressive zone, and therefore it may not be possible to produce fractures in real rocks if there is no core stub. As the borehole drilling proceeds and the core stub grows, the maximum tensile stresses in the stub should increase, leading to the development of fractures. As shown in the models, once the stub length is 0.25d or greater, the orientation of stresses within the core does not change significantly. This conclusion is consistent with the results of *Li and Schmitt* [1997] who found that for stub lengths greater than 0.2d, there is little change in the fracture morphology.

4.5 Summary

The set of models described above provides a systematic evaluation of the development of fractures within borehole cores during drilling. It was found that the crustal in-situ state of stress is the dominant control on fracture morphology; variations in Poisson's ratio and core stub length are a second order effect. The relationship between crustal stress and fracture morphology is clearly demonstrated in Figure 4.7. The next chapter provides further discussion of these
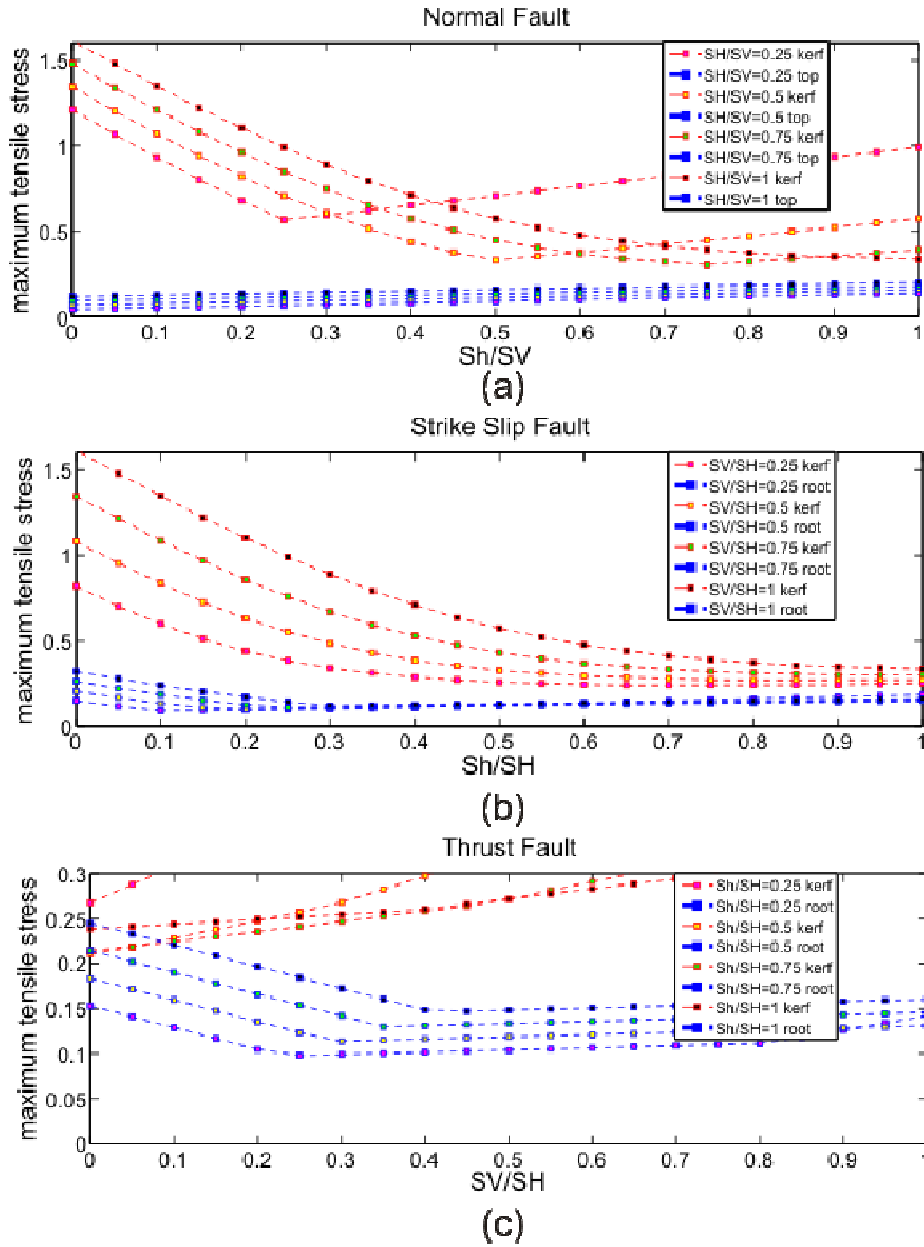
Figure 4.20: Variations in the magnitude of global maximum tensile stress in different stress regime with a Poisson's ratio of 0.25 and stub length of 0.5d. (a) Normal fault regime. (b) Strike slip fault regime. (c) Thrust fault regime.

results, along with suggestions for future work.

4.6 References

Li, Y. Y., and D. R. Schmitt (1997a), Effects of Poisson's ratio and core stub length on bottomhole stress concentrations, *International Journal of Rock Mechanics and Mining Sciences*, *34*, 761-773.

Li, Y. Y., and D. R. Schmitt (1997b), Well-bore bottom stress concentration and induced core fractures, *Aapg Bulletin-American Association of Petroleum Geologists*, *81*, 1909-1925.

Li, Y. Y., and D. R. Schmitt (1998), Drilling-induced core fractures and in situ stress, *Journal of Geophysical Research-Solid Earth*, *103*, 5225-5239.

Maury, V., F. J. Santarelli, and J. P. Henry (1988), Core Discing: A review, paper presented at *Sangorm Syposium: Rock Mechanics in Africa*, International Society of Rock Mechanics: South African National Group on Rock Mechanics, Royal Swazi Spa, Swaziland, November 3-4, 1988.

Chapter 5

Discussions and Conclusions

5.1 Assessment of the 3D models

The main objective of this thesis research was to develop a 3D numerical modelling approach for calculating the trajectory of tensile fractures in borehole cores. The first step was to model the stress distribution in the vicinity of the bottom of the borehole, in which the in situ (far field) crustal stress, borehole and core stub geometry, and elastic parameters of the rock (specifically Young's modulus and Poisson's ratio) are assigned. This was accomplished with the use of the finite element software package ANSYS$^{\text{TM}}$. A variety of finite element mesh configurations and element types were tested in order to find a model set-up in which the stress was computed accurately. One outcome of this thesis research is the documentation of the 110 test (Section 3.4.2), in which the stress orientation at a symmetry boundary is used to determine the validity of the model results. This test can be applied to any model that has a symmetry boundary condition.

The stress models demonstrate that regions of tensional stress exist in the vicinity of the borehole bottom, even when the in situ stress is entirely compressive as illustrated by Figure 3.8. Such stresses may lead to damage and failure of the core stub material. A Matlab$^{\text{TM}}$ program was developed to model the 3D trajectory of

189

fractures in the borehole core, under the assumption that the fractures occur through tensile failure in a rock with no intrinsic strength. The point of global maximum tensile stress was used as the fracture initiation point, and the fracture plane was assumed to propagate in the direction perpendicular to the least compressive stress direction. A numerical modelling approach using nodes distributed on a "forest" of vertical straws was developed to calculate the 3D fracture trajectory through the borehole core.

This is the first study to calculate 3D fracturing of a core stub. The tensile failure criteria used in this thesis is identical to that of *Li and Schmitt* [1997; 1998]. In their work, *Li and Schmitt* also used ANSYS^{TM} to compute the 3D stress field, but the fracture calculations were only carried out in 2D along the two symmetry planes of the 3D volume, i.e. the $\Phi=0°$ plane and $\Phi=90°$ plane. It is important to compare the 3D fracture results of this study to the 2D fractures of *Li and Schmitt* [1998]. Figure 5.1 illustrates the predicted fracture trajectories for the 2D and 3D cases for several different states of in situ stress. All models use a core stub length of 0.25d (where d is the diameter of the core) and a Poisson's ratio of 0.25. The left column is the previous 2D result, and right column is the 3D result. After comparison, we can see that a 3D disc shape is generated for stress condition SV:SH:Sh=1:0.5:0.5 and that intersection line with the symmetry plane is same as the 2D result. The 3D petal centreline shape is generated under SV:SH:Sh=1:0.5:0.25, and the intersection line with $\Phi=90°$ plane is same as 2D result. The fracture trajectory is tangential to the $\Phi=0°$ plane, so there is no intersection line with this plane. A 3D petal shape is generated under SV:SH:Sh=1:0.5:0. The intersection line with the $\Phi=90°$ plane is the same as the 2D result. The fracture does not intersect with the $\Phi=0°$ plane.
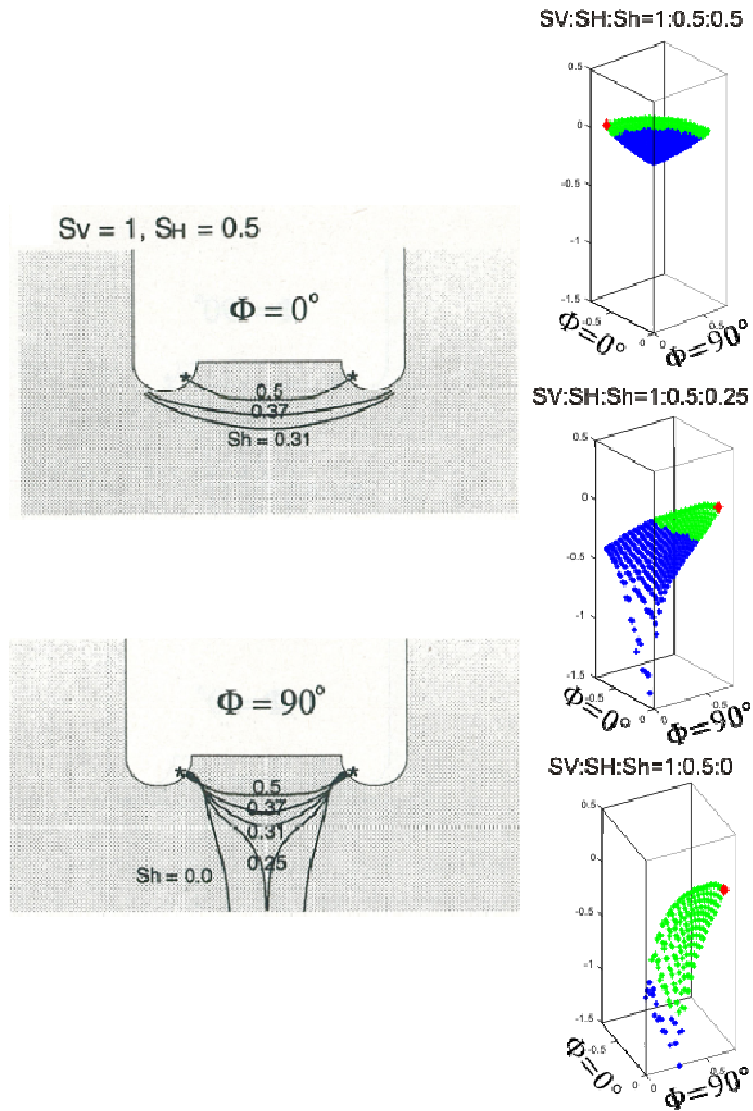
Figure 5.1: Comparison between 2D and 3D tensile fracture models when the stub length is 0.25d and Poisson's ratio is 0.25. The 2D results (left column) are from Li and Schmitt [1998] (courtesy of the American Geophysical Union, according to their reasonable use policy). Note that both plots use SV:SH=1:0.5. The value of Sh is given in next to the fractures (black lines) on the $\Phi=0°$ and 90° planes. The entire width of the borehole is shown, by plotting the fracture in one quadrant and its mirror image. The 3D results (right column) are from this study, with SV:SH:Sh values given above each plot. Only one quadrant of the borehole is plotted.

191

Overall, when tensile fractures in the 3D models start on the either $\Phi=0°$ or $\Phi=90°$ plane, the fracture trajectory along the plane is nearly identical to the 2D fractures calculated by *Li and Schmitt* [1998]. The fracture geometry along this plane is usually the primary indicator of the overall fracture shape (e.g., whether it is a disk, saddle, petal or petal centre-line), and therefore the distribution of fracture shapes for various states of in situ stress obtained by *Li and Schmitt* [1998] is similar to that obtained in this study (e.g., Figure 4.7). However, the major benefit of using the full 3D fracture models is that the unique 3D fracture shape may be obtained. This is especially important for saddle-shaped, petal or petal center-line fractures, as these can exhibit complex 3D geometries (e.g., Figure 4.4 and 4.5). This may be important for assessing actual fractures observed in cores. Given that the computational expense of computing the full 3D fracture is not significantly greater than a 2D calculation, it is recommended that the 3D fracture model be used for future analysis of the origin of borehole fractures.

5.2 Controls on Drilling-induced Core Fractures

Using the stress modelling procedure described in Chapter 3, a database was constructed of the stress field around the vicinity of a borehole for the three 'base' solutions (V, H, and h). These base solutions can be combined using the principle of superposition to obtain any in-situ crustal stress state. The database includes base solutions for five different core stub lengths (0, 0.125d, 0.25d, 0.375d, 0.5d, where d is the diameter of the core), and five different Poisson's ratio values (0.05, 0.15, 0.25, 0.35, 0.45).

The database was used to construct models for a variety of in-situ stress conditions, stub lengths and Poisson's ratio to explore their effects on the generation of fractures within the core. In agreement with earlier 2D studies [e.g., *Li and Schmitt*, 1998], it was found that fracture morphology is primarily determined by the in-situ stress field. Figure 4.7 summarizes the relationship between in situ crustal stress and fracture morphology, and Figure 4.8 shows the variation in maximum tensile stress for different in situ stress conditions (using a core stub length of 0.25 times the core diameter and a Poisson's ratio of 0.25). The following conclusions can be drawn:

1. In the normal fault stress regime (SV>SH>Sh), when Sh is small or SV is large, petal and petal-centreline fractures are predicted. For low Sh, the maximum tensile stress values have a comparable magnitude to SV at the kerf, and thus this is where fractures should initiate. With an increasing Sh, the maximum tensile stress at the kerf decreases, and the fracture shape changes to a saddle. As the horizontal stresses become more isotropic, cup fractures (low SV) and disk fractures (high SV) are found, and fractures may initiate at either the kerf or in the centre of the core.

2. In the strike-slip fault regime (SH>SV>Sh), saddle fractures are predicted for most stress conditions, except where Sh is much less than SV. In this case, petal-centreline fractures occur. At low values of Sh, the maximum tensile stresses have a similar magnitude to SH, and fractures are predicted to initiate at the kerf. With increasing Sh the fracture initiation point may occur in the centre of the core, and the maximum tensile stress decreases, suggesting that it may be more difficult to initiate fractures.

3. In the thrust fault regime (SH>Sh>SV), saddles are found when Sh is relatively small, and flat disks occur at larger Sh. For most conditions, the maximum tensile stress is less than 25% of SH, and therefore it may be difficult to initiate fractures in this stress regime. The largest values of tensile stress are found when SH is 2-4 times larger than Sh, and therefore this condition has the highest likelihood fracturing the core, producing a saddle fracture.

Variations in Poisson's ratio and core stub length have only a minor effect on fracture morphology. For most cases, neither the fracture shape nor location of fracture initiation changed significantly over the range of Poisson's ratio values used in this study. However, it was observed that the magnitude of maximum tensile stress increases with increasing Poisson's ratio, and thus fractures are more likely to develop in rocks with a high Poisson's ratio.

The models also show that when the core stub length is 0.25d or greater, there is little change in the fracture initiation point or fracture geometry, but with increasing stub length, the magnitude of maximum tensile stress increases. For stub lengths less than 0.25d, there is more variability in the stress distribution and the magnitude of tensile stress is quite small. The models in this study are static models, but they provide insight into the instantaneous stress state in the core during drilling. The models suggest that fractures may only occur for longer cores, once the maximum tensile stress exceeds the rock strength; i.e., it is unlikely to get a fracture during the initial stages of drilling. Once the core has reached a length of 0.25d, there will be no significant change in the stress distribution, and thus the fracture geometry is not expected to change with further drilling.

The model results may provide information about why fractures appear to be evenly spaced in the core stub (e.g., Figure 1.1). As the core stub initially grows, the tensile stresses will increase, until they exceed the rock strength and fracturing occurs. Fracture propagation through the core will reduce stresses in the core stub, effectively "resetting" the stresses in core stub below the fracture. With continued drilling, then stresses within this lower stub will increase until a fracture is generated. This process will repeat as the borehole is drilled, yielding a core with a series of evenly spaced fractures of the same morphology. In this proposed model, the fracture spacing reflects the length of core needed to result in tensile stresses that exceed rock strength, under the in-situ crustal stress conditions.

5.3 Limitations of models and future work

In the numerical models in this study, a number of simplifying assumptions were invoked. It is important to recognize how these assumptions may affect the conclusions of this study and how the models may be improved in the future. First, the rocks in the models are considered to isotropic, linearly elastic materials. Clearly, real rocks can be heterogeneous and may be anisotropic. In addition, there may be regions of weakness within a rock volume, such as previously damaged areas or the presence of weak minerals (e.g., clays or quartz), and fractures may exploit these areas.

The stress modelling here has neglected some important aspects of the drilling process. Future work will need to calculate the influence of wellbore fluid pressure as a boundary condition and then look how the stress distributions will change when the borehole is not aligned with a principal stress. *Li* [1997] already

started this but more needs to be done. Second order effects can then be examined beginning with rock anisotropy, inclusion of pore fluid pressure, and poro-elastic effects.

Further, it was assumed that the fractures occur through tensile failure, and the fractures propagate in the direction perpendicular to the local least compressive stress. In all cases considered here, fractures started in a region of tensile stress, but most fractures then entered an area of compression. It is unlikely that an actual fracture would occur where there is compression. It should also be noted that real rocks will have an inherent tensile strength, such that they will not undergo fracturing unless the local stress exceeds their strength. No failure criterion was used in this study, but this could easily be implemented in future work. Such criteria could also be used to stop the fractures. Furthermore, future work should consider other criteria of fracturing in the rock. For example, regions of high shear stress may lead to shear failure within the core, which maybe important when the borehole is not vertical but has some angle relative to horizontal plane. Therefore shear stress may be much stronger than normal stress in some particular directions, which may cause shear failure of rock.

There are several aspects of the fracture modelling algorithm that could be improved in future work. In this study, the fracture propagation modelling is carried out through the use of a vertical straws distributed through the core. The fracture propagates laterally outward from the point of initiation through the straws. As it intersects adjacent straws, the stress state of the nearest node of that straw is used as the stress state of cutting point, and the collection of cutting points on the straws is used to define the fracture surface. Owing to the close

vertical spacing of nodes on the straws (as defined in the original finite element mesh used for the stress calculations), this approach is believed to yield reasonable results. More accurate results may be achieved if the actual intersection point on the straw was used and the stress field at this point was interpolated from the nearest nodes. However, interpolation is computationally expensive, and it is unclear if this would lead to significantly better results; this should be explored in future work.

The use of vertical straws in the fracture calculations means that fractures with a near horizontal trajectory can be traced through the model domain. In many of the cases examined, the stress field is such that the least compressive stress direction was nearly vertical, and therefore the vertical straws worked well. However, this approach cannot be used to trace fractures that propagate vertically. This was observed in Figure 4.16(a), 4.17(a), and 4.18(b), where the cutting plane caused by least compressive stress is nearly vertical, and therefore no cutting point is defined adjacent to the point of fracture initiation. This is a fundamental limitation of the modelling approach employed here and should be addressed in future studies. One way to solve this problem would be to introduce horizontal straws which could be cut by a vertically propagating fracture. Such a set-up may be required to understand the conditions under which core-edge fractures may occur (see Figure 1.2 for illustration). This is the only type of fracture not produced in the current set of numerical models.

This thesis has primarily focused on tensile fractures within the core stub that initiate at the point of global maximum tensile stress. As shown in Chapter 4, there are other regions of the core that are under tensile stress. For example, in

Figure 4.5(a), the point of maximum tensile stress is located at inner kerf, which is where the modelled fracture is assumed to originate. However, significant tensile stresses are also observed in core top, and therefore secondary fractures could be produced here. Thus, in some cases, there may be several different fractures within the core stub.

Furthermore, tensile stresses are also observed in the wall of the borehole in several of the models (e.g., Figure 4.6(e) and (f)). This suggests that fractures could be produced within the borehole wall during drilling. Future work should examine the conditions under which these may occur and whether they exhibit distinct morphologies that reflect the in-situ stress state. It is expensive to extract intact core from a borehole, so many boreholes are drilled by crushing up and extracting the rock. In this case, scans of the borehole wall may reveal fracture patterns that can be linked to the in-situ stress as discussed in Chapter 2. It will be important for future researchers to examine the link between the drilling induced core fractures and drilling induced wall fractures. As indicated by *Kulander et al.*, [1990], it is likely based on observation of the petal-centreline fracture surface that they must extend beyond the borehole.

In summary, this research demonstrates the existence of regions of tensional stress at the base of the borehole and confirms the results of previous modeling studies that the distinct fracture morphologies observed in borehole cores are consistent with tensile failure. This is the first study to compute 3D fracture geometries using the simplified tensile stress criterion. It was observed that fracture morphologies are primarily dependent on the far field crustal stress, suggesting that the fractures can be used as an indicator of the in situ crustal stress field in the

vicinity of a borehole. However, further work is needed to assess the validity of the model results. In particular, laboratory studies of rock deformation are needed to confirm the development of fractures in actual rock samples. Note some work has been done to date (Figure 2.14).

It would also be useful to compare the inferred crustal stress from core fracture morphologies with independent constraints on in situ stress (e.g., from borehole breakout studies). This is actually the ultimate goal of this research because having better information on the state of stress will require that we obtain as much data from various methods as possible. As such, it would be highly useful to add drilling induced core fractures to the already well developed tools of borehole breakouts and drilling induced fractures and hydraulic fracture techniques.

5.4 References

Li, Y. Y., and Schmitt, D. R. (1997a), Effects of Poisson's ratio and core stub length on bottomhole stress concentrations, *International Journal of Rock Mechanics and Mining Sciences*, *34*, 761-773.

Li, Y. Y., and Schmitt, D. R. (1997b), Well-bore bottom stress concentration and induced core fractures, *Aapg Bulletin-American Association of Petroleum Geologists*, *81*, 1909-1925.

Li, Y. Y., and Schmitt, D. R. (1998), Drilling-induced core fractures and in situ stress, *Journal of Geophysical Research-Solid Earth*, *103*, 5225-5239.

APPENDICES

Appendix 1: Description of the database of base solutions for stress field

A1.1 Introduction to database

Five different model geometries were generated to account for the five difference stub lengths (see Figure 3.3). The two Microsoft Excel™ files data11.xls and data12.xls contain all the nodal coordinate numbers in model 1 which corresponds to the case when the stub length is zero. In each Excel™ file there are four columns: column 1 corresponds to node number, column 2 to x coordinate, column 3 to y, column 4 to z. Two files were used, as there were too many nodes for one file. Following the same format, we have data21.xls, data22.xls, data31.xls, data32.xls, data41.xls, data42.xls, data51.xls, data52.xls for the remaining four models (see Table A1.1).

The modeled stress field for the base solutions (V, H, h) is also saved in Excel™ files. The file name follows the standard format $data\alpha\beta3b\gamma\Omega\varsigma.xls$, where:

- α represents stub length in the file name, $\alpha=1$ is the file for when the stub length is 0, $\alpha=2$ is when the stub length is 0.005, $\alpha=3$ is when the stub length is 0.01, $\alpha=4$ is when the stub length is 0.015, and $\alpha=5$ is when the stub length is 0.02.

- β represents Poisson's ratio in the file name, $\beta=1$ is when Poisson's ratio is 0.05, $\beta=2$ is when Poisson's ratio is 0.15, $\beta=3$ is when Poisson's ratio is 0.25, $\beta=4$ is when Poisson's ratio is 0.35, $\beta=5$ is when Poisson's ratio is 0.45.

- $b\gamma$ represents the boundary pressure in the file name, bH means maximum horizontal boundary pressure, bh means minimum horizontal boundary pressure, bv means overburden boundary pressure. Ω is for distinguishing the horizontal stress, when Ω is "max", it means the stress field is SV=0, SH=1, Sh=0. When Ω is min, it means the stress is SV=0, SH=0, Sh=1. If Ω is ignored, then it means the stress field is SV=1, SH=0, Sh=0.

- finally ς represents the file number, $\varsigma=1$ means file number 1, $\varsigma=2$ means file number 2. This is because the amount of data does not fit in one Excel™ file.

Overall, this yields 25 combinations for different stub lengths and different Poisson's ratios for a given stress base solution. As there are three base solutions (V, H, h), each with 2 Excel™ files, we can see there are 25*3*2=150 files for loading stress data. Within each Excel™ file, there are seven columns: the first column is node number, the second column is Sxx, the third column is Syy, the forth column is Szz, the fifth column is Sxy, the sixth column is Syz, and the seventh column is Sxz. Note that S is the 3D stress tensor.

Therefore, we have a total of 10 Excel™ files for coordinate number, and 150 Excel™ files for stress data, and thus there are 160 Excel™ files exist in the data base. They are ready for invoked

by the main program for calculating fracture trajectories. The following Table A1.1 lists all these files.

A1.2 List of coordinate number files and stress data files

Table A1.1: Base solution and coordinate file name

Table A1.1 (a): Base solution and coordinate file storage when Poisson's ratio is 0.05

File Type	Coordinate #	SV	SH	Sh
Poisson's Ratio	0.05			
Stub Length				
0.000	data11.xls, data12.xls	data113bV1.xls,data113bV2.xls	data113bHmax1.xls,data113bHmax2.xls	data113bhmin1.xls, data113bhmin2.xls
0.005	data21.xls, data22.xls	data213bV1.xls,data213bV2.xls	data213bHmax1.xls,data213bHmax2.xls	data213bhmin1.xls, data213bhmin2.xls
0.010	data31.xls, data32.xls	data313bV1.xls,data313bV2.xls	data313bHmax1.xls,data313bHmax2.xls	data313bhmin1.xls, data313bhmin2.xls
0.015	data41.xls, data42.xls	data413bV1.xls,data413bV2.xls	data413bHmax1.xls,data413bHmax2.xls	data413bhmin1.xls, data413bhmin2.xls
0.020	data51.xls, data52.xls	data513bV1.xls,data513bV2.xls	data513bHmax1.xls,data513bHmax2.xls	data513bhmin1.xls, data513bhmin2.xls

Table A1.1 (b): Base solution and coordinate file storage when Poisson's ratio is 0.15

File Type	Coordinate #	SV	SH	Sh
Poisson's Ratio	0.15			

Stub Length				
0.000	data11.xls, data12.xls	data123bV1.xls, data123bV2.xls	data123bHmax1.xls, data123bHmax2.xls	data123bhmin1.xls, data213bhmin2.xls
0.005	data21.xls, data22.xls	data223bV1.xls, data223bV2.xls	data223bHmax1.xls, data223bHmax2.xls	data223bhmin1.xls, data223bhmin2.xls
0.010	data31.xls, data32.xls	data323bV1.xls, data323bV2.xls	data323bHmax1.xls, data323bHmax2.xls	data323bhmin1.xls, data323bhmin2.xls
0.015	data41.xls, data42.xls	data423bV1.xls, data423bV2.xls	data423bHmax1.xls, data423bHmax2.xls	data423bhmin1.xls, data423bhmin2.xls
0.020	data51.xls, data52.xls	data523bV1.xls, data523bV2.xls	data523bHmax1.xls, data523bHmax2.xls	data523bhmin1.xls, data523bhmin2.xls

Table A1.1 (c): Base solution and coordinate file storage when Poisson's ratio is 0.25

File Type	Coordinate #	SV	SH	Sh
Poisson's Ratio	0.25			
Stub Length				
0.000	data11.xls, data12.xls	data133bV1.xls, data133bV2.xls	data133bHmax1.xls, data133bHmax2.xls	data133bhmin1.xls, data133bhmin2.xls
0.005	data21.xls, data22.xls	data233bV1.xls, data233bV2.xls	data233bHmax1.xls, data233bHmax2.xls	data233bhmin1.xls, data233bhmin2.xls
0.010	data31.xls, data32.xls	data333bV1.xls, data333bV2.xls	data333bHmax1.xls, data333bHmax2.xls	data333bhmin1.xls, data333bhmin2.xls
0.015	data41.xls, data42.xls	data433bV1.xls, data433bV2.xls	data433bHmax1.xls, data433bHmax2.xls	data433bhmin1.xls, data433bhmin2.xls
0.020	data51.xls, data52.xls	data533bV1.xls, data533bV2.xls	data533bHmax1.xls, data533bHmax2.xls	data533bhmin1.xls, data533bhmin2.xls

Table A1.1 (d): Base solution and coordinate file storage when Poisson's ratio is 0.35

File Type	Coordinate #	SV	SH	Sh
Poisson's Ratio	0.35			
Stub Length				
0.000	data11.xls, data12.xls	data143bV1.xls, data143bV2.xls	data143bHmax1.xls, data143bHmax2.xls	data143bhmin1.xls, data143bhmin2.xls
0.005	data21.xls, data22.xls	data243bV1.xls, data243bV2.xls	data243bHmax1.xls, data243bHmax2.xls	data243bhmin1.xls, data243bhmin2.xls
0.010	data31.xls, data32.xls	data343bV1.xls, data343bV2.xls	data343bHmax1.xls, data343bHmax2.xls	data343bhmin1.xls, data343bhmin2.xls
0.015	data41.xls, data42.xls	data443bV1.xls, data443bV2.xls	data443bHmax1.xls, data443bHmax2.xls	data443bhmin1.xls, data443bhmin2.xls
0.020	data51.xls, data52.xls	data543bV1.xls, data543bV2.xls	data543bHmax1.xls, data543bHmax2.xls	data543bhmin1.xls, data543bhmin2.xls

Table A1.1 (e): Base solution and coordinate file storage when Poisson's ratio is 0.45

File Type	Coordinate #	SV	SH	Sh
Poisson's Ratio	0.45			
Stub Length				
0.000	data11.xls, data12.xls	data153bV1.xls, data153bV2.xls	data153bHmax1.xls, data153bHmax2.xls	data153bhmin1.xls, data153bhmin2.xls
0.005	data21.xls, data22.xls	data253bV1.xls, data253bV2.xls	data253bHmax1.xls, data253bHmax2.xls	data253bhmin1.xls, data253bhmin2.xls

0.010	data31.xls, data32.xls	data353bV1.xls, data353bV2.xls	data353bHmax1.xls, data353bHmax2.xls	data353bhmin1.xls, data353bhmin2.xls
0.015	data41.xls, data42.xls	data453bV1.xls, data453bV2.xls	data453bHmax1.xls, data453bHmax2.xls	data453bhmin1.xls, data453bhmin2.xls
0.020	data51.xls, data52.xls	data553bV1.xls, data553bV2.xls	data553bHmax1.xls, data553bHmax2.xls	data553bhmin1.xls, data553bhmin2.xls

APPENDIX 2: Description of MATLAB^{TM} codes

A2.1 Organization of MATLAB^{TM} codes

There are four parts in the MATLAB^{TM} program package that I wrote for this thesis: data files, main program, output functions, and single functions. Data files are those Excel^{TM} files exported from ANSYS^{TM}, which include coordinates files and stress data files (see appendix1). The main program is what takes the data files and where the user input the desired parameters for computing the stress field (through superposition of the base solutions), generating fractures and plotting the results. Output functions are used to carry out the output options that are chosen by the user when running the main program. Single functions are used to realize some single function and can be invoked by the other programs to make the program neat, clean, and easy to understand. All programs are listed in Table A2.1.

For the purpose of generating 3D fractures, the MATLAB^{TM} code main.m carries out the superposition and tracks the growth of a tensile fracture. The program object11.m is invoked by main.m, automatically carries out the calculations to plot the fracture surface in 3D, using the appropriate user inputs (for example, stub length, Poisson's ratio, in situ stress state). There are also different output options that include carrying out Kirsch test, statistics checking for the 110 test, and plotting fractures on the outside surface of core.

A2.2 Introduction to interface

The program main.masks the user to input parameters for the desired model and output. First the user must give the stub length (by choosing from five options) and then Poisson's ratio (also choose from five options). After the input, the user needs to wait about 20 seconds while the codes read the Excel^{TM} files which match the stub length and Poisson's ratio that are just inputted.

The next input parameters are: smallest x, biggest x, smallest y, biggest y, smallest z, biggest z. These define the area of the model that the user is interested in. The program will then only take the data within this interested area rather than all the data in the model. This allows the program to run faster and to make the output plots more focused on that particular area. For the purpose of fracture tracing in the borehole core stub, it is recommended to set the parameters as: smallest x is -0.03, the biggest x is 0, the smallest y is 0, the biggest y is 0.03, the smallest z is -0.06, the biggest z is 0.02. Most of the fractures generated in this thesis are based on these parameters.

After specifying the area of interest, it is necessary to input the boundary pressures (SV, SH, Sh – i.e., the in situ stress). The Pascal unit is used here, so 20 MPa would be input as 2e7. Logically speaking, maximum horizontal stress (SH) should be bigger than the minimum horizontal stress (Sh). However, the program is sufficiently flexible that it will still work if the value of Sh is bigger than SH. However, when interpreting the output plots, the user should remember that in this case SH is actually the minimum horizontal stress, while Sh is the maximum horizontal stress.

The program then asks for the value of the Young's modulus. Young's modulus won't have influence on stress distribution in our model, so this parameter will not affect the results. However, the recommended value is 1 GPa, which should be input as 1e10.

The next input parameter is the format for displaying the results. There are currently thirteen options for this, and the user chooses one by giving the option number. For certain options, the program will continue to ask more questions related to that option. The first 9 options are only for the purpose of representing the stress distribution from different point of view (i.e., they do not provide any information about fractures). Options 10 to 13 display information related to the fracture modelling and the Kirsch test used to check the accuracy of the modelled stress field (see Chapter 3):

- Option 10 plots the distribution of vertical straws in the model and the initial point of fracture, straw head is shown with a blue dot, and initial fracture point is a red dot. In the case of equal horizontal in situ stresses, there are not only one initial point, but an initial line instead. However, in this case, only one initial point on the symmetry plane is plotted. In the fracture tracing algorithm, this point is used to initiate the fracture. This does not introduce any errors into the fracture calculations, as the model is symmetric so initiating the fracture at any point on the line would yield the same fracture surface.

- Option 11 is the most important in this research, as it produces a plot of the fracture 3D result.

- Option 12 plots the hoop stress around the borehole versus angle at different distances from the bottom of the borehole (i.e., the Kirsch test used in Chapter 3). It should be noted that when the chosen distance is close to borehole bottom, the hoop stress versus will not agree with the Kirsch analytic solution, owing to perturbations associated with the geometry of the borehole.

- Option 13 gives a plot of the fracture on the core outer surface. It is plotted on a 2D plane with a horizontal axis that corresponds to the angle around the borehole. This plot can provide insight into how a fracture may appear on the outer surface of a core.

A2.3 Function description

Table A2.2: Brief description of source codes function

Function Name	Function Description
main.m	Main Program
object1.m	2D one principal stress projection plot
object3.m	2D one dominate stress projection plot
object5.m	2D two principal stress projection plot
object6.m	2D two dominate stress projection plot
object7.m	3D principal three stress plot
object8.m	3D principal one stress plot
object9.m	3D dominate one stress plot
object10.m	Straw distribution plot
object11.m	3D fracture plot
object12.m	Kirsch test
object13.m	Core surface fracture

APPENDIX 3: MATLAB^{TM} codes developed

Main.m

```
clear all;
close all;
clc;
sx=input(['what is your stub length ? \n',...
    'option#1  0\noption#2  0.005\noption#3  0.01\noption#4  0.015\n',...
    'option#5  0.02\ninput your choice :    ']);
y=input(['what is your poisson ration ?\noption#1  0.05\noption#2  0.15\n',...
    'option#3  0.25\noption#4  0.35\noption#5  0.45\ninput your choice :   ']);
sxy=sx*10+y;
zuobiao1tot=xlsread(['data' num2str(sx) '1.xls']);
zuobiao2tot=xlsread(['data' num2str(sx) '2.xls']);
stressV1tot=xlsread(['data' num2str(sxy) '3bV1.xls']);
stressV2tot=xlsread(['data' num2str(sxy) '3bV2.xls']);
stressH1tot=xlsread(['data' num2str(sxy) '3bHmax1.xls']);
stressH2tot=xlsread(['data' num2str(sxy) '3bHmax2.xls']);
```

```matlab
stressh1tot=xlsread(['data' num2str(sxy) '3bhmin1.xls']);
stressh2tot=xlsread(['data' num2str(sxy) '3bhmin2.xls']);
[zuobiaoS,stressV,stressH,stressh,x1,x2,y1,y2,z1,z2]=...
    f10(zuobiao1tot,zuobiao2tot,stressV1tot,stressV2tot,stressH1tot...
    ,stressH2tot,stressh1tot,stressh2tot);%sort data by x-y-z range

SV=input('tell me your SV (Pa) ?   ');
SV=SV/2e7;
SH=input('tell me your SH ? (Pa)   ');
SH=SH/2e7;
Sh=input('tell me your Sh ?  (Pa)  ');
Sh=Sh/2e7;
E=input('tell me your E ?  (Pa)  ');
E=E/1e10;
[zuobiao,stress]=f0(zuobiaoS,stressV,stressH,stressh,...
    SV,SH,Sh,E);%superposition

output=input(['what is your option for output ?\noption#1:    ',...
    '2D one principal stress projection plot\noption#2:    ',...
    '\2D fracture plot due to one principal stress\noption#3:    ',...
    '2D one dominate stress projection plot\noption#4:    2D fracture plot due to '...
    'one dominate stress',...
    '\noption#5:    2D two pricipal stress projection plot\noption#6:    2D ',...
    'two dominate stress projection plot\noption#7:    3D principal three stress plot\noption#8:    ',...
    '3D principal one stress plot\noption#9:    3D dominate one stress plot',...
    '\noption#10:   straw distribution plot\noption#11:   ',...
    '3D fracture plot\noption#12:  KIRSCH\noption#13:   core surface fracture',...
    '\noption#14:   regime\nyour choice is  ?  ']);
if output==1
    object1(zuobiao,stress,x1,x2,y1,y2,z1,z2);
elseif output==2
    object2;
elseif output==3
    object3(zuobiao,stress,x1,x2,y1,y2,z1,z2);
elseif output==4
    object4;
elseif output==5
    object5(zuobiao,stress,x1,x2,y1,y2,z1,z2);
elseif output==6
    object6(zuobiao,stress,x1,x2,y1,y2,z1,z2);
elseif output==7
    object7(zuobiao,stress,x1,x2,y1,y2,z1,z2);
elseif output==8
    object8(zuobiao,stress,x1,x2,y1,y2,z1,z2);
elseif output==9
    object9(zuobiao,stress,x1,x2,y1,y2,z1,z2);
elseif output==10
    object10(zuobiao,stress,x1,x2,y1,y2,z1,z2,sx);
elseif output==11
    object11(zuobiao,stress,x1,x2,y1,y2,z1,z2,sx);
```

```matlab
elseif output==12
    object12(zuobiao,stress,x1,x2,y1,y2,z1,z2);
elseif output==13
    object13(zuobiao,stress,x1,x2,y1,y2,z1,z2,sx);
elseif output==14
    object14;
else
    disp('SORRY, WRONG NUMBER');
end

object1.m
function object1(zuobiao,stress,x1,x2,y1,y2,z1,z2)

cylin=f1(zuobiao);%cartesian change to cylindrical coordinate

[cylinp,phi]=f4(cylin);%to get plane data with phi angle

carte(:,1)=cylinp(:,1);
[carte(:,2),carte(:,3),carte(:,4)]=pol2cart(cylinp(:,3),cylinp(:,2),cylinp(:,4));%cylindrical change to
cartesian coordinate

a=size(carte);
b=a(1,1);
for i=1:b
    r(i,1)=find(carte(i,1)==stress(:,1));
end
stress1=stress(r,:);%form the data matrix we need

tensor=f2(stress1);

ev=f3(tensor);

proj=f7(ev,phi);%to get projection value and vector

f11(carte,proj,x1,x2,y1,y2,z1,z2)%plot 2D one principal stress projection bar

object3.m
 function object3(zuobiao,stress,x1,x2,y1,y2,z1,z2)

cylin=f1(zuobiao);%cartesian change to cylindrical coordinate

[cylinp,phi]=f4(cylin);%to get plane data with phi angle

carte(:,1)=cylinp(:,1);
[carte(:,2),carte(:,3),carte(:,4)]=pol2cart(cylinp(:,3),cylinp(:,2),cylinp(:,4));%cylindrical change to
cartesian coordinate

a=size(carte);
b=a(1,1);
for i=1:b
```

```
   r(i,1)=find(carte(i,1)==stress(:,1));
end
stress1=stress(r,:);%form the data matrix we need

tensor=f2(stress1);

ev=f3(tensor);

ev1=f12(ev);

proj=f7(ev1,phi);%to get projection value and vector

f13(carte,proj,x1,x2,y1,y2,z1,z2)%plot 2D one dominate stress projection bar


object5.m

function object5(zuobiao,stress,x1,x2,y1,y2,z1,z2)

cylin=f1(zuobiao);%cartesian change to cylindrical coordinate

[cylinp,phi]=f4(cylin);%to get plane data with phi angle

carte(:,1)=cylinp(:,1);
[carte(:,2),carte(:,3),carte(:,4)]=pol2cart(cylinp(:,3),cylinp(:,2),cylinp(:,4));%cylindrical change to
cartesian coordinate

a=size(carte);
b=a(1,1);
for i=1:b
   r(i,1)=find(carte(i,1)==stress(:,1));
end
stress1=stress(r,:);%form the data matrix we need

tensor=f2(stress1);

ev=f3(tensor);

proj=f7(ev,phi);%to get projection value and vector

f14(carte,proj,x1,x2,y1,y2,z1,z2)%plot 2D two principal stress projection bar


object6.m
function object6(zuobiao,stress,x1,x2,y1,y2,z1,z2)

cylin=f1(zuobiao);%cartesian change to cylindrical coordinate

[cylinp,phi]=f4(cylin);%to get plane data with phi angle
```

```
carte(:,1)=cylinp(:,1);
[carte(:,2),carte(:,3),carte(:,4)]=pol2cart(cylinp(:,3),cylinp(:,2),cylinp(:,4));%cylindrical change to
cartesian coordinate

a=size(carte);
b=a(1,1);
for i=1:b
   r(i,1)=find(carte(i,1)==stress(:,1));
end
stress1=stress(r,:);%form the data matrix we need

tensor=f2(stress1);

ev=f3(tensor);

ev1=f12(ev);

proj=f7(ev1,phi);%to get projection value and vector

f15(carte,proj,x1,x2,y1,y2,z1,z2)%plot 2D two dominate stress projection bar

object7.m
function object7(zuobiao,stress,x1,x2,y1,y2,z1,z2)

tensor=f2(stress);

ev=f3(tensor);

a=size(zuobiao);
b=a(1,1);
s=[0.1,0.5,1,5,10];
scale=input(['what is the scale you want ? \noption#1  very small\noption#2',...
  ' small\noption#3  medium\noption#4  big\noption#5  very big\nyour choice is  ?  ']);
scale=s(scale)*1e-9;
axis([x1,x2,y1,y2,z1,z2]);
axis equal;
box on;
hold on;
for i=1:b
  if ev(i,2)>0
  plot3([zuobiao(i,2)-scale*ev(i,2)*ev(i,3)/2,zuobiao(i,2)+scale*ev(i,2)*ev(i,3)/2],...
     [zuobiao(i,3)-scale*ev(i,2)*ev(i,4)/2,zuobiao(i,3)+scale*ev(i,2)*ev(i,4)/2],...
     [zuobiao(i,4)-scale*ev(i,2)*ev(i,5)/2,zuobiao(i,4)+scale*ev(i,2)*ev(i,5)/2],...
     'color','r','linewidth',2);
  else
    plot3([zuobiao(i,2)-scale*ev(i,2)*ev(i,3)/2,zuobiao(i,2)+scale*ev(i,2)*ev(i,3)/2],...
     [zuobiao(i,3)-scale*ev(i,2)*ev(i,4)/2,zuobiao(i,3)+scale*ev(i,2)*ev(i,4)/2],...
     [zuobiao(i,4)-scale*ev(i,2)*ev(i,5)/2,zuobiao(i,4)+scale*ev(i,2)*ev(i,5)/2],...
     'color','g','linewidth',2);
  end
```

```matlab
hold on;
if ev(i,6)>0
plot3([zuobiao(i,2)-scale*ev(i,6)*ev(i,7)/2,zuobiao(i,2)+scale*ev(i,6)*ev(i,7)/2],...
    [zuobiao(i,3)-scale*ev(i,6)*ev(i,8)/2,zuobiao(i,3)+scale*ev(i,6)*ev(i,8)/2],...
    [zuobiao(i,4)-scale*ev(i,6)*ev(i,9)/2,zuobiao(i,4)+scale*ev(i,6)*ev(i,9)/2],...
    'color','b','linewidth',2);
else
  plot3([zuobiao(i,2)-scale*ev(i,6)*ev(i,7)/2,zuobiao(i,2)+scale*ev(i,6)*ev(i,7)/2],...
    [zuobiao(i,3)-scale*ev(i,6)*ev(i,8)/2,zuobiao(i,3)+scale*ev(i,6)*ev(i,8)/2],...
    [zuobiao(i,4)-scale*ev(i,6)*ev(i,9)/2,zuobiao(i,4)+scale*ev(i,6)*ev(i,9)/2],...
    'color','y','linewidth',2);
end
hold on;
if ev(i,10)>0
plot3([zuobiao(i,2)-scale*ev(i,10)*ev(i,11)/2,zuobiao(i,2)+scale*ev(i,10)*ev(i,11)/2],...
    [zuobiao(i,3)-scale*ev(i,10)*ev(i,12)/2,zuobiao(i,3)+scale*ev(i,10)*ev(i,12)/2],...
    [zuobiao(i,4)-scale*ev(i,10)*ev(i,13)/2,zuobiao(i,4)+scale*ev(i,10)*ev(i,13)/2],...
    'color','c','linewidth',2);
else
  plot3([zuobiao(i,2)-scale*ev(i,10)*ev(i,11)/2,zuobiao(i,2)+scale*ev(i,10)*ev(i,11)/2],...
    [zuobiao(i,3)-scale*ev(i,10)*ev(i,12)/2,zuobiao(i,3)+scale*ev(i,10)*ev(i,12)/2],...
    [zuobiao(i,4)-scale*ev(i,10)*ev(i,13)/2,zuobiao(i,4)+scale*ev(i,10)*ev(i,13)/2],...
    'color','k','linewidth',2);
end
hold on;
end

hold off;
object8.m
function object8(zuobiao,stress,x1,x2,y1,y2,z1,z2)

tensor=f2(stress);

ev=f3(tensor);

a=size(zuobiao);
b=a(1,1);
w=input('which principal stress you want to plot ?  ');
if w==1
   n=2;
else if w==2
     n=6;
   else
     n=10;
   end
end
s=[0.1,0.5,1,5,10];
scale=input(['what is the scale you want ? \noption#1  very small\noption#2',...
  ' small\noption#3  medium\noption#4  big\noption#5  very big\nyour choice is  ?  ']);
scale=s(scale)*1e-9;
```

```matlab
axis([x1,x2,y1,y2,z1,z2]);
axis equal;
box on;
hold on;
for i=1:b
   if ev(i,n)>0
   plot3([zuobiao(i,2)-scale*ev(i,n)*ev(i,n+1)/2,zuobiao(i,2)+scale*ev(i,n)*ev(i,n+1)/2],...
      [zuobiao(i,3)-scale*ev(i,n)*ev(i,n+2)/2,zuobiao(i,3)+scale*ev(i,n)*ev(i,n+2)/2],...
      [zuobiao(i,4)-scale*ev(i,n)*ev(i,n+3)/2,zuobiao(i,4)+scale*ev(i,n)*ev(i,n+3)/2],...
      'color','r','linewidth',2);
   else
     plot3([zuobiao(i,2)-scale*ev(i,n)*ev(i,n+1)/2,zuobiao(i,2)+scale*ev(i,n)*ev(i,n+1)/2],...
      [zuobiao(i,3)-scale*ev(i,n)*ev(i,n+2)/2,zuobiao(i,3)+scale*ev(i,n)*ev(i,n+2)/2],...
      [zuobiao(i,4)-scale*ev(i,n)*ev(i,n+3)/2,zuobiao(i,4)+scale*ev(i,n)*ev(i,n+3)/2],...
      'color','g','linewidth',2);
   end
   hold on;
end

hold off;

object9.m

function object9(zuobiao,stress,x1,x2,y1,y2,z1,z2)

tensor=f2(stress);

ev=f3(tensor);

ev1=f12(ev);

a=size(zuobiao);
b=a(1,1);
w=input(['which dominate stress you want to plot ? \n',...
   'option#1: biggest\noption#2: medium\noption#3: smallest\nyour choice is ?  ']);
if w==1
   n=2;
else if w==2
     n=6;
   else
     n=10;
   end
end
s=[0.1,0.5,1,5,10];
scale=input(['what is the scale you want ? \noption#1  very small\noption#2',...
   ' small\noption#3  medium\noption#4  big\noption#5  very big\nyour choice is  ?  ']);
scale=s(scale)*1e-9;
axis([x1,x2,y1,y2,z1,z2]);
axis equal;
box on;
```

```matlab
hold on;
for i=1:b
   if ev1(i,n)>0
   plot3([zuobiao(i,2)-scale*ev1(i,n)*ev1(i,n+1)/2,zuobiao(i,2)+scale*ev1(i,n)*ev1(i,n+1)/2],...
      [zuobiao(i,3)-scale*ev1(i,n)*ev1(i,n+2)/2,zuobiao(i,3)+scale*ev1(i,n)*ev1(i,n+2)/2],...
      [zuobiao(i,4)-scale*ev1(i,n)*ev1(i,n+3)/2,zuobiao(i,4)+scale*ev1(i,n)*ev1(i,n+3)/2],...
      'color','r','linewidth',2);
   else
      plot3([zuobiao(i,2)-scale*ev1(i,n)*ev1(i,n+1)/2,zuobiao(i,2)+scale*ev1(i,n)*ev1(i,n+1)/2],...
      [zuobiao(i,3)-scale*ev1(i,n)*ev1(i,n+2)/2,zuobiao(i,3)+scale*ev1(i,n)*ev1(i,n+2)/2],...
      [zuobiao(i,4)-scale*ev1(i,n)*ev1(i,n+3)/2,zuobiao(i,4)+scale*ev1(i,n)*ev1(i,n+3)/2],...
      'color','g','linewidth',2);
   end
   hold on;
end

hold off;

object10.m
function object10(zuobiao,stress,x1,x2,y1,y2,z1,z2,sx)

[original,ideal,mark]=f6(zuobiao,stress,sx);

if mark==1
   lr=ideal(1,2);
   [straw,separate]=f5(lr,sx);
   [x,y,z]=pol2cart(straw(:,2),straw(:,1),straw(:,3));%cylindrical change to cartesian coordinate
   axis([x1,x2,y1,y2,z1,z2]);
   hold on;
   axis equal;
   hold on;
   box on;
   plot3(0,lr,ideal(1,4),'or','markerfacecolor','r');
   hold on;
   plot3(x,y,z,'d');
   hold off;
end

if mark==2
   lr=ideal(1,2);
   [straw,separate]=f21(lr,sx);
   [x,y,z]=pol2cart(straw(:,2),straw(:,1),straw(:,3));%cylindrical change to cartesian coordinate
   axis([x1,x2,y1,y2,z1,z2]);
   hold on;
   axis equal;
   hold on;
   box on;
   plot3(0,lr,ideal(1,4),'or','markerfacecolor','r');
   hold on;
   plot3(x,y,z,'d');
```

```matlab
   hold off;
end

if mark==3
   lr=ideal(1,2);
   [straw,separate]=f8(lr,sx);
   [x,y,z]=pol2cart(straw(:,2),straw(:,1),straw(:,3));%cylindrical change to cartesian coordinate
   axis([x1,x2,y1,y2,z1,z2]);
   hold on;
   axis equal;
   hold on;
   box on;
   plot3(-lr,0,ideal(1,4),'or','markerfacecolor','r');
   hold on;
   plot3(x,y,z,'d');
   hold off;
end

if mark==4
   lr=ideal(1,2);
   [straw,separate]=f22(lr,sx);
   [x,y,z]=pol2cart(straw(:,2),straw(:,1),straw(:,3));%cylindrical change to cartesian coordinate
   axis([x1,x2,y1,y2,z1,z2]);
   hold on;
   axis equal;
   hold on;
   box on;
   plot3(-lr,0,ideal(1,4),'or','markerfacecolor','r');
   hold on;
   plot3(x,y,z,'d');
   hold off;
end

if mark==5
   [straw,separate]=f16(sx);
   [x,y,z]=pol2cart(straw(:,2),straw(:,1),straw(:,3));%cylindrical change to cartesian coordinate
   axis([x1,x2,y1,y2,z1,z2]);
   hold on;
   axis equal;
   hold on;
   box on;
   plot3(0,0,ideal(1,4),'or','markerfacecolor','r');
   hold on;
   plot3(x,y,z,'d');
   hold off;
end

if mark==6
   [original,ideal,jiaodu]=f24(zuobiao,stress);
   if jiaodu==1
```

```matlab
        [straw,separate]=f5(ideal(1,2),sx);
    else
        [straw,separate]=f8(ideal(1,2),sx);
    end
    [a,b,c]=pol2cart(ideal(1,3),ideal(1,2),ideal(1,4));
    [x,y,z]=pol2cart(straw(:,2),straw(:,1),straw(:,3));%cylindrical change to cartesian coordinate
    axis([x1,x2,y1,y2,z1,z2]);
    hold on;
    axis equal;
    hold on;
    box on;
    plot3(a,b,c,'or','markerfacecolor','r');
    hold on;
    plot3(x,y,z,'d');
    hold off;
end

object11.m
function object11(zuobiao,stress,x1,x2,y1,y2,z1,z2,sx)

[original,ideal,mark]=f6(zuobiao,stress,sx);
[a,b,c]=pol2cart(original(1,3),original(1,2),original(1,4));
originalc=[original(1,1),a,b,c,original(1,5:8)];
[a,b,c]=pol2cart(ideal(1,3),ideal(1,2),ideal(1,4));
idealc=[ideal(1,1),a,b,c,ideal(1,5:8)];
d=0.04;%this is radius of borehole used for normalization

if mark==1
    lr=ideal(1,2);
    [straw,separate]=f5(lr,sx);
    [x,y,z]=pol2cart(straw(:,2),straw(:,1),straw(:,3));%cylindrical change to cartesian coordinate
    strawc=[x,y,z];

    tensor=f2(stress);
    ev=f3(tensor);
    ev1=f12(ev);

    n=size(separate);
    n=n(1,1);

    cp1=originalc(1,2:8);
    cp=originalc(1,2:8);
    for i=1:n
        if i==1
            st=[strawc(1,:),strawc(1,3)-z1];
            cp2=f17(zuobiao,ev1,cp1,st);
            judge=f19(cp2,strawc(1,3),z1);
        else
            st=[strawc(sum(separate(1:i-1,1))+1,:),strawc(sum(separate(1:i-1,1))+1,3)-z1];
            cp2=f17(zuobiao,ev1,cp1,st);
```

215

```matlab
                judge=f19(cp2,strawc(sum(separate(1:i-1,1))+1,3),z1);
            end

            if judge==4
                cp1=cp2;
                cp=[cp;cp2];
            else
                break;
            end

            for j=2:separate(i,1)
                if i==1
                    st=[strawc(j,:),strawc(j,3)-z1];
                    cp2=f17(zuobiao,ev1,cp2,st);
                    judge=f19(cp2,strawc(j,3),z1);
                else
                    st=[strawc(sum(separate(1:i-1,1))+j,:),strawc(sum(separate(1:i-1,1))+j,3)-z1];
                    cp2=f17(zuobiao,ev1,cp2,st);
                    judge=f19(cp2,strawc(sum(separate(1:i-1,1))+j,3),z1);
                end

                if judge==4
                    cp=[cp;cp2];
                else
                    break;
                end
            end
        end
        f20(cp,x1,x2,y1,y2,z1,z2);
        plot3(0/d,lr/d,ideal(1,4)/d,'dr','markersize',11,'markerfacecolor','r');
        hold off;
end

if mark==2
    lr=ideal(1,2);
    [straw,separate]=f21(lr,sx);
    [x,y,z]=pol2cart(straw(:,2),straw(:,1),straw(:,3));%cylindrical change to cartesian coordinate
    strawc=[x,y,z];

    tensor=f2(stress);
    ev=f3(tensor);
    ev1=f12(ev);

    n=size(separate);
    n=n(1,1);

    cp1=originalc(1,2:8);
    cp=originalc(1,2:8);
    for i=1:n
        if i==1
```

```matlab
            st=[strawc(1,:),strawc(1,3)-z1];
            cp2=f17(zuobiao,ev1,cp1,st);
            judge=f19(cp2,strawc(1,3),z1);
        else
            st=[strawc(sum(separate(1:i-1,1))+1,:),strawc(sum(separate(1:i-1,1))+1,3)-z1];
            cp2=f17(zuobiao,ev1,cp1,st);
            judge=f19(cp2,strawc(sum(separate(1:i-1,1))+1,3),z1);
        end

        if judge==4
            cp1=cp2;
            cp=[cp;cp2];
        else
            break;
        end

        for j=2:separate(i,1)
            if i==1
                st=[strawc(j,:),strawc(j,3)-z1];
                cp2=f17(zuobiao,ev1,cp2,st);
                judge=f19(cp2,strawc(j,3),z1);
            else
                st=[strawc(sum(separate(1:i-1,1))+j,:),strawc(sum(separate(1:i-1,1))+j,3)-z1];
                cp2=f17(zuobiao,ev1,cp2,st);
                judge=f19(cp2,strawc(sum(separate(1:i-1,1))+j,3),z1);
            end

            if judge==4
                cp=[cp;cp2];
            else
                break;
            end
        end
    end
    f20(cp,x1,x2,y1,y2,z1,z2);
    plot3(0/d,lr/d,ideal(1,4)/d,'dr','markersize',11,'markerfacecolor','r');
    hold off;
end

if mark==3
    lr=ideal(1,2);
    [straw,separate]=f8(lr,sx);
    [x,y,z]=pol2cart(straw(:,2),straw(:,1),straw(:,3));%cylindrical change to cartesian coordinate
    strawc=[x,y,z];

    tensor=f2(stress);
    ev=f3(tensor);
    ev1=f12(ev);

    n=size(separate);
```

```matlab
    n=n(1,1);

    cp1=originalc(1,2:8);
    cp=originalc(1,2:8);
    for i=1:n
        if i==1
            st=[strawc(1,:),strawc(1,3)-z1];
            cp2=f17(zuobiao,ev1,cp1,st);
            judge=f19(cp2,strawc(1,3),z1);
        else
            st=[strawc(sum(separate(1:i-1,1))+1,:),strawc(sum(separate(1:i-1,1))+1,3)-z1];
            cp2=f17(zuobiao,ev1,cp1,st);
            judge=f19(cp2,strawc(sum(separate(1:i-1,1))+1,3),z1);
        end

        if judge==4
            cp1=cp2;
            cp=[cp;cp2];
        else
            break;
        end

        for j=2:separate(i,1)
            if i==1
                st=[strawc(j,:),strawc(j,3)-z1];
                cp2=f17(zuobiao,ev1,cp2,st);
                judge=f19(cp2,strawc(j,3),z1);
            else
                st=[strawc(sum(separate(1:i-1,1))+j,:),strawc(sum(separate(1:i-1,1))+j,3)-z1];
                cp2=f17(zuobiao,ev1,cp2,st);
                judge=f19(cp2,strawc(sum(separate(1:i-1,1))+j,3),z1);
            end

            if judge==4
                cp=[cp;cp2];
            else
                break;
            end
        end
    end
    f20(cp,x1,x2,y1,y2,z1,z2);
    plot3(-lr/d,0/d,ideal(1,4)/d,'dr','markersize',11,'markerfacecolor','r');
    hold off;
end

if mark==4
    lr=ideal(1,2);
    [straw,separate]=f22(lr,sx);
    [x,y,z]=pol2cart(straw(:,2),straw(:,1),straw(:,3));%cylindrical change to cartesian coordinate
    strawc=[x,y,z];
```

218

```matlab
tensor=f2(stress);
ev=f3(tensor);
ev1=f12(ev);

n=size(separate);
n=n(1,1);

cp1=originalc(1,2:8);
cp=originalc(1,2:8);
for i=1:n
    if i==1
        st=[strawc(1,:),strawc(1,3)-z1];
        cp2=f17(zuobiao,ev1,cp1,st);
        judge=f19(cp2,strawc(1,3),z1);
    else
        st=[strawc(sum(separate(1:i-1,1))+1,:),strawc(sum(separate(1:i-1,1))+1,3)-z1];
        cp2=f17(zuobiao,ev1,cp1,st);
        judge=f19(cp2,strawc(sum(separate(1:i-1,1))+1,3),z1);
    end

    if judge==4
        cp1=cp2;
        cp=[cp;cp2];
    else
        break;
    end

    for j=2:separate(i,1)
        if i==1
            st=[strawc(j,:),strawc(j,3)-z1];
            cp2=f17(zuobiao,ev1,cp2,st);
            judge=f19(cp2,strawc(j,3),z1);
        else
            st=[strawc(sum(separate(1:i-1,1))+j,:),strawc(sum(separate(1:i-1,1))+j,3)-z1];
            cp2=f17(zuobiao,ev1,cp2,st);
            judge=f19(cp2,strawc(sum(separate(1:i-1,1))+j,3),z1);
        end

        if judge==4
            cp=[cp;cp2];
        else
            break;
        end
    end
end
f20(cp,x1,x2,y1,y2,z1,z2);
plot3(-lr/d,0/d,ideal(1,4)/d,'dr','markersize',11,'markerfacecolor','r');
hold off;
end
```

```matlab
if mark==5
    [straw,separate]=f16(sx);
    [x,y,z]=pol2cart(straw(:,2),straw(:,1),straw(:,3));%cylindrical change to cartesian coordinate
    strawc=[x,y,z];

    tensor=f2(stress);
    ev=f3(tensor);
    ev1=f12(ev);

    n=size(separate);
    n=n(1,1);

    cp1=originalc(1,2:8);
    cp=originalc(1,2:8);
    for i=1:n
        if i==1
            st=[strawc(1,:),strawc(1,3)-z1];
            cp2=f17(zuobiao,ev1,cp1,st);
            judge=f19(cp2,strawc(1,3),z1);
        else
            st=[strawc(sum(separate(1:i-1,1))+1,:),strawc(sum(separate(1:i-1,1))+1,3)-z1];
            cp2=f17(zuobiao,ev1,cp1,st);
            judge=f19(cp2,strawc(sum(separate(1:i-1,1))+1,3),z1);
        end

        if judge==4
            cp1=cp2;
            cp=[cp;cp2];
        else
            break;
        end

        for j=2:separate(i,1)
            if i==1
                st=[strawc(j,:),strawc(j,3)-z1];
                cp2=f17(zuobiao,ev1,cp2,st);
                judge=f19(cp2,strawc(j,3),z1);
            else
                st=[strawc(sum(separate(1:i-1,1))+j,:),strawc(sum(separate(1:i-1,1))+j,3)-z1];
                cp2=f17(zuobiao,ev1,cp2,st);
                judge=f19(cp2,strawc(sum(separate(1:i-1,1))+j,3),z1);
            end

            if judge==4
                cp=[cp;cp2];
            else
                break;
            end
        end
    end
```

```
        end
    f20(cp,x1,x2,y1,y2,z1,z2);
    plot3(0/d,0/d,ideal(1,4)/d,'dr','markersize',11,'markerfacecolor','r');
    hold off;
end

if mark==6
    [original,ideal,jiaodu]=f24(zuobiao,stress);
    [a,b,c]=pol2cart(original(1,3),original(1,2),original(1,4));
    originalc=[original(1,1),a,b,c,original(1,5:8)];
    [a,b,c]=pol2cart(ideal(1,3),ideal(1,2),ideal(1,4));
    idealc=[ideal(1,1),a,b,c,ideal(1,5:8)];

    if jiaodu==1
        [straw,separate]=f5(ideal(1,2),sx);
    else
        [straw,separate]=f8(ideal(1,2),sx);
    end
    [x,y,z]=pol2cart(straw(:,2),straw(:,1),straw(:,3));%cylindrical change to cartesian coordinate
    strawc=[x,y,z];

    tensor=f2(stress);
    ev=f3(tensor);
    ev1=f12(ev);

    n=size(separate);
    n=n(1,1);

    cp1=originalc(1,2:8);
    cp=originalc(1,2:8);
    for i=1:n
        if i==1
            st=[strawc(1,:),strawc(1,3)-z1];
            cp2=f17(zuobiao,ev1,cp1,st);
            judge=f19(cp2,strawc(1,3),z1);
        else
            st=[strawc(sum(separate(1:i-1,1))+1,:),strawc(sum(separate(1:i-1,1))+1,3)-z1];
            cp2=f17(zuobiao,ev1,cp1,st);
            judge=f19(cp2,strawc(sum(separate(1:i-1,1))+1,3),z1);
        end

        if judge==4
            cp1=cp2;
            cp=[cp;cp2];
        else
            break;
        end

        for j=2:separate(i,1)
            if i==1
```

```
            st=[strawc(j,:),strawc(j,3)-z1];
            cp2=f17(zuobiao,ev1,cp2,st);
            judge=f19(cp2,strawc(j,3),z1);
        else
            st=[strawc(sum(separate(1:i-1,1))+j,:),strawc(sum(separate(1:i-1,1))+j,3)-z1];
            cp2=f17(zuobiao,ev1,cp2,st);
            judge=f19(cp2,strawc(sum(separate(1:i-1,1))+j,3),z1);
        end

        if judge==4
            cp=[cp;cp2];
        else
            break;
        end
      end
   end
   f20(cp,x1,x2,y1,y2,z1,z2);
   plot3(a/d,b/d,c/d,'dr','markersize',11,'markerfacecolor','r');
   hold off;
end


object12.m
function object12(zuobiao,stress,x1,x2,y1,y2,z1,z2)

h=input('what is your z value ?    ');
z=0.05;%need to be adjust by experience
r=0.0008;%need to be adjust by experience
t=1e-3;

cylin=f1(zuobiao);
a=size(cylin);
a=a(1,1);
b=1;
for i=1:a
   if cylin(i,2)<(0.04+r) & cylin(i,2)>(0.04-r) & cylin(i,4)>0
      cylinr(b,:)=cylin(i,:);
      stressr(b,:)=stress(i,:);
      b=b+1;
   end
end

a1=size(cylinr);
a1=a1(1,1);
for j=1:25
   m(j,1)=pi-(j-1)*pi/48;
   b1=1;
   for k=1:a1
     if cylinr(k,3)<(m(j,1)+t) & cylinr(k,3)>(m(j,1)-t) & cylinr(k,4)<(h+z) &cylinr(k,4)>(h-z)
        s(b1,:)=stressr(k,:);
```

```
      tao(b1,1)=stressr(k,2)*(sin(m(j,1))^2)-
2*stressr(k,5)*sin(m(j,1))*cos(m(j,1))+stressr(k,3)*(cos(m(j,1))^2);
      b1=b1+1;
    end
  end
  taothita(j,1)=(max(tao)+min(tao))/2;
end

for l=1:25
  thita(l,1)=pi-m(l,1);
end

plot(thita,taothita,'d');


object13.m

function object13(zuobiao,stress,x1,x2,y1,y2,z1,z2,sx)

[original,ideal,mark]=f6(zuobiao,stress,sx);
[a,b,c]=pol2cart(original(1,3),original(1,2),original(1,4));
originalc=[original(1,1),a,b,c,original(1,5:8)];
[a,b,c]=pol2cart(ideal(1,3),ideal(1,2),ideal(1,4));
idealc=[ideal(1,1),a,b,c,ideal(1,5:8)];

if mark==1
  lr=ideal(1,2);
  [straw,separate]=f5(lr,sx);
  [x,y,z]=pol2cart(straw(:,2),straw(:,1),straw(:,3));%cylindrical change to cartesian coordinate
  strawc=[x,y,z];

  tensor=f2(stress);
  ev=f3(tensor);
  ev1=f12(ev);

  n=size(separate);
  n=n(1,1);

  cp1=originalc(1,2:8);
  cp=originalc(1,2:8);
  for i=1:n
    if i==1
      st=[strawc(1,:),strawc(1,3)-z1];
      cp2=f17(zuobiao,ev1,cp1,st);
      judge=f19(cp2,strawc(1,3),z1);
    else
      st=[strawc(sum(separate(1:i-1,1))+1,:),strawc(sum(separate(1:i-1,1))+1,3)-z1];
      cp2=f17(zuobiao,ev1,cp1,st);
      judge=f19(cp2,strawc(sum(separate(1:i-1,1))+1,3),z1);
    end
```

```matlab
        if judge==4
            cp1=cp2;
            cp=[cp;cp2];
        else
            break;
        end

        for j=2:separate(i,1)
            if i==1
                st=[strawc(j,:),strawc(j,3)-z1];
                cp2=f17(zuobiao,ev1,cp2,st);
                judge=f19(cp2,strawc(j,3),z1);
            else
                st=[strawc(sum(separate(1:i-1,1))+j,:),strawc(sum(separate(1:i-1,1))+j,3)-z1];
                cp2=f17(zuobiao,ev1,cp2,st);
                judge=f19(cp2,strawc(sum(separate(1:i-1,1))+j,3),z1);
            end

            if judge==4
                cp=[cp;cp2];
            else
                break;
            end
        end
    end
    f25(cp,z1,z2);
end

if mark==2
    lr=ideal(1,2);
    [straw,separate]=f21(lr,sx);
    [x,y,z]=pol2cart(straw(:,2),straw(:,1),straw(:,3));%cylindrical change to cartesian coordinate
    strawc=[x,y,z];

    tensor=f2(stress);
    ev=f3(tensor);
    ev1=f12(ev);

    n=size(separate);
    n=n(1,1);

    cp1=originalc(1,2:8);
    cp=originalc(1,2:8);
    for i=1:n
        if i==1
            st=[strawc(1,:),strawc(1,3)-z1];
            cp2=f17(zuobiao,ev1,cp1,st);
            judge=f19(cp2,strawc(1,3),z1);
        else
```

```
            st=[strawc(sum(separate(1:i-1,1))+1,:),strawc(sum(separate(1:i-1,1))+1,3)-z1];
            cp2=f17(zuobiao,ev1,cp1,st);
            judge=f19(cp2,strawc(sum(separate(1:i-1,1))+1,3),z1);
        end

        if judge==4
            cp1=cp2;
            cp=[cp;cp2];
        else
            break;
        end

        for j=2:separate(i,1)
            if i==1
                st=[strawc(j,:),strawc(j,3)-z1];
                cp2=f17(zuobiao,ev1,cp2,st);
                judge=f19(cp2,strawc(j,3),z1);
            else
                st=[strawc(sum(separate(1:i-1,1))+j,:),strawc(sum(separate(1:i-1,1))+j,3)-z1];
                cp2=f17(zuobiao,ev1,cp2,st);
                judge=f19(cp2,strawc(sum(separate(1:i-1,1))+j,3),z1);
            end

            if judge==4
                cp=[cp;cp2];
            else
                break;
            end
        end
    end
    f25(cp,z1,z2);
end

if mark==3
    lr=ideal(1,2);
    [straw,separate]=f8(lr,sx);
    [x,y,z]=pol2cart(straw(:,2),straw(:,1),straw(:,3));%cylindrical change to cartesian coordinate
    strawc=[x,y,z];

    tensor=f2(stress);
    ev=f3(tensor);
    ev1=f12(ev);

    n=size(separate);
    n=n(1,1);

    cp1=originalc(1,2:8);
    cp=originalc(1,2:8);
    for i=1:n
        if i==1
```

```matlab
            st=[strawc(1,:),strawc(1,3)-z1];
            cp2=f17(zuobiao,ev1,cp1,st);
            judge=f19(cp2,strawc(1,3),z1);
        else
            st=[strawc(sum(separate(1:i-1,1))+1,:),strawc(sum(separate(1:i-1,1))+1,3)-z1];
            cp2=f17(zuobiao,ev1,cp1,st);
            judge=f19(cp2,strawc(sum(separate(1:i-1,1))+1,3),z1);
        end

        if judge==4
            cp1=cp2;
            cp=[cp;cp2];
        else
            break;
        end

        for j=2:separate(i,1)
            if i==1
                st=[strawc(j,:),strawc(j,3)-z1];
                cp2=f17(zuobiao,ev1,cp2,st);
                judge=f19(cp2,strawc(j,3),z1);
            else
                st=[strawc(sum(separate(1:i-1,1))+j,:),strawc(sum(separate(1:i-1,1))+j,3)-z1];
                cp2=f17(zuobiao,ev1,cp2,st);
                judge=f19(cp2,strawc(sum(separate(1:i-1,1))+j,3),z1);
            end

            if judge==4
                cp=[cp;cp2];
            else
                break;
            end
        end
    end
    f25(cp,z1,z2);
end

if mark==4
    lr=ideal(1,2);
    [straw,separate]=f22(lr,sx);
    [x,y,z]=pol2cart(straw(:,2),straw(:,1),straw(:,3));%cylindrical change to cartesian coordinate
    strawc=[x,y,z];

    tensor=f2(stress);
    ev=f3(tensor);
    ev1=f12(ev);

    n=size(separate);
    n=n(1,1);
```

```
        cp1=originalc(1,2:8);
        cp=originalc(1,2:8);
        for i=1:n
          if i==1
              st=[strawc(1,:),strawc(1,3)-z1];
              cp2=f17(zuobiao,ev1,cp1,st);
              judge=f19(cp2,strawc(1,3),z1);
          else
              st=[strawc(sum(separate(1:i-1,1))+1,:),strawc(sum(separate(1:i-1,1))+1,3)-z1];
              cp2=f17(zuobiao,ev1,cp1,st);
              judge=f19(cp2,strawc(sum(separate(1:i-1,1))+1,3),z1);
          end

          if judge==4
              cp1=cp2;
              cp=[cp;cp2];
          else
              break;
          end

          for j=2:separate(i,1)
            if i==1
                st=[strawc(j,:),strawc(j,3)-z1];
                cp2=f17(zuobiao,ev1,cp2,st);
                judge=f19(cp2,strawc(j,3),z1);
            else
                st=[strawc(sum(separate(1:i-1,1))+j,:),strawc(sum(separate(1:i-1,1))+j,3)-z1];
                cp2=f17(zuobiao,ev1,cp2,st);
                judge=f19(cp2,strawc(sum(separate(1:i-1,1))+j,3),z1);
            end

            if judge==4
                cp=[cp;cp2];
            else
                break;
            end
          end
        end
      end
      f25(cp,z1,z2);
    end

if mark==5
    [straw,separate]=f16(sx);
    [x,y,z]=pol2cart(straw(:,2),straw(:,1),straw(:,3));%cylindrical change to cartesian coordinate
    strawc=[x,y,z];

    tensor=f2(stress);
    ev=f3(tensor);
    ev1=f12(ev);
```

```
    n=size(separate);
    n=n(1,1);

    cp1=originalc(1,2:8);
    cp=originalc(1,2:8);
    for i=1:n
        if i==1
            st=[strawc(1,:),strawc(1,3)-z1];
            cp2=f17(zuobiao,ev1,cp1,st);
            judge=f19(cp2,strawc(1,3),z1);
        else
            st=[strawc(sum(separate(1:i-1,1))+1,:),strawc(sum(separate(1:i-1,1))+1,3)-z1];
            cp2=f17(zuobiao,ev1,cp1,st);
            judge=f19(cp2,strawc(sum(separate(1:i-1,1))+1,3),z1);
        end

        if judge==4
            cp1=cp2;
            cp=[cp;cp2];
        else
            break;
        end

        for j=2:separate(i,1)
            if i==1
                st=[strawc(j,:),strawc(j,3)-z1];
                cp2=f17(zuobiao,ev1,cp2,st);
                judge=f19(cp2,strawc(j,3),z1);
            else
                st=[strawc(sum(separate(1:i-1,1))+j,:),strawc(sum(separate(1:i-1,1))+j,3)-z1];
                cp2=f17(zuobiao,ev1,cp2,st);
                judge=f19(cp2,strawc(sum(separate(1:i-1,1))+j,3),z1);
            end

            if judge==4
                cp=[cp;cp2];
            else
                break;
            end
        end
    end
    f25(cp,z1,z2);
end

if mark==6
    [original,ideal,jiaodu]=f24(zuobiao,stress);
    [a,b,c]=pol2cart(original(1,3),original(1,2),original(1,4));
    originalc=[original(1,1),a,b,c,original(1,5:8)];
    [a,b,c]=pol2cart(ideal(1,3),ideal(1,2),ideal(1,4));
    idealc=[ideal(1,1),a,b,c,ideal(1,5:8)];
```

```matlab
if jiaodu==1
   [straw,separate]=f5(ideal(1,2),sx);
else
   [straw,separate]=f8(ideal(1,2),sx);
end
[x,y,z]=pol2cart(straw(:,2),straw(:,1),straw(:,3));%cylindrical change to cartesian coordinate
strawc=[x,y,z];

tensor=f2(stress);
ev=f3(tensor);
ev1=f12(ev);

n=size(separate);
n=n(1,1);

cp1=originalc(1,2:8);
cp=originalc(1,2:8);
for i=1:n
   if i==1
      st=[strawc(1,:),strawc(1,3)-z1];
      cp2=f17(zuobiao,ev1,cp1,st);
      judge=f19(cp2,strawc(1,3),z1);
   else
      st=[strawc(sum(separate(1:i-1,1))+1,:),strawc(sum(separate(1:i-1,1))+1,3)-z1];
      cp2=f17(zuobiao,ev1,cp1,st);
      judge=f19(cp2,strawc(sum(separate(1:i-1,1))+1,3),z1);
   end

   if judge==4
      cp1=cp2;
      cp=[cp;cp2];
   else
      break;
   end

   for j=2:separate(i,1)
      if i==1
         st=[strawc(j,:),strawc(j,3)-z1];
         cp2=f17(zuobiao,ev1,cp2,st);
         judge=f19(cp2,strawc(j,3),z1);
      else
         st=[strawc(sum(separate(1:i-1,1))+j,:),strawc(sum(separate(1:i-1,1))+j,3)-z1];
         cp2=f17(zuobiao,ev1,cp2,st);
         judge=f19(cp2,strawc(sum(separate(1:i-1,1))+j,3),z1);
      end

      if judge==4
         cp=[cp;cp2];
      else
```

```
            break;
          end
        end
      end
    end
    f25(cp,z1,z2);
end
```

f0.m

```
function [zuobiao,stress]=f0(zuobiaoS,stressV,stressH,stressh,SV,SH,Sh,E)

zuobiao=zuobiaoS;

sV=(SV/E)*stressV(:,2:7);

sH=(SH/E)*stressH(:,2:7);

sh=(Sh/E)*stressh(:,2:7);

stress=[zuobiao(:,1),(sV+sH+sh)];
```

f1.m

```
function f1out=f1(zuobiao)
[thita,r,z]=cart2pol(zuobiao(:,2),zuobiao(:,3),zuobiao(:,4));
f1out=[zuobiao(:,1),r,thita,z];
```

f2.m

```
function f2out=f2(f2in)
f2out=[f2in(:,1:2),f2in(:,5),f2in(:,7),f2in(:,5),f2in(:,3),f2in(:,6),...
    f2in(:,7),f2in(:,6),f2in(:,4)];
```

f3.m

```
function f3out=f3(f3in)
a=size(f3in);
b=a(1,1);
for i=1:b
    f3out(i,1)=f3in(i,1);
    l=2;
    for j=1:3
        for k=1:3
        ftemp(j,k)=f3in(i,l);
        l=l+1;
        end
    end
    [evec,eval]=eig(ftemp);
```

```
      f3out(i,2)=eval(1,1);
      f3out(i,3)=evec(1,1);
      f3out(i,4)=evec(2,1);
      f3out(i,5)=evec(3,1);
      f3out(i,6)=eval(2,2);
      f3out(i,7)=evec(1,2);
      f3out(i,8)=evec(2,2);
      f3out(i,9)=evec(3,2);
      f3out(i,10)=eval(3,3);
      f3out(i,11)=evec(1,3);
      f3out(i,12)=evec(2,3);
      f3out(i,13)=evec(3,3);
end


f4.m

function [f4out,phi]=f4(f4in)
phi=input('what is the phi angle correspond to plane you want (unit:degree)??   ');
phi=(180-phi)*pi/180;
tolerance=1e-2;
r=find(f4in(:,3)<phi+tolerance & f4in(:,3)>phi-tolerance);
f4out=f4in(r,:);


f5.m

function [straw,separate]=f5(lr,sx)

dr=0.001;%need to adjust later, ANSYS related
ds1=pi/48;%need to adjust later, ANSYS related

n=floor(lr/dr);
yushu=rem(lr,dr);
ls=round(pi/2/ds1+1);
delta=(ls-1)/(n+1);

for i=1:(n+1)
   incycle(i,1)=round(ls-round((i-1)*delta));
   if incycle(i,1)~=1
      dsn(i,1)=pi/2/(incycle(i,1)-1);
   else
      dsn(i,1)=0;
   end
end
incycle(n+2,1)=1;
dsn(n+2,1)=0;

separate=incycle;

if sx==1
```

```
head(1,1)=lr;
head(2,1)=lr-yushu;
for i=1:n-1
   head(i+2,1)=head(2,1)-i*dr;
end
head(n+2,1)=0;
for j=1:n+2
   head(j,2)=pi/2;
   head(j,3)=0;
end
end

if sx==2
head(1,1)=lr;
head(2,1)=lr-yushu;
for i=1:n-1
   head(i+2,1)=head(2,1)-i*dr;
end
head(n+2,1)=0;
for j=1:n+2
   head(j,2)=pi/2;
   if head(j,1)<=0.03 & head(j,1)>=0.021339745%consider different model
      head(j,3)=0.01-sqrt(0.01^2-(head(j,1)-0.03)^2);
   else
      head(j,3)=0.005;
   end
end
end

if sx==3
head(1,1)=lr;
head(2,1)=lr-yushu;
for i=1:n-1
   head(i+2,1)=head(2,1)-i*dr;
end
head(n+2,1)=0;
for j=1:n+2
   head(j,2)=pi/2;
   if head(j,1)<=0.03 & head(j,1)>=0.02%consider different model
      head(j,3)=0.01-sqrt(0.01^2-(head(j,1)-0.03)^2);
   else
      head(j,3)=0.01;
   end
end
end

if sx==4
head(1,1)=lr;
head(2,1)=lr-yushu;
for i=1:n-1
```

```matlab
      head(i+2,1)=head(2,1)-i*dr;
   end
head(n+2,1)=0;
for j=1:n+2
   head(j,2)=pi/2;
   if head(j,1)<=0.03 & head(j,1)>0.02%consider different model
      head(j,3)=0.01-sqrt(0.01^2-(head(j,1)-0.03)^2);
   else
      head(j,3)=0.015;
   end
end
end

if sx==5
head(1,1)=lr;
head(2,1)=lr-yushu;
for i=1:n-1
   head(i+2,1)=head(2,1)-i*dr;
end
head(n+2,1)=0;
for j=1:n+2
   head(j,2)=pi/2;
   if head(j,1)<=0.03 & head(j,1)>0.02%consider different model
      head(j,3)=0.01-sqrt(0.01^2-(head(j,1)-0.03)^2);
   else
      head(j,3)=0.02;
   end
end
end

k=0;
for u=1:n+2
   for v=1:incycle(u,1)
      straw(v+k,1)=head(u,1);
      straw(v+k,2)=head(u,2)+(v-1)*dsn(u,1);
      straw(v+k,3)=head(u,3);
   end
   k=k+incycle(u,1);
end

f6.m

function [original,ideal,mark]=f6(zuobiao,stress,sx)

if sx==1
   dingbian=0;
elseif sx==2
   dingbian=0.005;
elseif sx==3
   dingbian=0.01;
```

```matlab
elseif sx==4
   dingbian=0.015;
else
   dingbian=0.02;
end

cylin=f1(zuobiao);%cartesian change to cylindrical coordinate

a=f9(stress,cylin);%to find initial point information

tollerance=1e-3;%need to adjust by experence

original=a;
ideal=a;
mark=6;

if a(1,2)<=0.03 & a(1,2)>=0.02 & a(1,3)<pi/2+tollerance & a(1,3)>pi/2-tollerance
   original=a;
   ideal=[a(:,1:2),pi/2,a(:,4:8)];
   mark=1;
end

if a(1,4)<=dingbian+tollerance & a(1,4)>=dingbian-tollerance & a(1,3)<pi/2+tollerance &
a(1,3)>pi/2-tollerance
   original=a;
   ideal=[a(:,1:2),pi/2,dingbian,a(:,5:8)];
   mark=2;
end

if a(1,2)<=0.03 & a(1,2)>=0.02 & a(1,3)<pi+tollerance & a(1,3)>pi-tollerance
   original=a;
   ideal=[a(:,1:2),pi,a(:,4:8)];
   mark=3;
end

if a(1,4)<=dingbian+tollerance & a(1,4)>=dingbian-tollerance & a(1,3)<pi+tollerance &
a(1,3)>pi-tollerance
   original=a;
   ideal=[a(:,1:2),pi,dingbian,a(:,5:8)];
   mark=4;
end

if a(1,2)<0.002
   original=a;
   ideal=[a(:,1:1),0,0,a(:,4:8)];
   mark=5;
end

f7.m
function f7out=f7(f7in,phi)
```

```
uv1=[cos(phi),sin(phi),0];
uv2=[0,0,1];

A=f7in(:,3:5)';
a=size(A);
b=a(1,2);
for i=1:b
A1(i,:)=(dot(A(:,i),uv1))'*uv1+(dot(A(:,i),uv2))'*uv2;
end

B=f7in(:,7:9)';
for j=1:b
B1(j,:)=(dot(B(:,j),uv1))'*uv1+(dot(B(:,j),uv2))'*uv2;
end

C=f7in(:,11:13)';
for k=1:b
C1(k,:)=(dot(C(:,k),uv1))'*uv1+(dot(C(:,k),uv2))'*uv2;
end

f7out=[f7in(:,1:2),A1,f7in(:,6),B1,f7in(:,10),C1];


f8.m

function [straw,separate]=f8(lr,sx)

dr=0.001;%need to adjust later, ANSYS related
ds1=pi/48;%need to adjust later, ANSYS related

n=floor(lr/dr);
yushu=rem(lr,dr);
ls=round(pi/2/ds1+1);
delta=(ls-1)/(n+1);

for i=1:(n+1)
   incycle(i,1)=round(ls-round((i-1)*delta));
   if incycle(i,1)~=1
      dsn(i,1)=pi/2/(incycle(i,1)-1);
   else
      dsn(i,1)=0;
   end
end
incycle(n+2,1)=1;
dsn(n+2,1)=0;

separate=incycle;

if sx==1
```

```
head(1,1)=lr;
head(2,1)=lr-yushu;
for i=1:n-1
    head(i+2,1)=head(2,1)-i*dr;
end
head(n+2,1)=0;
for j=1:n+2
    head(j,2)=pi;
    head(j,3)=0;
end
end

if sx==2
head(1,1)=lr;
head(2,1)=lr-yushu;
for i=1:n-1
    head(i+2,1)=head(2,1)-i*dr;
end
head(n+2,1)=0;
for j=1:n+2
    head(j,2)=pi;
    if head(j,1)<=0.03 & head(j,1)>=0.021339745%consider different model
        head(j,3)=0.01-sqrt(0.01^2-(head(j,1)-0.03)^2);
    else
        head(j,3)=0.005;
    end
end
end

if sx==3
head(1,1)=lr;
head(2,1)=lr-yushu;
for i=1:n-1
    head(i+2,1)=head(2,1)-i*dr;
end
head(n+2,1)=0;
for j=1:n+2
    head(j,2)=pi;
    if head(j,1)<=0.03 & head(j,1)>=0.02%consider different model
        head(j,3)=0.01-sqrt(0.01^2-(head(j,1)-0.03)^2);
    else
        head(j,3)=0.01;
    end
end
end

if sx==4
head(1,1)=lr;
head(2,1)=lr-yushu;
for i=1:n-1
```

```matlab
        head(i+2,1)=head(2,1)-i*dr;
    end
    head(n+2,1)=0;
    for j=1:n+2
        head(j,2)=pi;
        if head(j,1)<=0.03 & head(j,1)>0.02%consider different model
            head(j,3)=0.01-sqrt(0.01^2-(head(j,1)-0.03)^2);
        else
            head(j,3)=0.015;
        end
    end
end

if sx==5
head(1,1)=lr;
head(2,1)=lr-yushu;
for i=1:n-1
    head(i+2,1)=head(2,1)-i*dr;
end
head(n+2,1)=0;
for j=1:n+2
    head(j,2)=pi;
    if head(j,1)<=0.03 & head(j,1)>0.02%consider different model
        head(j,3)=0.01-sqrt(0.01^2-(head(j,1)-0.03)^2);
    else
        head(j,3)=0.02;
    end
end
end

k=0;
for u=1:n+2
    for v=1:incycle(u,1)
        straw(v+k,1)=head(u,1);
        straw(v+k,2)=head(u,2)-(v-1)*dsn(u,1);
        straw(v+k,3)=head(u,3);
    end
    k=k+incycle(u,1);
end


f9.m

function f9out=f9(stress,cylin)

tensor=f2(stress);

ev=f3(tensor);

ev1=f12(ev);
```

```
N=max(max(ev1(:,2)));

[r,c]=find(N==ev1);

f9out(1:1,1:4)=cylin(r:r,1:4);

f9out(1:1,5:8)=ev1(r:r,2:5);
```

f10.m

```
function [zuobiaoS,stressV,stressH,stressh,x1,x2,y1,y2,z1,z2]=f10(zuobiao1tot,zuobiao2tot,...
    stressV1tot,stressV2tot,stressH1tot,stressH2tot,stressh1tot,stressh2tot)
zuobiao=[zuobiao1tot;zuobiao2tot];
stressVV=[stressV1tot;stressV2tot];
stressHH=[stressH1tot;stressH2tot];
stresshh=[stressh1tot;stressh2tot];
tollerance=1e-9;
x1=input('what is smallest x ?   ');
x2=input('what is biggest x ?   ');
y1=input('what is smallest y ?   ');
y2=input('what is biggest y ?   ');
z1=input('what is smallest z ?   ');
z2=input('what is biggest z ?   ');
a=size(zuobiao);
b=a(1,1);
r=find(zuobiao(:,2)>x1-tollerance & zuobiao(:,2)<x2+tollerance & ...
    zuobiao(:,3)>y1-tollerance & zuobiao(:,3)<y2+tollerance &...
    zuobiao(:,4)>z1-tollerance & zuobiao(:,4)<z2+tollerance);
zuobiaoS=zuobiao(r,:);
stressV=stressVV(r,:);
stressH=stressHH(r,:);
stressh=stresshh(r,:);
```

f11.m

```
function f11(f11in1,f11in2,x1,x2,y1,y2,z1,z2)

w=input('which one stress projection you want to plot  ? :  ');

if w==1
   n=2;
else if w==2
      n=6;
   else
      n=10;
   end
end
```

```
a=size(f11in1);
b=a(1,1);
s=[0.1,0.5,1,5,10];
scale=input(['what is your scale choice?   \noption#1 : very small\noption#2',...
': small\noption#3 : medium\noption#4 : big\noption#5 : very big\nyour choice=   ? ']);
scale=s(scale)*1e-9;
axis([x1,x2,y1,y2,z1,z2]);
axis equal;
box on;
hold on;
for i=1:b
   if f11in2(i,n)>0
   plot3([f11in1(i,2)-
scale*f11in2(i,n)*f11in2(i,n+1)/2,f11in1(i,2)+scale*f11in2(i,n)*f11in2(i,n+1)/2],...
      [f11in1(i,3)-
scale*f11in2(i,n)*f11in2(i,n+2)/2,f11in1(i,3)+scale*f11in2(i,n)*f11in2(i,n+2)/2],...
      [f11in1(i,4)-
scale*f11in2(i,n)*f11in2(i,n+3)/2,f11in1(i,4)+scale*f11in2(i,n)*f11in2(i,n+3)/2],...
      'color','r','linewidth',2);
   else
      plot3([f11in1(i,2)-
scale*f11in2(i,n)*f11in2(i,n+1)/2,f11in1(i,2)+scale*f11in2(i,n)*f11in2(i,n+1)/2],...
      [f11in1(i,3)-
scale*f11in2(i,n)*f11in2(i,n+2)/2,f11in1(i,3)+scale*f11in2(i,n)*f11in2(i,n+2)/2],...
      [f11in1(i,4)-
scale*f11in2(i,n)*f11in2(i,n+3)/2,f11in1(i,4)+scale*f11in2(i,n)*f11in2(i,n+3)/2],...
      'color','g','linewidth',2);
   end
   hold on;
end

hold off;


f12.m

function f12out=f12(f12in)

a=size(f12in);
b=a(1,1);
f12out(:,1)=f12in(:,1);
for i=1:b
   if f12in(i,2)>f12in(i,6) & f12in(i,2)>f12in(i,10)
      f12out(i:i,2:5)=f12in(i:i,2:5);
   elseif f12in(i,6)>f12in(i,2) & f12in(i,6)>f12in(i,10)
      f12out(i:i,2:5)=f12in(i:i,6:9);
   else
      f12out(i:i,2:5)=f12in(i:i,10:13);
   end
```

```matlab
    if f12in(i,2)>f12in(i,6) & f12in(i,2)<f12in(i,10)
        f12out(i:i,6:9)=f12in(i:i,2:5);
    elseif f12in(i,6)>f12in(i,2) & f12in(i,6)<f12in(i,10)
        f12out(i:i,6:9)=f12in(i:i,6:9);
    else
        f12out(i:i,6:9)=f12in(i:i,10:13);
    end
    if f12in(i,2)<f12in(i,6) & f12in(i,2)<f12in(i,10)
        f12out(i:i,10:13)=f12in(i:i,2:5);
    elseif f12in(i,6)<f12in(i,2) & f12in(i,6)<f12in(i,10)
        f12out(i:i,10:13)=f12in(i:i,6:9);
    else
        f12out(i:i,10:13)=f12in(i:i,10:13);
    end
end


f13.m

function f13(f13in1,f13in2,x1,x2,y1,y2,z1,z2)

w=input(['which dominate stress projection you want to plot  ? :  ',...
    '\noption#1  biggest  \noption#2  medium  \noption#3  smallest\nyour choice is   ? ']);
if w==1
    n=2;
else if w==2
        n=6;
    else
        n=10;
    end
end

a=size(f13in1);
b=a(1,1);
s=[0.1,0.5,1,5,10];
scale=input(['what is your scale choice?   \noption#1 : very small\noption#2',...
': small\noption#3 : medium\noption#4 : big\noption#5 : very big\nyour choice=   ? ']);
scale=s(scale)*1e-9;
axis([x1,x2,y1,y2,z1,z2]);
axis equal;
box on;
hold on;
for i=1:b
    if f13in2(i,n)>0
    plot3([f13in1(i,2)-
scale*f13in2(i,n)*f13in2(i,n+1)/2,f13in1(i,2)+scale*f13in2(i,n)*f13in2(i,n+1)/2],...
        [f13in1(i,3)-
scale*f13in2(i,n)*f13in2(i,n+2)/2,f13in1(i,3)+scale*f13in2(i,n)*f13in2(i,n+2)/2],...
        [f13in1(i,4)-
scale*f13in2(i,n)*f13in2(i,n+3)/2,f13in1(i,4)+scale*f13in2(i,n)*f13in2(i,n+3)/2],...
```

```
        'color','r','linewidth',2);
    else
        plot3([f13in1(i,2)-
scale*f13in2(i,n)*f13in2(i,n+1)/2,f13in1(i,2)+scale*f13in2(i,n)*f13in2(i,n+1)/2],...
        [f13in1(i,3)-
scale*f13in2(i,n)*f13in2(i,n+2)/2,f13in1(i,3)+scale*f13in2(i,n)*f13in2(i,n+2)/2],...
        [f13in1(i,4)-
scale*f13in2(i,n)*f13in2(i,n+3)/2,f13in1(i,4)+scale*f13in2(i,n)*f13in2(i,n+3)/2],...
        'color','g','linewidth',2);
    end
    hold on;
end

hold off;


f14.m

function f14(f14in1,f14in2,x1,x2,y1,y2,z1,z2)

w=input('what is the first one of two principal stress projection you want to plot  ? :  ');

if w==1
    n=2;
else if w==2
        n=6;
    else
        n=10;
    end
end

w1=input('what is the second one of two principal stress projection you want to plot  ? :  ');

if w1==1
    n1=2;
else if w1==2
        n1=6;
    else
        n1=10;
    end
end

a=size(f14in1);
b=a(1,1);
s=[0.1,0.5,1,5,10];
scale=input(['what is your scale choice for first one?   \noption#1 : very small\noption#2',...
': small\noption#3 : medium\noption#4 : big\noption#5 : very big\nyour choice=   ?  ']);
scale=s(scale)*1e-9;
scale1=input(['what is your scale choice for second one?   \noption#1 : very small\noption#2',...
': small\noption#3 : medium\noption#4 : big\noption#5 : very big\nyour choice=   ?  ']);
```

```matlab
scale1=s(scale1)*1e-9;
axis([x1,x2,y1,y2,z1,z2]);
axis equal;
box on;
hold on;
for i=1:b
    if f14in2(i,n)>0
    plot3([f14in1(i,2)-
scale*f14in2(i,n)*f14in2(i,n+1)/2,f14in1(i,2)+scale*f14in2(i,n)*f14in2(i,n+1)/2],...
        [f14in1(i,3)-
scale*f14in2(i,n)*f14in2(i,n+2)/2,f14in1(i,3)+scale*f14in2(i,n)*f14in2(i,n+2)/2],...
        [f14in1(i,4)-
scale*f14in2(i,n)*f14in2(i,n+3)/2,f14in1(i,4)+scale*f14in2(i,n)*f14in2(i,n+3)/2],...
        'color','r','linewidth',2);
    else
        plot3([f14in1(i,2)-
scale*f14in2(i,n)*f14in2(i,n+1)/2,f14in1(i,2)+scale*f14in2(i,n)*f14in2(i,n+1)/2],...
        [f14in1(i,3)-
scale*f14in2(i,n)*f14in2(i,n+2)/2,f14in1(i,3)+scale*f14in2(i,n)*f14in2(i,n+2)/2],...
        [f14in1(i,4)-
scale*f14in2(i,n)*f14in2(i,n+3)/2,f14in1(i,4)+scale*f14in2(i,n)*f14in2(i,n+3)/2],...
        'color','g','linewidth',2);
    end
    hold on;
    if f14in2(i,n1)>0
    plot3([f14in1(i,2)-
scale1*f14in2(i,n1)*f14in2(i,n1+1)/2,f14in1(i,2)+scale1*f14in2(i,n1)*f14in2(i,n1+1)/2],...
        [f14in1(i,3)-
scale1*f14in2(i,n1)*f14in2(i,n1+2)/2,f14in1(i,3)+scale1*f14in2(i,n1)*f14in2(i,n1+2)/2],...
        [f14in1(i,4)-
scale1*f14in2(i,n1)*f14in2(i,n1+3)/2,f14in1(i,4)+scale1*f14in2(i,n1)*f14in2(i,n1+3)/2],...
        'color','b','linewidth',2);
    else
        plot3([f14in1(i,2)-
scale1*f14in2(i,n1)*f14in2(i,n1+1)/2,f14in1(i,2)+scale1*f14in2(i,n1)*f14in2(i,n1+1)/2],...
        [f14in1(i,3)-
scale1*f14in2(i,n1)*f14in2(i,n1+2)/2,f14in1(i,3)+scale1*f14in2(i,n1)*f14in2(i,n1+2)/2],...
        [f14in1(i,4)-
scale1*f14in2(i,n1)*f14in2(i,n1+3)/2,f14in1(i,4)+scale1*f14in2(i,n1)*f14in2(i,n1+3)/2],...
        'color','y','linewidth',2);
    end
    hold on;
end

hold off;


f15.m

function f15(f15in1,f15in2,x1,x2,y1,y2,z1,z2)
```

```matlab
w=input(['what is the first one of  dominate stress projection you want to plot  ? :  ',...
   '\noption#1  biggest  \noption#2  medium  \noption#3  smallest\nyour choice is   ? ']);

if w==1
   n=2;
else if w==2
      n=6;
   else
      n=10;
   end
end

w1=input(['what is the second one of dominate stress projection you want to plot  ? :  ',...
   '\noption#1  biggest  \noption#2  medium  \noption#3  smallest\nyour choice is   ? ']);

if w1==1
   n1=2;
else if w1==2
      n1=6;
   else
      n1=10;
   end
end

a=size(f15in1);
b=a(1,1);
s=[0.1,0.5,1,5,10];
scale=input(['what is your scale choice for first one?   \noption#1 : very small\noption#2',...
': small\noption#3 : medium\noption#4 : big\noption#5 : very big\nyour choice=   ? ']);
scale=s(scale)*1e-9;
scale1=input(['what is your scale choice for second one?   \noption#1 : very small\noption#2',...
': small\noption#3 : medium\noption#4 : big\noption#5 : very big\nyour choice=   ? ']);
scale1=s(scale1)*1e-9;
axis([x1,x2,y1,y2,z1,z2]);
axis equal;
box on;
hold on;
for i=1:b
   if f15in2(i,n)>0
   plot3([f15in1(i,2)-
scale*f15in2(i,n)*f15in2(i,n+1)/2,f15in1(i,2)+scale*f15in2(i,n)*f15in2(i,n+1)/2],...
      [f15in1(i,3)-
scale*f15in2(i,n)*f15in2(i,n+2)/2,f15in1(i,3)+scale*f15in2(i,n)*f15in2(i,n+2)/2],...
      [f15in1(i,4)-
scale*f15in2(i,n)*f15in2(i,n+3)/2,f15in1(i,4)+scale*f15in2(i,n)*f15in2(i,n+3)/2],...
      'color','r','linewidth',2);
   else
      plot3([f15in1(i,2)-
scale*f15in2(i,n)*f15in2(i,n+1)/2,f15in1(i,2)+scale*f15in2(i,n)*f15in2(i,n+1)/2],...
```

```
    [f15in1(i,3)-
scale*f15in2(i,n)*f15in2(i,n+2)/2,f15in1(i,3)+scale*f15in2(i,n)*f15in2(i,n+2)/2],...
    [f15in1(i,4)-
scale*f15in2(i,n)*f15in2(i,n+3)/2,f15in1(i,4)+scale*f15in2(i,n)*f15in2(i,n+3)/2],...
    'color','g','linewidth',2);
  end
  hold on;
  if f15in2(i,n1)>0
  plot3([f15in1(i,2)-
scale1*f15in2(i,n1)*f15in2(i,n1+1)/2,f15in1(i,2)+scale1*f15in2(i,n1)*f15in2(i,n1+1)/2],...
    [f15in1(i,3)-
scale1*f15in2(i,n1)*f15in2(i,n1+2)/2,f15in1(i,3)+scale1*f15in2(i,n1)*f15in2(i,n1+2)/2],...
    [f15in1(i,4)-
scale1*f15in2(i,n1)*f15in2(i,n1+3)/2,f15in1(i,4)+scale1*f15in2(i,n1)*f15in2(i,n1+3)/2],...
    'color','b','linewidth',2);
  else
    plot3([f15in1(i,2)-
scale1*f15in2(i,n1)*f15in2(i,n1+1)/2,f15in1(i,2)+scale1*f15in2(i,n1)*f15in2(i,n1+1)/2],...
    [f15in1(i,3)-
scale1*f15in2(i,n1)*f15in2(i,n1+2)/2,f15in1(i,3)+scale1*f15in2(i,n1)*f15in2(i,n1+2)/2],...
    [f15in1(i,4)-
scale1*f15in2(i,n1)*f15in2(i,n1+3)/2,f15in1(i,4)+scale1*f15in2(i,n1)*f15in2(i,n1+3)/2],...
    'color','y','linewidth',2);
  end
  hold on;
end

hold off;


f16.m

function [straw,separate]=f16(sx)

dr=0.001;%need to adjust later, ANSYS related
ds1=pi/48;%need to adjust later, ANSYS related

n=floor(0.03/dr);
ls=round(pi/2/ds1+1);
delta=(ls-1)/(n+1);

for i=1:(n+1)
  incycle(i,1)=round(ls-round((i-1)*delta));
  if incycle(i,1)~=1
    dsn(i,1)=pi/2/(incycle(i,1)-1);
  else
    dsn(i,1)=0;
  end
end
incycle(n+2,1)=1;
```

```
dsn(n+2,1)=0;

separate=flipud(incycle);

if sx==1
head(1,1)=0.03;
for i=1:n
    head(i+1,1)=head(1,1)-i*dr;
end
head(n+2,1)=0;
for j=1:n+2
    head(j,2)=pi/2;
    head(j,3)=0;
end
end

if sx==2
head(1,1)=0.03;
for i=1:n
    head(i+1,1)=head(1,1)-i*dr;
end
head(n+2,1)=0;
for j=1:n+2
    head(j,2)=pi/2;
    if head(j,1)<=0.03 & head(j,1)>=0.021339745%consider different model
        head(j,3)=0.01-sqrt(0.01^2-(head(j,1)-0.03)^2);
    else
        head(j,3)=0.005;
    end
end
end

if sx==3
head(1,1)=0.03;
for i=1:n
    head(i+1,1)=head(1,1)-i*dr;
end
head(n+2,1)=0;
for j=1:n+2
    head(j,2)=pi/2;
    if head(j,1)<=0.03 & head(j,1)>=0.02%consider different model
        head(j,3)=0.01-sqrt(0.01^2-(head(j,1)-0.03)^2);
    else
        head(j,3)=0.01;
    end
end
end

if sx==4
head(1,1)=0.03;
```

```matlab
for i=1:n
    head(i+1,1)=head(1,1)-i*dr;
end
head(n+2,1)=0;
for j=1:n+2
    head(j,2)=pi/2;
    if head(j,1)<=0.03 & head(j,1)>0.02%consider different model
        head(j,3)=0.01-sqrt(0.01^2-(head(j,1)-0.03)^2);
    else
        head(j,3)=0.015;
    end
end
end

if sx==5
head(1,1)=0.03;
for i=1:n
    head(i+1,1)=head(1,1)-i*dr;
end
head(n+2,1)=0;
for j=1:n+2
    head(j,2)=pi/2;
    if head(j,1)<=0.03 & head(j,1)>0.02%consider different model
        head(j,3)=0.01-sqrt(0.01^2-(head(j,1)-0.03)^2);
    else
        head(j,3)=0.02;
    end
end
end

k=0;
for u=1:n+2
    for v=1:incycle(u,1)
        straw(v+k,1)=head(u,1);
        straw(v+k,2)=head(u,2)+(v-1)*dsn(u,1);
        straw(v+k,3)=head(u,3);
    end
    k=k+incycle(u,1);
end
straw=flipud(straw);

f17.m

function f17out=f17(zuobiao,ev1,cp1,st)

A=cp1(1,5);
B=cp1(1,6);
C=cp1(1,7);
x0=cp1(1,1);
y0=cp1(1,2);
```

```
z0=cp1(1,3);
x1=st(1,1);
y1=st(1,2);
z1=st(1,3);
d3=st(1,4);

t=-(A*(x1-x0)+B*(y1-y0)+C*(z1-z0))/(C*d3);

x=x1;
y=y1;
z=z1+d3*t;

f17out=f18(x,y,z,zuobiao,ev1);
```

f18.m

```
function f18out=f18(x,y,z,zuobiao,ev1)

a=zuobiao(:,2:4);
b=[x,y,z];
k=dsearchn(a,b);
f18out=[x,y,z,ev1(k:k,2:5)];
```

f19.m

```
function f19out=f19(cp2,stz,z1)

tollerance=1e-5;%need to adjust by experence

if cp2(1,3)>stz+tollerance
    f19out=2;
elseif cp2(1,3)<z1-tollerance
    f19out=3;
    %{
    %the below two line is for check compressive zone, if use dominate
    %stress concept, we can remove it.
    elseif cp2(1,4)<0
    f19out=1;%reach compressive zone, think about it later
    %the above two line is for check compressive zone, if use dominate
    %stress concept, we can remove it.
    %}

else
    f19out=4;
end
```

```matlab
%{
elseif cp2(1,4)<0
    f19out=1;%reach compressive zone, think about it later
%}

f20.m

function f20(cp,x1,x2,y1,y2,z1,z2)

a=cp(:,1:3);
d=0.04;%this is radius of borehole used for normalization
axis([x1/d,x2/d,y1/d,y2/d,z1/d,z2/d]);
hold on;
axis equal;
hold on;
box on;
hold on;
%the following is tring to separate compressive zone and tensile zone
s=size(cp);
s1=s(1,1);
for i=1:s1
    if cp(i,4)<0
        plot3(a(i,1)/d,a(i,2)/d,a(i,3)/d,'ob','markerfacecolor','b');
    else
plot3(a(i,1)/d,a(i,2)/d,a(i,3)/d,'dg','markerfacecolor','g');
    end
end
hold on;


f21.m

function [straw,separate]=f21(lr,sx)

dr=0.001;%need to adjust later, ANSYS related
ds1=pi/48;%need to adjust later, ANSYS related

n=floor(0.03/dr);
ls=round(pi/2/ds1+1);
delta=(ls-1)/(n+1);

for i=1:(n+1)
    incycle(i,1)=round(ls-round((i-1)*delta));
    if incycle(i,1)~=1
        dsn(i,1)=pi/2/(incycle(i,1)-1);
    else
        dsn(i,1)=0;
    end
end
incycle(n+2,1)=1;
```

```
dsn(n+2,1)=0;

separate=flipud(incycle);
c=sum(separate);

if sx==1
head(1,1)=0.03;
for i=1:n
   head(i+1,1)=head(1,1)-i*dr;
end
head(n+2,1)=0;
for j=1:n+2
   head(j,2)=pi;
   head(j,3)=0;
end
end

if sx==2
head(1,1)=0.03;
for i=1:n
   head(i+1,1)=head(1,1)-i*dr;
end
head(n+2,1)=0;
for j=1:n+2
   head(j,2)=pi;
   if head(j,1)<=0.03 & head(j,1)>=0.021339745%consider different model
      head(j,3)=0.01-sqrt(0.01^2-(head(j,1)-0.03)^2);
   else
      head(j,3)=0.005;
   end
end
end

if sx==3
head(1,1)=0.03;
for i=1:n
   head(i+1,1)=head(1,1)-i*dr;
end
head(n+2,1)=0;
for j=1:n+2
   head(j,2)=pi;
   if head(j,1)<=0.03 & head(j,1)>=0.02%consider different model
      head(j,3)=0.01-sqrt(0.01^2-(head(j,1)-0.03)^2);
   else
      head(j,3)=0.01;
   end
end
end

if sx==4
```

```matlab
head(1,1)=0.03;
for i=1:n
   head(i+1,1)=head(1,1)-i*dr;
end
head(n+2,1)=0;
for j=1:n+2
   head(j,2)=pi;
   if head(j,1)<=0.03 & head(j,1)>0.02%consider different model
      head(j,3)=0.01-sqrt(0.01^2-(head(j,1)-0.03)^2);
   else
      head(j,3)=0.015;
   end
end
end

if sx==5
head(1,1)=0.03;
for i=1:n
   head(i+1,1)=head(1,1)-i*dr;
end
head(n+2,1)=0;
for j=1:n+2
   head(j,2)=pi;
   if head(j,1)<=0.03 & head(j,1)>0.02%consider different model
      head(j,3)=0.01-sqrt(0.01^2-(head(j,1)-0.03)^2);
   else
      head(j,3)=0.02;
   end
end
end

k=0;
for u=1:n+2
   for v=1:incycle(u,1)
      straw(v+k,1)=head(u,1);
      straw(v+k,2)=head(u,2)-(v-1)*dsn(u,1);
      straw(v+k,3)=head(u,3);
   end
   k=k+incycle(u,1);
end
straw=flipud(straw);

for a=1:n+2
   if straw(sum(separate(1:a,1))+1,1)>=lr
      b=a+1;
      break;
   end
end
separate=separate(b:n+2,1);
```

250

```matlab
straw=straw((c-sum(separate)+1):c,:);
yushu=rem(0.03-lr,dr);
if yushu~=0
   separate=[separate(1,1);separate];
   d=straw(1:separate(1,1),:);
 for l=1:separate(1,1)
   d(l,1)=d(l,1)-yushu;
 end
 straw=[d;straw];
end
```

f22.m

```matlab
function [straw,separate]=f22(lr,sx)

dr=0.001;%need to adjust later, ANSYS related
ds1=pi/48;%need to adjust later, ANSYS related

n=floor(0.03/dr);
ls=round(pi/2/ds1+1);
delta=(ls-1)/(n+1);

for i=1:(n+1)
   incycle(i,1)=round(ls-round((i-1)*delta));
   if incycle(i,1)~=1
      dsn(i,1)=pi/2/(incycle(i,1)-1);
   else
      dsn(i,1)=0;
   end
end
incycle(n+2,1)=1;
dsn(n+2,1)=0;

separate=flipud(incycle);
c=sum(separate);

if sx==1
head(1,1)=0.03;
for i=1:n
   head(i+1,1)=head(1,1)-i*dr;
end
head(n+2,1)=0;
for j=1:n+2
   head(j,2)=pi/2;
   head(j,3)=0;
end
end

if sx==2
```

```matlab
head(1,1)=0.03;
for i=1:n
   head(i+1,1)=head(1,1)-i*dr;
end
head(n+2,1)=0;
for j=1:n+2
   head(j,2)=pi/2;
   if head(j,1)<=0.03 & head(j,1)>=0.021339745%consider different model
      head(j,3)=0.01-sqrt(0.01^2-(head(j,1)-0.03)^2);
   else
      head(j,3)=0.005;
   end
end
end

if sx==3
head(1,1)=0.03;
for i=1:n
   head(i+1,1)=head(1,1)-i*dr;
end
head(n+2,1)=0;
for j=1:n+2
   head(j,2)=pi/2;
   if head(j,1)<=0.03 & head(j,1)>=0.02%consider different model
      head(j,3)=0.01-sqrt(0.01^2-(head(j,1)-0.03)^2);
   else
      head(j,3)=0.01;
   end
end
end

if sx==4
head(1,1)=0.03;
for i=1:n
   head(i+1,1)=head(1,1)-i*dr;
end
head(n+2,1)=0;
for j=1:n+2
   head(j,2)=pi/2;
   if head(j,1)<=0.03 & head(j,1)>0.02%consider different model
      head(j,3)=0.01-sqrt(0.01^2-(head(j,1)-0.03)^2);
   else
      head(j,3)=0.015;
   end
end
end

if sx==5
head(1,1)=0.03;
for i=1:n
```

```
      head(i+1,1)=head(1,1)-i*dr;
   end
   head(n+2,1)=0;
   for j=1:n+2
      head(j,2)=pi/2;
      if head(j,1)<=0.03 & head(j,1)>0.02%consider different model
         head(j,3)=0.01-sqrt(0.01^2-(head(j,1)-0.03)^2);
      else
         head(j,3)=0.02;
      end
   end
end

k=0;
for u=1:n+2
   for v=1:incycle(u,1)
      straw(v+k,1)=head(u,1);
      straw(v+k,2)=head(u,2)+(v-1)*dsn(u,1);
      straw(v+k,3)=head(u,3);
   end
   k=k+incycle(u,1);
end
straw=flipud(straw);

for a=1:n+2
   if straw(sum(separate(1:a,1))+1,1)>=lr
      b=a+1;
      break;
   end
end
separate=separate(b:n+2,1);


straw=straw((c-sum(separate)+1):c,:);
yushu=rem(0.03-lr,dr);
if yushu~=0
   separate=[separate(1,1);separate];
   d=straw(1:separate(1,1),:);
 for l=1:separate(1,1)
   d(l,1)=d(l,1)-yushu;
 end
 straw=[d;straw];
end

f23.m

function [straw,separate]=f23(ideal)

lr=ideal(1,2);
thita=ideal(1,3);
```

```
lz=ideal(1,4);

dr=0.001;%need to adjust later, ANSYS related
ds1=pi/48;%need to adjust later, ANSYS related

n=floor(0.03/dr);
ls=round(pi/2/ds1+1);
delta=(ls-1)/(n+1);

for i=1:(n+1)
   incycle(i,1)=round(ls-round((i-1)*delta));
   if incycle(i,1)~=1
      dsn(i,1)=pi/2/(incycle(i,1)-1);
   else
      dsn(i,1)=0;
   end
end
incycle(n+2,1)=1;
dsn(n+2,1)=0;

separate=flipud(incycle);
c=sum(separate);

head(1,1)=0.03;
for i=1:n
   head(i+1,1)=head(1,1)-i*dr;
end
head(n+2,1)=0;
for j=1:n+2
   head(j,2)=pi;
   if head(j,1)<=0.03 & head(j,1)>=0.02
      head(j,3)=0.01-sqrt(0.01^2-(head(j,1)-0.03)^2);
   else
      head(j,3)=0.01;
   end
end

k=0;
for u=1:n+2
   for v=1:incycle(u,1)
      straw(v+k,1)=head(u,1);
      straw(v+k,2)=head(u,2)-(v-1)*dsn(u,1);
      straw(v+k,3)=head(u,3);
   end
   k=k+incycle(u,1);
end
straw=flipud(straw);

for a=1:n+2
   if straw(sum(separate(1:a,1))+1,1)>lr
```

```
        b=a+1;
        break;
    end
end
separate=separate(b:n+2,1);
straw=straw((c-sum(separate)+1):c,:);

ls1=round((thita-pi/2)/(ds1/2)+1);
separate=[ls1;separate];
yushu=rem((thita-pi/2),(ds1/2));

straw1(1,1)=lr;
straw1(1,2)=thita;
straw1(1,3)=lz;
straw1(2,1)=lr;
straw1(2,2)=thita-yushu;
straw1(2,3)=lz;
for t=3:ls1
    straw1(t,1)=lr;
    straw1(t,2)=straw1(t-1,2)-(ds1/2);
    straw1(t,3)=lz;
end

straw=[straw1;straw];

f24.m

function [original,ideal,jiaodu]=f24(zuobiao,stress)

cylin=f1(zuobiao);%cartesian change to cylindrical coordinate

tensor=f2(stress);

ev=f3(tensor);

ev1=f12(ev);

tollerance=1e-9;
a=find(cylin(:,2)>0.02-tollerance & cylin(:,2)<0.03+tollerance & ...
    cylin(:,3)>pi/2-tollerance & cylin(:,3)<pi/2+tollerance &...
    cylin(:,4)>-tollerance & cylin(:,4)<0.01+tollerance);
cylina=cylin(a,:);
ev1a=ev1(a,:);
N=max(max(ev1a(:,2)));
[r,c]=find(N==ev1a);
originala(1:1,1:4)=cylina(r:r,1:4);
originala(1:1,5:8)=ev1a(r:r,2:5);

tollerance=1e-9;
b=find(cylin(:,2)>0.02-tollerance & cylin(:,2)<0.03+tollerance & ...
```

```matlab
        cylin(:,3)>pi-tollerance & cylin(:,3)<pi+tollerance &...
        cylin(:,4)>-tollerance & cylin(:,4)<0.01+tollerance);
cylinb=cylin(b,:);
ev1b=ev1(b,:);
N=max(max(ev1b(:,2)));
[r,c]=find(N==ev1b);
originalb(1:1,1:4)=cylinb(r:r,1:4);
originalb(1:1,5:8)=ev1b(r:r,2:5);

if originala(1,5)>=originalb(1,5)
    original=originala;
    ideal=[original(:,1:2),pi/2,original(:,4:8)];
    jiaodu=1;
else
    original=originalb;
    ideal=[original(:,1:2),pi,original(:,4:8)];
    jiaodu=3;
end


f25.m

function f25(cp,z1,z2)

a=cp(:,1:3);
[thita,r,z]=cart2pol(a(:,1),a(:,2),a(:,3));
b=size(r);
b=b(1,1);
tollerance=1e-5;%need to adjust by experance
c=1;
for i=1:b
    if r(i,1)<(0.02+tollerance) & r(i,1)>(0.02-tollerance)
        xthita(c,1)=(pi-thita(i,1))*180/pi;
        yr(c,1)=r(i,1);
        zz(c,1)=z(i,1);
        c=c+1;
    end
end

axis([0,90,z1,z2]);
hold on;
plot(xthita,zz,'d');
hold off;
```